Structure and electronic properties of Ge-based 2D crystals

Davide Sciacca

Université de Lille

iemn

Université de Lille

École Doctorale Sciences Pour l'Ingénieur

IEMN - Institut d'électronique de microélectronique et de nanotechnologie

Thesis to be defended by Davide SCIACCA

On the 25th January, 2021

In order to become Doctor from Université de Lille

Academic Field **Electronic, microelectronic, nanoelectronic and micro-waves**

Structure and electronic properties of Ge-based 2D crystals

Structure et propriétés électroniques des matériaux 2D à base de germanium

Thesis supervised by	Bruno GRANDIDIER	Supervisor
	Pascale DIENER	Co-Supervisor

Committee members

Referees	Andrew MAYNE	ISMO (Orsay)	
	Laurence MASSON	CINaM (Marseille)	
Examiners	Henri HAPPY	IEMN (Lille)	Committee President
	Geoffroy PREVOT	INSP (Paris)	
Supervisors	Bruno GRANDIDIER	IEMN (Lille)	
	Pascale DIENER	ISEN - IEMN (Lille)	

Contents

Introduction **5**

1 Context: Germanene and 2D materials **7**
1.1 2D stability . . . 7
1.2 Graphene electronic properties . . . 9
1.2.1 Corrections and sublattice asymmetry . . . 14
1.2.2 Landau Levels and Quantum Hall Effect . . . 14
1.2.3 Spin-orbit coupling and Quantum Spin Hall Effect . . . 16
1.3 Alternatives to graphene: group IV elements . . . 18
1.3.1 Germanene on Al(111) . . . 21
1.4 Germanane . . . 27
1.4.1 GeH . . . 27
1.4.2 $GeCH_3$ . . . 29

2 Methods **33**
2.1 Scanning Tunneling Microscopy . . . 33
2.1.1 The tunnel effect . . . 33
2.1.2 Expression of the tunnel current . . . 34
2.1.3 Building a real microscope . . . 36
2.2 Scanning Tunneling Spectroscopy . . . 39
2.2.1 Distance versus bias: z(V) . . . 39
2.2.2 Current vs distance: I(z) . . . 39
2.2.3 Current vs bias: I(V) . . . 40
2.2.4 Lock-in amplifier . . . 41
2.2.5 Current Imaging Tunneling Spectroscopy . . . 46
2.2.6 Temperature broadening . . . 47
2.3 Artefacts in STM/STS . . . 48
2.4 The Omicron LT-STM . . . 53
2.5 Multi-probe STM . . . 56
2.5.1 Probe-spacing dependence . . . 56
2.5.2 Other 4-points resistance configurations . . . 58
2.6 Omicron 4-probe RT-STM . . . 60
2.7 Density Functional Theory . . . 62
2.7.1 The many-body problem . . . 62
2.7.2 The Hohenberg-Kohn theorem and Kohn-Sham equations . . . 63
2.7.3 Exchange-correlation functional . . . 66
2.7.4 From pseudopotentials to PAW . . . 67
2.7.5 Iterative schemes for ionic relaxation . . . 70
2.7.6 Iterative schemes for Kohn-Sham eigenstates . . . 71

2.7.7 VASP input and outputs . . . 72
2.7.8 Simulation of STM images . . . 74
2.7.9 Projected Density of States calculation . . . 75
2.7.10 Molecular dynamics calculation . . . 76

3 Scanning Tunneling Spectroscopy of Germanene on Al(111) 77
3.1 Growth of germanene on Al(111) . . . 78
3.2 Germanene spectroscopic characterization . . . 81
3.3 Tip-induced evolution of germanene islands . . . 85
3.4 Tip artefacts in spectroscopy of a 2D material . . . 87

4 Germanene edges on Al(111) 91
4.1 STM/STS of germanene nanosheet edges on Al(111) . . . 92
4.2 Theoretical investigation of the Ge/Al(111) interface . . . 96
4.2.1 Crystal structure from STM measurements . . . 96
4.2.2 Comparison of the growth mechanism of silicene and germanene . . . 96
4.2.3 Adsorption of Ge on Al(111) . . . 98
4.3 3×3 germanene nanosheet on Al(111): full Ge structure . . . 102
4.3.1 Simulated STM contrast of the nanosheet edge . . . 102
4.3.2 The particular case of the 145° oriented edge . . . 105
4.4 3×3 germanene nanosheet on Al(111): Al as top atom on the edge . . . 107
4.4.1 Simulated STM contrast of the edge . . . 107
4.4.2 The particular case of the 145° oriented edge . . . 109
4.5 Composition of the 3×3 germanene nanosheet on Al(111) with incomplete unit cell on the edge . . . 110
4.6 $\sqrt{7} \times \sqrt{7}$ germanene nanosheet on Al(111) edges . . . 115

5 Transport properties of $GeCH_3$ 117
5.1 $GeCH_3$ synthesis . . . 118
5.2 Choice for a host substrate . . . 118
5.3 Chemical composition of the microflakes . . . 121
5.4 Adhesion of the microflakes on the substrate . . . 125
5.5 Analysis of the charging under SEM irradiation . . . 128
5.6 Transport properties . . . 131
5.6.1 Transport in non-hydrated microflakes . . . 131
5.6.2 Transport in hydrated microflakes . . . 140

Conclusion 145

Abstract

In this thesis, we have studied the properties of two 2D materials made of germanium: germanene, the equivalent of graphene, and a multilayer stack of germanene terminated with methyl groups. Due to a buckled atomic structure and a strong spin orbit coupling, these materials stand out from graphene and graphite. Although much studied in theory, their physical properties remain little characterized.

In the case of germanene, the study of this material was carried out by depositing germanium on an aluminum (111) surface in ultra-high vacuum. For relatively low temperatures, around 100° C, the growth of germanene is epitaxial with two structures: the (3×3) reconstruction and the ($\sqrt{7} \times \sqrt{7}$) reconstruction. Scanning tunneling microscopy has been used to deepen our knowledge of these phases. First of all, we were interested in the electronic properties. Spectroscopic measurements were carried out at temperatures of 77K and 5K. Unfortunately, they did not reveal the true nature of germanene due to the strong electronic coupling of this material with the aluminum surface.Throughout an unexpected diversity of spectra, this analysis showed the weak adhesion of germanene to the Al(111) surface, which leads to frequent contamination of the apex of the tip of the microscope by atoms of the area.

In addition to spectroscopic measurements, the growth of small-sized sheets enabled the study of the edge structure. Observations by tunneling microscopy showed that these sheets grow in the plane of the aluminum atomic terraces. Their edges generally present a clearer contrast than the rest of the sheet. To better understand this change of contrast, ab-initio calculations based on density functional theory (DFT) have been performed. They showed the key role of aluminum atoms in the formation of edges, with both zigzag or armchair structures.

Unlike single-sheet germanene which requires an epitaxial growth, germanane crystals can be chemically synthesized, which ensures the electronic decoupling of the material from its environment. We carried out a multi-physics analysis of such crystals passivated by methyl groups, which revealed two types of crystals. The largest, around 10 micrometres in lateral dimension, are polycrystalline, contain water molecules intercalated between the layers or have oxidized surfaces and become charged under electron irradiation due to the presence of isopropanol at the interface with the host substrate. The smallest, identified as the purest, are the most prone to being characterized by ultra-high vacuum four-probe transport measurements. These measurements showed a transport of holes, which occurs in the volume of the microstructure. This unexpected bulk transport for a lamellar material suggests the presence of defects and imperfection in the plane of the layers, which calls for a better control of the synthesis of these crystals.

Résumé

Dans cette thèse, nous avons étudié les propriétés de deux matériaux 2D constitués de germanium: le germanène, l'équivalent du graphène, et un empilement multicouche de germanane à terminaison méthyle. En raison d'une structure atomique gauchie et d'un couplage spin orbite important, ces matériaux se démarquent du graphène et du graphite. Bien que très étudiés théoriquement, leurs propriétés physiques restent encore peu caractérisées.

Dans le cas du germanène, l'étude de ce matériau a été réalisée en déposant du germanium sur une surface d'aluminium (111) sous ultravide. Pour des températures de croissance relativement basses, autour de 100°C, le germanène est épitaxié avec deux structures: la phase (3×3) et la phase ($\sqrt{7} \times \sqrt{7}$). La microscopie à effet tunnel a été utilisée pour approfondir notre connaissance de ces phases. Dans un premier temps nous nous sommes intéressés aux propriétés électroniques. Des mesures spectroscopiques par microscopie à effet tunnel ont été réalisées à des températures de 77K et 5K. Elles n'ont malheureusement pas permis de conclure quant à la véritable nature du germanène en raison du fort couplage électronique de ce matériau avec la surface d'aluminium. Toutefois, au travers d'une diversité inattendue de spectres, cette analyse a révélé la faible adhésion du germanène à la surface Al(111), ce qui conduit à une contamination fréquente de l'apex de la pointe du microscope par les atomes de la surface.

Parallèlement aux mesures spectroscopiques, la croissance de feuillets aux dimensions réduites a permis d'étudier la structure des bords des feuillets. Les observations par microscopie à effet tunnel montrent que ces feuillets croissent dans le plan des terrasses atomiques d'aluminium. Leurs bords présentent généralement un contraste plus clair que le reste du feuillet. Pour mieux comprendre ce changement de contraste, des calculs ab-initio basés sur la théorie de la fonctionnelle de la densité (DFT), ont été développés. Ils ont montré le rôle clé des atomes d'aluminium dans la formation des bords possédant quelque soit la structure zigzag ou "armchair".

A l'inverse du germanène mono-feuillet qui requiert une épitaxie, des cristaux de germanane peuvent être synthétisé par voie chimique, ce qui assure un découplage électronique du matériau avec son environnement. Nous avons réalisé une analyse multiphysique de tels cristaux passivés par des groupements méthyles, qui révèlent deux types de cristaux. Les plus gros, autour de 10 μm de dimension latérale, sont polycristallins, recèlent des molécules intercalées entre les feuillets ou possèdent des surfaces oxydés et se chargent sous irradiation électronique en raison de la présence d'isopropanol à l'interface avec le substrat hôte. Les plus petits, identifiés comme les plus purs, sont les plus enclins à être caractérises par des mesures de transport à quatre pointes en ultravide. Ces mesures ont montré un transport de trous, qui se produit en volume. Ce résultat inattendu pour un matériau lamellaire suggère la présence de défauts et d'imperfection dans le plan des feuillets qui appellent à un meilleur contrôle de la synthèse des cristaux pour rendre possible l'étude des propriétés physiques fondamentales de ces cristaux.

Acknowledgements

My PhD thesis was long and complicated. A research project is already a bet in itself, but when things go south, not working as expected, you really start wandering in unexplored lands. It is difficult to come out of them alone. I was not.

First, I would like to express my gratitude to all the members of the Physics group at IEMN. My supervisor Bruno Grandidier and my co-supervisor Pascale Diener chose me 3 years and a half ago for the Germanene project and supported me along the way in a very professional way, helping to find new paths to follow when we were stuck in dead-ends. Maxime Berthe taught me about tunneling microscopy and he was always available for a conversation about my discovery of his region, the North. Isabelle Lefebvre taught me DFT and she was always available for help. Louis Biadala, while technically uninvested in my thesis, gave me a lot of useful advises and he was a nice companion in chill moments. Yannick Lambert helped me along the way, particularly in the few times I put my feet in the clean room. I need also to thank all the administrative assistants, Florence Senez, Emmanuelle Gillman, Nora Benbahlouli and Andy Ledent: my coming from abroad demanded often more work than usually necessary.

While in Lille, I met a lot of other wonderful people. First, my three PhD companions along the way: Nemanja, Vincent and Nathali. I can not describe how easier it was to go along this path thanks to them. We were complementary in a lot of a manners and it is strange to part our ways now. A special thanks to Vincent, because we arrived together and I would have spent a lot of evenings alone at home if it was not for him. There are other PhDs and post-doc to thank, I will name just a few: Pierre, Hugo, Cécile, Michel and Kamila. We established a very pleasant group, and I wish them good luck for the time left in IEMN.

I need to thank also my various roommates during the years. Garance was my cinema companion and we discovered Lille together; Daphné shared with me her love for life and taught me a lot by being so different from me; finally, Arthur and Thibaut, we made a good trio and I am sad to leave you behind.

Living abroad means leaving people behind, so a special thanks goes to all the people that helped me at a distance and fought with me to keep our friendship alive: Giulio, Valentina, Chiara and Marco are the main ones, but the list should go on. I received a lot of support also by the SWGOH guild, especially while I was working during the night: someone was always awake to keep me company.

My family always supported my choices and gave me the opportunity to follow the path I wanted: thanking them is not enough for their encouragement and unconditional love. I would have wanted to be nearer to my grandmother who fought with cancer during these years, and my brother who started university, possibly his biggest challenge so far, especially now during the Covid pandemic.

Finally, I need to thank my girlfriend Erika. It is almost four years that we started this adventure together, and being apart has not been easy. During the PhD she saw me at my lowest, and she has always been by my side.

Introduction

Two-dimensional (2D) materials have provided an incredible number of toy systems to test exotic physics as never before, as the Quantum Hall Effect [1], Quantum Spin Hall Effect [2], topological states of matter and unconventional superconductivity [3], representing an unprecedented success for condensed matter physics.

However, not all the properties of 2D materials' building blocks are equally known nowadays. When the limitations of graphene started to hinder the applications (due to the lack of an energy gap and the difficulty of large scale production), other naturally layered materials received attention. Technological advances allowed the creation of artificial graphene layers, when the lateral confinement is induced via a carefully produced patterning of a 2D electron gas [4]. On the other hand, elements that prefer an sp^3 hybridization have been forced in a 2D shape thanks to the epitaxial deposition on a substrate. This is the case of the analogues of graphene with elements of the IV group, meaning silicon and germanium. These equivalents, thanks to different chemical properties, would allow the exploitation of the topological physics that graphene has hidden in an inaccessible temperature range. However, these analogues of graphene can only be stabilized by a host substrate. Therefore, to be able to benefit from their properties, it is crucial to first understand how the interaction with the substrates modifies the properties of the 2D layer. This was the initial goal of the thesis dealing with the synthesis of germanene on Al(111).

This dissertation is divided in five chapters. The first one introduces the reader to the Dirac and exotic physics of graphene and how this evolves when others similar elements are considered. The experimental synthesis of Si and Ge structures are analysed, focusing in particular on germanene on Al(111), which will be the focus of the following research. The chapter ends presenting a chemical route to obtain a multilayer functionalized version of germanene ($GeCH_3$), promoted by the separation from the substrate properties and the possibility of exploitation of the Quantum Spin Hall Effect at room temperature as for the monolayer counterpart.

The second chapter describes the experimental techniques required for the characterization of the electronical properties of the Ge/Al(111) and $GeCH_3$ systems: single-probe and multi-probe scanning tunneling microscope, and the theoretical framework to interpret the experimental observations, density functional theory.

The third chapter focuses on the synthesis in ultra-high vacuum of germanene on Al(111) and the study of its electronic properties via scanning tunneling spectroscopy. It will be shown that the reconstruction induced by the presence of Al(111) and the interaction with the substrate hinder the analysis of the properties of the free-standing germanene. A rationalization of the unexpected variety of spectra will reveal a weak adhesion of germanene to the Al(111) and the necessity of a reference in tunneling spectroscopy for 2D materials, a practice often overlooked.

The fourth chapter will combine density functional theory and tunneling experiments to analyze the interface between germanene and Al(111). The interest resides in the fascinating physics of the 2D material edges. The experimental observations will be explained via the key role of aluminium atoms in the formation of the edges.

In order to get rid of the deleterious interaction with a host substrate, the last chapter will focus on $GeCH_3$ flakes. In contrast to the previous single germanene layers from vapor, the $GeCH_3$ microflakes are chemically synthesized. A thorough multi-physics analysis of these microstructures will classify them into two categories depending on their chemical and mechanical properties. Such an identification will be essential to account for the limited transport properties of the microflakes.

Chapter 1

Context: Germanene and 2D materials

1.1 2D stability

The physical intuition acquired in the solid state physics class tells us that there is nothing keeping a 2D layer from falling apart. Compared to the cohesion energy, thermal oscillations in the z direction are generally big enough to let a first atom escape. After that, the neighbouring atoms will feel the absence of the attractive/repulsive force exerted by the missing atom and eventually force the material to a 3D configuration to minimize energy.

Peierls and Landau where the first to address the problem of the stability of low dimensional materials [5, 6]. Peierls used two approaches, a qualitative one for the general one-dimensional case and a quantitative one based on the harmonic approximation. The qualitative argument stands on the fact that in one dimension every atom divides the chain in two parts. If we artificially move one atom to the right, and consequently all the right half-chain, the left half will not feel the out-of-equilibrium because this atom is the only intermediary. This is not true in 3D: there are infinite paths to connect two atoms, even if some atoms are displaced.

To prove it rigorously, Peierls took a crystal lattice composed of N atoms of mass M. We can write the displacement vector of an atom at distance m from the equilibrium as a periodic function, composition of traveling waves:

$$u_m = \frac{1}{\sqrt{N}} \sum_f \sum_{j=\pm 1} b_{fj} e^{i(f \cdot m + w_{fj} t)} \tag{1.1}$$

where f is a real number with $-\pi < f < \pi$ that indicates the axis of propagation of the single wave, j in which direction the wave propagates and w_{fj} its frequency. A similar equation holds for the displacement in 3D, apart from a sum from $j = \pm 1$ to ± 3. The total energy is equal to $E = M \sum_f \sum_j |b_{fj}|^2 w_{fj}^2$. The equivalent energy in a quantum harmonic oscillator is given by $E = \frac{1}{2} \sum_f \sum_j N_{fj} \hbar w_{fj}$, where $N_{fj} = 0, 1, 2, ..$ is the quantum number. The comparison between the two equations gives us the coefficient $b_{fj} = \sqrt{\frac{\hbar}{2M w_{fj}}} N_{fj}$.

To test the stability and demonstrate the difference between the 1D and the 3D case, it is necessary to study the displacements between two atoms, m and m', at a finite temperature T. A single value is not representative, an average on the possible configurations via their statistical probability is needed. In the thermal equilibrium, the statistical average of N_{fj} is given by the Planck equation:

$$\bar{N_{fj}} = \frac{1}{e^{\frac{\hbar w_{fj}}{kT}} - 1} \tag{1.2}$$

In the limit of high temperatures, where the $\hbar w / kT$ factor is small, the exponential can be developed

to obtain:

$$\bar{N_{fj}} = \frac{kT}{\hbar w_{fj}} - \frac{1}{2} \tag{1.3}$$

The average displacements between two atoms for the 1D case in the high temperature limit is then given by:

$$(u_m - u_{m'})^2 = 2\frac{1}{2\pi}\int df \frac{\hbar}{2Mw_{fj}}[1-\cos(f, m-m')]N_{fj} = \frac{kT}{\pi M}\int df \frac{1-\cos(f,m-m')}{w_f^2} \tag{1.4}$$

The factor $1/2\pi$ comes from the substitution of the sum on f with an integral. In 3D along the x direction the equation is more complicated:

$$\begin{aligned}(u_m - u_{m'})_x^2 &= \frac{2}{(2\pi)^3}\sum_j \int\int\int df_x df_y df_z\, \epsilon_{fj}^{x2}\, \frac{kT}{2Mw_{fj}^2}[1-cos(f,m-m')] = \\ &= \frac{kT}{M(2\pi)^3}\sum_j \int\int\int df_x df_y df_z \frac{\epsilon_{fj}^{x2}}{w_{fj}^2} - \sum_j \int\int\int df_x df_y df_z\, \frac{\epsilon_{fj}^{x2}}{w_{fj}^2} cos(f, m-m')\end{aligned} \tag{1.5}$$

where $\epsilon = e^{if}$ and $\epsilon^x = e^{i\sum_{fj} f N_{fj}}$. The same equation is valid for y and z.

In 3D we can proceed in the following way: every integral is finite, the first does not depend on $(m-m')$ while the second goes to zero for big values of that difference. The first integral gives then the limite of fluctuation for an infinitely big distance. When the gap between two atoms goes to infinity, the fluctuation between these two atoms tends to a finite number, which in the case of low enough temperature is shorter than the lattice parameter. In 1D we can't divide the integral in two terms: in fact both would diverge because now the volume element is df instead of f^2df, which does not compensate the denominator that goes to zero for $f = 0$. Now the main contribution to the integral comes from big waves ($f \sim 0$): it is then possible to take the sound speed as constant and extend the integral to infinity. The result is:

$$(u_m - u_{m'})^2 = \frac{2kTd^2}{2\pi Mv^2}|m-m'|\int_{-\infty}^{\infty}\frac{1-cosx}{x^2}dx = \frac{kT}{Mv^2}d|m-m'| \tag{1.6}$$

In conclusion, fluctuations depend on the square root of the distance if we assume a one dimensional chain in the harmonic approximation. This demonstration can be quite easily extended to the 2D case, showing there cannot be a long-range ordered structure.

However, the harmonic approximation is not valid in every context and from the anharmonic properties of a material rise a lot of interesting physics. Another and more general approach is needed. In the meantime, L. Landau developped his theory of phase transitions and used it to answer to the question of 2D stability. According to the Landau theory, the transition is related to a broken symmetry of the system. In the words of Landau:

> One even finds the strange statement that there is no essential difference at all between liquids and crystals, and that continuous transitions between them are possible. However, liquids differ essentially from crystals in that they are isotropic in contrast to anisotropic crystals. Every transition from a crystal to a liquid or to a crystal of a different symmetry is associated with the disappearance or appearance of some elements of symmetry. But elements of symmetry are either present or absent; no intermediate case is possible. Therefore, continuous transitions (in the same sense that transitions between liquid and gas are continuous) connected with change of the symmetry of the body are absolutely impossible.

In fact the work of Landau came not so long after the first exact formulation of crystal lattice given by Peierls and based on the role of correlations at infinity that we just discussed. The interest of Landau was for those transitions where the state of the body (specifically the energy) changes continuously even though the symmetry changes discontinuously: second-order phase transitions. His conclusion was:

> Besides phase transitions, the only other possible transitions are those continuous in the sense that, at the transition point, no jump in the state of the body occurs (in particular, there is no latent heat), but the symmetry changes suddenly. Such transitions are inevitably followed by a jump in the specific heat. These transitions are related to transition of a crystal to the disordered state.

Landau was then convinced of the unlikelihood of a phase transition from a 3D-symmetry to a 2D-symmetry maintaining ordered state. Unfortunately, also Landau theory is known to be misleading near critical points, so this can not be considered a generalized demonstration.

In 1967, Hohenberg [7] applied statistical physics and the Bogoliubov inequality to the cases where there is a broken symmetry. In particular, he concluded on the impossibility of having long range orders such as superconductivity and superfluidity in one and two dimensions. On the contrary, some computer experiments had already indicated a transition to a 2D crystalline ordered state, like the study of Alder on phase transitions in elastic disks [8]. The approach of Hohenberg should then be extended. The interaction considered so far was in fact too local to be applied to a crystal. In superfluidity and superconductivity, the energies of order-destroying fluctuations are kinetic, and therefore they are not affected by the number of particles interacting with a single one. In a crystal, the important energy is not kinetic, but potential: every atom could in principle diffuse and interact with all the other particles. The pair potential has then to satisfy restrictions which were not necessary before.

This extension was made by Mermin in 1968 [9], and it seemed to rule out the conventional crystalline long-range order in two dimensions for power-law potentials of the Lennard-Jones type.

However, the door was not closed. In 1987 Nelson and Peliti [10] performed a theoretical study on the intricate interplay between crystalline order and thermal fluctuations in crystalline membranes. They showed that the anharmonic coupling between in-plane and out-of-plane lattice vibrations is of crucial importance for the stability of a membrane: without this anharmonic coupling the membrane would be crumpled. As a result of this anharmonic coupling, the membrane becomes overall more or less flat, but it displays strong intrinsic corrugations (ripples) that are characterized by a power-law behaviour of the atomic-displacement correlations functions. The system remains approximately 2D (with typical out-of-plane displacements that are much smaller than the sample size) and approximately crystalline (with a crystalline order which is preserved at finite, but very large distances). The anharmonic properties are then responsible for an interesting and counterintuitive phenomenon.

1.2 Graphene electronic properties

Despite the study of Nelson and Peliti the synthesis of a bidimensional free-standing layer lagged behind, and this in spite of its big practical interest. Modern technology is extensively based on the possibility of controling electronic properties of a material by applying an external field, and the focus had mostly been on semiconductors. However, scaling these kind of materials and in particular oxides is no longer the suitable way to increase the performance of devices, because the limit where the quantum processes are more important than the classical laws of transport has been reached. The temptation to develop an all-metallic transistor that could be scaled down to much smaller sizes, consuming less energy and operating at high frequency, has been present for a long

time in the scientific community. The limitation for this application is the requirement of atomically thin metal films, due to the electric field screening at extremely short distances, even less than 1 nanometer. Furthermore, the surface charge that can be induced by field effect is small compared to usual bulk carrier concentrations. An atomic thickness could not be produced until 2004 in any metal: thermodynamically unstable and discontinuous films were the only product available. This resulted in no notable field effect (superior to 1%) observed for any metal or semimetal.

In their seminal paper "Electric field effect in atomically thin carbon films" published on Science [11] in 2004, Andrej Gejm and his colleagues at the University of Manchester in the UK reported the creation of single graphene sheets by peeling them off from a graphite substrate using scotch tape (a process later called mechanical exfoliation), transferred the sheets on top of a SiO_2 substrate and characterized them there, distinguishing between single and multiple layers via an optical microscope. Later on it was found that graphene does not need a substrate to be stable, but can be freely suspended from a scaffolding [12], separating its properties from those induced by the substrate; furthermore, bilayer [13] and multilayer sheets [14] can be prepared and characterized.

Previously disguised also in carbon nanotubes [15], a graphene sheet rolled into a cylinder, and fullerenes [16], small areas of a graphene sheet sewn together to form an approximately spherical surface, graphene is interesting also for its electronic proprties. Described back in 1947 [17] and reprised recently [18], the electronic structure of graphene has a linear dispersion around the Fermi level and as a consequence the charge carriers are Dirac fermions [19].

Let us consider a perfectly flat and free-standing graphene sheet. The electronic structure of an isolated C atom is $(1s)^2(2s)^2(2p)^4$: in a solid-state environment the 1s electrons remain inert, while the 2s and 2p electrons hybridize. If four sp^3 orbitals are created, establishing a tetrahedral bonding pattern, the result is diamond, a good insulator of $\sim 5eV$. The alternative is the honeycomb lattice of graphene: three sp^2 orbitals, forming 120° angles in a plane, leaving outside a pure p-orbital.

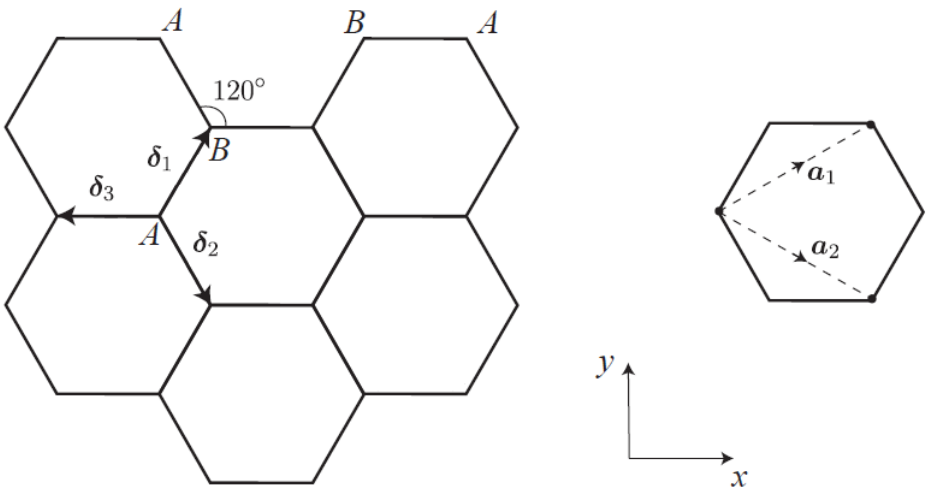

Figure 1.1: Honeycomb lattice with two inequivalent sublattices.

The honeycomb lattice is not a Bravais lattice, but it is composed by two inequivalent hexagonal sublattices, here labeled A and B. One sublattice environment is the mirror image of the atoms of the other sublattice. For the crystal description, it is convenient to choose as primitive lattice vectors of the Bravais lattices A (the components are an $x - y$ function):

$$\vec{\mathbf{a}}_1 = \tfrac{a}{2}(3, \sqrt{3}), \quad \vec{\mathbf{a}}_2 = \tfrac{a}{2}(3, -\sqrt{3}) \tag{1.7}$$

where a is the nearest-neighbor C-C distance (~ 1.42 Å) and $\vec{a}_i$ have been chosen as in figure 1.1. For an A-sublattice atom, the three nearest neighbor vectors in real space are then given by:

$$\vec{\delta}_1 = \frac{a}{2}(1,\sqrt{3}), \quad \vec{\delta}_2 = \frac{a}{2}(1,-\sqrt{3}), \quad \vec{\delta}_3 = -a(1,0) \tag{1.8}$$

with those for the B-sublattice being the negative of these.

The reciprocal lattice vectors $\vec{k}_1$ and $\vec{k}_2$ are defined by the condition $\vec{a}_i\,\vec{k}_j = 2\pi\delta_{ij}$:

$$\vec{\mathbf{k}}_1 = \frac{2\pi}{3a}(1,\sqrt{3}), \quad \vec{\mathbf{k}}_2 = \frac{2\pi}{3a}(1,-\sqrt{3}) \tag{1.9}$$

The First Brillouin Zone (FBZ) of the reciprocal lattice is obtained in the standard way, as bounded by the planes bisecting the vectors to the nearest reciprocal lattice points. The resulting FBZ is an hexagon rotated with respect to the original honeycomb by $\pi/2$.

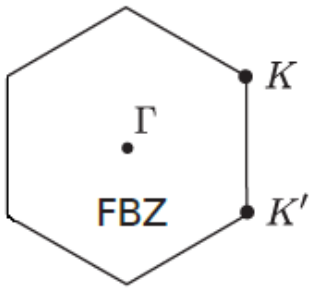

Figure 1.2: First Brillouin Zone of the honeycomb lattice.

As for the direct lattice, two mirror sublattices are present. Between the six points at the corners of the FBZ, two groups of three are equivalent, so we can consider in the following only two inequivalent corners that we label K and K' as in the figure 1.2. Their positions in momentum space are given by:

$$\vec{\mathbf{K}} = \frac{2\pi}{3a}(1,\tfrac{1}{\sqrt{3}}), \quad \vec{\mathbf{K}}' = \frac{2\pi}{3a}(1,-\tfrac{1}{\sqrt{3}}) \tag{1.10}$$

The basic approach to derive the electronic band structure of graphene is a Tight-Binding (TB) model where we consider only the hopping between nearest neighbors $\vec{\delta}_i$ $(i = 1, 2, 3)$. The relevant atomic orbital is the single π C orbital which is oriented normal to the plane of the lattice, left unfilled by the bonding electrons but able to accommodate two electrons with spin projection ± 1. We need the Hamiltonian of the system. To write it, we denote the orbital on atom i with spin σ by (i, σ), and the corresponding creation operator by $a^\dagger_{i\sigma}$ ($b^\dagger_{i\sigma}$) for an atom on site $\vec{R}_i$ in the A (B) sublattice. The nearest-neighbor TB Hamiltonian has then the simple form:

$$H_{\mathrm{TB},n.n.} = -t \sum_{i,j=n.n./\sigma} (a^\dagger_{i\sigma} b_{j\sigma} + \mathrm{H.c.}) \tag{1.11}$$

The the nearest-neighbor hopping matrix element t sets the overall scale of the π-derived energy band and its numerical value is around 2.75 eV [18].

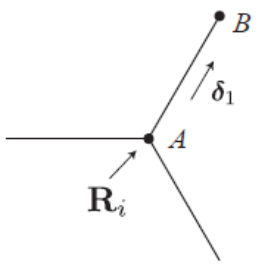

Figure 1.3: Notation for A, B and R^0_i.

In order to understand the nature of the electronic states which arise from this simple Hamiltonian, and later on examine the corrections which can be added, it is convenient to write the TB eigenfunctions in the form of a spinor, i.e. an element of a vector space which transforms as spin. The components of these spinors correspond to the amplitudes on the A and B atoms respectively within the unit cell labeled by a reference point $\vec{\mathbf{R}}_i^0$. As notation, only dictated by convenience, let us choose B to be separated from A by the previously defined $\vec{\delta}_i$ and $\vec{\mathbf{R}}_i^0$ at the position of A as shown in figure 1.3. The TB eigenfunctions have then the form:

$$\begin{bmatrix}\alpha_k \\ \beta_k\end{bmatrix} = \sum_k exp(i\vec{k}\cdot\vec{R_i^0}) \begin{bmatrix}a_i^\dagger\, e^{-i\vec{k}\cdot\vec{\delta_1}/2} \\ b_i^\dagger\, e^{i\vec{k}\cdot\vec{\delta_1}/2}\end{bmatrix} \tag{1.12}$$

$a_i^\dagger$ creates an electron on the A atom in the cell i, while $b_i^\dagger$ creates an electron on the B atom in cell i. The multiplication factor $e^{\pm i\vec{k}\cdot\vec{\delta_1}/2}$ in the spinor components is beforehand inserted in order to simplify the following formalism. The resulting Hamiltonian in the k-representation with this notation is purely off-diagonal:

$$H_k = \begin{bmatrix}0 & \Delta_k \\ \Delta_k^* & 0\end{bmatrix} \quad \Delta_k = -t\sum_{l=1}^3 \exp(i\vec{k}\cdot\vec{\delta}_l) \tag{1.13}$$

Via the explicit expression for the nearest neighbor vectors $\vec{\delta}_l$ in 1.8 we obtain:

$$\Delta_k = -t\exp[-ik_x a(1+2\exp(i\frac{3k_x a}{2})\cos\frac{\sqrt{3}}{2}k_y a)] \tag{1.14}$$

It follows that the eigenvalues ϵ_k of $\hat{H}_k$ are:

$$\epsilon_k = \pm|\Delta_k| = \pm t\sqrt{1+4\cos\frac{3k_x a}{2}\,\cos\sqrt{3}\,\frac{k_y\,a}{2}+4\cos^2\frac{\sqrt{3}}{2}k_y a} \tag{1.15}$$

We can then look for the k-values for which Δ_k (hence ϵ_k) is zero. From equation 1.15 the following conditions are derived:

$$\tfrac{3k_x a}{2} = 2n\pi, \quad \cos\tfrac{\sqrt{3}}{2}k_y a = -1/2 \ \ (n \text{ integral}) \tag{1.16}$$

or

$$\tfrac{3k_x a}{2} = (2n+1)\pi, \quad \cos\tfrac{\sqrt{3}}{2}k_y a = 1/2 \ \ (n \text{ integral}) \tag{1.17}$$

The first choice gives k_y outside the FBZ, but the second (with $n=0$) is satisfied exactly at the corner points K and K' which we previously identified. With a bit of foreshadowing, let's label them "Dirac points".

A first interesting property is easily derived about the Density of States (DOS), the number of states n occupied for each level of energy ϵ, $dn/d\epsilon$. The energy band is exactly symmetric about the point $\epsilon_k = 0$, and this condition is met only at the two Dirac points, not on a complete surface as in typical metals (in 2D a line). It follows that for exactly half filling of the band the DOS at the Fermi level is exactly zero. In fact, undoped graphene has exactly 1 electron per spin per atom (2 per unit cell): taking spin into account the band is exactly half filled. Undoped graphene is then a perfect semimetal. Remember that a semimetal is defined as having zero DOS for $\epsilon = 0$ (where ϵ is the energy measured with respect to the Fermi energy) but a nonzero DOS for $\epsilon > 0$.

We pick $\vec{\mathbf{k}}$ close to a Dirac point $\vec{\mathbf{K}}$ ($\vec{\mathbf{K}}'$ has equivalent physical nature) to study the energy spectrum and eigenfunctions. It is convenient to define the 2D vector $\vec{\mathbf{k}}$-$\vec{\mathbf{K}}$ as $\vec{\mathbf{q}}$ to exploit Taylor-McLaurin series. Expanding the expression for Δ_k around $\vec{\mathbf{q}} = 0$, we find:

$$\Delta(\vec{\mathbf{q}}) =\sim 2t\, e^{-iK_x a}\vec{\mathbf{q}}\cdot\vec{\nabla}_k(e^{3ik_x a}\cos\frac{\sqrt{3}}{2}k_y a)_{\vec{\mathbf{k}}=\vec{\mathbf{K}}} = -\frac{3ta}{2}[\exp(-iK_x a)(iq_x - q_y)] \tag{1.18}$$

The constant factor $exp(-iK_x a)$ does not affect the physics, then we can extract it and thus write:

$$\Delta(\vec{\mathbf{q}}) = \hbar v_F(q_x + iq_y)(1 + \mathcal{O}(q/K^2)), \quad v_F = 3ta/2\hbar \sim 10^6 m/s \tag{1.19}$$

A fascinating way to rewrite the Hamiltonian by exploiting Pauli matrices σ is the following:

$$H = \hbar v_F \begin{bmatrix} 0 & q_x + iq_y \\ q_x - iq_y & 0 \end{bmatrix} = \hbar v_F \, \sigma \cdot q, \quad \boxed{\epsilon(q) = \pm \hbar v_F |q|} \tag{1.20}$$

The eigenvalues are a function only of the magnitude of $\vec{\mathbf{q}}$ and not its direction in the 2D space. The Hamiltonian in 1.20 retraces exactly that of an ultra-relativistic (or massless) particle of spin 1/2, with the speed of light c replaced by the Fermi velocity v_F, which is a factor ~ 300 smaller.

The eigenfunctions are, in the surroundings of the point $\vec{\mathbf{K}}$ and $\vec{\mathbf{K}}'$:

$$\psi^{\pm}_{(K)}(k) = \tfrac{1}{\sqrt{2}} \begin{bmatrix} \exp^{-i\theta_q/2} \\ \pm \exp^{i\theta_q/2} \end{bmatrix}, \quad \theta_q = \arctan(q_x/q_y) \tag{1.21}$$

$$\psi^{\pm}_{(K')}(k) = \frac{1}{\sqrt{2}} \begin{bmatrix} \exp^{-i\theta_q/2} \\ \pm \exp^{i\theta_q/2} \end{bmatrix} \tag{1.22}$$

We can now obtain the explicit expression for the DOS. For nonzero ϵ, the DOS will be proportional to the number of states that have $|\vec{\mathbf{q}}| = |\epsilon|/\hbar v_F$. Since the number of states per unit area with q-values less than q near a Dirac point is $q^2/2\pi$, the DOS associated with this point is:

$$\frac{dn_K(\epsilon)}{d\epsilon} = \frac{1}{\hbar v_F} \frac{dn_K}{dq} = \frac{1}{\pi(\hbar v_F)^2} \, \epsilon \tag{1.23}$$

Since there are two Dirac points, the total DOS is twice this:

$$\boxed{\frac{dn_K(\epsilon)}{d\epsilon} = \frac{2}{\pi(\hbar v_F)^2} \, \epsilon} \tag{1.24}$$

It is interesting to derive the effect of doping, which could also arise from the presence of defects, as by corrugation of the graphene layer (variation of the hybridization character) or point defects (vacancies). At zero doping, as we have seen, the lower half of the band is filled exactly up to the Dirac points. If a suitable gate voltage is applied to the graphene relative to the substrate we induce a nonzero charge. This is equivalent to injecting electrons in the upper half of the Dirac cones or holes in the lower half. If the temperature is low enough, the electrons will form a degenerate Fermi sea and we can define a Fermi surface (in 2D a line) and the corresponding Fermi wave vector q_F. Taking into account the spin and valley degeneracies, we find:

$$q_F = \sqrt{\pi n_s}, \quad n_s = \text{no. of (extra) electrons/unit area} \tag{1.25}$$

We can define an effective mass m^* in the usual way by $m^* = \hbar q_F / v_F$, and then find that:

$$\boxed{m^* = \frac{\sqrt{\pi}\hbar}{v_F} \sqrt{n_s}} \tag{1.26}$$

The most straightforward measurement of the effective mass is cyclotron resonance, which is identical to the previous one in an isotropic system. Cyclotron mass m_c^* is quite generally given, in the semiclassical limit, by the expression $m_c^* = (1/2\pi)(\partial A/\partial\epsilon)$, where A is the k-space area enclosed by an orbit of energy ϵ; for our case this expression is just $\hbar q_F/v_F$, in fact equal to m^*. Cyclotron resonance experiments on graphene verified that m* is proportional to $\sqrt{n_s}$ as predicted [20].

1.2.1 Corrections and sublattice asymmetry

The first correction of the result so far obtained is the introduction of the second-nearest-neighbor hopping, via some matrix element t'. In the honeycomb lattice, all second-nearest neighbors are on the same sublattice (A or B) as the original atom and are equivalent. This produces a term:

$$H_{n.n.n.} = -\frac{t'}{2} \sum_{i,j=n.n.n.,\sigma} (a^\dagger_{i\sigma} a_{j\sigma} + b^\dagger_{i\sigma} b_{j\sigma} + \text{H.c.}) \tag{1.27}$$

with a factor $1/2$ to avoid overcounting. This term is exactly symmetric between the A and B sublattices: it gives then a contribution $-t'f(k)$, which is proportional, in the spinor representation, to the unit matrix. The explicit expression of $f(k)$ is:

$$f(k) = \sum_{ij=n.n.n.} [\exp(i\vec{k} \cdot \vec{K_{ij}}) + \text{H.c.}] = \sum_{ij=n.n.n.} \cos(\vec{k} \cdot \vec{R_{ij}}) \tag{1.28}$$

The perfect symmetry of the band around $\epsilon = 0$ is broken, because the term $-t'f(k)$ is added to both the upper and the lower branches. The Dirac point will no longer correspond to $\epsilon = 0$, but to a shifted value. The degeneracy of the two solutions at the Dirac points $\vec{\mathbf{K}}$ and $\vec{\mathbf{K}}'$ is not broken.

Another important feature which does not vary after this improvement is the value of the effective mass. Using the next-nearest-neighbor values of $\vec{R_{ij}}$, which have become the primitive lattice vectors $\vec{\mathbf{a}_i}, \vec{\mathbf{a}_j}, \mathbf{a}_i - \vec{\mathbf{a}}_j$ and their negatives, we can write $f(k)$ as:

$$f(k) = [2\cos(\sqrt{3}k_y a) + 4\cos(\frac{\sqrt{3}}{2}k_y a)\cos(\frac{3}{2}k_x a)] \tag{1.29}$$

The value of $f(k)$ at the Dirac points is $+3t'$ and $f'(3t')$ is zero. This means that the Dirac points are extremes of $f(k)$. The next-nearest-neighbor hopping does not strongly modify the Hamiltonian of equation 1.20, apart for the constant $3t'$ of no physical interest. Expanding the Hamiltonian to terms of order q^2, one finds that as expected from the sixfold symmetry the t' term is isotropic around $\vec{\mathbf{K}}$. However, the original t term introduces a trigonal dependence ($\sim \sin 3\theta_q$, where $\theta_q = \tan^{-1} q/q_x$). Nonetheless, the order of magnitude of this term is $\sim q/K$ relative to the Dirac one, and it is usually neglected in analysis of experiments.

The value of t' is not well known from experiments, but ab initio calculations find $0.02t \lesssim t' \lesssim 0.2t$ depending on the TB parametrization [18] . These calculations also include the effect of a third-nearest-neighbors hopping, which has a value of around 0.07 eV. A TB fit to cyclotron resonance experiments finds $t' \sim 0.1eV$ [20].

1.2.2 Landau Levels and Quantum Hall Effect

The strong incentive for research in graphene came from the Dirac character of its charge carriers, which led to a mobility up to 15 000 $\text{cm}^2V^{-1}s^{-1}$ for graphene on SiO_2 substrate [11, 19] and 200 000 $\text{cm}^2V^{-1}s^{-1}$ for suspended sample [21].

Dirac fermions lead also to other interesting properties under magnetic fields. The presence of a perpendicular magnetic field B allows the appearance of a sequence of Landau levels with square-root dependence on the field:

$$\epsilon_N = sgn(N)\sqrt{2e\hbar v_F^2 |N| B} \qquad N = 0, \pm 1, \pm 2, ... \tag{1.30}$$

In the non-relativistic regime, Landau Levels' energy is linear in B, $\epsilon_N = (N+1/2)\frac{\hbar e}{mc}B$. Of particular importance is the existence of a zero-energy state $N = 0$, observed by many different experimental probes, from Shubnikov-de Haas oscillations in single layer graphene [19, 22] to infrared spectroscopy [23] and scanning tunneling spectroscopy [24], as seen in figure 1.4.

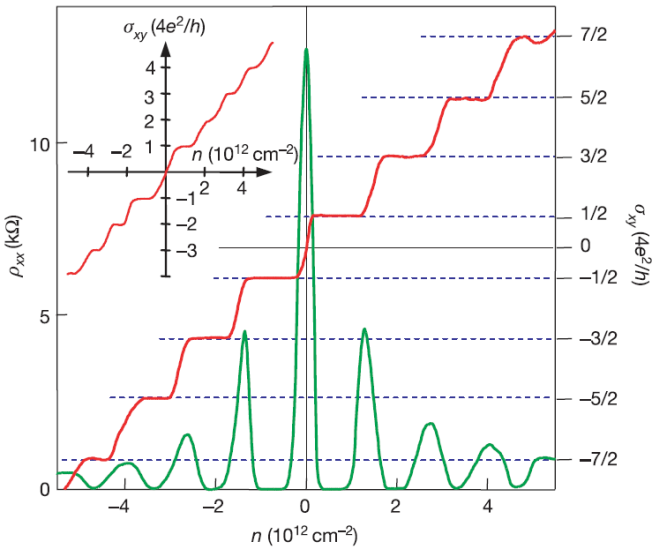

Figure 1.4: Hall conductivity σ_{xy} and longitudinal resistivity ρ_{xx} of monolayer graphene as a function of charge-carrier concentration acquired at $B = 14$ T and T = 4K. Inset: σ_{xy} in bilayer graphene where the quantization sequence is normal and occurs at integer ν. Adapted from [19].

This influences the Hall conductivity, which has a very particular behaviour in a bidimensional system. In fact, Hall conductivity σ_{xy} as a function of charge-carrier concentration presents plateaux that correspond to half-integer of the quantum conductance:

$$\boxed{\sigma_{xy} = (N + \frac{1}{2})\frac{4e^2}{h} = \nu\frac{4e^2}{h}} \tag{1.31}$$

where ν is known as the filling factor. This phenomenon, known as Integer Quantum Hall effect (IQHE) [1], stems directly from the filling of the quantized Landau Levels in a bidimensional system with high mobility. Lowering B shrinks the capacity of Landau levels (eB/h in non-relativistic regime), and then electrons for certain B_i will completely fill some levels, with all the higher Landau levels empty. At these special points on the magnetic field axis, the magnetoresistance ρ_{xx} drops. The Hall conductivity on the other hand has wide plateaux.

In fact, even with an extreme care every 2D system has defects and impurities. When a Landau level is being filled with electrons, some of the electrons get trapped in defects. They no longer participate in the electron conduction, not affecting the density of carriers measurements. However, the defects continue to be filled and emptied, acting as a reservoir of carriers and keeping the Landau levels in the energetically flat part for a finite region of the magnetic field, and not just for a single value of B. There would be no IQHE without imperfections in the sample.

Laughlin explained the quantization of the Hall conductance in terms of a pump which moves electrons through the bulk of a Hall cylinder, from one edge to the other of the cylinder [25]. This arguments leads to the existence of localized conducting states at the edges, with a precise chirality. In fact the filling factor ν counts the number of conducting chiral channels at the edges of the system and is insensitive to its geometry, impurity and interactions of electrons [26, 27, 28, 29].

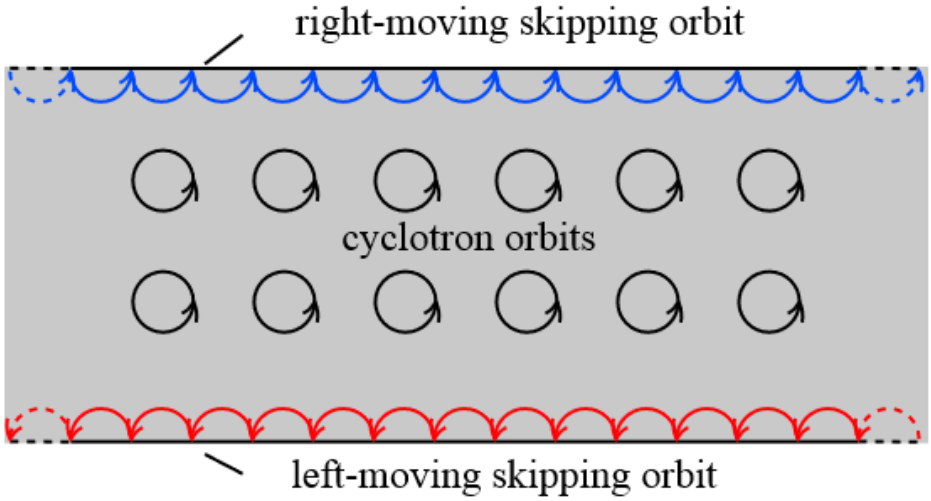

Figure 1.5: Schematic of the creation of the chiral edge states from the bulk Landau Levels.

What is the unconventionality of graphene? An usual 2D system presents an Hall conductivity of $\nu e^2/h$. Degeneration g should be added, equal to 4 for graphene because there are 2 spin states and 2 Dirac cones. However, at half-filling (at the Dirac point) there should be a Hall plateau at $N = 0$ with $\sigma_{xy} = 0$, which is not possible due to the presence of a Landau Level at $N = 0$. Because of the presence of the zero mode shared by the 2 Dirac points, there are exactly 2×(2N+1) occupied states that are transferred from one edge to another. This produces the prefactor of 1.31.

1.2.3 Spin-orbit coupling and Quantum Spin Hall Effect

A second parameter which influences the gap-opening is spin-orbit interaction, which is also source of other exotic physics. Spin-orbit coupling is a relativistic correction due to the interaction between spin and orbital momentum inside a potential, acting like an effective magnetic field experienced by electrons in their rest system. It acts as a process in which an electron changes simultaneously its spin and angular momentum or moves from one orbital wave function to another. Its microscopic form is:

$$H_{SO} = \frac{1}{2\left(m_e c\right)^2}(\nabla V \times \vec{p}) \cdot \vec{S} \tag{1.32}$$

The mixing of spin and orbital motion is large in heavy ions, but carbon is a light atom, so the expected effect is weak. Two different interactions can be considered, the intrinsic and Rashba spin-orbit interaction:

$$H_{\mathrm{SO;int}} = \Delta_{\mathrm{so}} \hat{\Psi}^{\dagger} \sigma_z s_z \tau_z \hat{\Psi} \tag{1.33}$$

$$H_{\mathrm{SO;Ras}} = \lambda_R \hat{\Psi}^{\dagger} \left(-\sigma_y s_x + \sigma_x s_y \tau_z\right) \hat{\Psi} \tag{1.34}$$

where σ and τ are Pauli matrices, with $\sigma_z = \pm 1$ describing states on the A/B sublattices and $\tau_z = \pm 1$ the K/K' valley degrees of freedom. s is a Pauli matrix acting on actual spin space. Δ_{SO} is the spin-orbit coupling and λ_R is the Rashba coupling. Intrinsic spin-orbit coupling depends strongly on the crystal symmetry; Rashba term on the other hand is allowed when the mirror symmetry is broken, either by a perpendicular field or by interaction with a substrate.

The symmetries of these spin-orbit interactions allow the formation of a gap because the spin-dependent shift of the orbitals has a different sign for the two sublattices. For $\lambda_R = 0$, Δ_{SO} leads to

an energy gap $2\Delta_{SO}$ with $\epsilon(q) = \pm\sqrt{(\hbar v_F q)^2 + \Delta_{SO}^2}$. For $0 < \lambda_R < \Delta_{SO}$ the energy gap $2(\Delta_{SO} - \lambda_R)$ remains finite. For $\lambda_R > \Delta_{SO}$ the gap closes, giving a zero gap semiconductor. The gap generated by the term $\sigma_z s_z \tau_z$ has opposite signs at the $\vec{\mathbf{K}}$ and $\vec{\mathbf{K}}'$ points. Differently from a sublattice potential as σ_z or $\sigma_z s_z$, where the ground states would be adiabatically connected to simple insulating phases at strong coupling where the two sublattices are decoupled, $\sigma_z s_z \tau_z$ has no strong coupling limit. To connect smoothly between the states generated by $\sigma_z s_z \tau_z$ and σ_z there has to be a point where the gap vanishes (figure 1.6), separating ground states with distinct topological order.

As for IQHE from Laughlin argument, if $\lambda_R = 0$ the bulk topological order requires the presence of gapless edge states. Kane and Mele [2] demonstrated that these states persist even in the case $\lambda_R \neq 0$, provided that $\lambda_R < \Delta_{SO}$. The edge states are not chiral, because each edge has states propagating in both directions. However, the edge states are "spin filtered", meaning that opposite spin propagate in opposite directions. The charge conductivity is then zero, and the quantized spin conductivity is:

$$\boxed{\sigma_{xy}^{s} = \frac{e}{2\pi}} \tag{1.35}$$

Following the previous terminology, this phenomenon is called Quantum Spin Hall Effect (QSHE). It can be seen as two copies of the Quantum Hall Effect, one for each spin (figure 1.7). It is different from the spin Hall effect because this phase is topologically distinct from a band insulator. The spin filtered edge states produce dissipationless current at $T = 0$ (ballistic transport), while at T > 0 backscattering is allowed, leading to a finite conductivity. [30].

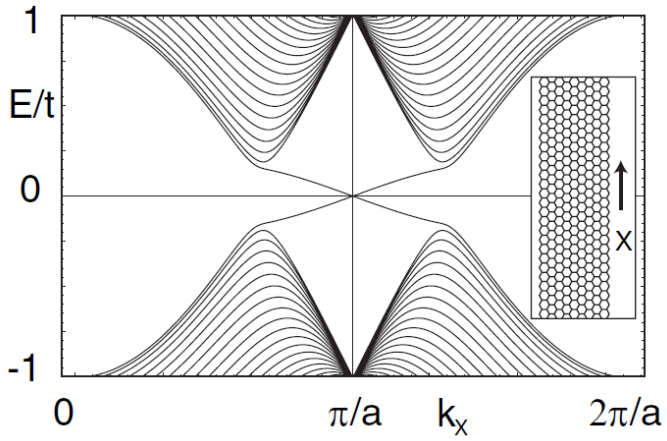

Figure 1.6: 1D energy bands for a strip of graphene of zig-zag border (inset). The bands crossing the gap are spin filtered edge states. Reproduced from [2].

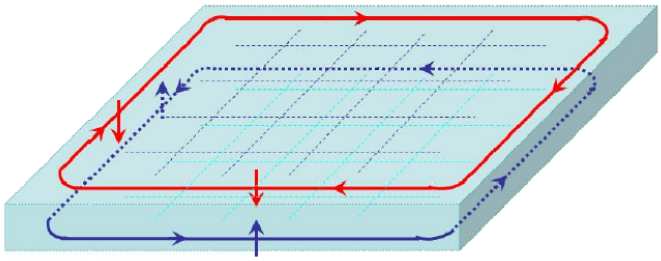

Figure 1.7: Representation of the two edge currents, for the two spin components. Reproduced from [30].

In their seminal work Kane and Mele calculated λ_R for reasonable values of internal electric field, obtaining $\sim$ 0.5 mK ($4 \cdot 10^{-5}$ meV). The value of Δ_{SO} they obtained was of 1.2 K (0.1 meV), compatible with $\lambda_R < \Delta_{SO}$. However, following calculations [31, 32] led to a way smaller value of the spin-orbit gap of 10^{-3} meV, around 0.01K. This made the observation of QSHE in graphene an extraordinary experimental challenge.

Bernevig proposed a strain gradient to create Landau Levels in a typical semiconductor, in order to observe QSHE in absence of external magnetic field [30]. This proposition was however far from the experimental possibilities. His group proposed the possibility of the observation of QSHE in HgTe-CdTe quantum wells [33], later on performed by Konig and coworkers [34], measuring the electrical conductance due to the edge states at 1.4 K. The dissipationless nature of the edge states in HgTe-CdTe quantum wells was then experimentally proved by Roth and coworkers [35], confirming the strong interest in this kind of material for a future generation of spintronics devices for low-power information processing. Other heterostructures have been found to exhibit the same topological properties, like InAs/GaSb quantum wells [36], but still limited to very low temperatures. As shown in figure 1.8, the higher temperature observed has been in monolayer tungsten ditelluride (WTe_2), with QSHE measurable up to 100K [37].

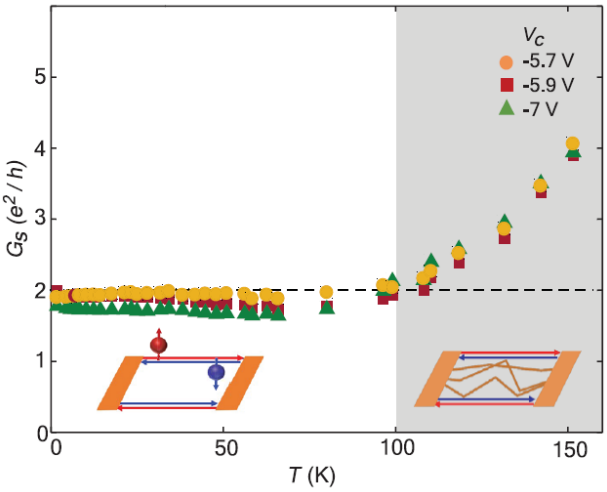

Figure 1.8: Temperature dependence of the edge conductance at a few representative gate voltages for a WTe_2 device. The conductance is dominated by the QSHE up to about 100 K. The right schematic depicts the onset of bulk-state contribution to the conductance. Adapted from [37].

1.3 Alternatives to graphene: group IV elements

In the last section, we have seen that the QSHE has been observed in WTe_2. This compound is a transition metal dichalcogenide (TMDC), a family of layered materials of the type MX_2, with M a transition metal atom (Mo, W, etc) and X a chalcogen atom (S, Se and Te). This class has been deeply studied as a possible alternative to graphene and could provide a compromise between mobility and on-off ratio [38].

Another option are materials with the same band structure but bigger spin-orbit coupling, which as previously demonstrated is responsible of a bigger band gap opening. This allows a bigger on-off ratio in field effect transistor, and QSHE should be observed at an accessible temperature. The group IV elements like Si, Ge and Sn are perfect candidates. However, these elements tend to morph into stable 3D forms as their lateral size increases. Only an epitaxial growth on top of a substrate

can suppress the deleterious thermal vibrations that are responsible for such transformations. A memory of this predilection can be found in their characteristic sp^3-like hybridization which results in a minimal energy configuration with one of the two sublattices uplifted compared to the other, a property called **buckling**.

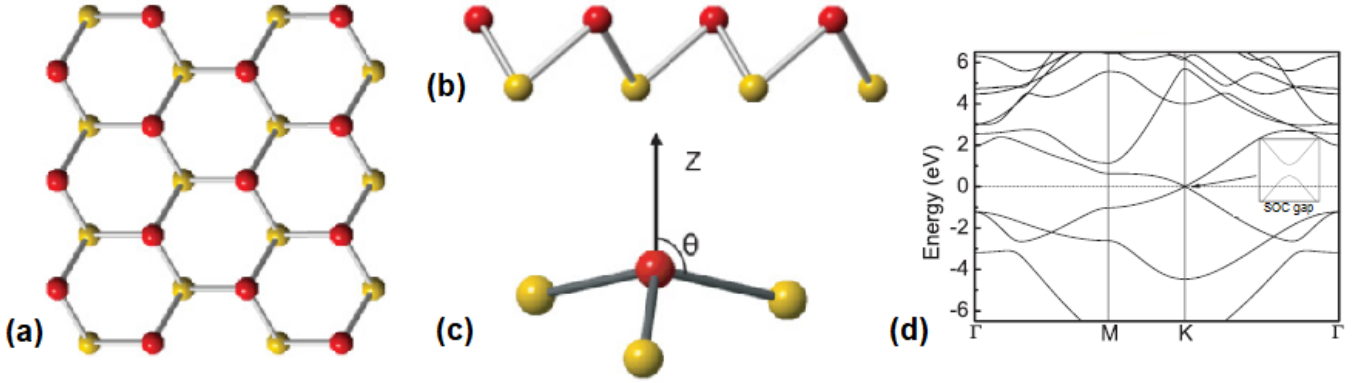

Figure 1.9: (a-b) Ball and stick model of group IV buckled honeycomb, with red and yellow inequivalent sublattices. (c) Definition of the angle θ between the X-X bond and the z direction normal to the plane. (d) Band structure of low-buckled group IV elements, with SOC gap in inset. Adapted from [39].

	Graphene	**Silicene**	**Germanene**	**Stanene**
a (Å)	2.46	3.86	4.02	4.70
θ (deg)	90	101.7	106.5	107.1
Δ_{SO}^{1st} (meV)	0	3.9	43	29.9
Δ_{SO}^{2nd} (meV)	0.0013	0.073	3.3	34.5
λ_R (meV)	0	0.7	10.7	9.5
Gap (TB) (meV)	0.0026	7.9	93	129
Gap (FP) (meV)	0.008[a]	1.55[b]	23.9[b]	73.5
v_F (TB) (10^5 m/s)	9.80	5.52	4.57	4.85
v_F (FP) (10^5 m/s)	8.46	5.42	5.24	4.70

Table 1.1: Parameters for 2D materials made of group IV elements. Lattice parameters a and angles θ for lowest energy configuration, Δ_{SO} at first and second and λ_R order via TB calculations, energy gap and Fermi velocity from TB and first principle (FP) calculations. When not stated, the data are taken from [39]. a from [32]. b from [40].

As we can see from Table 1.1, the spin-orbit gaps of silicene, germanene and stanene are respectively 1.55, 23.9 and 73.5 meV, equivalent to a temperature of 17, 277 and 850K. Germanene and stanene temperatures in particular are characterized by easily experimentally accessible temperatures.

Silicene growth was first suggested in 2010 by the group of G. Le Lay for self-aligned nanoribbons by depositing Si on Ag(110) [41, 42]. Later in 2012 the same group reported evidence for silicene growth on Ag(111) [43]. Other reported substrates were $ZrB_2(0001)$ [44], Ir(111) [45], HOPG [46] and MoS_2 [47], with the two latter which have been later disproved [48, 49]. Deposition on gold leads to alloy formation in the initial stages of growth, and then disappears as the coverage is increased towards a monolayer [50, 51, 52]. After years of intense research efforts on these substrates a lot of difficulties still hindered the exploration of the exotic 2D physics presented above. Silicene on Ag(111), the most studied, is strongly coupled to the metallic substrate [53] and loses its Dirac characteristics [54]. It

also grows in multiple phases (4x4, $\sqrt{13} \times \sqrt{13}R13.9°$, $2\sqrt{3} \times 2\sqrt{3}$R30° and others [55], referred to Ag(111)) with limited spatial extent.

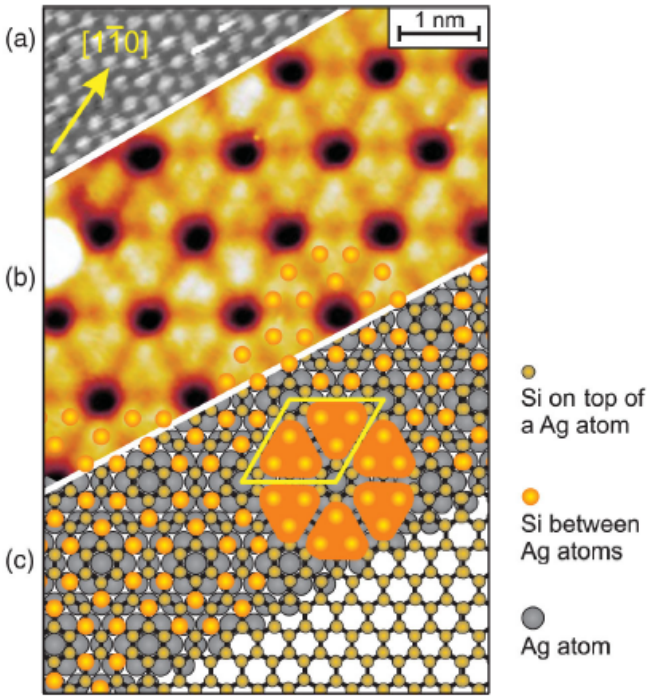

Figure 1.10: STM images of a) the clean Ag(111) surface, (b) the silicene sheet with a 4x4 reconstruction. (c) Model of silicene on Ag(111). Adapted from [43].

Multiple tentative growths were reported for germanene: on Ag(111) [56], Pt(111) [57], Au(111) [58] and Ge_2Pt clusters [59, 60, 61, 62, 63].

For the Ge/Ag(111) system, even if a dual phase was reported to be germanene [64], it was found that Ge reacts with Ag at room temperature to form a Ag_2Ge alloy for 1/3 ML of Ge deposited [65]. For higher coverages a more disordered hexagonal structure with higher relative content of Ge is observed. Ge atoms move in a three-step process: exchange between an Ag adatom and a Ge inserted atom, diffusion on the surface of the Ge atom, and reinsertion through exchange with a surface Ag atom. This hinders the formation of a true germanene layer above.

On Pt (111), Li et al. observed a low energy electron diffraction (LEED) pattern characteristic of a single $\sqrt{19} \times \sqrt{19}$R23.4° reconstruction, but without honeycomb structure in the high resolution STM images. This work was later addressed as formation of an alloy by Svec and coworkers, similar to the structure they found on silicene [66] and previously reported for germanium [67].

For gold, Davila et al. reported a LEED pattern with a multiphase diffraction spot system, relevant of multiple but ordered 2D crystals: $\sqrt{7} \times \sqrt{7}$R19°, 5×5 and $\sqrt{19} \times \sqrt{19}$R23.4°. While promising properties like Dirac behaviour were claimed for the monolayer [68], the obvious drawback is that, as silicene, the multi-phase does not allow a good control for electronics. While renewed interest for gold arose in the few-layer version [69], later the very existence of germanene phases on gold was questioned due to presence of both Au and Ge in the topmost layer [70, 71, 72].

Later, other metallic growths were reported on Ag(111) with an AlN buffer layer [73], by segregation through Ag(111) films on Ge(111) [74], on the semi-metallic Sb(111) [75], and two semiconducting substrate: on MoS_2 [76, 77] and on Ge(111) [78]. Another candidate as substrate, graphite, reported by Persichetti et al. [79], was later disproved by Peng and coworkers [48]. Multi-layer growth were reported for Cu(111) [80, 81] and for Si back in 2015 by Tsai et al. [82].

1.3.1 Germanene on Al(111)

The choice of Al(111) as substrate in this thesis, apart from the lower cost compared to Au or Pt, was justified by its hexagonal symmetry and a lattice parameter close to that expected for the growth of germanene (a_{germ} predicted between 0.392 and 0.406 nm, and $a_{Al(111)}$=0.405 nm) [83]. Additionally, aluminium is a simple metal, without surface reconstruction, and its surface electron density is dominated by *s*-type orbitals [84].

Another feature to be considered are the surface states. A Shockley-type surface state can be described by electrons trapped in the potential well formed by the crystal edge (where the energy gap reflects the electron normal to the surface) and the surface barrier potential extending into the vacuum (asymptotically represented by the image potential of the electron in front of the surface). These states can be easily measured via scanning tunneling spectroscopy and affect the electronic properties of an adlayer, especially if their energy is around the Fermi level in the case of a Dirac material. However, the Al(111) six-fold coordinated electron distribution is little influenced by the perturbation induced by the loss of translational symmetry due to the surface [84] and there are no Shockley-type surface states reported near the Fermi level. Two states can be found in literature, with binding energy of 4.68 and 0.7 eV, with much more uncertainty on the second one [85]. This is a remarkable difference with silicene on Ag(111), where a peak due a surface state can be found, within -0.1V and +0.05V from the Fermi level, depending on the temperature [86], or with graphene on metal substrates such as Ir(111) [87].

These features motivated the group of professor Carmelo Pirri at the Institut de Sciences des Matériaux de Mulhouse (IS2M) to study the growth of a 2D layer of germanene on Al(111). Their successful recipe contained the following steps:

- All experiments to be performed in UHV with base pressure in the low 10^{-11} mbar regime;
- Clean Al surface via multiple cycles of sputtering and annealing at 500°C until a sharp Al(1×1) LEED pattern is obtained. XPS confirms the cleanliness of the surface and STM does not show any spikes on Al(111) possibly due to oxidation;
- Sublimation of germanium onto Al(111) maintained at a temperature of 87±10°C, with a very low flux of about 0.005nm/min. A 3×3 pattern appears in LEED;

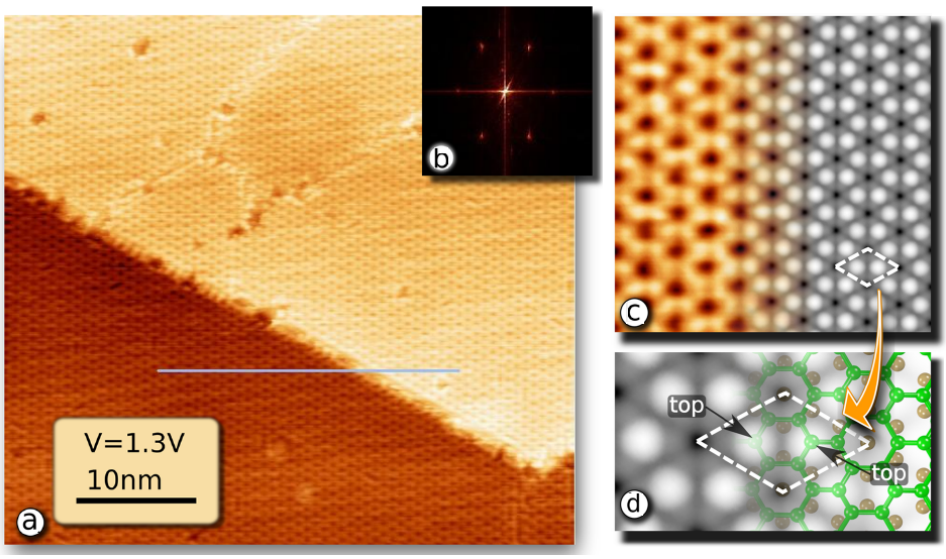

Figure 1.11: (a) STM image of the 2T configuration, with relative FFT (b). (c) Comparison between the real and simulated STM image following the model presented in (d). Ge atoms are green, Al atoms are brown. Adapted from [83].

Following the reports in [83] and [88], this growth claimed to produce **two stable configurations** in the STM contrast, both related to an underlying honeycomb structure: germanene 2T and germanene 1H. The nomenclature indicates the number and the position of the germanium atom in an upper position.

Germanene 2T configuration is characterized by 2 upper Ge atoms among 8 atoms in the unit cell, positioned above two other underlying aluminium atoms. Its adsorption energy by DFT is -0.48 eV/atom. The terraces height is $\Delta h = 0.24$ nm, almost precisely $\Delta h_{Al} = 0.234$ nm of the aluminium substrate terraces. The superstructure is (3×3), corresponding to a lattice vector of $d_{Ge,Ge} = 0.85$ nm in the STM image and LEED images. Vertically, DFT simulations show a difference $\Delta z = 0.123$ nm between Ge atoms and $\Delta z' = 0.061$ nm between Al atoms. This buckling is bigger than the one predicted in the low-buckled structures of free-standing germanene (0.065 nm) and smaller than the high-buckled one (0.223 nm). The Ge(down)-Ge(down) distance is 0.265 nm, the Ge(top)-Ge(down) distance is 0.260 nm, bigger of the Ge-Ge(bulk) of 0.245 nm and of the Ge-Ge in free-standing germanene of 0.233-0.244 nm. Finally, the Ge(down)-Al distance is 0.279 nm and the Ge(up)-Al distance is 0.302 nm. The Electron Localization Function (ELF) images seems to confirm no covalent bonding between Ge and Al: there's a strong electrostatic interaction (-0.75 eV/atom) balanced by a strong Ge and Al deformation energy (0.23 and 0.04 eV/atom). There's a Bader charge transfer of 2.43 electrons from Al to Ge.

Germanene 1H configuration is characterized by 1 top atom among 8 Ge atoms, positioned on a hollow site, or three-fold site. Its adsorption energy by DFT is -0.48 eV/atom, same as germanene 2T. In this configuration, Δz is 0.406 nm between the upper Ge and the top Al layer, 0.153 nm between Ge-Ge (bigger than 0.123 nm of 2T), while $\Delta z'$ is 0.013nm (smaller than 0.061 nm of 2T). The Ge-Ge distances are in the 0.258-0.261 range. Seven Ge atoms are 0.262 nm far from an Al atom, smaller than 0.279 nm of 2T structure. There's more interaction between Al and Ge layers in ELF: the electrostatic interaction is lower (-0.69 eV/atom), and so deformation energy for Al and Ge (0.01 and 0.2 eV/atom). The Bader charge transferred from Al to Ge is 1.94, lower than the one of germanene 2T.

Fukaya and coworkers [89] presented a similar model of the adlayer based on total-reflection high-energy positron diffraction (TRHEPD) which could explain the 1H configuration.

A switch between one structure and the other has been proposed at room temperature during STM measurements applying a 2V bias [88]. The calculated barrier height is 0.11 eV/unit cell for transformation in both directions.

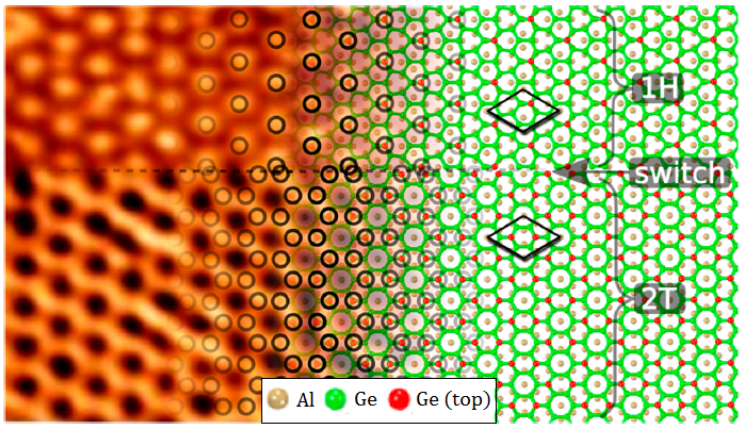

Figure 1.12: Superimposition of the calculated network and experimental (V=+1 V) STM image, showing the structural change from the 2T configuration to the 1H one. Adapted from [88].

No other groups reported the 2T structure in their studies. On the contrary, it was recently proposed that more than a real structure, the 2T configuration is produced by a tip artefact. In fact, as they show in their analysis, Muzychenko et al. [90] proved that it is possible to reproduce the 2T structure via a "volontary" modification of the tip, in particular when the tip is double and the apex is not a tungsten atom but another chemical species. A double tip of only W atoms produces ghost terraces of lower height, but still showing hexagonal contrast everywhere, while on the main terrace the contrast becomes honeycomb in the second case. To understand the previous misassignment as a second phase, they tested the stability of the honeycomb structure on high voltages and low bias currents (high gap resistance), while they showed it was easily destroyed with low voltages and high bias currents (low gap resistance). On the contrary, the hexagonal structure of 3×3 1H was maintained without any remarkable changes within tunneling bias range from ± 5 mV to ±2.5 V.

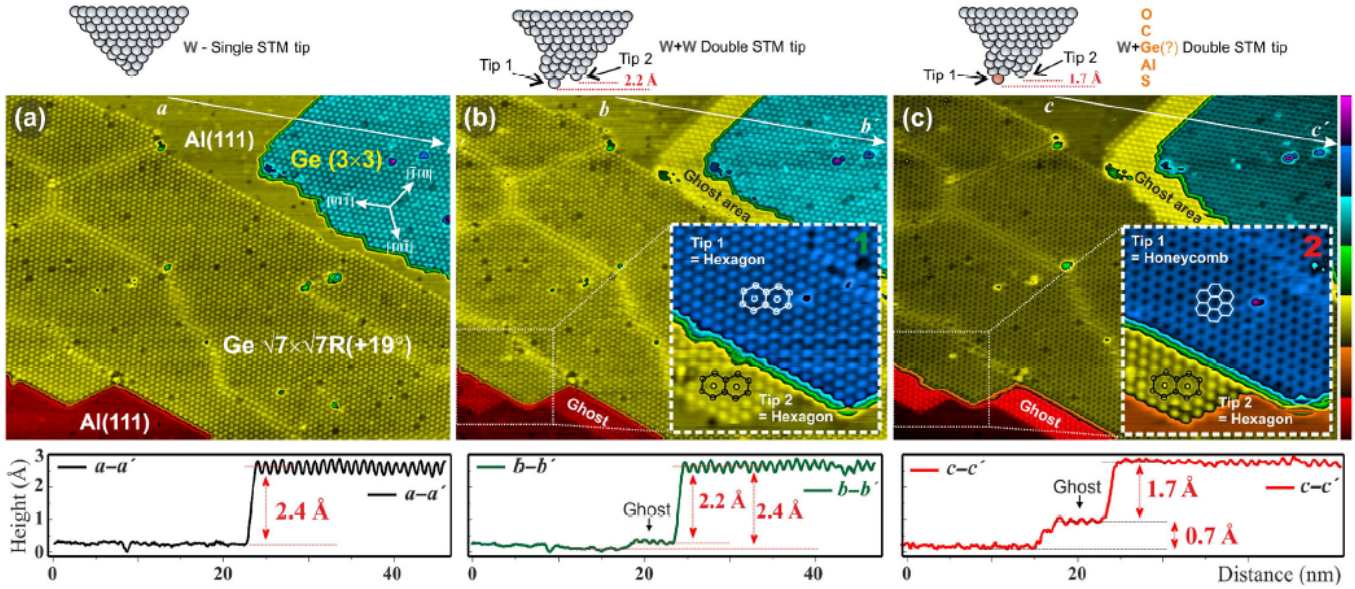

Figure 1.13: Tip-dependent STM contrast of single-layer germanene islands. (a)–(c). Filled-states STM topography images of exactly the same Al(111) surface area containing both (3×3) and ($\sqrt{7} \times \sqrt{7}$)R(+19°) germanene phases in dependence of STM tip conditions: (a) normal W-terminated STM tip (b) double W-terminated STM tip; (c) double STM tip with apex of different chemical nature. Height profiles shown at the bottom of the images are taken along white arrows aa', bb' and cc' on (a)–(c) respectively. Inset in (b) and (c): zoomed-in STM topography images of the area indicated by white-dotted box respectively. The Al(111) surface area, germanene phases and main crystallographic directions of the substrate are indicated in (a) and the same for (b) and (c). Reproduced from [90].

The interesting question that arises is if the Dirac cone is preserved in the growth of germanene on Al(111). If the structure of the adlayer is modified compared to free-standing germanene, it is possible that spin-orbit coupling is not able to open a gap in the band structure. Germanene 2T structure was the subject of a study to answer this question by Liu and coworkers [91], who found that the band structures of germanene mix with the bands of the Al substrate. This happens also for silicene on Ag [92] and germanene on Ag [93]. Interestingly, studying just the band structure of the modified germanene layer the authors found that the Dirac cone around K/K' survives the structural change and a new linear crossing of Fermi level is present at the D point, which for symmetry reasons is present 3 times in the Brillouin zone. Together with the K/K' couple, it means 8 Dirac points for the system. Spin orbit coupling lifts the spin degeneracy and as a result the valence and conduction bands still touch at K point, but with a quadratic dispersion, while a little gap of 4 meV is opened at D point.

Even if the solubility of Ge in Al and viceversa is very low, at the point of considering them immiscible [94], the possible role of surface alloys between aluminium and germanium has been taken into account in the work of Fang [95] and Martinez [96].

The first study focuses via ab-initio calculations on the very first stages of growth via placing atom by atom on the Al(111) surface. 3 different structures mode are considered, HH (only hexagons), HT (hexagons and triangles) and HP (hexagons and pentagons), depending on which configurations are produced in Ge_N clusters, with N growing from 1 to 12. HH and HT are energetically favorable compared to HP, which is on average ~ 0.6 eV higher in energy. (HL) sheet on pure Al(111) surface while the HT mode would lead to a single atomic-thick Kagome lattice (KL) sheet. Unluckily, the HP mode would be the one to produce a buckled honeycomb structure (BHS) as structure 2T. The 1H structure is calculated to be 0.2 eV unfavorable compared to the 2T. This suggests that the BHS-1H structure would be suppressed in the first stages of growth, but it's possible to retain it from a phase transition from the BHS-2T, as previously showed [88]. Though they are 84 meV/atom unfavorable in energy, only the BHS-1H and the 2T structures reproduce the experimental STM between the models herein proposed. Their large scale production is however questioned by constant temperature first principles molecular dynamics simulations (FPMD) which point towards a major instability of the HP structure in the first phases of dynamics.

The goal of the paper was then to show how these limitations could be overcome if a buffer layer of Al_2Ge alloy was present between Al(111) and germanene. Considering the substitution of Al atoms with Ge ones, this process would be energetically favorable compared to adlayer deposition, and a periodic alloy would be promoted following DFT calculations. The presence of the alloy would turn almost all ground states of Ge_N clusters into HP mode. Again, BHS-2T is preferential of 0.32 eV compared to BHS-1T. The transition between the two phases would be energy activated with a barrier of 0.22 eV. Additional FPMD shows that there are only slight distorsions of BHS-type structures on alloy in 5ps, compared to the collapse on pristine Al(111).

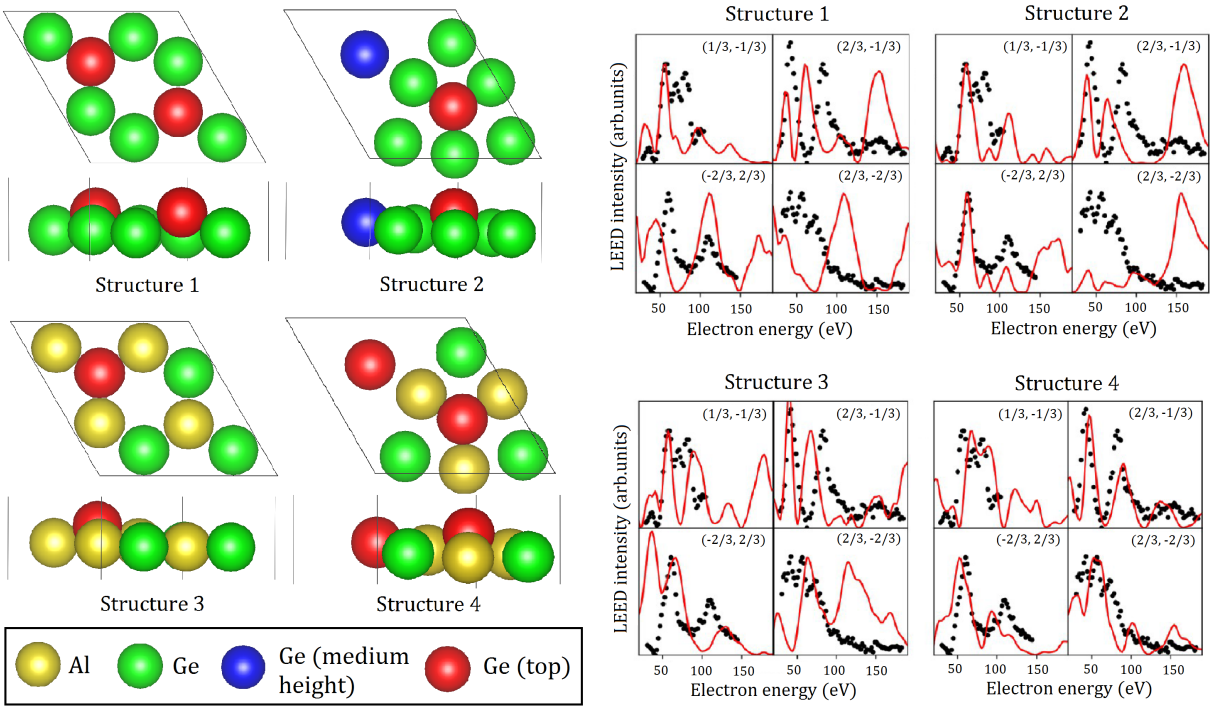

Figure 1.14: (Left) Structures 1 and 2 correspond to configurations with pure Ge in the top layer, while structures 3 and 4 correspond to Ge-Al alloy in the top layer considered in [96]. (Right) Comparison between experimental and simulated LEED I-V curves. For each structure, the simulated I-V curves (red lines) corresponding to four fractional spots ((1/3 -1/3), (2/3 -1/3), (-2/3 2/3), and (2/3 -2/3)) are compared to the experimental data (black circles). Adapted from [96].

The work of Martinez and coworkers [96] focuses on the contrary on using surface-sensitive techniques to prove the structure of the deposited material. The most important technique herein is Time Of Flight Direct Recoil Spectroscopy (TOF-DRS). The idea behind the technique is the study of the trajectories of the ions before and after scattering, which will be affected by a combination of shadowing and blocking effects, with cones of radius of the order of 0.1 nm. As a result, the particles that reach the detector must come mainly from the outermost surface layer.

The authors expected a disappearance of the peak relative to Al at the mono-layer deposition, but instead Al never disappeared from the spectra. They inferred this result from the angle-dependence and using different projectiles a Ge/Al ratios within the range of $0.6 < \text{Ge/Al} < 1.5$. Based on this ratio, they proposed four structures and performed simulations of intensity of fractional spots. There is a clear disagreement with the experimental I-V curves of the simulated ones for the structures which have only Ge atoms in the top layer (structures 1 and 2 in figure 1.14). A better agreement is with structures 3 and 4, in particular 4 (3 does not match well 2/3 -1/3 and not at all 2/3 -2/3). The conclusion went then towards structure 4, which matches with the BHS-2T structure in STM images. We previously mentioned this structure to be created by a tip artefact. Lacking STM images in the paper to compare with previous results, the question remains open.

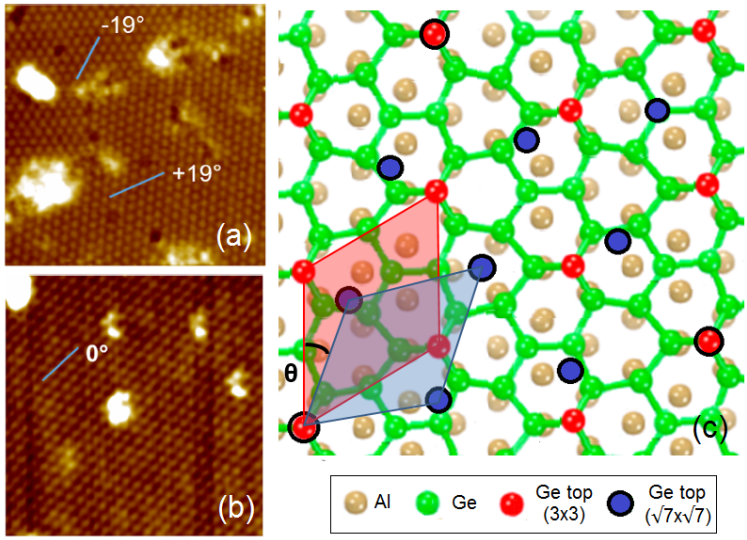

Figure 1.15: (a) $\sqrt{7} \times \sqrt{7}$R19° reconstructions, vs (b) 3×3 reconstruction, reproduced from [97]. (c) Adaptation of figure from [83] to add the $\sqrt{7} \times \sqrt{7}$R19° top atoms, in blue.

These two studies do not take strongly into consideration a second reconstruction of germanene on Al(111), reported for the first time almost simultaneously in september and december 2017, respectively. In the first work, Wang and coworkers [97] reported a growth performed at higher temperatures than the 87±10°C of IS2M group, around 200°C, which resulted in the coexistence of the 3×3 and a new $\sqrt{7} \times \sqrt{7}$R19° reconstruction. This phase is characterized by a periodicity of 7.5 Å, multiple possible domains with different orientation, ± 19° related to 3×3. This structure can be obtained by a different position of the periodic layer of atoms compared to Al underneath.

In figure 1.15 the 3×3 reconstruction is showed, with yellow Al atoms, green germanene in-plane atoms and red-buckled atoms. The $\sqrt{7} \times \sqrt{7}$R19° can be obtained if instead of 3 hollow sites away the next hollow site is chosen on the 19° orientation (blue top atoms, the rest of the structure underneath is not showed for clarity, red atoms circled in black are shared by the two structures). A tentative interpretation of XPS Ge-3d core levels is furnished to match with the proposed superstructure. The electronic difference between both structures would be weak. The germanene layer gains totally 1.80 and 2.32 electrons in the 3×3 and $\sqrt{7} \times \sqrt{7}$ models, respectively, from Al atoms. In the 3×3 model, lower Ge atoms gain between 0.18 and 0.4 electrons/atom, while top Ge loses 0.15 electrons. The charge transfer calculation of the $\sqrt{7} \times \sqrt{7}$ model shows higher transfer for lower Ge atoms, which

gain between 0.31 and 0.4 electrons/atom, while top Ge loses 0.14 electrons. The adsorption energy is -0.45 eV/atom and -0.46 eV/atom for 3×3 and $\sqrt{7} \times \sqrt{7}$.

Additional information on this structure can be obtained in the work of Endo and coworkers [98]. They claimed a growth at almost room temperature [Al(111) was indirectly heated by the thermal flux], and separately came to the same conclusion about the superstructure identity. Their DFT calculations match those of Wang. STS measurements were performed, and later used with DFT simulated LDOS to adfirm the absence of Al atoms in the upper layer. As expected for 3×3, also $\sqrt{7} \times \sqrt{7}$ germanene sees Al partial DOS submerge that of Ge atoms. Ge partial DOS maintains a Dirac cone at Γ even in this modified structure. However, the complete DOS suggests hybridization between Al and Ge atoms. The authors went further by measuring the dI/dV map at low temperature, observing the absence of a standing wave near step edges, which would be present if Ge formed a 2D electronic band. Several round shapes were observed in dI/dV, which were associated to Ar bubbles interferences.

The range of temperature was enlarged by Muzychenko and coworkers, who reported that between 27°C and 200°C both germanene phases nucleate and grow independently from each other and regardless of Al substrate temperature. They observed multiple domains for $\sqrt{7} \times \sqrt{7}$ while bigger single domains for 3×3, which they justified due to the bigger mechanical strain of the first structure, 6.2% vs 13.9%.

The range was finally clarified by the IS2M group [99], who showed how the ratio between 3×3 and $\sqrt{7} \times \sqrt{7}$ grows with temperature. Real-time STM acquired during growth by the group of Geoffroy Prevot in Paris showed also that the 3×3 phase grows at the expense of the $\sqrt{7} \times \sqrt{7}$ [99]. However, even if the proportion of $\sqrt{7} \times \sqrt{7}$ diminishes, the two phases always coexist in the temperature range between 31°C and 215°C. The $\sqrt{7} \times \sqrt{7}$ is also less stable in temperature: it disappears around 227°C in the LEED spectra, while the 3×3 is still only strongly attenuated. A recipe to grow only one of the two phases does not exist yet. This recipe could be inferred by the knowledge of the exact crystalline structure, which is for the moment unknown. X-Ray Diffraction results are still expected to confirm the up-to-now claimed structures.

While lot of attention has then been devoted to perfecting the growth of germanene on Al(111) and understanding its structure, no information has been provided yet about the electronic properties of the main phase, the 3×3 recontruction. Scanning tunneling spectroscopy (which will be presented in the next chapter) is a suitable technique to probe the electronic properties of a conductive material in a pollution-free environment and at low temperature. The cryogenic measurements at 5K, which corresponds to a thermal energy of ~ 0.4 meV, is sufficient to probe the expected gap of 23 meV. We will present the results of these measurements and their rationalization in chapter 3. As for graphene, due to the different reconstructions the growth of germanene is limited in lateral dimension. The interesting properties of 2D materials edges in nanoribbons could then be a way of exploiting germanene on Al(111). However, no analysis has been performed yet on how the interaction with the substrate modifies the edges of germanene. We will face this problem in chapter 4.

1.4 Germanane

The aromatic bonds of 2D materials like graphene can be saturated with hydrogen atoms: this process leads to a 2D hydrocarbon called graphane in the full hydrogenated picture, or just hydrogenated graphene in the partial one [100, 101]. Every atom of carbon is then bonded with 3 other neighbouring atoms of carbon and one atom of hydrogen. The flat benzene cell of graphene evolves in a cyclohexane one, which is not flat, with bond length evolving from 1.42Å in graphene to 1.52-1.56Å in graphane, while C-H bond length is 1.1Å [102].

Graphene hydrogenation is interesting for H storage [103] and for the cataytic production in the interstellar medium [104]. On the other hand, the symmetry breaking between the two sublattice produces a gap opening, between 3.5 and 3.7 eV [102] depending on the resulting cyclohexane configuration, boat or chair/twist [105]. The band-gap has also been shown to decrease with the increase of the sheet dimension [105] or via the Van der Waals interaction with other graphane-like sheets [106, 107], allowing then its engineering.

Similarly to graphane, the hydrogenated version of silicene and germanene have been predicted to have a gap between 3 and 4 eV [108, 109, 110]. However, the origin of this gap is slightly different. For graphane, the presence of hydrogen causes the formation of nearly free electron states near the bottom of the conduction band at the Γ-point; for germanane and silicane the lowest unoccupied state at Γ is almost unchanged, but quantum-confinement effects produce a shift upward of the lowest bulk-unoccupied state (at L for silicane, X for germanane) which is responsible for the bulk indirect gap [111]. Depending on the atomic configuration, this results for silicane in a direct (for boatlike) or indirect gap (for chairlike), while the gap is always direct for germanane [109].

One way of obtaining hydrogenated 2D materials is via exposition to hydrogen plasma, a successful technique for single layers, both exfoliated [112] and CVD ones [113]. The mechanism of the bonding has also been imaged [114] and a stabilization of the C-H bond has been consequently been proposed exploiting acoustic waves [115]. However, only hydrogenated graphene has been produced in this way. The exact amount of bonded hydrogen is difficult to obtain via most of the surface characterization techniques, and up to this day it is mostly based on D/G peaks ratio in Raman spectra [100].

Another way of obtaining an hydrogenated 2D material is by exploiting already existing layered materials via a chemical substitution. In particular, it has been shown that the Zintl phases [116] such as $CaSi_2$ and $CaGe_2$ can be made to react with HCl in solution to produce layered silicon and germanium solids [117, 118, 119]: this technique is called topochemical (or topotactic) deintercalation.

1.4.1 GeH

The first report of GeH dates back to 2000 [117], then reprised by the Goldbergers's group [120]. β-$CaGe_2$ can be obtained by sealing stoichiometric ratios of Ca and Ge in a quartz tube, annealing to 950-1050°C and cooling over a period of 2-10 days [120]. Another way is a co-deposition of Ca and Ge on Ge(111) by molecular epitaxy [121], which produces just $CaGe_2$ and not other phases, compared to Ca deposition on Ge(111) [122], but the grain dimension is in the micrometer range. These crystals were then left in aqueous HCl at -30/-40°C for a period from 12h to 8 days. The reaction which takes place is:

$$n\mathrm{CaGe_2} + 2n\mathrm{HCl} \rightarrow (\mathrm{GeH})_{2n} + n\mathrm{CaCl_2} \tag{1.36}$$

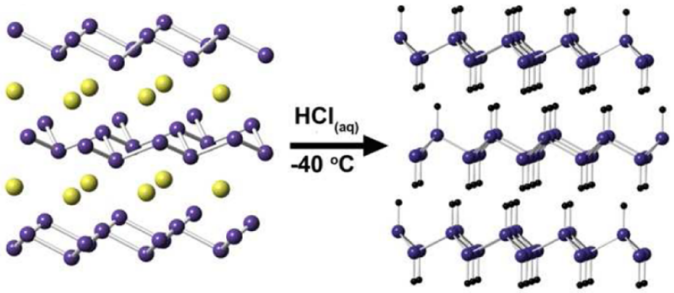

Figure 1.16: Synthesis of GeH via topochemical deintercalation. Adapted from [120].

X-ray diffraction (XRD) shows a 2H unit cell, which means 2 GeH layers per hexagonal c-unit cell spacing, with $a = 3.880$ Å and $c = 11.04$ Å. Every layer is then 5.5 Å, slightly bigger than $CaGe_2$ 5.1Å, due to the replacement of Ca^{2+} with two Ge-H bonds. This thickness has been later confirmed by Atomic Force Microscopy (AFM) measurements [120]. A halo in electron diffraction patterns is present and it is due to a c-axis disorder. This is originated by the turbostratic disorder, meaning small rotation angle between layers plus random translations. The rotation angle is limited to $\pm$ 3° before decomposition of the GeH van der Waals layers [123].

One important analysis is the **Fourier transform infrared spectroscopy (FTIR)**. Multiple peaks are possibly present, to be assigned to the material itself and possible impurities:

- Ge-H bending mode is around 550-600 cm^{-1}, while Ge-H stretching mode is around 2000 cm^{-1}, at $\sim$ 100 cm^{-1} from the equivalent hydrogenated amorphous films [124];
- The observation of peaks in the 1300-1700 cm^{-1} and 3400-3600 cm^{-1} ranges corresponds to O-H bending and stretching modes, which could be explained by the presence of crystal water between the layers of GeH [125, 126];
- Ge-O-Ge peak is between 800 and 1000 cm^{-1} and it is due to oxidation, starting from the external layers;

FTIR can be compared to **Raman spectroscopy**. The main Ge-Ge stretch (E_2 mode) is measured around 300 cm^{-1} and a second vibrational mode is present at 228 cm^{-1}, ascribed to 2D A_1 mode [120]. Thickness-dependent Raman was complicated by the photothermal degradation at low laser intensity and the overlap of the higher order silicon peaks of the SiO_2 with those of interest [120].

X-ray photoelectron spectroscopy (XPS) shows just a peak for Ge $2p_{3/2}$ at 1217.8 eV, relative to Ge^+ state of oxidation. In case of oxidation $Ge^{2+/3+}$ can appear around 1219 eV.

Absorption measurements performed via diffuse reflectance absorption (DRA) suggest a gap between 1.6 and 1.65, complicated by a long Urbach tail, sign of disorder and presence of defects [120]. For a small number of layers, 1-6, the band-gap oscillates between 1.47 and 1.66 eV, depending also on the stacking sequence [127].

Vogg reported a **photoluminescence spectra** show a peak around 1.55 eV (920 nm), with a linewidth of 0.3 eV and a very low quantum yield, around 1% [117, 128]. Goldberger's group did not observe any PL [120].

The **oxidation** as a function of time was studied via with FTIR and XPS: after 60 days there was no resurgence of Ge-O modes between 800 and 1000 cm^{-1}, which proves bulk does not oxidize. XPS tests the surface oxidation and shows a shoulder relative to $Ge^{2+/3+}$ at 1219.3 eV which amounts to

19.5% of the signal after 1 month, 29.7% after 5 months and disappears after Ar etching [120].

Temperature-stability was studied via thermogravimetric analysis (TGA), DRA, XRD, Raman and pair distribution function (PDF) measurements. The ensemble of these informations show that amorphization occurs starts around 75° and finishes around 175°, below the temperature of dehydrogenation (200-250°C) [120, 129].

Transport properties have been investigated via a 4-probe analysis of thermal conductivity, which gave 0.53 ± 0.09 W m^{-1} K^{-1} as result [130]. This decreased to 0.29 ± 0.05 W m^{-1} K^{-1} after amorphization. P, Ga and As doped samples have also been studied [131, 132], by incorporating the elements into the precursor $CaGe_2$. Resistance dropped by three orders of magnitude or more for these samples when measured in water-containing atmospheres due to water activation of the dopants center. A few devices have also been investigated [133, 134, 135]. A carrier mobility of 150 cm^2/Vs has been measured at 77K (70 cm^2/V s at room temperature) [136].

It deserves to be noted that contrarily to what reported so far a successful dehydrogenation without amorphization of the material has been recently reported and interpreted as the formation of multilayer germanene [137]. The resistivity after annealing to between 170 and 210 °C (depending on flakes thickness) goes down from 3 Ω for the most resistive one to $10^{-7}\Omega$.

1.4.2 $GeCH_3$

An alternative to GeH has been proposed, exploiting a methyl termination to saturate the bonds [138]. In a phase-transfer method, $CaGe_2$ is immersed in a biphasic CH_3I/H_2O solvent, in which water helps the insertion and inward diffusion of CH_3. The complete reaction is:

$$n\mathrm{CaGe_2} + 2n\mathrm{CH_3I} \xrightarrow{H_2O} n\mathrm{Ge(CH_3)_2} + n\mathrm{CaI_2} \tag{1.37}$$

XRD gives an hexagonal 2H unit cell with $a = 3.96$Å, and $c = 17.26$Å (8.63Å per layer). The 3Å more compared to GeH were justified by the difference between double Ge-C and Ge-H bond length (1.95 vs 1.52 Å) and van der Waals radi of -CH_3 and -H (2 vs 1.2 Å). AFM measurements showed a smallest step of 1.2 nm [138]

FTIR gives some variation in characteristic frequencies:

- Ge-H around 2000 cm^{-1} is substituted by Ge-C around 580 cm^{-1}, even if Ge-H survives in a 90:10 ratio;
- CH_3 rocking mode is found around 778 cm^{-1}, bending mode at 1237 and 1403 cm^{-1}, and stretching mode at 2907 and 2974 cm^{-1};
- O-H and Ge-O-Ge modes could be observed in the previously reported regions;
- H_2O intercalated between layers can appear with its characteristic stretching mode at 1615 cm^{-1} and bending mode at 3380 cm^{-1};

Raman spectroscopy so far proved the presence of a 299 cm^{-1} to be ascribed to Ge-Ge and a 594 cm^{-1} which appears for methyl functionalization [139].

XPS reports a slighlty shifted peak of Ge $2p_{3/2}$ at 1217.5 eV, compared to 1217.8 eV of Ge-H, but it is consistent with CH_3-terminated Ge(111).

Thermal stability for device exploitation was a major concern for GeH. Its study via TGA, DRA, XRD and PL show an amorphization that starts at 250° and CH_3 evaoration at 300°. $GeCH_3$ is then

more thermally stable than its full-hydrogen counterpart.

Methyl group was chosen because Ge(111) and Si(111) surfaces CH_3-terminated are more resilient to oxidation than H-terminated ones, which are highly air reactive. Air and water exposure after synthesis do not increase further the Ge-O signal if present, confirming that the oxidation takes place during the synthesis and that the Ge-CH_3 bond is stable as expected. In the phase-transfer method an HCl treatment is needed to substitute Ge-O bonds with Ge-Cl. These bonds however are weak, and reconvert to Ge-O after air exposure. A complete water-free synthesis however is not possible, because water helps to coordinate Ca^{2+} before methylation, acting as a proton source to transport the ion in solution [140]. To increase CH_3:H ratio a one-pot method has been proposed, which contemplates a reaction between $CaGe_2$, CH_3I, and H_2O in an CH_2CN solvent. In this way a 95:5 was obtained and the product is oxide-free [140]. However, similarly to GeH, the surface oxidizes over time as indicated by FTIR+XPS analysis. The one pot-method improves also thermal stability, bringing CH_3 desorption temperature to 420°C.

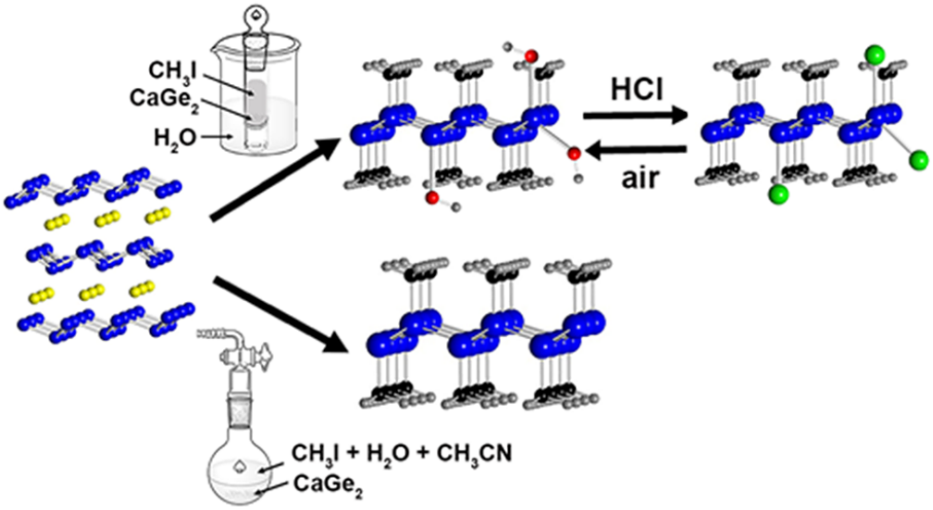

Figure 1.17: Two synthetic approaches of $GeCH_3$ via topochemical deintercalation. Adapted from [140].

$GeCH_3$ has strong **photoluminescence** (PL) emission between 1.7 [138] and 1.8 eV [139] (700-730nm, red), consistent with **DRA** measurement of an absorption onset at 1.69 eV. The fwhm is 250 meV for phase-transfer method and 180 meV for one-pot method. Quantum yield was measured around 0.23%. The PL intensity is proportional to the number of layers between 13 and 65, and in this range the emission center is not thickness dependent. In case of oxidation, the peak double and blue-shifts at 1.76 and 1.9 eV [140]. Water can also intercalate between the $GeCH_3$ layers, while this is not the case for GeH [141]. The presence of intercalated water can produce an intense additional luminescence around 1.9 eV, caused by local distorsions due to the dative interactions of H_2O with the $GeCH_3$ framework.

Temperature-dependent continuous wave and time-resolved PL measurements performed on the ensemble and on single flakes showed that at high temperature the linewidth is due to homogenous broadening. When temperature is lowered at 5K, a second peak appears at lower energy due to intra-gap trap states; this hypothesis is confirmed by the increase of overall lifetime as T decreases, due to a slower rate of trap-assisted recombination (low energy peak) than band-to-band recombination (high energy peak) [139].

These kind of defects were studied for both GeH, $GeCH_3$ and $Ge(CH_3)_{0.6}H_{0.4}$ via Depth-Resolved

Cathodoluminescence (DRCL), Surface Photovoltage spectroscopy (SPS) and DFT [142]. The different techniques identify the same kind of defects, suggesting that the vacancy of -H and -CH_3 termination does not produce intragap states and that the germanium scaffold is the responsible. Based on a 1.6 eV gap, a Ge vacancy with 1 passivating hydrogen produces a state 0.8 eV below the conduction band. A Ge divacancy with 1 passivating hydrogen is responsible for a state 1.4 eV below conduction band, while the same defect with no passivating hydrogen produces a defect 0.95-1 eV above valence band.

Theoretical calculations have shown that the hole mobility of $GeCH_3$ is 1.4×10^4 cm^2/Vs while electron mobility is 6.71×10^3 cm^2/Vs, along armchair direction [143]. No experimental measurement has been reported so far.

Both GeH [144] and $GeCH_3$ [145] are predicted to be Quantum Spin Hall insulators at high temperature under strain, but due to its low temperature stability the practical exploitation of GeH in a device is difficult. With 12% strain, relative to the equilibrum lattice constant, $GeCH_3$ has no imaginary phonon modes yet, indicating that it is still stable. At this strain value however it has become a semimetal and *s-p* inversion is produced at the Fermi level. The Spin-orbit coupling then opens a gap of 161 meV, which makes this effect measurable at room temperature.

While most of the characterization that has been performed was through optical means, a wider insight into transport properties of $GeCH_3$ is lagging behind. The multi-probe STM setup (which will be presented in the next chapter) is a suitable technique to characterize these properties in an ultra-high vacuum environment and at the nanometric level. The use of moving contacts is particularly adapted to chemically synthesised micro- and nanostructures which have been dispersed randomly on a substrate via drop-casting. Our aim is to probe and to understand the transport mechanism, with the interplay between intra-layer and inter-layer conduction, and a first measurement of the resisitvity and doping character of GeCH3.

Chapter 2

Methods

2.1 Scanning Tunneling Microscopy

2.1.1 The tunnel effect

At the beginning of $20th$ century the theory of quantum mechanics completely overturned the vision we had of the world. Most of the basic principles that seemed acquired and well known had to be rethought following the new paradigm of a probability-driven physics. One of the counterintutive principles that were discovered in this period is the quantum tunneling effect.

Imagine to be in front of a small stone wall in the english countryside and you need to go on the other side to reach your travel companions: you will need some energy to step on the wall and descend on the other side. In the process, you have to spend energy, supplied by your muscles. Your experience tells you not to try just hitting the wall until you arrive on the other side.

Quantum mechanics, on the other hand, tells us a counterintutive thing happens at the microscopic level. In fact, if a particle meets the equivalent of a wall, a step of finite energy, there's a chance the particle will pass through even if it does not have the necessary energy, and this probability decreases exponentially with the depth of this step in the movement direction (= the depth of the wall). This effect has been exploited since the 1957, when Leo Esaki produced the first tunnel diode with the electrons [146], for which he won the Nobel prize in 1973.

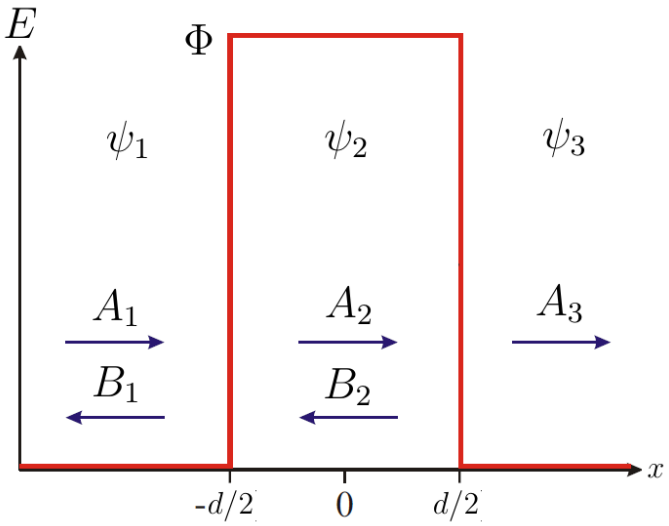

Figure 2.1: Schematics of 1D tunnel barrier of width d in the x direction.

Let's see a demonstration of the dependence on the thickness of the electron tunneling through a barrier, like that shown in figure 2.1. The barrier thickness is d. Let's take two areas separated by a potential barrier of value Φ. The electrons with energy $E < \Phi$ are described by their wave function ψ_1, ψ_2 and ψ_3 that verify Schrödinger's equation in their respective region:

$$\begin{aligned} \frac{-\hbar^2}{2m}\frac{\partial^2\psi_1}{\partial x^2} &= E\psi_1 \\ \frac{-\hbar^2}{2m}\frac{\partial^2\psi_2}{\partial x^2} + \Phi\psi &= E\psi_2 \\ \frac{-\hbar^2}{2m}\frac{\partial^2\psi_3}{\partial x^2} &= E\psi_3 \end{aligned} \tag{2.1}$$

where $\hbar$ is the Planck constant and m the electron mass. With the hypothesis of no reflection at $x = +\infty$, the general solutions of this kind of system are:

$$\begin{aligned} \varphi_1(x) &= A_1 e^{ikx} + B_1 e^{-ikx} \\ \varphi_2(x) &= A_2 e^{\alpha x} + B_2 e^{-\alpha x} \\ \varphi_3(x) &= A_3 e^{ikx} \end{aligned} \tag{2.2}$$

with A_i and B_i the incident and reflected part of each wave in region $i = 1, 2, 3$, $k = \sqrt{\frac{2m}{\hbar^2}E}$ and $\alpha = \sqrt{\frac{2m}{\hbar^2}(\Phi - E)}$. The transmission coefficient gives the probability that an electron crosses the barrier:

$$T(E) = \left|\frac{A_3}{A_1}\right|^2 \tag{2.3}$$

We have 5 coefficients and just 4 border conditions (continuity and derivability at $x = \pm d/2$), then we will be able to write 4 coefficients as a function of the 5th. We choose A_3. The solution of the system gives:

$$T(E) = \left|\frac{A_3}{A_1}\right|^2 = \frac{1}{1 + \frac{\Phi^2}{4E(\Phi - E)} sinh^2(\alpha d)} \tag{2.4}$$

The transmission coefficient $T(E)$ is not zero, and this means that the electrons are able to cross the barrier due to their undulatory nature. The probability is not constant, but depends on the thickness of the barrier.

Until 1982, quantum tunneling was used in superconductors and surface studies via metal-insulator-metal sandwich structures with a solid-state insulator. This classic tunneling technique however had 2 main limitations: (1) no further modification of the surface could be performed after the creation of the tunnel junction, and (2) only spatial information laterally averaged over 100nm or more could be obtained, due to the limitations of lithographic techniques. Even if this last point is less valid nowadays due to technology advancement, the first remains actual. In 1982, Binnig and Rohrer at IBM Zurich thought of using vacuum itself as tunnel barrier, providing both access to the tunnel electrodes at any time and a spatial resolution to the nanometric level by appropriately shaping one of the electrodes. The instrument they invented is called Scanning Tunneling Microscope [147].

2.1.2 Expression of the tunnel current

The transmission coefficient is not an easily measurable physical quantity. Its equation can be further developed to obtain the actual value of the tunnel current. In the treatment so far none of the electrodes were polarized and as a result the current which flows in one direction is perfectly balanced by the current in the other one. In order to obtain a useful equation for the feedback

current, we need to apply a non-zero voltage. At a given bias eV applied on the sample, we need to integrate the transmission coefficient $T(E, eV)$ of the electrons across the barrier to all energy states in the sample, between energies ranging from $E_{F,sample}$ to $E_{F,Tip}$, respectively the Fermi level of the sample and the tip. The latter is equal to $E_{F,sample}+eV$ at $T = 0$K. We can then rewrite it as an integral between 0 and eV, given the common area below the curve. The integration gives:

$$I = \int_0^{eV} T(E, eV)\rho_{tip}(E - eV)\rho_{sample}(E)dE \tag{2.5}$$

with ρ_{tip} and ρ_{sample} the local densities of electronic states of respectively the tip and the sample.

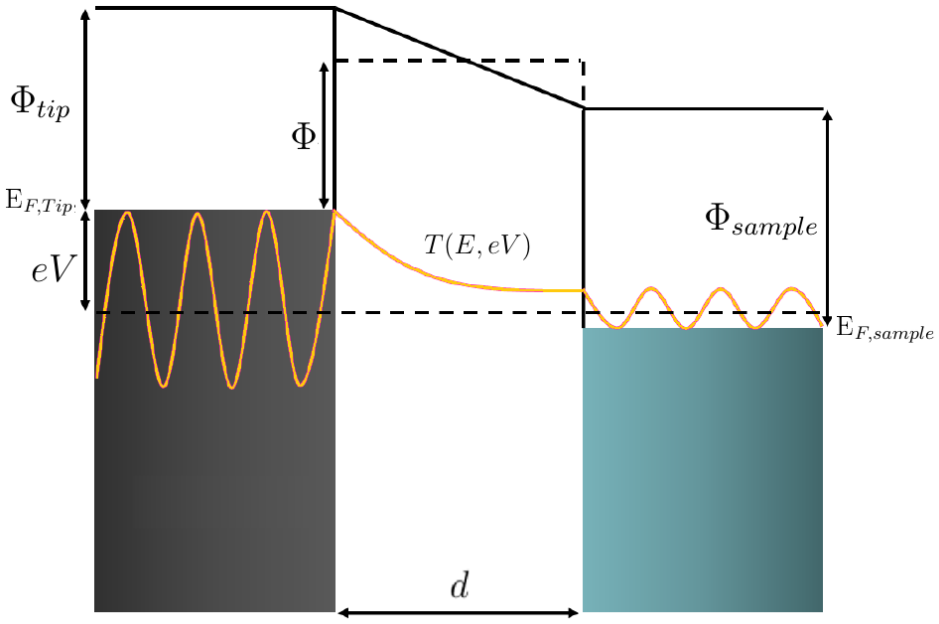

Figure 2.2: Schematic diagram of the tunnel junction of the STM. Adapted from [148]

There are some common approximations which can make the physical understanding of the process easier:

- The polarization eV of the electrodes is usually small compared to the height of the tunneling barrier Φ. In this conditions the trapezoidal barrier can be simplifed in a square barrier with averaged height:

$$E_{SB} = \frac{\Phi_{tip} + \Phi_{sample}}{2} - \frac{eV}{2} \tag{2.6}$$

  In this way we can use equation 2.4 with E_{SB} as height of the barrier, otherwise we would require a correction to take into account polarization;

- For an usual metal whose work function is around 4 eV (example, tungsten, 4.5 eV), $\alpha = \sqrt{\frac{2m}{\hbar^2}(\Phi - E)} \sim 1$ Å^{-1} at small energies. This means that when the barrier d increases of 1 Å, the transmission coefficient decreases by e^{-2}, around 0.1 (a factor of 10). The transmission coefficent can then be simplified to:

$$T(E) \sim \frac{16E(\Phi - E)}{\Phi^2} exp[-2d\sqrt{\frac{2m}{\hbar^2}(\Phi - E)}] \tag{2.7}$$

  Since the distance between electrodes is expected to be the order of a few angströms, we can simplify $T(E)$ formula and use equation 2.7:

$$T(E) \sim \frac{16E(E_{SB} - E + \frac{eV}{2})}{E_{SB}^2} exp(-2d\sqrt{\frac{2m}{\hbar^2}(E_{SB} - E + \frac{eV}{2})}) \tag{2.8}$$

Inserting this equation into 2.5 gives:

$$I = \int_0^{eV} \frac{16E(E_{SB} - E + \frac{eV}{2})}{E_{SB}^2} exp(-2d\sqrt{\frac{2m}{\hbar^2}(E_{SB} - E + \frac{eV}{2})})\rho_{tip}(E - eV)\rho_{sample}(E)dE \quad (2.9)$$

which for biases much lower than the average barrier height it becomes:

$$I = 16exp(-2d\sqrt{\frac{2m}{\hbar^2}E_{SB}}) \int_0^{eV} \frac{E - eV}{E_{SB}} \rho_{tip}(E - eV)\rho_{sample}(E)dE \quad (2.10)$$

The current depends then exponentially on the distance between the electrodes and it allows a very fine tuning of this value.

2.1.3 Building a real microscope

The idea behind the scanning of a surface via Tunnel Effect is then simple: create a tunnel junction by approaching a metallic tip very near to the surface to be able to detect a tunneling current. The simplest morphology can be obtained by keeping the tip position constant in z, moving it across the sample and interpreting the variation of tunneling current as function of the surface roughness via its exponential dependence from the distance. This is however risky, because the microscopic roughness can be higher than the distance required between tip and sample to obtain a non-negligible tunnel current. We would need in fact a very flat area to perform a fixed z scan without crashing the tip. Instead of keeping z constant, the more used option is a fixed constant tunneling current. To achieve this, multiple features are needed:

- A very sharp metallic tip, to average the signal on the smallest area possible;
- A system that allows us to bring the tip close to the sample within the nanometer without crashing it, and finely tune this distance with a less than angström resolution;
- A high sensibility to discriminate between very low currents;
- A feedback loop system to adapt the position of the tip in function of tunneling current fast enough compared to the scan speed;
- An isolation from external vibrations which would easily made the tip touch the sample;

The system proposed by Binnig and Rohrer in 1982 [147] and then better explained in 1983 [149] is reported in figure 2.3.

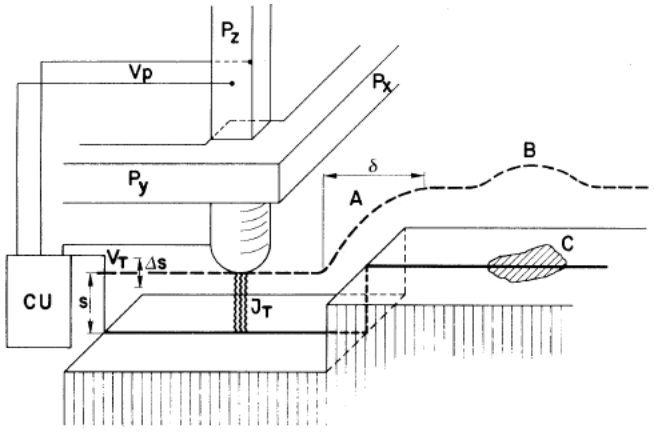

Figure 2.3: Original schematics of the first STM setup. Reproduced from [147].

To produce sharp tips, they cut W or Mo wires of about 1 mm diameter, grounded at one end at roughly 90°. This tips were characterized by an overall radii of less than a micrometer, but the rough grinding process was claimed to create rather sharp minitips, which were in fact the ones responsible for a good spatial resolution, depending on the closest one to the feature to be observed. They managed to obtain 20 Å lateral resolution. This could be improved by "gently touching" the surface, gathering some atoms and bringing the resolution down to 10 Å. By applying high field (10^8 V/cm) for half an hour they reached even higher resolution. Nowadays the most common way of preparing tips is electrochemical etching. For W tips for example, a solution of NaOH is prepared, the W wire is dipped into it with a voltage applied, and the joint action of the etching and gravity produces atomically sharp tips.

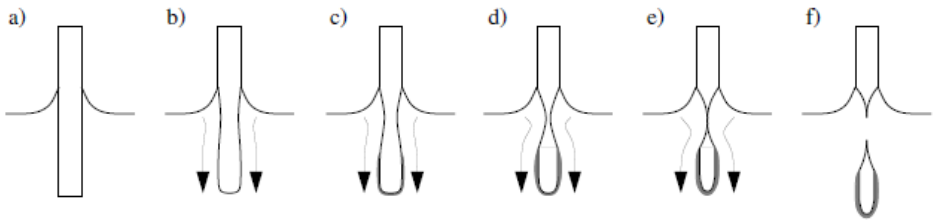

Figure 2.4: Illustration of the phases of chemical etching via NaOH which leads to a W tip formation. a) the formation of the meniscus. b) to e) the flow of WO_4 towards the end of the wire, the formation of a dense layer of WO_4 around the bottom of the wire and the necking of phenomenon in the meniscus. f) the lower part breaks due to gravity, the tip is formed. Reproduced from [150]

The high precision necessary for the tip movements was obtained via a rough drive named "louse" consisting of a piezoelectric plate, with a sample holder on top, resting on three metal feet, separated by high-dielectric constant insulators from the metal groundplates. The feet were clamped electrostatically to the ground-plate by applying a voltage. The body of the louse could be elongated and contracted with an appropriate clamping sequence of the feet, moving the louse in any direction in steps between 100 Å and 1 micrometer, and up to 30 steps/s. Then a rectangular piezodrive moved the tip with a range of some micrometers in each direction. The system nowadays is not very different, with a rough drive and piezoelectric tube, which moves the tip around the sample.

The feedback loop exploits a typical Proportional-Integral-Derivative (PID) controller. P term is related to the present error between measured value and setpoint current; I term accounts for the past values of this difference, integrating them; D term accounts for the rate of future change, estimated by the derivative of the current. The right settings of a proper displacement for P and time constants for I and D allows the system to maintain the setpoint current within a small error bar.

To achieve the necessary isolation from external vibrations, Binnig and Rohrer initially used a superconducting magnetic levitation system. After that, they switched to a two-stage spring system, reaching a stability of the gap between sample and tip of about 0.2 Å. Today the system is usually placed on a spring floor and then the STM inside the UHV chamber is damped with Eddy currents.

Even if the STM is separated from external vibrations, a wire of 2 millimeters length (in the case of LT-STM and high-resolution tips of 4-probe) vibrates between 1 Hz and 3-4 Hz when it is moving on a micrometer/nanometer scale. Therefore, one can be concerned about creating vibration of the tip itself. However, the lower vibration mode of a tip of this dimension is usually way higher, even compared to the piezo working regime (5-10 kHz). The lowest resonance frequency in the bending mode of a long uniform rod, clamped at one end and free at the other end, was derived by Lord Rayleigh in 1825:

$$f = \frac{0.07 D v_s}{L^2} \tag{2.11}$$

where v_s is the velocity of sound in the rod (given by $\sqrt{Y/\rho}$, with Y Young modulus and ρ its density), while L and D are length and diameter of the rod. This equation can be used to estimate the bending eigenfrequencies of the whole tip, not the end part. For a wire of 0.2 mm diameter and 2 mm of length, the lowest bending eigenfrequency of the tungsten wire has a value of around 15 kHz. For the final part of the wire, the microtip, the frequency is even higher. For a constant aspect ratio (D/L) of an object, the eigenfrequency scales inverse to the size of the object ($f \propto 1/L$). When an object is scaled down in size, the vibration frequency rise as $\propto 1/L$. The risk of exciting resonance modes of the tip is then avoided.

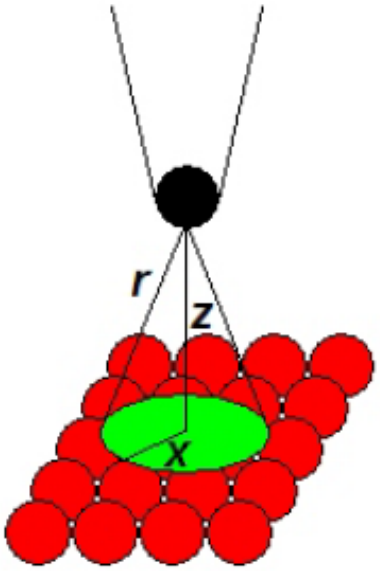

Figure 2.5: Lateral resolution of the STM. Reproduced from [151]

While the vertical resolution of the microscope is strongly connected to the minimum movement attainable with the piezo system, the lateral resolution is connected to the dimension of the tip. Assuming that just the last part of the tip contributes to the current, and ideally just the last atom, we can suppose that this atom has a wavefunction of s type described by:

$$|\Psi|^2 = \frac{e^{-2\alpha r}}{r^2} \tag{2.12}$$

with $r = \sqrt{x^2 + z^2}$ as seen in figure 2.5. As $z >> x$, r is approximated by:

$$r \approx z + \frac{x^2}{2z} \tag{2.13}$$

Then:

$$|\Psi|^2 \approx \frac{e^{-2\alpha z}}{z^2} e^{-\alpha \frac{x^2}{z}} \tag{2.14}$$

which is a gaussian function in x, of full width at half maximum of:

$$\Delta x \approx \sqrt{\frac{2z}{\alpha}} \tag{2.15}$$

The height of the tip is $z = R + d$, where R is the radius of curvature of the apex, and d the tip sample distance. For tungsten tip with a low bias, we calculated that $\alpha \sim 1^{-1}$. The tip sample distance in scanning conditions is between 4 to 8 Å, as controlled contact experiences have shown [152, 153, 154, 155]. Following Tersoff and Hamann's approach [156], the height of the tip can be taken equal to the radius of curvature R of the tip, which is of several nanometers and bigger than the tip-sample separation. Thus the lateral resolution is:

$$\Delta x \approx 1.4\sqrt{R} \tag{2.16}$$

For a very sharp tip with a radius of curvature of R=100 Å the equation gives $\Delta x = 14$ Å. The experimental resolution is much higher than this value. The reason is that the atomic resolution is due to atomic-sized protrusions at the apex of the tip with very small radius of curvature. If one takes a tip-sample distance $d = 5$ Å, and an equal value for the radius of the apex, the resolution to be achieved is 4.4 Å.

A more realistic result was calculated by Sacks [157], who took into account tip-sample couplings and other symmetries of the orbitals like p or d, instead of just s, explaining the high experimental resolutions.

2.2 Scanning Tunneling Spectroscopy

The analysis of morphology at the atomic level has pushed technology forward, but this is not the only contribution that STM gave to material science. In fact, the morphology is usually obtained by keeping the polarization constant and regulating the distance between the sample and the tip to keep also I stable, while changing $x-y$ positions on the sample. If $x-y$ are kept fixed a whole new family of measurements, called spectroscopic ones, is opened. Between the 3 main parameters I, d and V, one is kept constant, the second is ramped while measuring the third one. For practical reasons, we consider usually the z position of the tip compared to a reference instead of the vacuum gap d which is more difficult to determine. In this way, 6 types of spectroscopy are possible: $I(z), I(V), z(V), z(I), V(z)$ and $V(I)$. Mainly three of these are used in reality while the 3 others do not provide very useful information.

2.2.1 Distance versus bias: z(V)

Let's start with the mode more similar to morphological scan. The feedback loop is kept closed (constant current I), and V is ramped on a certain $X-Y$ position. z will be then adjusted to maintain I constant, resulting in the variation of z as function of V. This mode allows to measure the height of the barrier via the resonances in the localized states in it. When eV becomes comparable to $\Phi_{SB} = \frac{\Phi_{sample}+\Phi_{tip}}{2}$ the shape of the barrier gradually becomes triangular, and when eV becomes bigger than Φ_{SB}, oscillations of the tip-sample distance are detected because of field emission resonances. The first experiments to show resonances due to localized states in the barrier were done by Binnig and Rohrer [158]. This mode can also be used to test the "health" of the tip, checking if these resonances are observed or not and exploiting the oscillation in z to clean it from contaminants. To obtain physical information however this mode is not broadly used, even if it can easily detect variation of both tip and sample conductivity, because broad spectra with both negative and positive bias cannot be performed or the tip would enter in contact with the sample at $V = 0$.

2.2.2 Current vs distance: I(z)

As previously seen, current is exponentially dependent on the tip-sample distance. The decay constant α is related to the work-function of the tip and the sample:

$$I \propto e^{-2\alpha d} \tag{2.17}$$

where:

$$\alpha = \sqrt{\frac{2m}{\hbar^2}\left(\frac{\Phi_{tip}+\Phi_{sample}}{2} - \frac{eV}{2}\right)} \tag{2.18}$$

This spectroscopic mode is useful to identify the work function of the tip, or of the sample, by keeping the tip in fixed position, opening the feedback loop, and ramping the distance z at constant V, while measuring I. This is another test to be reassured of the good state of the tip: not obtaining an exponential dependence is a strong indication of the presence of an artefact, possibly due to the tip itself.

2.2.3 Current vs bias: I(V)

Current vs bias spectroscopy is the most powerful characterization of tunnel microscopy. It allows to measure the electronic behaviour and electric characteristics at the atomic scale. Feenstra, Thompson and Fein performed the first measurements keeping the feedback loop open, with then tip-sample distance constant and measuring current variation vs V ramping [159].

Most of the spectroscopic measurements that are performed are elastic. This means that mainly the electrons at the center of the Brillouin zone, with $\vec{k} = 0$, contribute to the current. This can seem a limitation in principle , but most of semiconductor have their gap at Γ.

We have previously derived an equation for the tunneling current, under certain safe assumptions. If we suppose also a constant density of states for the tip, then we can take the term out of the integral in 2.5:

$$I \propto \rho_{tip} \int_0^{eV} T(E, eV)\rho_{\text{sample}}(E)\mathrm{d}E \tag{2.19}$$

then deriving this equation we obtain:

$$\frac{\partial I}{\partial V} \propto e\rho_{tip}\rho_{sample}(eV)T(eV, eV) + e\rho_{tip}\int_0^{eV} \frac{\mathrm{d}}{\mathrm{d}eV}[T(E, eV)]\rho_{sample}(E)\mathrm{d}E \tag{2.20}$$

A concern can be raised observing this equation, which depends on the sample density of states, but not with a simple proportionality. The transmission coefficient $T(E, eV)$ exponentially increasing with the bias, there is a larger contribution of the states lying at higher energy with respect to the states closer to the Fermi level. In the presence of a band gap this would produce a significative distortion of the relative amplitudes of the states, and also produce a false width of the gap itself. How to get rid of this exponential dependence? Feenstra and coworkers [160] showed that the differential conductance can be normalized by the ratio I/V in order to cancel the exponential dependence of $T(E, eV)$:

$$\frac{\frac{\partial I}{\partial V}}{\frac{I}{V}} \propto \frac{\rho_{\text{sample}}(eV) + \int_0^{eV} \frac{\partial}{\partial eV}[T(E, eV)]\frac{\rho_{\text{sample}}(E)}{T(eV,eV)}\mathrm{d}E}{\frac{1}{eV}\int_0^{eV} \frac{T(E,eV)}{T(eV,eV)}\rho_{\text{sample}}(E)\mathrm{d}E} \tag{2.21}$$

We can safely consider the second term of the numerator as a slowly varying background. The variation of this ratio are then mainly related to $\rho_{sample}(eV)$ behaviour. Thus:

$$\frac{\frac{\partial I}{\partial V}}{\frac{I}{V}} \propto \rho_{\text{sample}}(eV) \tag{2.22}$$

This is an important result. It means that it is possible to obtain the Local Density of States (LDOS) of the sample from measured $I(V)$ curves [159, 161], independent of the tip-sample separation. It gives access to single electronic levels without the need of a two-level transition as in optical spectroscopy, mostly avoiding coulombian and excitonic effects. This technique works well with metals and small band gap materials. There are some corrections to be made when working with wide band gaps:

- The I/V ratio has an higher order of infinitesimal than $\frac{\partial I}{\partial V}$, i.e. it decreases to zero faster when V $\to$ 0. As a result, the ratio $\frac{\frac{\partial I}{\partial V}}{\frac{I}{V}}$ is divergent at the edges of the gap [162]. A solution is applying an exponential convolution to I/V, which results in a broadening:

$$\frac{\bar{I}}{V} \equiv \int_{-\infty}^{+\infty} \frac{I\left(V'\right)}{V'} \exp\left[\frac{-\left|V'-V\right|}{\Delta V}\right] \mathrm{d}E \tag{2.23}$$

  ΔV is chosen of the order of the band gap of the sample in order to avoid a significant amplification of the noise level in the band gap. This process does not induce any shift of the peaks position, suppressing the divergence at the edges without loss of information;

- The ratio $\frac{\frac{\partial I}{\partial V}}{\frac{I}{V}}$ can give rapidly oscillating and incoherent results when the current decreases in the band-gap, i.e. with a bad signal-to-noise ratio. Another way to counterbalance the exponential dependence of the current against distance is acting on the tip position during the scan, in order to keep the exponential argument constant:

$$I \propto \exp(-2d\sqrt{\frac{2m}{\hbar^2}}\sqrt{\Phi - \frac{|eV|}{2}}) \tag{2.24}$$

  The varying parameters in the exponential argument during the scan are d and eV. We can set:

$$d(V)\sqrt{1 - \frac{|eV|}{2\Phi}} = d_0 \tag{2.25}$$

  where d_0 is a constant corresponding to the tip-sample distance at $V = 0$. For small values of V (smaller than Φ) a Taylor expansion gives:

$$d(V) = d_0\left(1 + \frac{|eV|}{4\Phi}\right) \tag{2.26}$$

  We conclude that in order to gain sensitivity in the band gap region of semiconductors the tip can be approached closer to the sample following a linear ramp against V. If $I(V)$ contains both positive and negative voltages, the ramp has to be set in order to have a minimum of the triangle wave at $V = 0$. With d_0=10Å, Φ = 4.5eV, the slope to be counterbalanced is 0.56Å/V.

2.2.4 Lock-in amplifier

The derivative of the current vs voltage was discussed up to this point but no information was given about how to obtain it. The first approach can be to numerically derivate the current. This is a fast and easy method, but the output is very noisy: due to mechanical instabilities and electronic amplifiers, a wide-band noise (up to some kHz) is inherently included in the measurement and is amplified with the derivation of the current. The major contribution of the noise is a low frequency $1/f$ noise that cannot be removed from numerically calculated derivatives.

The solution is an analog derivation of the signal. Lock-in amplifiers are the key: these instruments use a phase sensitive detection to measure the amplitude of small AC signals filtering out the noise, by shifting the interesting part of the signal to a reference frequency.

What are the key elements of a basic lock-in amplifier?

- **AC amplifier**: it is a simple voltage amplifier combined with a certain number of filters. In this way, only a certain range of frequency is amplified, cutting all the other frequencies;
- **Voltage Controlled Oscillator**: it is a voltage oscillator which is able to synchronize with an external reference value in phase and frequency, and then to shift this signal between 0 and 360°. This is the very basic feature: nowadays lock-in have their internal function generator which provides the reference signal as set by the user (amplitude, frequency, phase shift).
- **Phase Sensitive Detector (multiplier)**: it is a circuit that takes two signal $V_{in,1}$ and $V_{in,2}$ and produces as output V_{out}=$V_{in,1}\times$ $V_{in,2}$.
- **Low pass filter**: it is a normal RC low pass filter where it is possible to set the cut frequency by changing values of C and R;
- **DC amplifier**: a simple continuous DC amplifier;

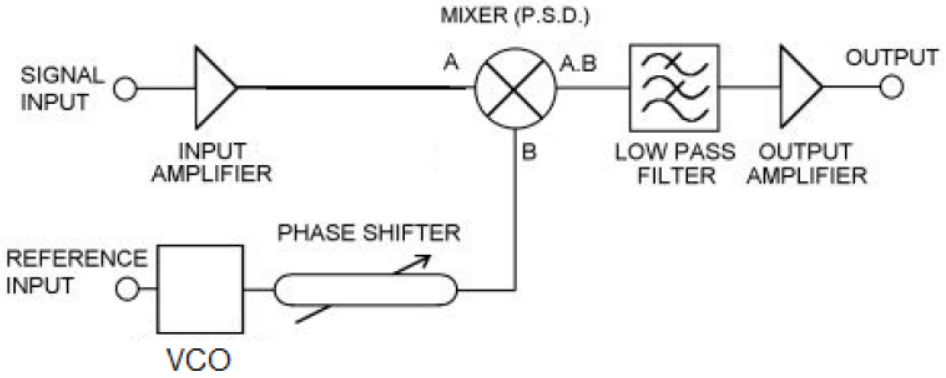

Figure 2.6: Lock-in basic schematics.

Lock-in behaviour in time domain

Let's start with a signal $v_{in} = V_0\cos(wt)$, affected by a noise $n(t)$. We send this signal as input of the AC amplifier. If we are not interested in amplifying signals with other frequencies than w, then we can set the filters inside as necessary. We define G_{ac} the amplification gain for signal of frequency w and $G(f)$ the gain for other frequencies. At the exit of the AC amplifier we have:

$$v_{AC}(t) = G_{ac}V_0\cos(\omega t) + G(f)n(t) \tag{2.27}$$

This voltage is then multiplied by the PSD with a reference signal:

$$R(t) = 1\cos(\omega t + \phi) \tag{2.28}$$

with ϕ generic phase due to electronics delays. The product gives:

$$\begin{gathered} v_{PSD}(t) = v_{AC}(t)\cdot R(t) = \\ v_{PSD}(t) = [(G_{ac}V_0\cos(\omega t) + G(f)n(t)]\cos(\omega t + \phi) = \\ G_{ac}V_0\cos(\omega t)\cdot\cos(\omega t + \phi) + G(f)n(t)\cos(\omega t + \phi) \end{gathered} \tag{2.29}$$

We can use a trigonometric addition formula to simplify the previous one:

$$\cos\alpha \cdot \cos\beta = (1/2)[\cos(\alpha-\beta)+\cos(\alpha+\beta)] \tag{2.30}$$

We obtain:

$$\mathrm{v}_{PSD}(t) = \frac{G_{ac}V_0}{2}[\cos(2\omega t+\phi)+\cos\phi] + G(f)n(t)\cos(\omega t+\phi) \tag{2.31}$$

or:

$$v_{PSD}(t) = \frac{G_{ac}V_0}{2}\cos\phi + G(f)n(t)\cos(\omega t+\phi) + \frac{G_{ac}V_0}{2}\cos(2\omega t+\phi) \tag{2.32}$$

Let's focus on the second term. In particular, we can use a Fourier transform and rewrite:

$$n(t) = Re\left[C\int \mathrm{d}\omega'\eta(\omega')\,e^{i\omega' t}\right] = C\int \mathrm{d}\omega'\eta(\omega')\cos\omega' t \simeq \sum_{\omega'}\eta(\omega')\cos\omega' t \tag{2.33}$$

Inserting this into the full equation, and taking out from the sum the term $w' = w$ we obtain (applying again the trigonometric addition formula):

$$\begin{aligned} v_{PSD}(t) =& \frac{G_{ac}V_0}{2}\cos\phi + \frac{G_{ac}V_0}{2}\cos(2\omega t+\phi) + \frac{G_{ac}\eta(\omega)}{2}[\cos\phi+\cos(2\omega t+\phi)] + \\ &+ \sum_{\omega'\neq\omega}\frac{G(\omega'/(2\pi))\,\eta(\omega')}{2}\left[\cos\left[(\omega'+\omega)t+\phi\right]+\cos\left[(\omega'-\omega)t-\phi\right]\right] \end{aligned} \tag{2.34}$$

Then equation 2.34 represents the signal out from the multiplier. We can clearly see that just some terms are constant, not depending from the time, while other are all periodical with frequency $2w$ (most important term) and $(w+w')$ or $(w'-w)$ (parts due to background noise). If we could isolate the time independent component (zero frequency), we would have:

$$v_{PSD}(t) = V_{PSD} = \frac{G_{ac}V_0}{2}\cos\phi + \frac{G_{ac}\eta(\omega)}{2}\cos\phi \tag{2.35}$$

The second term of 2.35 can be ignored. Indeed it is sufficient to chose a frequency w for the modulation which is different from typical noise sources and their harmonics (like 50 Hz of electrical network). In this way we can assume to just have white noise. The intensity of noise for single frequency is then little apart from well identified noise sources, and $\eta(w)$ is then negligible if w is different from the sources of noise. Just the continuous component gives in good approximation by:

$$v_{PSD}(t) = V_{PSD} = \frac{G_{ac}V_0}{2}\cos\phi \tag{2.36}$$

To select just low frequency/no frequency signal we use a low pass filter which takes $v_{PSD}(t)$ as source signal.

In principle we don't know the phase ϕ. This is why VCD is able to shift the reference signal. If we send $R'(t)$=$\sin(wt+\phi)$, with similar calculations we obtain:

$$\begin{aligned} v'_{PSD}(t) =& \frac{G_{ac}V_0}{2}\sin\phi + \frac{G_{ac}V_0}{2}\sin(2\omega t+\phi) + \frac{G_{ac}\eta(\omega)}{2}[-\sin\phi+\sin(2\omega t+\phi)] + \\ &+ \sum_{\omega'\neq\omega}\frac{G(\omega'/(2\pi))\,\eta(\omega')}{2}\left[\sin\left[(\omega'+\omega)t+\phi\right]+\sin\left[(\omega-\omega')t-\phi\right]\right] \end{aligned} \tag{2.37}$$

We then again consider just the constant signal in time, and consider low the single frequency amplitude:

$$v'_{PSD}(t) = V'_{PSD} = -\frac{G_{ac}V_0}{2}\sin\phi \tag{2.38}$$

We then have two output signals, which are amplified by the DC amplificator to get:

$$\begin{aligned} V_{\text{out1}} &= \frac{G_{dc}G_{ac}V_0}{2}\cos\phi \\ V_{\text{out2}} &= -\frac{G_{dc}G_{ac}V_0}{2}\sin\phi \end{aligned} \tag{2.39}$$

Switching to polar coordinates:

$$\begin{aligned} V_\rho &= \sqrt{V_{\text{out1}}^2 + V_{\text{out2}}^2} = \frac{G_{dc}G_{ac}V_0}{2} \\ V_\phi &= \arctan\frac{V_{\text{out2}}}{V_{\text{out1}}} = \phi \end{aligned} \tag{2.40}$$

Knowing G_{dc} and G_{ac} which are set by the user, it's easy to obtain V_0. The other equation gives us the information about the electronic delays.

Lock-in behaviour in frequency domain

The lock-in behaviour is more intuitive if described in the frequency domain [163]. Let's suppose to have a signal of frequency f_0=200Hz synchronized at a lock-in amplifier. We want to obtain the amplitude V_0 with $\omega = 2\pi f_0$.

The power spectrum of a signal is obtained by plotting the spectral density of power vs frequency. In other words, given a signal $v(t)$, to obtain its spectrum we need to do Fourier transform to shift in frequency domain and then calculate the square magnitude to obtain power:

$$S_v(f) = F.T.\left[|v(t)|^2\right] \tag{2.41}$$

In figure 2.7(a) the power spectrum of the signal at the lock-in input is plotted. It contains the frequency f_0 200 Hz, together with noises peaks like 60Hz and relative harmonics which comes from environment (the formalism is adapted from an US article, where the 110V AC line is set on 60Hz, not as the 50Hz in Europe).

The signal passes through AC amplifier. With a well chosen filter the output signal is properly amplified around f_0 while the rest is attenuated (Figure 2.7(b)). Apart from f_0=180Hz, too close to the desired signal, all other frequencies are in fact lowered in intensity.

At this point we multiply the signal with the reference of frequency f_0 in PSD (2.7(c)). The multiplication brings to doubling of the number of peaks. Every peak at given frequency f_p divides into 2 peaks at $f_0 + f_p$ and $f_0 - f_p$. The information we desire now is contained in the peaks at $f = 0$ Hz and $f = 400$ Hz. In a similar way, the third harmonics of $f = 60$ Hz now is at 20 or 380 Hz.

At this point we send the signal into a low pass filter, to select $f = 0$ Hz. We set the cut frequency $f_c = 1/RC$, in this case for example $1/100 = 0.01$ Hz. Every signal higher than 0.01 Hz is highly attenuated. What is left is what is desired. This series of operation in the end allowed to transfer the signal in the range 199-200 Hz to interval 0-1 Hz and cut out the rest. Then the DC amplifier gives the output of the lock-in (figure 2.7(d)).

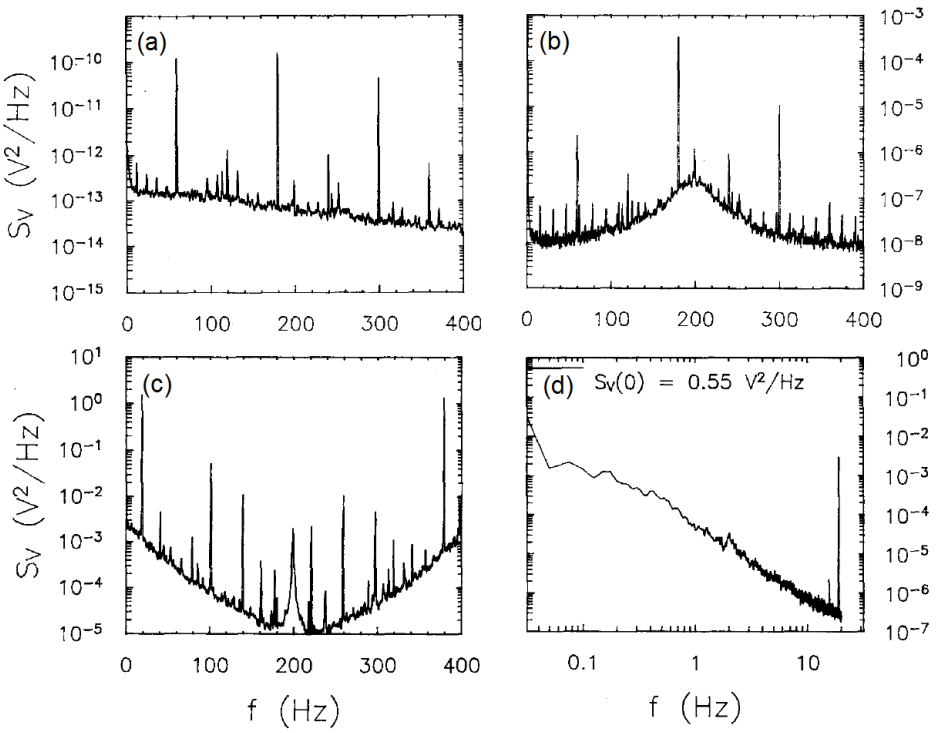

Figure 2.7: (a) Graph of the power spectral density of the input signal. (b) Power spectral density of the output of the AC amplifier stage. (c) Power spectral density of the output of the multiplier stage. (d) Power spectral density at the output of the DC amplifier. The desired signal at DC, $S_V(0)$ = 0.55 V^2/Hz, is the only significant signal. Adapted from [163].

Derivative of a real-time STS signal with a lock-in

After discussing how a lock-in amplifier is used to filter the noise of a periodic signal, we pass on its usefulness to measure the derivative of the current. In fact this is a natural consequence of applying a lock-in amplifier not to a periodic signal with a well defined frequency, but instead to a curve with no particular characteristic frequency. We can intuitively guess why looking at the image:

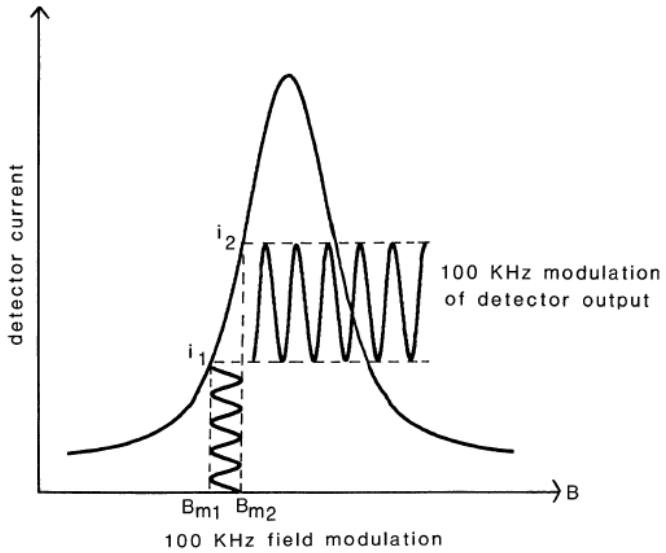

Figure 2.8: Modulation of a Lorentzian signal via a periodic signal.

The modulating signal has a finite amplitude and can't be applied on an infinitesimally short period of time. This means that it will always give an average information of a certain extent of the curve.

Remembering that the final output is proportional to the amplitude of the multiplied signal, this value will be clearly higher if the derivative of the curve is bigger in the considered region.

Let's prove it mathematically. When the polarization eV is modulated by a sinusoidal carrier of small amplitude $eV_{mod}sin(\omega_{mod}t + \phi)$, the tunneling current can be expanded into the following Taylor series:

$$I\left(eV + eV_{mod}\sin\left(\omega_{mod}t + \varphi\right)\right) = \sum_{n=0}^{\infty} \frac{I^{(n)}(eV)}{n!}\left[eV_{mod}\sin\left(\omega_{mod}t + \varphi\right)\right]^n \tag{2.42}$$

If the frequency of modulation, $f_{mod} = \frac{\omega_{mod}}{2\pi}$, is set high compared to the speed of the current feedback loop, the oscillations will not perturb the STM image or spectrum. Typically the frequency of modulation f_{mod} is chosen between 500 Hz and 10kHz, the higher allowed by the cut frequency of the current amplifier. In fact, if we expand the equation up to the second order:

$$\begin{aligned} I\left(eV + eV_{\mathrm{mod}}\,\sin\left(\omega_{\,\mathrm{mod}}\,t + \varphi\right)\right) = \\ I(eV) + I''(eV)\frac{e^2V_{\mathrm{mod}}^2}{4} \\ +I'(eV)eV_{\mathrm{mod}}\,\sin\left(\omega_{\,\mathrm{mod}}\,t + \varphi\right) \\ -I''(eV)\frac{e^2V_{\mathrm{mod}}^2}{4}\cos\left(2\omega_{\,\mathrm{mod}}\,t + 2\varphi\right) + o\left(e^2V_{\mathrm{mod}}^2\,\sin^2\left(\omega_{\,\mathrm{mod}}\,t + \varphi\right)\right) \end{aligned} \tag{2.43}$$

When the bias is modulated, the first and second derivatives of the current are carried by its first and second harmonics. If we repeat the previous calculations on this equation, we obtain that the output of the lock-in is:

$$Output = I'(eV)\frac{eV_{mod}}{2}\cos\left(\varphi - \varphi_{ref}\right) \tag{2.44}$$

which is, as said, proportional to the derivative of the tunneling current.

There are some real life issues in the application of a lock-in amplifier to an STM tip. In fact, we need wires to connect the lock-in and the STM tip-sample system, and these wires form a capacitance. The modulation creates then a parasitical sinusoidal current of the same frequency as the modulation. Depending on the capacitance value, this current can be unpredictably huge compared to the tunnel current, settling as a serious obstacle to the dynamical resolution of the lock-in. We can hope that due to the capacitive nature of the system the 90° phase shift compared to the tunnel current allows its removal by adding the opposite signal, derivated from the reference.

Attention must be paid also to the broadening caused on dI/dV by the integration over time of the modulation signal, which gives a half round shaped curve of diameter $2\mathrm{eV}_{mod}$ and that Klein et al. called "the instrumental resolution function" [164]. This function is convoluted all the time with the real LDOS spectrum, but as long as eV_{mod} remains smaller than the desired energy resolution there won't be any significant broadening. However, in some cases the Signal/Noise ratio requires an increase of the modulation amplitude to extract the signal and in these cases it is observable, and even stronger on the second derivative.

2.2.5 Current Imaging Tunneling Spectroscopy

Current Imaging Tunneling Spectroscopy (CITS) is one of the strongest tool provided by Tunnel Microscopy in term of electronic characterization. It consists on the acquisition of a STS curve for every pixel of the STM topographic image. In this way the topographic and spectroscopic features

are intimately linked due to their almost simultaneous acquisition.

In a real situation where the drift of the piezoelectric tube over time has to be considered, it can be convenient to acquire an STS curve only on a grid superimposed to the STM image. Let's consider for example a CITS with a 512 x 512 pixels STM image with a 64 x 64 grid of I(V) curves. The first topographic pixel is acquired, then a spectroscopic curve. The tip scans normally for 7 pixels, then acquires another I(V) curve. This process is repeated until the first horizontal line is complete. The following 7 horizontal lines are scanned as a normal STM image. The 9th line is then measured as the first line, by acquiring an I(V) curve every 8 pixels. The final result is an STM image and a grid of a total of 4096 I(V) spectra.

The dimension of the STM image, both physical and in pixels, as the dimension of the STS grid, are chosen both for scientific reasons (the dimension of the feature to be observed in STM as the supposed typical length of the spatial dependence of the I(V) characteristics) and experimental limitations (the typical drift at the temperature of the scan). The applied voltage and the feedback current have to be chosen in order to obtain a morphology of good quality and at the same time I(V) curves in the range of interest. In order to avoid instabilities in the spectra, which are enhanced in the derivative of the current, the starting voltage for the I(V) curve coincides with the applied voltage of the STM image. For example, the study of the I(V) features at voltages near a band-edge (conduction or valence band) for a semiconductor of both large or small gap can be problematic because often the current signal decreases rapidly to noise level, leading the tip to crash into the surface during the scan. Depending on the sample not every applied voltage is suitable for imaging, and a low value of feedback current avoids the risk of tip-sample interactions but, on the other hand, often produces a low signal that makes the I(V) features resolution difficult.

2.2.6 Temperature broadening

Up to this point we did not consider the effect of the temperature on the tunneling measurements. For topographic measurements, the effect is mostly an higher drift of piezoelectric motors and an higher thermal energy of surface atoms, which overall reduces the definition of STM images. The impact however is bigger for spectroscopic measurements, for electrons from different electronic levels participate in the tunneling process in an interval depending from k_BT, where k_B is the Boltzmann constant.

Electrons distribution obeys the Fermi-Dirac statistics $f_n(E)$:

$$f_n(E) = \frac{1}{1 + \exp\left(\frac{E - E_{F_n}}{k_B T}\right)} \tag{2.45}$$

Then equation 2.5 can be rewritten as:

$$I \propto \int_{-\infty}^{+\infty} \left[f_{sample}(E) - f_{tip}(E - eV)\right] T(E, eV) \rho_{tip}(E - eV) \rho_{sample}(E) dE \tag{2.46}$$

The term $T(E, eV)$ adds a background to the spectra which for small energies compared to the barrier height can be neglected. Assuming again ρ_{tip} constant, the first derivative of the current is:

$$\frac{\partial I}{\partial V} \propto \rho_T \int_{-\infty}^{+\infty} \frac{\partial}{\partial V} f_T(E - eV) \rho_{sample}(E) dE \tag{2.47}$$

which is a convolution between the derivative of the tip Fermi-Dirac distribution (temperature dependent) and the sample DOS ρ_{sample}:

$$\frac{\partial}{\partial V} f_{tip}(E - eV) = -\frac{1}{k_B T} \frac{\exp\left(\frac{E-eV-E_F}{k_B T}\right)}{\left[1 + \exp\left(\frac{E-eV-E_F}{k_B T}\right)\right]^2} \tag{2.48}$$

As we can see in figure 2.9, at $T = 4K$ sharp peaks are observed. The increase of T produces a progressive smoothing due to the term $\frac{\partial}{\partial V} f_T(E - eV)$. This broadening will impede the observation of the 23 meV gap of germanene if it survives the interaction with Al(111), requiring low temperature measurements

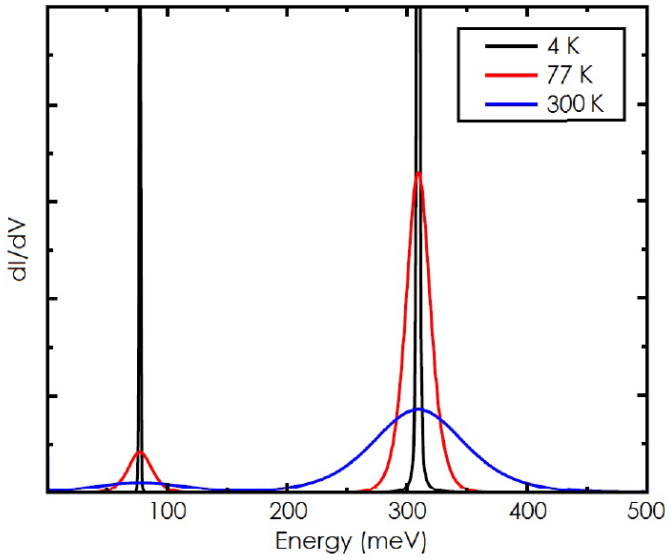

Figure 2.9: Temperature broadening at 4K (attainable with liquid helium), 77K (attainable with liquid nitrogen) and 300K (room temperature) of the Dirac-like peaks. Reproduced from [151].

2.3 Artefacts in STM/STS

One common mistake in Scanning Tunneling Microscopy/Spectroscopy is that users forget that they are actually dealing with a metallic tip swept on the surface by a piezoelectric scanner. Every microscopy is affected by artefacts. We always need to interpret STM morphology and STS spectroscopy as the product not only of the sample properties, but as those of a tunnel junction, which does not always respect all the assumption we made so far.

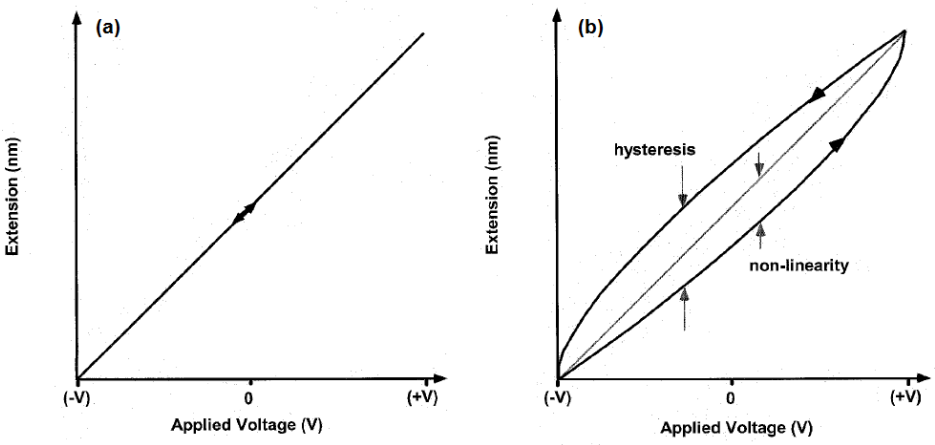

Figure 2.10: Ideal (a) and non-ideal (b) behaviour of the piezoelectric tube.

The first source of artefacts is the scanner: the piezoelectric ceramics do not always work ideally. An ideal behaviour implies a linear response in the extension/retraction in nanometers per applied Volt. Piezoelectrics on the contrary can be affected by:

- Non-linear behaviours: nm/V is not the same for every voltage magnitude;
- Hysteresis: the response traces a different path depending on the direction of the voltage change;
- Creep: the delay in motion due to a sudden voltage change. The tube continues to move even if the voltage is already fixed. The result is a lateral topographic smoothing due to the voltage steps;
- Ringing: if PID frequencies are too high, the tube oscillates and the image is dominated by noise;

A small hysteresis of the tip is always present and it is strongly affected by temperature, leading to a drift of the scanning area over time. Working at a lower temperature allows a bigger stability on the same area for a larger amount of time (a drift of a few nanometers in hours).

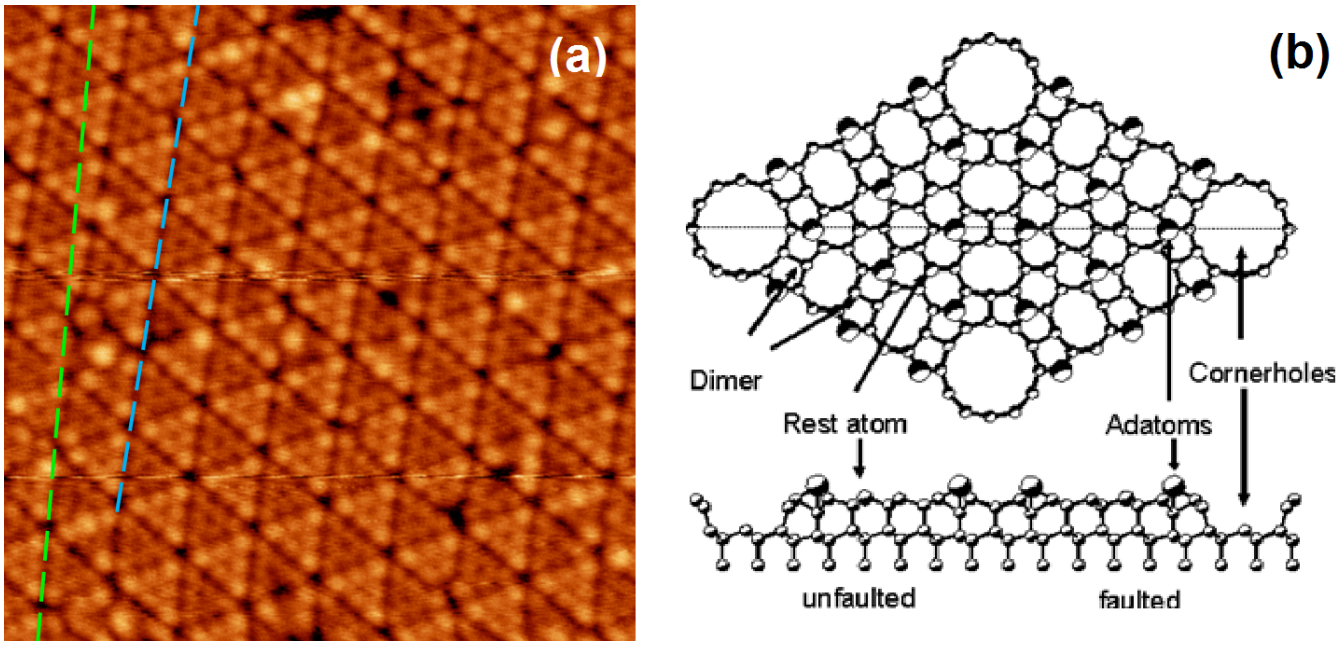

Figure 2.11: (a) 20 × 20 nm image of the 7 × 7 reconstruction of Si(111) surface (V=-1.3V, I=50pA), whose atomistic model is shown in (b). In the first lines of the $x - y$ scan the piezoelectric tube is still drifting and it can be seen from the green dashed line that the line between corner-holes is rotating. The blue dashed lines shows the area where the tip has stabilized. This effect disappears after repetitive scans on the same area.

The second source of artefacts is the tip. We can distinguish between artefacts with an ideal tip, and artefacts with a non-ideal tip.

In the case of an ideal metallic tip with an atomically-sized apex, the convolution effect due to the finite dimension of the tip with features of the same dimensionality (atomic protrusions, pores, holes and trenches) has to be considered. Convolution affects the geometry also for inaccessible areas from the vertical direction.

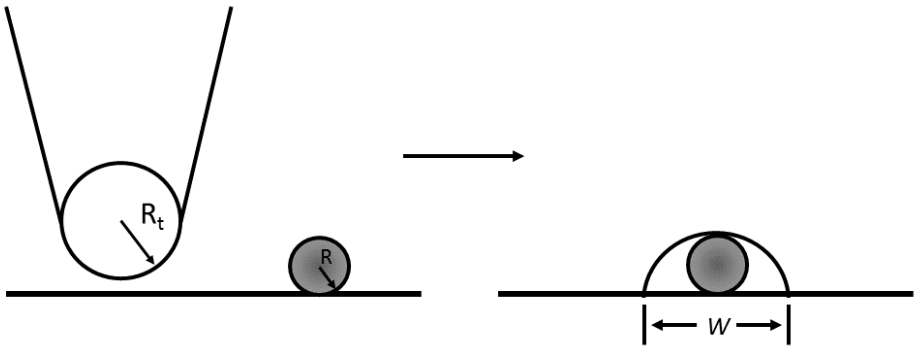

Figure 2.12: Example of broadening effect of the tip on an atomic-sized feature due to its dimensionality. The dimension of the feature on the STM line scan is W instead of R.

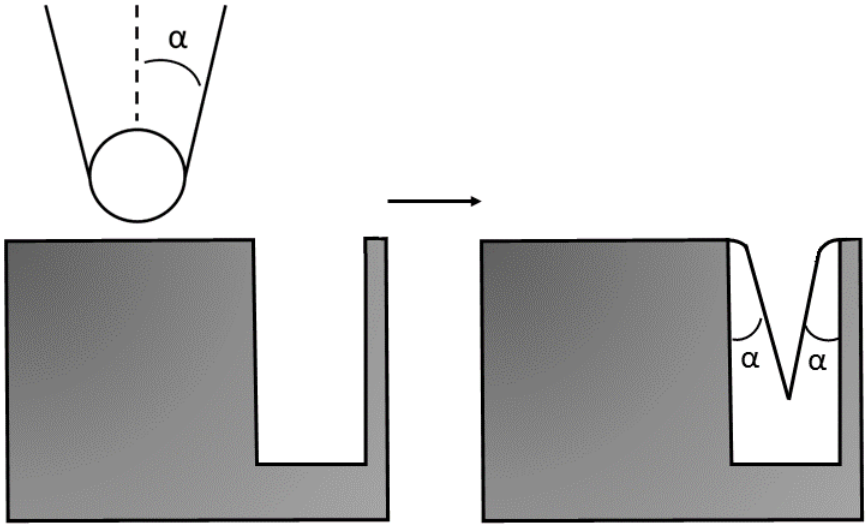

Figure 2.13: Example of the dimension and angle geometry of the tip on an atomically-sized hole.

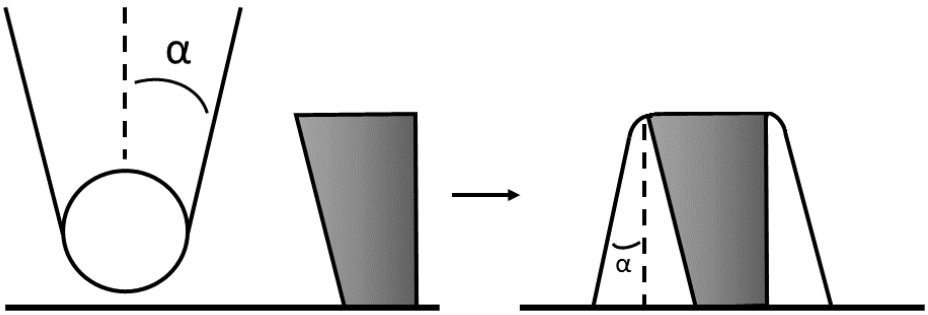

Figure 2.14: Example of smoothing effect of the tip due to inaccessible areas.

The wave vector of the electronic states of the tip does not always correspond always with one of the sample, in particular for semiconductors and semimetals. This difference was first dramatically observed for graphite surfaces [165, 166], in which a different morphology from the expected hexagonal one was observed. Tersoff showed this effect to be characteristic of materials where the Fermi surface has collapsed to a point at the corner of the surface Brillouin zone [156]. In this case the STM image corresponds to an individual state, giving an image whose periodicity is that of the unit cell, regardless of the underlying atomic structure.

Another effect which needs to be accounted for is the electric field and chemical attraction due to the presence of the tip [167]. Tekman and Ciraci distinguished between 3 regimes, as function of the tip-sample separation [168]: contact or chemical, tip-induced localized states (TILS) and nearly-independent electrodes. The TILS are states which form into the tunnel barrier at intermediate separations and add a current term which has to be accounted for in the analysis of topology and spectroscopy. The electric field of the tip is not the one of a point charge at the surface, but has finite extensions in (x, y) directions. It is equivalent to a charged disk at several Å above the surface. When the tip is not far enough from the surface, it creates a confinement potential and induce a band bending in the sample area below for semiconducting materials. The z confinement depends on the solution of the Poisson equation, while the (x, y) directions can be treated via an Hartree 2D approach. The resulting quantum dot energies give us access to the tip-induced band bending in the material. [169]. The large current-dependent corrugation obtained from an STM study of graphite indicated the importance of tip-sample forces causing different local elastic deformations of the sample [170]. For this and the previous reasons, it is always important to perform a voltage and current-dependent analysis of the topology in order to discriminate between physical and measurement-induced features.

A complete family of artefacts is introduced when the tip does not fit the atomic-sized apex picture. A broader apex leads to a lower resolution on the nanometric scale, due to a bigger area on which the signal is averaged and then smoothed, but this is not the most substantial problem. If the tip has not been properly prepared and/or it interacted detrimentally with the sample during the scan, it can happen that two or more competing protrusions contribute to the tunnel current which is measured. The spacing between protrusions can be of the order of hundreds of nanometers, in which case it will not affect the measurements on a smaller scale. In a less congenial case, multiple protrusions will be present in the range of interest. In this situation, every protrusions will probe every detail on the surface individually during the $x - y$ scan, leading to a false multiplication of the same feature, as a superposition of multiple shifted STM images. An example is shown in figure 2.15. This STM image has been acquired on Al(111) after Ge deposition in a clusterized area. Fig. 2.15(a) shows that the same cluster (in dashes circles) contributed to tunnel current in multiple areas, feature which is explained by a multiple-terminated tungsten tip. Fig. 2.15(b) shows on the other hand the multiplication of Al(111) terraces, where which the "ghost" ones can be spotted due to a much lower step height.

A multiple tip is not troublesome for topology only: spectroscopic information on a nanometric scale is not always reliable when the current is averaged on multiple areas far from each other. Multiple tips can also introduce separate different features in the STS characteristics [171]. It is not easy to recover a single-tip from a multiple-tip on a very small scale: previous tip conditioning methods as $z(V)$ and $I(V)$ can be tentatively used, or a controlled crash in case we are dealing with a metallic sample. Otherwise a freshly prepared tip is needed.

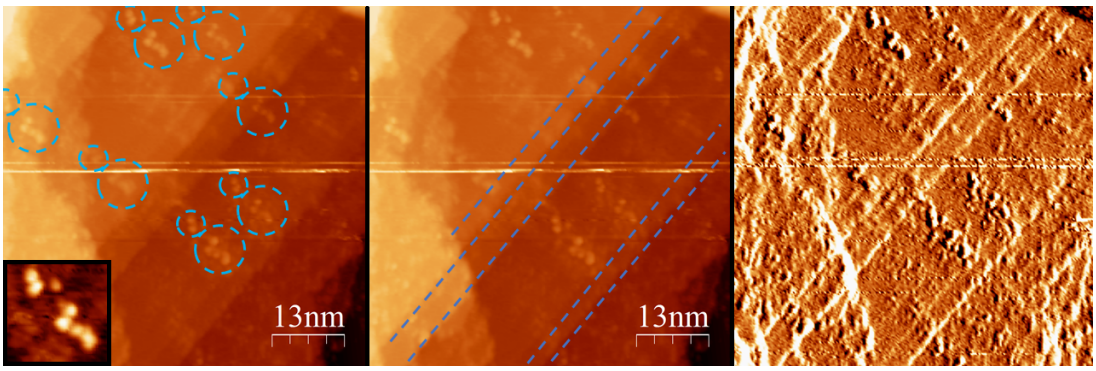

Figure 2.15: (a) Al(111) STM morphology where repeated cluster (shown in inset) due to a multiple STM tip are highlighted. (b) Same as (a), with multiplied Al(111) terraces which are highlighted. (c) Corresponding feedback current image of (b).

Another assumption that was made is the uniformity of the tip density of states in a few eV around the Fermi level. If the tip does not have a uniform metallic DOS, the sample DOS is convoluted with the tip one, producing shifts and additions of peaks in the electronic features [172]. It is then useful to have the possibility to test the tip DOS during the measurements, and necessary to interpret the spectra evolution over time [173]. The non-uniform DOS does not always affect morphology: the tip can still produce high-quality atomic resolution images of the topology. The non-uniform DOS can be due to intrinsic reasons or the adsorption of elements from the surface. In case of a multiple tip whose effect is voltage dependent, this can also be due to two protrusions of different chemical identity [174]. It is easier to get rid of an adsorbate than reform a tip, with the previously described mechanisms.

2.4 The Omicron LT-STM

The Low Temperature STM is an ultra-high vacuum (UHV) setup that allows the morphologic and electronic characterization of samples at different temperatures, depending on the cryogenics used (Liquid Nitrogen, 77K, or Liquid Helium, 4.7K). It consists of a preparation chamber, where samples are inserted via a load-lock and manipulation of the samples (heating/degassing, ion bombardment, Raman spectroscopy, evaporations) and tips (preparation under UHV) can be performed, and an analysis chamber where the microscope is contained into a double cryostat. The setup is shown in figure 2.16.

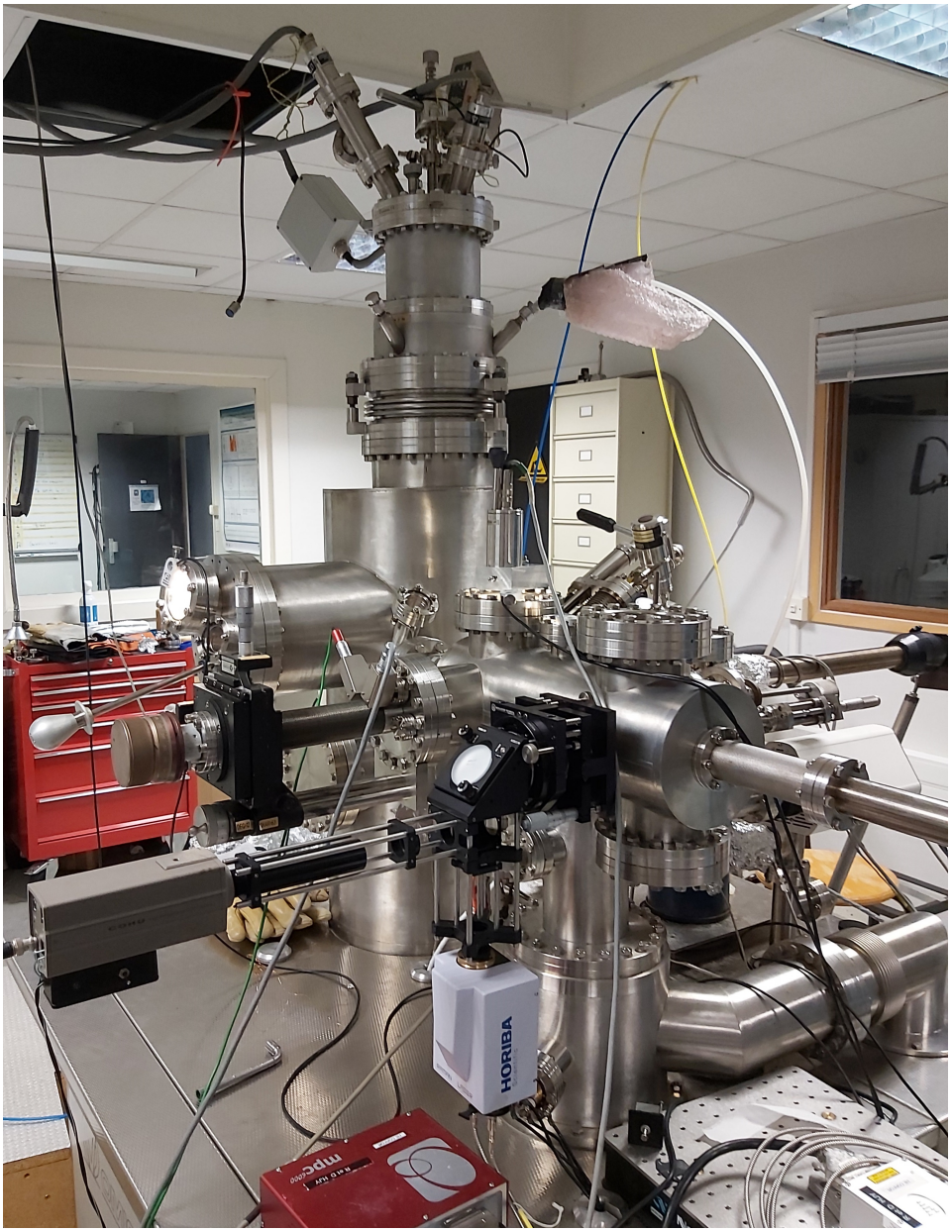

Figure 2.16: LT-STM used in this work.

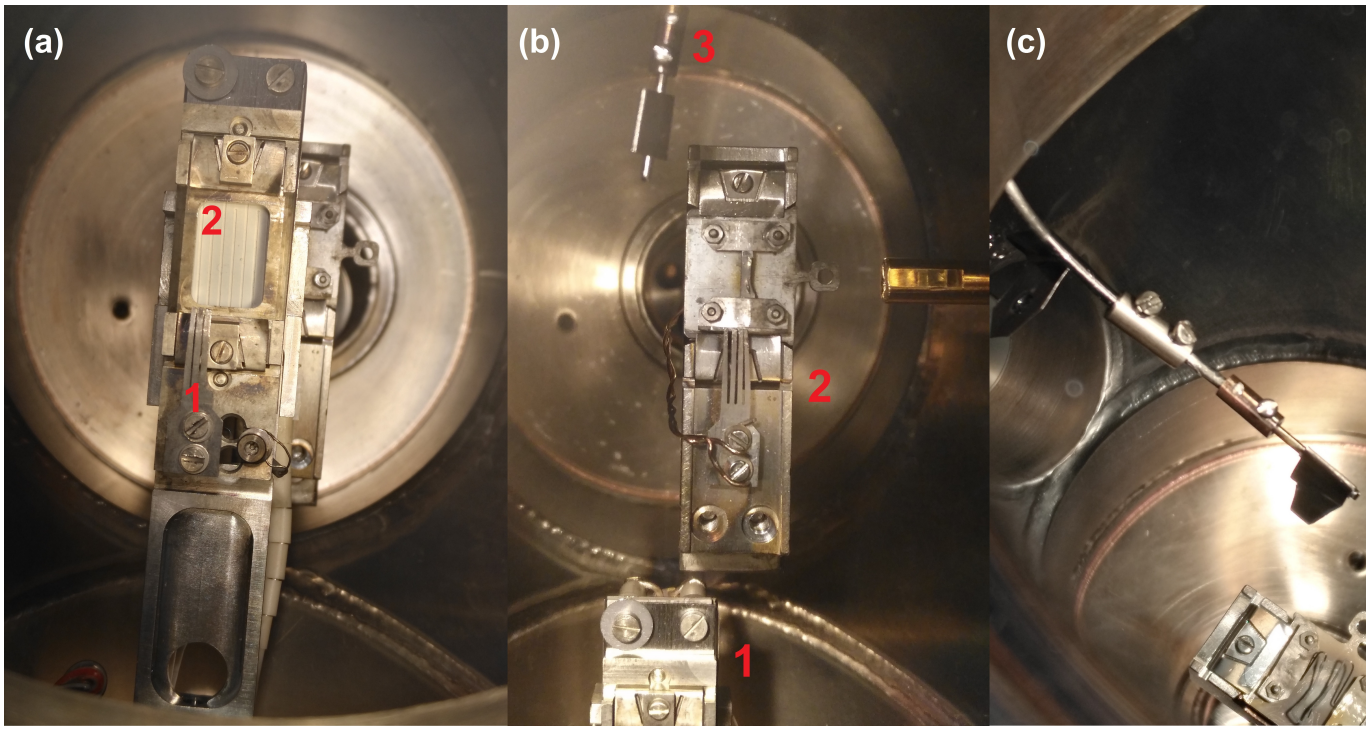

Figure 2.17: Manipulation stages of the preparation chamber. (a) Main manipulation stage, with direct voltage electrode (1) or indirect resistive (2) heating. (b) First manipulation stage (1), second manipulation stage (2) with Ge(001) crystal, and electrical contact to degas W tips (3). (c) Electrical contact to degas W tips.

Base vacuum in the chambers is obtained via pairs of rotative + turbomolecular pumps, which allow to pump down to the 10^{-9} mbar regime. Due to the mechanical vibration induced by the pumps, the vacuum during the measurements is usually preserved via ionic pumps + titanium sublimation pumps (TSP), with lower pressure in the low 10^{-11} mbar regime.

Tip and samples can be loaded in the load-lock and transferred into the preparation chamber, where a storage area is present. A main manipulation stage allows semiconductor surface preparation via indirect resistive heating or direct application of a voltage (Figure 2.17(a)). In this process, the internal temperature is checked via a thermocouple on the main manipulation stage or via an external pyrometer, which is limited to temperatures higher than 250°C. Degassing can be checked via a Quadrupole Mass Spectrometer (QMS). Metallic surface preparation can be performed via an Ion Gun, which uses Ne or Ar. Via another electrical contact on this stage tips can be degassed up to 1200°C to remove the tungsten oxide layer (WO_4^-) produced during the electrochemical etching with NaOH in distilled water (Figure 2.17(b-c)). A second manipulation stage is present (Figure 2.17(b)), to perform thermal evaporations on a substrate or mechanical transfers from a sample to another. Raman spectroscopy measurements in UHV can performed also via a dedicated stage and optical access, with an external optical circuit of excitation from a laser and collection coupled to a spectrometer.

The LT-STM chamber contains of a storage carrousel. The STM head is inserted into two cryostats: the external one acts as a shield for the internal one, and is filled with liquid nitrogen, while the internal one can be filled with liquid nitrogen or helium. For 77K measurements the cryostat has to be filled every 3 days, while external one at least once per day. For 5K measurements, the internal filling lasts one day and external nitrogen filling is needed twice a day. STM tip is mounted on a piezo stage, which is suspended via three soft springs and an additional damping system based on a non-periodic eddy current damping mechanism (Figure 2.18). The maximum scan area with the piezoelectric tube depends on the temperature: 5 μm at 300K, 1.5 μm at 77K, 1 μm at 5K. A lock-in amplifier is connected to the preamplification stage to obtain the analog derivative of the current. SCALA and Nanonis softwares have been used for managing STM measurements.

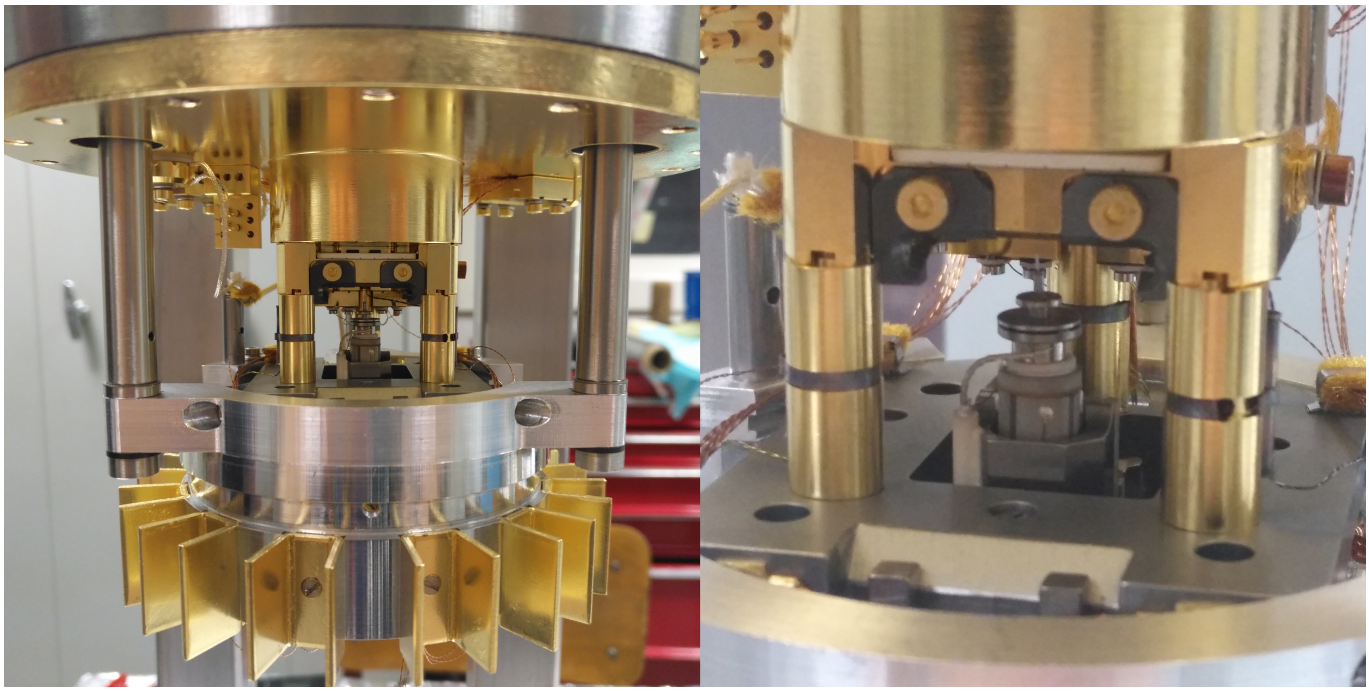

Figure 2.18: LT-STM head outside of the vacuum chamber.

2.5 Multi-probe STM

The evolution of the technology from microelectronics to nanoelectronics demanded to be able to perform electronic transport measurements at the nanoscale. The typical approach is to use lithography to depose metallic contacts. However, this technique has a few limitations:

- It does not allow to keep under vacuum the "as grown" nanostructures, modifying then their properties via air exposition;
- It does not allow a flexible set of contacts;
- It produces 'invasive' (low ohmic) contacts;

A solution is represented by multi-probe STM. When 4 STM tips are controlled individually, 4-points measurements at the nanoscale can be performed. The use of 4 tips allows to ignore the contact resistance, which can be of the order of the MΩ due to the small area of contact. Performing a measurement with only two tips puts the resistance of the sample in series with these contact resistances, strongly distorting the result. The use of a 4-probe technique separates the injection of current and the measurement of the voltage drop, as shown in Figure 2.19. Independently from the contact resistance R_1 and R_4 of the injecting electrodes, the current which flows into the sample is the same I_{source} injected by the source. Due to the high value of R_2 and R_3, the current which flows into the voltmeter (red lines circuit) is very low and can be neglected. Consequently, the voltage drop at R_2 and R_3 is also low. This means the resistance of the sample is simply the voltage $V_{measure}$ divided by the injected current I_{source}. The 4-point method allows not only to measure the actual value of the sample resistance but also to understand how the transport works.

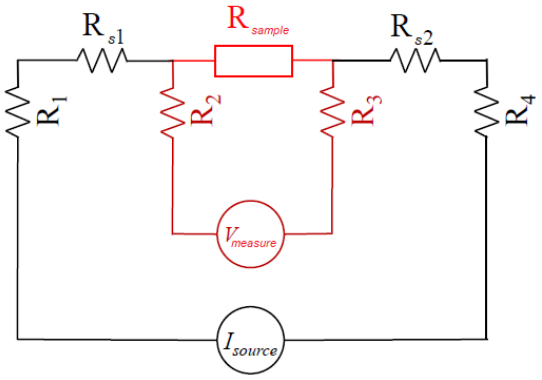

Figure 2.19: Electrical scheme showing a typical 4-point resistance measurements. The black lines indicate the current injection electrodes. The red lines indicate the voltage drop measurement electrodes. R_{sample} is the resistance to be measured; R_i is the contact resistance of the corresponding electrode; R_{s1} and R_{s2} is the resistance of the sample left out between the injecting electrodes and potential probe ones.

2.5.1 Probe-spacing dependence

At the macroscopical scale, an electrical current can flow through a semiconductor material in a 4-probe measurement in multiple paths:

- Through the surface states, associated to the surface reconstruction of the material;
- Through a space charge area produced by the band bending of the states in contact with the vacuum, right below the surface;

- Through the bulk states, characteristics of the material and independent from the surface;

At the micrometer/submicrometer scale, the main contribution comes from the first two factors. This difference is highlighted in Figure 2.20.

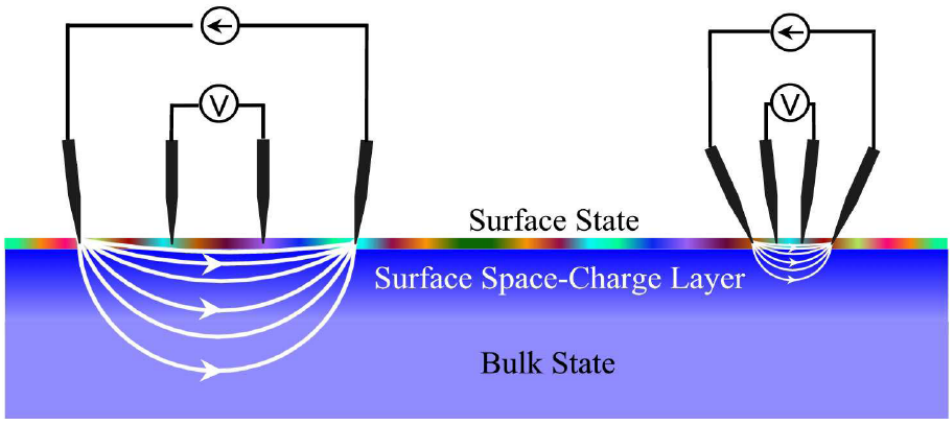

Figure 2.20: (a) Macro and (b) micro-four point probe methods to measure electrical conductance. Reproduced from [175].

This difference leads to different behaviours of the 4-probe resistance when the distance between the probes is varied. If we assume the sample as a homogeneous and isotropic semi-infinite three-dimensional resistive material, the resistance R measured by a 4 point probe in linear configuration as a function of the distance d is given by [176]:

$$R = \frac{\rho_{3D}}{2\pi d} \tag{2.49}$$

where ρ_{3D} is the bulk the resistivity, usually expressed in Ω cm. This relation is showed in figure 2.21 by the blue band for a Si sample whose ρ_{3D} = 5-15 Ω cm. It can be seen that this relation is followed by the experimental data of the 7×7 reconstruction of Si(111) for the spacings between d = 1-100 μm. The sample is 0.4 mm thick, and when d becomes larger than 100 μm the current penetrates to the bottom of the sample, and the field lines start to be compressed by the geometry. At larger d than 100μm another equation then applies:

$$R = \frac{\rho_{3D} L}{S} \tag{2.50}$$

where L is the length of the measured area, equal to $3d$, and S is the cross-section of the sample. The other curve shown in Figure 2.21, corresponding to the $(\sqrt{3} \times \sqrt{3})$-Ag surface, does not respect these equations. When the resistance of an infinite two-dimensional sheet is measured by a linear four point probe of spacing d, the measured resistance is written as:

$$R = \frac{ln2}{2\pi} \cdot \rho_{2D} \tag{2.51}$$

where ρ_{2D} is the sheet resistance, which is equivalent to the 3D resistivity divided by the thickness of the sheet t:

$$\rho_{2D} = \frac{\rho_{3D}}{t} \tag{2.52}$$

The $(\sqrt{3} \times \sqrt{3})$-Ag surface follows roughly this tendency.

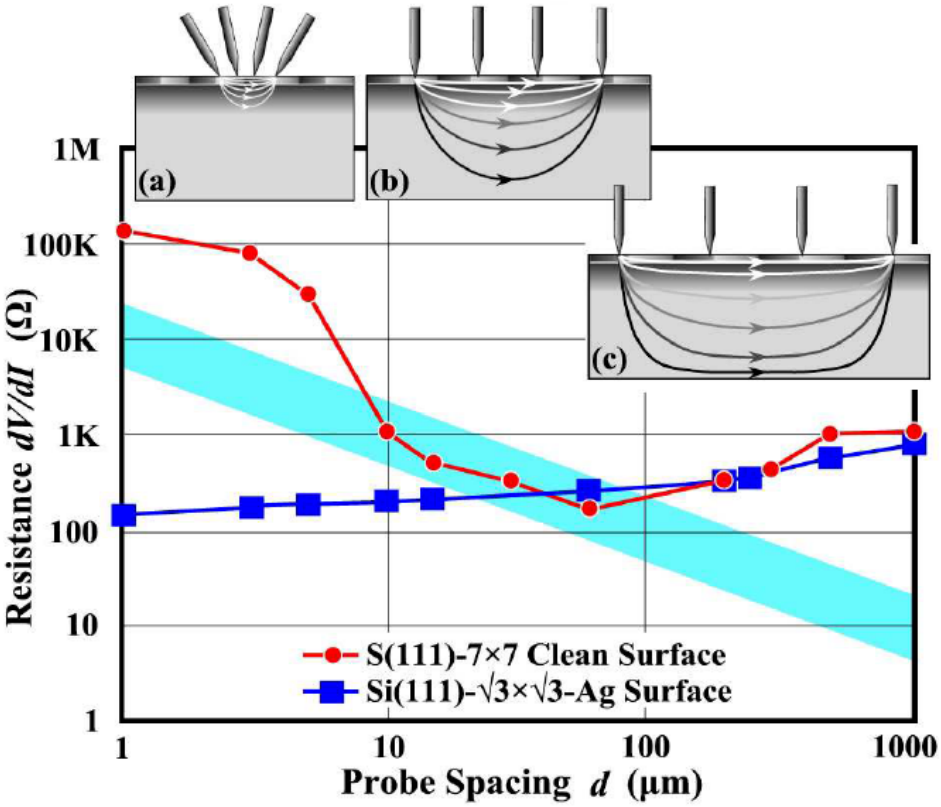

Figure 2.21: Resistance dependence of a Si crystal as a function of the tip separation d, for a Si(111)-7×7 surface (red curve) and a Si(111)-$\sqrt{3} \times \sqrt{3}$-Ag surface (blue curve). The blue stripe represents the resistance for ρ = 5-15 Ω cm in the case of a tridimensional transport. The insets show 3 different configurations for the current distribution inside the Si sample. Reproduced from [175].

2.5.2 Other 4-points resistance configurations

The theorem of Van der Pauw [177] allows to exploit other configurations than just a linear equidistant one. An arbitrary configuration of the tips, as that shown in Figure 2.22(a), follows a general equation for the 3D and 2D case:

$$R_{3D}^{4p}\left(\vec{s}_1,\vec{s}_2,\vec{s}_3,\vec{s}_4\right) = -\frac{\rho_{3D}}{2\pi}\cdot\left[\frac{1}{|\vec{s}_3-\vec{s}_1|}-\frac{1}{|\vec{s}_3-\vec{s}_4|}-\frac{1}{|\vec{s}_2-\vec{s}_1|}+\frac{1}{|\vec{s}_2-\vec{s}_4|}\right] \tag{2.53}$$

$$R_{2D}^{4p}\left(\vec{s}_1,\vec{s}_2,\vec{s}_3,\vec{s}_4\right) = -\frac{\rho_{2D}}{2\pi}\ln\left[\frac{|\vec{s}_3-\vec{s}_4|\cdot|\vec{s}_2-\vec{s}_1|}{|\vec{s}_3-\vec{s}_1|\cdot|\vec{s}_2-\vec{s}_4|}\right] \tag{2.54}$$

where the vectors $\vec{s}_i$ (i=1,2,3,4) start from a common reference point $\vec{r}_0$. These formulas reduce to equations 2.49 and 2.51 for the linear equidistant configuration.

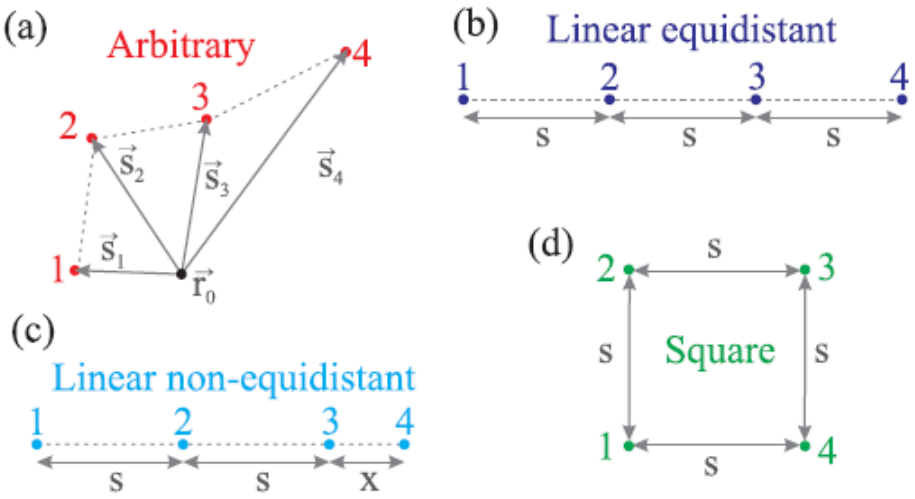

Figure 2.22: Reproduced from [176]

From these equations the resistances for 3D and 2D case in the linear not-equidistant can also be calculated (Figure 2.22(c)). The linear non equidistant configuration is a powerful tool to discriminate between a 2D and a 3D transport because only a tip is moved while the other 3 are left in contact at a distance s from each other. As a function of the distance x from the nearest tip, the resistance in the 3D and 2D case is given by:

$$R^{4p}_{3D}(s,x) = \frac{\rho_{3D}}{2\pi} \cdot \left[\frac{1}{x} + \frac{1}{2s} - \frac{1}{s+x}\right] \tag{2.55}$$

$$R^{4p}_{2D}(s,x) = \frac{\rho_{2D}}{2\pi} \left[\ln\left(\frac{2s}{x}\right) - \ln\left(\frac{s}{x+s}\right)\right] \tag{2.56}$$

The last configuration in Figure 2.22(d) is the square one. This configuration is very useful because it allows to probe conductivity anisotropy in two perpendicular directions without recontacting the tips. A single measurement gives:

$$R_{\text{square}} = \frac{V}{I} = \frac{1}{2\pi\sqrt{\sigma_x\sigma_y}} \times \ln\left(1 + \frac{\sigma_y}{\sigma_x}\right) \tag{2.57}$$

However, the preferential conductivity axes are not forcefully the ones chosen for the first measurement. To locate them the square must be rotated and the dependence of the resistance R from the angle θ is:

$$R(\theta) = C \cdot \ln\left(\frac{\left(\frac{\sigma_x}{\sigma_y}+1\right)^2 - 4\cos^2\theta\sin^2\theta\left(\frac{\sigma_x}{\sigma_y}-1\right)^2}{\left(\sin^2\theta + \frac{\sigma_x}{\sigma_y}\cos^2\theta\right)^2}\right) \tag{2.58}$$

with $C = 1/\left(4\pi\sqrt{\sigma_x\sigma_y}\right)$. The fit of the experimental data with these equations provides the components σ_x and σ_y of a sample with anisotropic conductivity, expressed in $\Omega^{-1}/\square$. If we want to rely these values with a 3D resistivity, the reciprocal must be calculated and then multiplied by the thickness, following equation 2.52.

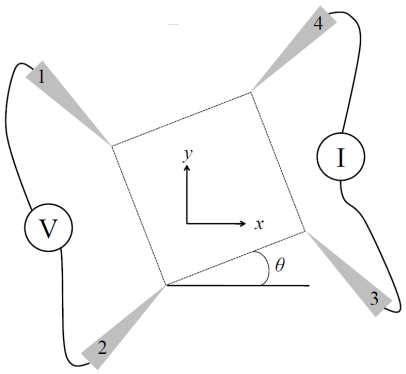

Figure 2.23: Square configuration of 4-tips STM to find the angular dependence of conductivity.

2.6 Omicron 4-probe RT-STM

The 4-probe RT-STM of IEMN is an UHV setup which integrates a chamber for sample and tip preparation with an analysis chamber, where the multi-probe measurements are performed.

The base vacuum in the chamber is obtained in a similar manner of the LT-STM (section 2.4). Both preparation and analysis chamber are provided of a couple of rotative + turbomolecular pumps, plus an ionic pump which is used during the measurements to keep pressure in the 10^{-9}-10^{-10} mbar regime.

A SAS with a storage of 6 objects is present to insert both tips and samples. A similar storage is present in the preparation chamber. A manipulation stage allows the degassing of W tips with a tantalium electrical contact, or sample preparation via a couple of direct voltage injection or resistive heating.

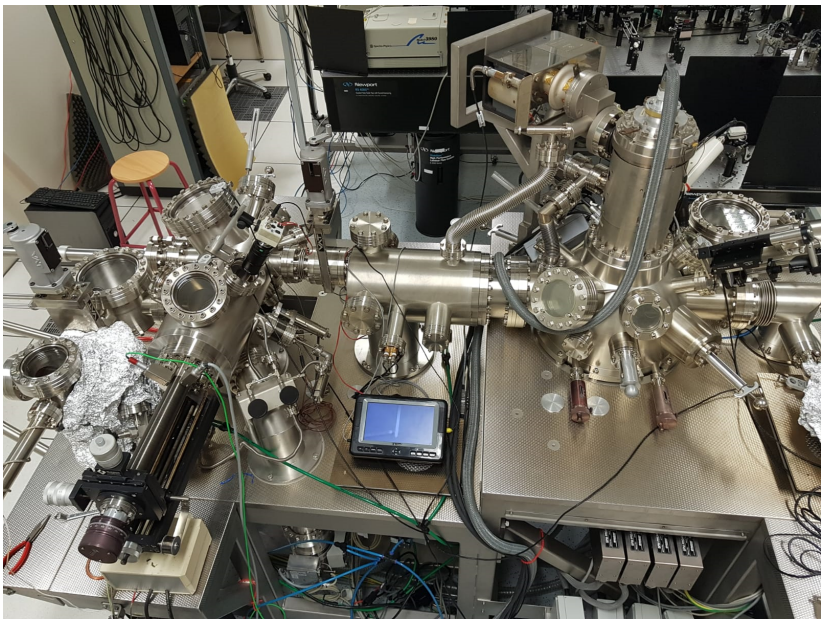

Figure 2.24: 4-probe STM setup.

The analysis chamber contains the platform with the 4 scanners for the tips. Not all the tips are equivalent. A single high-resolution scanner is present (usually indicated as tip 3), and 3 low resolution scanners. This differentiates also how the tips are prepared: low resolution tips are longer (a few cm) compared to high resolution ones (a few mm). Every tip can be moved in the X, Y, Z direction, while the sample holder at the center of the chamber only in X, Y ones. While the rough positioning of the tips can be done by eye, a fine positioning is performed via an SEM placed

right above the analysis chamber. The SEM is characterized by a higher working distance than conventional SEMs in order to have the necessary space below for sample and tips. The system is managed by 4 Nanonis controller for single-point measurements, while for transport measurements a control program written in LabVIEW manages two Keithley voltage sources, each one connected to two tips.

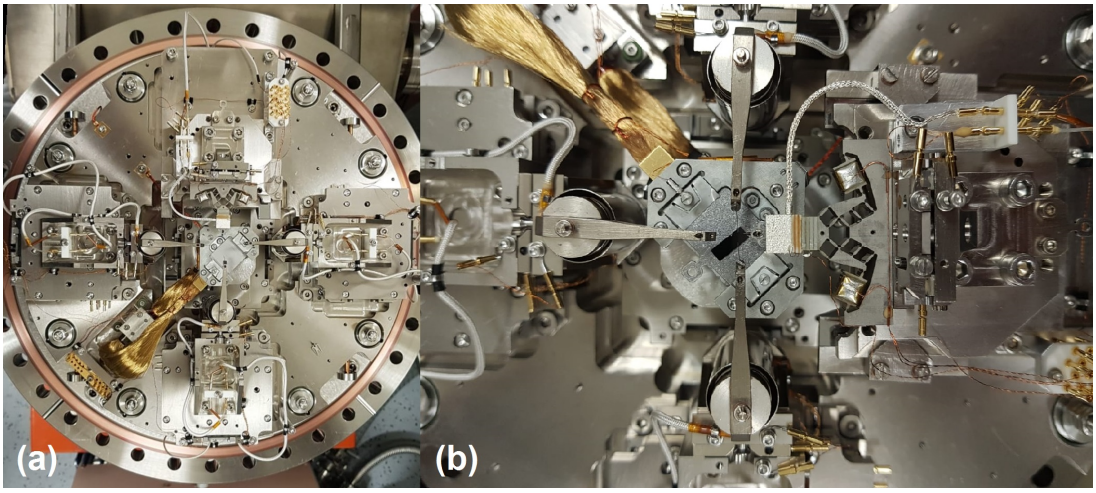

Figure 2.25: (a) Open analysis chamber. (b) Zoom on the 4 scanners and the sample holder.

2.7 Density Functional Theory

Density Functional Theory (DFT) ab-initio calculations have been used in this thesis to understand the growth mechanism of germanene in the top layer of Al(111) crystal and the nanoribbons boundary between germanene and the Al top layer. For this purpose the Vienna ab-initio simulation package (VASP) has been used [178, 179, 180, 181]. This theory allows to compute properties of condensed matter systems when the exact solution of quantum formalism is not available. To completely describe the quantum mechanical behaviour of a stationary system of N interacting particles, it is necessary to calculate its many particle wavefunction. The Schrödinger equation is the direct way to obtain it. However, since the motion of each electron is coupled to that of the other electrons in the system, in practice the equation is too much computationally demanding to be solved. Approximations are needed.

This section contains an introduction to the key concepts of the density functional formalism. The rewriting of the Schrödinger equation in the Kohn-Sham equations (section 2.7.2) leads to an iterative scheme to calculate both ionic and electronic wavefunctions (section 2.7.5-2.7.6). A first approximation will be needed for the exchange and correlation part of the effective potential (section 2.7.3). Other choices have to be made for the wavefunction's basis set and a computationally suitable approximation of a full-electron potential (section 2.7.4). All of these options, which are the result of 60 and more years of theoretical study, will materialize in the choice of parameters to launch a calculation with the VASP package to obtain the structural relaxation of a 2D nanosheet of germanene on Al(111), and the corresponding simulated density of states and STM images (section 2.7.7).

2.7.1 The many-body problem

The Schrödinger equation for a stationary system of N interacting electrons can be written as:

$$\hat{H}\Psi\left(\mathbf{r}_i;\mathbf{R}_i\right) = E\Psi\left(\mathbf{r}_i;\mathbf{R}_i\right) \tag{2.59}$$

where E is the energy of the system, $\Psi\left(\mathrm{r}_i;\mathrm{R}_i\right)$ the electronic wavefunction, with r_i is the position of the electron i and R_i those of the atomic nuclei i. The Hamiltonian of the system is defined as:

$$\hat{H} = \left(\hat{T}_{\text{ion}} + \hat{W}_{\text{ion-ion}}\right) + \left(\hat{T}_{\text{el}} + \hat{W}_{\text{el-el}}\right) + \hat{V}_{\text{el-ion}} \tag{2.60}$$

The first term on the right hand side of the expression 2.60 represents the kinetic energy (operator $\hat{T}$), divided in ionic and electronic contribution; the second term the Coulomb interaction energy (operator $\hat{W}$), and the last term the mutually attractive forces between ions and electrons (operator $\hat{V}$). In the first quantization picture the terms are given by:

$$\hat{T}_{\text{ion}} = \sum_a \left(-\frac{-\hbar^2}{2M_{\text{ion},a}}\nabla_a^2\right), \quad \hat{W}_{\text{ion-ion}} = \frac{1}{2}\frac{1}{4\pi\varepsilon_0}\sum_{aa'}\frac{Z_a Z_{a'} e_0^2}{|\mathbf{R}_a - \mathbf{R}_a|} \tag{2.61}$$

$$\hat{T}_{\text{el}} = \sum_i \left(-\frac{\hbar^2}{2m}\nabla_i^2\right), \quad \hat{W}_{\text{el-el}} = \frac{1}{2}\frac{1}{4\pi\varepsilon_0}\sum_{ij}\frac{e_0^2}{|\mathbf{r}_i - \mathbf{r}_j|} \tag{2.62}$$

where a and a' indicate different ions, i and j different electrons, and the physical quantities (mass, position and atomic number) are written respectively in uppercase and lowercase. The term which couples electrons and ions is:

$$\hat{V}_{\text{el-ion}} = \frac{1}{4\pi\varepsilon_0}\sum_{i,a}\frac{(-Z_a e_0^2)}{|\mathbf{r}_i - \mathbf{R}_a|} \tag{2.63}$$

In this study we will be mostly interested in the atomic and electronic structure of the crystal, which can be tested via STM/STS. The goal is to find the groundstate $|\Psi_0\rangle$ of the system, which is characterized by the lowest possible energy:

$$E_0 = \left\langle \Psi_0 | \hat{H} | \Psi_0 \right\rangle, \quad E_0 \leq E_i = \left\langle \Psi_i | \hat{H} | \Psi_i \right\rangle \forall i \tag{2.64}$$

The Hilbert space is enormous, then this problem is of no simple solution, even it has been proved via reductio ad absurdum that the solution is unique. A first important approximation comes from the observation that the mass of the electron is ~ 1836 times smaller than the mass of the proton. This means that the characteristic times of the electron dynamics are way smaller that the nuclei ones. Electrons can then be considered always in their ground state compared to the slow movement of the nuclei. This allows to write the total wave function as the product of the one governing the electrons and the one governing the nuclei:

$$\Psi(\mathbf{r}, \mathbf{R}) = \psi(\mathbf{r}; \mathbf{R})\chi(\mathbf{R}) \tag{2.65}$$

where $\mathbf{r}$ indicates the set of electrons position r_i and $\mathbf{R}$ the nuclei set R_j. This is the **Born-Oppenheimer approximation** [182]. Electrons are then governed by an effective Schrödinger equation where only the potential from the average nuclei position influences the motion:

$$\hat{H}_e \psi(\mathbf{r}; \mathbf{R}) = E_e(\mathbf{R})\psi(\mathbf{r}; \mathbf{R}) \tag{2.66}$$

where the electronic Hamiltonian is given by:

$$\hat{H} = \sum_{i=1}^{N_e} \left(-\frac{1}{2}\nabla_i^2 - \sum_{a=1}^{N_a} \frac{Z_a}{|\mathbf{r}_i - \mathbf{R}_a|} \right) + \frac{1}{2} \sum_{i,j \neq i}^{N_e} \frac{1}{|\mathbf{r}_i - \mathbf{r}_j|} \tag{2.67}$$

Atomic units have been used for equation 2.67 ($\hbar = m = e = 1/4\pi\epsilon_0 = 1$) and will be used in the following, unless otherwise stated. The coordinates of the nuclei enter now into the Schrödinger equation just as a normal parameter, with electron-nucleus interaction which can be thought as an external potential. A first electronic Schrödinger equation can be solved, and used as input for a subsequent nuclear Schrödinger equation. The nuclei can also be treated as classical particles in the simplest approximation. The optimization of the nuclear positions, in order to obtain the minimal energy configuration, is called **structural relaxation**, while the minimization of the energy of the electronic cloud at every ionic step is called **electronic relaxation**.

2.7.2 The Hohenberg-Kohn theorem and Kohn-Sham equations

Even considering a classical solution for nuclei, the electronic N-body Schrödinger equation to be solved is a second order partial differential equation in 3N variables. It is necessary to remember that Schrödinger equation close form solution has been found for H atom, while variational principle has been exploited for He fundamental state and H_2^+ [183]. While the numerical solution via direct diagonalization of the Hamiltonan in a chosen basis is possible, the scaling of this method with the number of electrons demands an unconceivable computational effort even for the smallest molecules. Other approximations next to the Born-Oppenheimer one are then necessary.

One of the first successful methods for solving the many-electron Schrödinger equation has been the **Hartree-Fock approximation** [184, 185, 186], where the wave function is restricted to a single Slater-determinant of single particle wave functions. However, while accurate for atoms and small molecules, the resulting calculation is still too computationally demanding for solids, for which it underestimates also the correlation energy.

A more attainable solution was proposed in 1964 [187]: Hohenberg and Kohn noted that the external potential, including nuclear one, completely determines the many-electron Hamiltonian and then the deriving solutions, including electron density $n(r)$. They went on demonstrating the opposite

is also true: a certain ground state density $n(r)$ can only be produced by a certain external potential. This one to one correspondence allows to express all the system properties as functionals of the ground state density $F[n]$. The strength of this approach relies on the fact that $F[n]$ does not explicitly depend on the external potential, but only on the density through kinetic energy and electron-electron interactions: it is then possible to define it independently of the system, and minimize the energy functional $E[n]$ to find the ground state. However, this minimization with respect to all densities does not lead to the ground state of the real system, because up to now the only restriction is that the spatial integration of the density gives the correct number of electrons. A constrained search, which allows also to construct an antisymmetric wavefunction, has to be done [188]. We are also in need of a form for the functional $F[n]$.

In 1965 Kohn and Sham made a huge step forward [189], giving a practical scheme to construct $F[n]$. The idea they had was to reformulate the Hamiltonian of the system via that of an auxilary one, consisting of non-interacting particles, subject to an effective external potential $v_{eff}(\mathbf{r_i})$ such that the two systems shared the same ground state density. The Hamiltonian of the auxiliary system is:

$$\hat{H}_{\text{aux}} = \sum_{i=1}^{N} \left[-\frac{1}{2}\nabla_i^2 + v_{\text{eff}}\left(\mathbf{r}_i\right) \right] \tag{2.68}$$

The electron-electron interaction term is not present and the Hartree-Fock approach is reusable, being the ground state consisting now of a single Slater determinant of single particle wave functions. The Schrödinger equation to be solved now takes the name of **Kohn-Sham equation**:

$$\left[-\frac{1}{2}\nabla^2 + v_{\text{eff}}(\mathbf{r}) \right] \psi_i(\mathbf{r}) = \epsilon_i \psi_i(\mathbf{r}) \tag{2.69}$$

The ground state density of such a system comes from its single particle wavefunctions:

$$n(\mathbf{r}) = \sum_i |\psi_i(\mathbf{r})|^2 \tag{2.70}$$

and the functional $F[n]$ needs just to consider the kinetic energy term:

$$F_{\text{aux}}[n] = T_{\text{aux}}[n] = \langle \Psi[n] | \hat{T} | \Psi[n] \rangle = -\frac{1}{2} \sum_{i=1} \int \psi_i(\mathbf{r}) \nabla^2 \psi_i(\mathbf{r}) \mathrm{d}\mathbf{r} \tag{2.71}$$

where the single particle wave functions are implicitly functionals of the density. We can use this result to redefine the density functional of the original system:

$$F[n] = T_{\text{aux}}[n] + \frac{1}{2} \iint \frac{n(\mathbf{r}) n\left(\mathbf{r}'\right)}{|\mathbf{r} - \mathbf{r}'|} \mathrm{d}\mathbf{r}\mathrm{d}\mathbf{r}' + E_{\text{xc}}[n] \tag{2.72}$$

The second term is the Hartree energy, i.e. the electrostatic energy from a classical charge distribution given by $n(r)$. The last term is called exchange-correlation energy functional and it is where all the unknown quantities of the system have been hidden. While this can seem just a shift of complexity to an equally difficult problem, this reformulation has turned out to be quite clever. This is because the first two terms, the kinetic energy and the electrostatic energy, are for a lot of systems the largest contribution to the ground state energy, while $E_{exc}[n]$ is a relatively small correction. A clarification on these two terms has to be made: nor $\psi_i(r)$ nor $T_{aux}[n]$ represent the real quantities for the system in exam, which should have been calculated directly by the exact many-body problem.

To progress further, a way of approximating the exchange-correlation functional is needed. An equation for the energy functional can come in help. In general, given an external potential $v_{ext}(r)$ with no further assumption:

$$E_v[n] = F[n] + \int n(\mathbf{r}) v_{\text{ext}}(\mathbf{r}) \mathrm{d}\mathbf{r} \tag{2.73}$$

Using the variational principle to minimize it:

$$\delta \left\{ E_v[n] - \mu(n(\mathbf{r})\mathrm{d}\mathbf{r} - N) \right\} = 0 \tag{2.74}$$

where μ is a Lagrange multiplier, introduced to constrain the minimization to densities with the right number of electrons. This is equivalent to look for which μ gives a zero functional derivative, and therefore:

$$\frac{\delta E_v}{\delta n(\mathbf{r})} = \frac{\delta F}{\delta n(\mathbf{r})} + v_{\mathrm{ext}}(\mathbf{r}) = \mu \tag{2.75}$$

Now, we can use equation 2.72 to substitute the explicit form of $F[n]$ after the approximation of Kohn-Sham:

$$\frac{\delta T_{\mathrm{aux}}[n]}{\delta n(\mathbf{r})} + v_{\mathrm{ext}}(\mathbf{r}) + \int \frac{n(\mathbf{r})}{|\mathbf{r} - \mathbf{r}'|}\mathrm{d}\mathrm{r}' + \frac{\delta E_{\mathrm{xc}}[n]}{\delta n(\mathbf{r})} = \mu \tag{2.76}$$

The Euler-Lagrange equation for the auxiliary system will be similar:

$$\frac{\delta T_{\mathrm{aux}}[n]}{\delta n(\mathbf{r})} + v_{\mathrm{eff}}(\mathbf{r}) = \mu_{\mathrm{aux}} \tag{2.77}$$

The basic principle of this approximation was that the two systems shared the same ground state density, which means the Lagrange multiplier, which acts as chemical potential here, is the same: $\mu = \mu_{aux}$. Equalizing the two we obtain the effective potential:

$$v_{\mathrm{eff}}(\mathbf{r}) = v_{\mathrm{ext}}(\mathbf{r}) + v_H[n](\mathbf{r}) + v_{\mathrm{xc}}[n](\mathbf{r}) \tag{2.78}$$

where v_H is the Hartree potential describing the classical repulsive potential from the electron density:

$$v_H[n](\mathbf{r}) = \int \frac{n\left(\mathbf{r}'\right)}{|\mathbf{r} - \mathbf{r}'|}\mathrm{d}\mathbf{r}' \tag{2.79}$$

and v_{xc} is the exchange-correlation potential:

$$v_{\mathrm{xc}}[n](\mathbf{r}) = \frac{\delta E_{\mathrm{xc}}[n]}{\delta n(\mathbf{r})} \tag{2.80}$$

Summarizing, a complicated many-body Schrödinger equation has been reduced to the much simpler single-electron Schrödinger equation 2.69 for an auxiliary non-interacting system. This however requires the effective potential 2.78, which depends on the solutions to the single-particle Schrödinger equation through the density. This means that the solution has to be done **iteratively**: a first guess of the ground state density must be done, then the effective potential is calculated, the Kohn-Sham equation is solved and this gives a new density as a result. This process is repeated until self-consistency is achieved, meaning the input and output density are the same (within a certain error bar). After solving the equation for electrons, the forces on ions have to be calculated following the Hellmann-Feynman theorem [190, 191, 192], and finally solving the Newton equation for the nuclei. The process can then start all over again from the new nuclear positions. The resolution of Kohn-Sham equations and subsequent ionic relaxation is summarized in Figure 2.26.

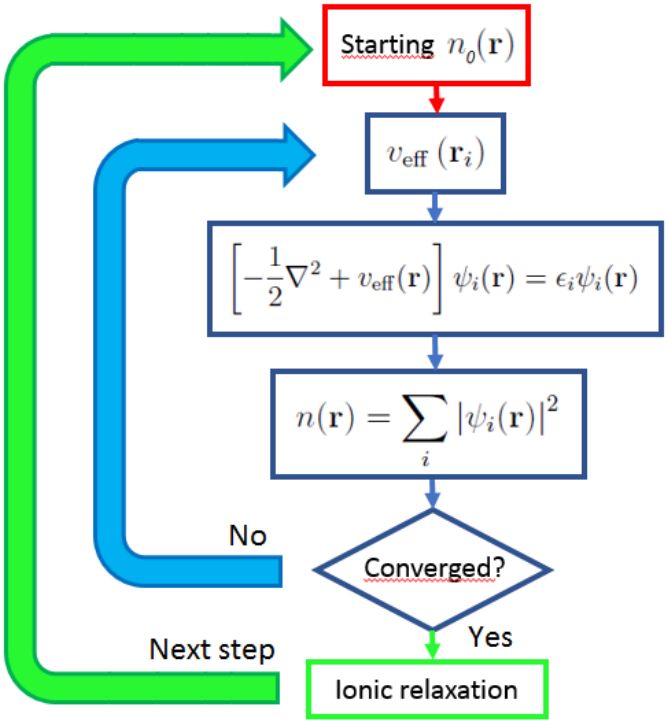

Figure 2.26: Summary scheme for the resolution of Kohn-Sham equations and subsequent ionic relaxation.

2.7.3 Exchange-correlation functional

The formulation of DFT so far is exact, apart from the error allowed in the accepted final density after the self-consistency process. However, this process relies on the existence of an exact functional $E_{xc}[n]$, which hides all the exchange and correlation contributions of the real many-body problems. While the Hartree-Fock approximation could be rewritten in a way similar to DFT, providing an exact form for exchange functional alone, this would rely on a single Slater determinant instead of a superposition, adding an error to be included in the correlation part and not providing a better approach to the combined exchange and correlation functional. An empirical approach has been proved successful for almost all properties of small molecules, via the so called B3LYP functional (Becke, 3-parameter, Lee–Yang–Parr) [193, 194]. This functional contains 8 empirical parameters, which prevent its application for larger and more homogeneous systems. Kohn and Sham proposed another approximation for this quantity [189], to be taken as the exchange and correlation energy of a homogeneous gas (HEG) with density $n(r)$. Being the homogenous gas density a constant, this works if we consider the system as locally having the xc-functional as the homogeneous electron gas one with same local density $n(r)$. This approximation is now known as the **Local Density Approximation (LDA)** and the functional can be written as:

$$E_{\text{xc}}^{\text{LDA}}[n] = \int n(\mathbf{r})\epsilon_{\text{xc}}^{\text{HEG}}(n(\mathbf{r}))\mathrm{d}\mathbf{r} \tag{2.81}$$

where $\epsilon_{\text{xc}}^{\text{HEC}}(n)$ is the exchange-correlation density of the homogeneous electron gas with a uniform density n. This is just a function of local density, not a functional, and it is well-known with a high accuracy. For systems where the electron density varies slowly in space it is a good approximation, and it allowed to describe succesfully the properties for many systems, even quite inhomogeneous, crystalline solid state systems.

LDA approach was then extended to tentatively achieve a higher accuracy for less homogeneous systems. **Generalized Gradient Approximation (GGA)** was a successful example [195, 196,

197]. It provides not only the homogeneous contribution of LDA but an effect of the inhomogeneity is included through an expansion in the gradient of the density:

$$E_{\mathrm{xc}}^{\mathrm{GGA}}[n] = \int n(\mathbf{r})\epsilon_{\mathrm{xc}}^{\mathrm{HEG}}(n(\mathbf{r}))F_{\mathrm{xc}}\left(n(\mathbf{r}), \nabla n(\mathbf{r}), \nabla^2 n(\mathbf{r}), \ldots\right) \tag{2.82}$$

where F_{xc} is the so-called enhancement factor, which modifies the local LDA contribution to the energy. With no further hypothesis, infinite terms are needed in the expansion because the series is divergent [198]. However, the hypothesis of some physically motivated requirements allowed the use of a finite series and are transferrable between different systems [199, 200]. The variety of this construction leads to a whole family of functionals. A particularly simple GGA functional is PBE [201], from Perdew, Burke and Ernzerhof. This is the functional which will be used throughout this thesis and it has proven quite succesful for solid-state physics.

2.7.4 From pseudopotentials to PAW

Other choices characterize the modern DFT approach for solid state physics:

- Kohn-Sham eigenfunctions need to be expanded in a certain basis. The open debate is between plane waves and localized basis functions;
- The interactions between the ionic core and the valence electrons can be described either via a full-potential, or by a pseudopotential which eliminates the nodal character of valence orbitals;
- There are different methods for determining the eigenstates of Kohn-Sham Hamiltonian, as for describing the electron-electron interaction;

GAUSSIAN [202] and SIESTA [203] softwares use a **localized functions basis**. This method is usually very efficient because it requires a small number of functions, reducing then the allocation of CPU. It produces a more straightforward physical interpretation for population analysis, projected density of states and similar physical entities. It is also less computationally demanding to add vacuum in a cell, compared to a plane-wave set. However, there are a few important disadvantages. This method demands a human and computational effort in the search for a good basis set before facing a realistic project, and has no systematic process to extend this basis further if needed (because the choice is not unique). Finally, the use of a pure atom-centered basis sets makes the treatment of the Pulay forces in a periodical system more difficult [204, 205].

In this thesis the **Vienna ab-initio simulation package (VASP)** developed by Georg Kresse and coworkers [178, 179, 180, 181] will be used. Some thoughtful choices were made, which we will try to understand in the following. The first is that the basis chosen for Kohn-Sham eigenfunctions is a **plane wave set**. Following the Slater idea [206] it has the form:

$$\psi^{\mathbf{k}+\mathbf{K}}(\mathbf{r}) = \frac{1}{\sqrt{\Omega}} e^{i(\mathbf{k}+\mathbf{K})\cdot\mathbf{r}} \tag{2.83}$$

The choice of the plane-wave set is motivated by the Car and Parrinello seminal paper [207] which introduced a main feature of nowadays DFT: the switch between direct and reciprocal space via Fast Fourier Transform (FFT) for different quantities of the system, because some operators (like kinetic energy) are diagonal in momentum space and others (potential energy) in direct space, allowing an higher efficiency. A plane-wave set is then more desirable for a number of reason:

- Apply FFT to switch between representations is easy;
- The convergence of a basis-set is easy to be checked, by just monitoring the eigenvalues and total energy as a function of the cut-off energy, which is the highest kinetic energy of plane-wave allowed within the base set;

- The calculation of the Hellmann-Feynman forces are calculated as expectation value of the Hamiltonian with respect to the ionic coordinates;
- There can be no superposition errors, differently from a local basis sets;

The switch between direct and reciprocal space is helped by the Monkhorst-Pack scheme [208], built on the Chadi-Cohen proposal [209], to generate sets of special points in the Brillouin zone to efficiently interpolate the periodic function used and subsequently integrate them with an higher computational performance.

Numerous works have been published to demonstrate that both plane-wave (VASP) and local basis (GAUSSIAN and SIESTA) methods provide consistent results [210, 211, 212], reassuring about the completeness and reliability of both basis.

There is an important consequence of the choice of plane-wave basis set: the full-potential has to be discarded in favor of a **pseudopotential** which eliminates the nodal character of valence orbitals, avoiding an explicit treatment for the strongly bound but chemically inert core electrons. There are mostly two approaches to generate pseudopotentials:

- The "norm-conservation" criterion [213] grants that inside the cut-off radius only the norm of all-electron and pseudo-wavefunction agree, while outside this radius they are identical. The derivative matches at a chosen reference energy and at cut-off radius;
- The "ultrasoft" pseudopotentials drop the norm-conservation [214], matching derivatives at two or more reference energies spanning the entire range of eigenvalues of the valence electrons;

Pseudopotentials have a certain limitations: sometimes non-linear core corrections are needed if the overlap between valence- and core-electrons densities is not completely negligible. Between the two approaches, first row elements and d/f electrons are more efficiently treated with ultrasoft potentials [215].

However every pseudopotential become very "hard" for these elements, so that a very large or complicated basis needs to be used. In fact not only the slow convergence of the core functions is problematic, because of their localized nature, but also the Fourier Transform convergence is slow due to Coulombic behaviour which requires a large number of K vectors. An alternative path to pseudopotentials has been proposed: "augmenting" the plane-wave basis with more localized functions.

The resulting augmented wave, compared to equation 2.83, has the form:

$$\psi^{\mathbf{k}+\mathbf{K}}(\mathbf{r}) = \frac{1}{\sqrt{\Omega}} \sum_{lm} i^l a_{lm}^{\mathbf{k}+\mathbf{K}} R_l(|\mathbf{r}-\mathbf{R}|; E) Y_{lm}(\mathbf{r}-\mathbf{R}) \tag{2.84}$$

where $R_l(r; E)$ represents a radial function for energy E and $Y_{lm}(r)$ are the spherical harmonics. The wave function is then divided into a partial-wave expansion with an atom-centered sphere and an envelope function outside the sphere, pairing the two at the cut-off radius. The secular equation to be solved is then:

$$\begin{gathered} det \left\| \int \psi^{\mathbf{k}+\mathbf{K}'}(\mathbf{r})(\hat{H}-E)\psi^{\mathbf{k}+\mathbf{K}}(\mathbf{r})d\mathbf{r} \right\| = 0 \\ \int \psi^{\mathbf{k}+\mathbf{K}'}(\mathbf{r})(\hat{H}-E)\psi^{\mathbf{k}+\mathbf{K}}(\mathbf{r})d\mathbf{r} = \left\{ \frac{\hbar^2}{2m}|\mathbf{k}+\mathbf{K}|^2 - E \right\} \delta_{\mathbf{K}',\mathbf{K}} + \Gamma^{\mathbf{APW}}_{\mathbf{K}',\mathbf{K}}(E) \end{gathered} \tag{2.85}$$

Matrix elements have non-linear energy dependence due to logarithmic derivatives of the radial functions. This augmented-plane-wave (APW) satisfies the boundary conditions as for the pseudopotential approach. However, the energy dependence of the matrix elements $\Gamma^{\mathbf{APW}}_{\mathbf{K}',\mathbf{K}}(E)$ requires searching poles of the determinants, and this problem was faced via the linear method proposed

by Andersen [216] and Koelling-Arbman [217]. The method evolved then in Linearized-augmented-plane-wave (LAPW): the philosophy was to remove the energy dependence of radial functions using Taylor expansion, avoiding the logarithmic derivative. Subsequently, it became clear that the potential approximation does not work in this context, especially for less packed and low-symmetry systems. Then Weinert proposed a full-potential method [218, 219], developing the Full-potential linearized augmented plane wave (FLAPW). This method is nowadays regarded as the benchmark in accuracy for DFT calculations in solids, but its computational effort is big.

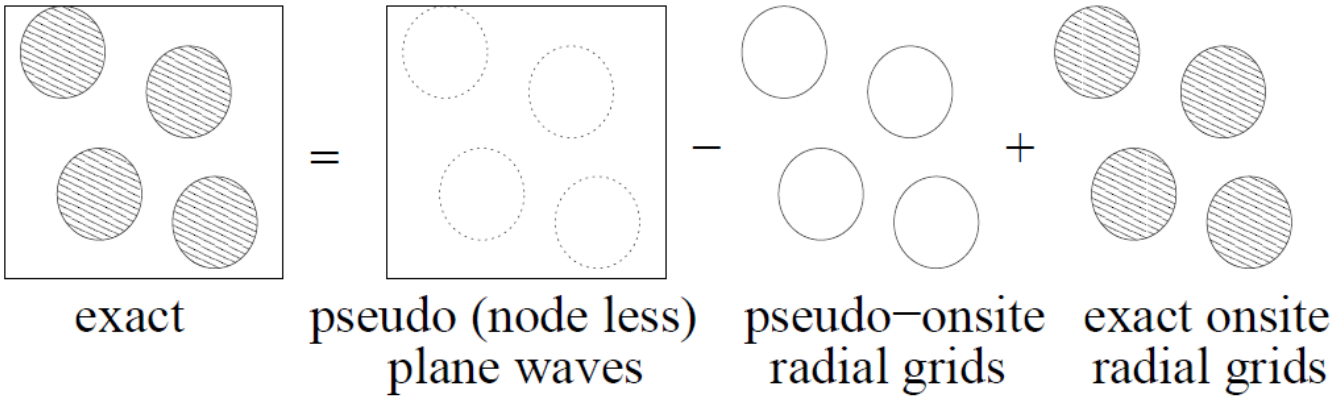

Figure 2.27: Sketch of PAW wavefunction decomposition, reproduced from [220].

To meet the accuracy of FLAPW with the computational agility of pseudopotentials, Blochl proposed the **projector-augmented wave (PAW) method** [221], which is the solution still used by VASP. A linear transformation is proposed from the pseudo-wavefunction to an all-electron wavefunction $\psi = \mathcal{T}\tilde{\psi}$ (still a single particle and not a many-body one). The new wavefunction, different from the old one just in the augmented region near the core, can be expanded into pseudo partial waves around the atoms:

$$\tilde{\psi} = \sum_i c_i \tilde{\phi}_i \tag{2.86}$$

Due to the linearity of the operator we chose for the transformation, every coefficient c_i can be written as an inner product with a set of projector functions:

$$c_i = \int p_i^* \tilde{\psi} d\mathbf{r} \tag{2.87}$$

where:

$$\int p_i^*(\mathbf{r}) \tilde{\phi}_j(\mathbf{r}) d\mathbf{r} = \delta_{ij} \tag{2.88}$$

The all-electron partial waves, $\phi_i = \mathcal{T}\tilde{\phi}_i$ are chosen usually as solutions of the Kohn-Sham equation for an isolated atom. The overal transformaton is then:

$$\mathcal{T} = 1 + \sum_i \int p_i^*(\mathbf{r})[\phi_i(\mathbf{r}) - \tilde{\phi}_i(\mathbf{r})] d\mathbf{r} \tag{2.89}$$

The exact function is then expressed as the pseudo partial waves, adding the exact onsite radial grids and subtracting the pseudo-onsite radial ones, as shown in Figure 2.27. The excellent agreement between the PAW wavefunctions and the all-electrons ones is shown in Figure 2.28, for different energies and angular momentum for the Mn atom.

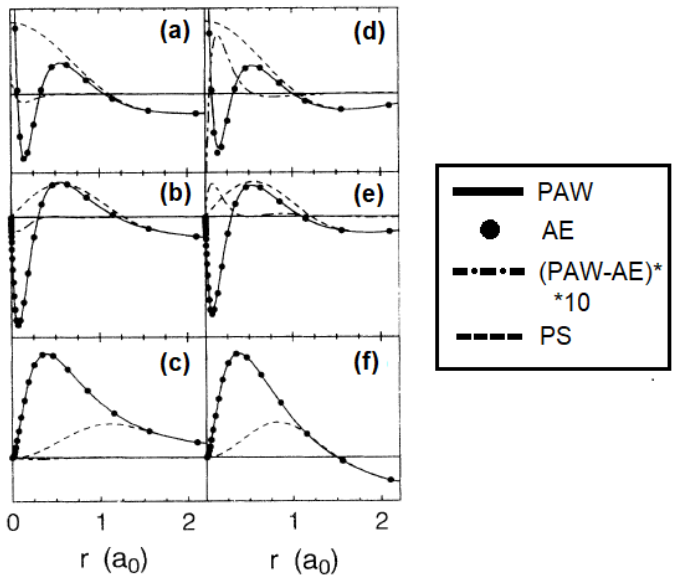

Figure 2.28: Comparison between Mn atomic wave functions using different methods for a given energy and angular momentum, adapted from [221]: PAW method (solid line), exact all-electron waves (bullets), their difference magnified by a factor 10 (dot dashed line), and pseudo-Hilbert wavefunctions (dashed). (a-c) are obtained at -8.16 eV, which lies in the valence band. (d-f) are obtained at +13.61 eV, which is far above the valence band region. (a)-(d) s-type wavefunctions. (b)-(e) p-type wavefunctions. (c)-(f) d-type wavefunctions.

Summarizing, an all-electron partial wave set describes the region between the cores, while inside the augmented region they can be any smooth continuation. VASP here uses spherical Bessel-functions, whose cut-off energy is calculated similar to plane waves and just a few are needed for convergence (4 in the original RRKJ scheme [222], but for PAW just 2 are needed).
VASP-PAW, which is still a frozen-core approximation, has been compared to the full-potential FLAPW [223, 224] an excellent agreement was demonstrated for all kind of materials.

2.7.5 Iterative schemes for ionic relaxation

The separate relaxation of ionic and electronic positions which we are going to describe is a paradigm that has been questioned in the past. Car and Parrinello, in 1985, proposed a profound variation of the methodology [207]. What they highlighted was the inefficiency of solving with high accuracy the Kohn-Sham equations for electronic configuration when the system was still far from the equilibrium ionic configuration. The Car-Parrinello (CP) method consisted in minimizing the total energy of the system simultaneously with respect to both electronic and ionic degree of freedoms. This idea triggered modern DFT potential, even if ironically the return to a traditional approach was quite fast. In fact there are two reasons for this regression. CP approach requires electrons and ions' degrees of freedom to be effectively decoupled, but while this condition is met for insulators and wide-gap semiconductors it is not met by narrow-gap materials and metals. In addition, the minimization of the total energy does not allow an efficient control of charge-density fluctuations during the self-consistency process. This phenomenon, called often "charge-sloshing", can even prevent the convergence of the cycle for metals.

The iterative scheme which is presented in Figure 2.26 was then readopted. As detailed by subsection 2.7.1, the nuclei will be treated as classical particles, by implementing an efficient version of $\sum_i \vec{F}_i = m_i \vec{a}_i$. The basic **Newtonian scheme** is [220]:

- Starting with the position $\vec{x_1}$ of the ion;

- Calculate the gradient $\vec{g}(\vec{x_1})$;
- Multiply with the inverse of the Hessian matrix B:

$$B_{ij} = \frac{\partial^2 f}{\partial x_i \partial x_j}$$

- Perform a step:

$$\vec{x_2} = \vec{x_1} - B^{-1}\vec{g}(\vec{x_1})$$

- Restart;

In principle, by inserting $\vec{g}(\vec{x_1}) = \frac{\partial f}{\partial x} = B(\vec{x_1} - \vec{x_0})$ one can find the minimum in one step. However this demands the precise knowledge of **B**, whose calculation is not possible in a reasonable time-span. Approximations are then needed.

The method of the **steepest descent** [220] approximates **B** by its largest eigenvalue Γ_{max}. This is because Hessian matrix eigenvalues are the vibrational frequencies of the system for ionic relaxation: the highest frequency mode determines then the maximum stable step-width. Usually the number of iterations needed for convergence is proportional to $\Gamma_{max}/\Gamma_{min}$, with Γ_{min} the lowest eigenvalue.

Quasi-Newton scheme maintains an iterative scheme, in order to reduce the number of steps to $\sqrt{\Gamma_{max}/\Gamma_{min}}$. One example is the **direct inversion in the iterative subspace (DIIS)** [225]. After a first step along the gradient via the steepest descent, from point $\vec{x_1}$ to $\vec{x_2}$, the goal is to search for a linear combination of the starting set of points which minimizes the gradient, $\vec{g_{best}} = \sum \alpha_i \vec{g_i}$, and calculate the corresponding position $\vec{x_{best}} = \sum \alpha_i \vec{x_i}$. The new position will be $\vec{x_3} = \vec{x_{best}} - \lambda \vec{g_{best}}$.

Alternatively, the **sequential conjugate gradient (CG)** method can be used [226, 227], which exploits line minimisation. After calculating the gradient at the current position, $\vec{g}\left(\vec{x}^N\right)$, the gradient is "conjugated" to the previous search direction using:

$$\vec{s}^N = \vec{g}\left(\vec{x}^N\right) + \gamma \vec{s}^{N-1} \quad \gamma = \frac{\left(\vec{g}\left(\vec{x}^N\right) - \vec{g}\left(\vec{x}^{N-1}\right)\right) \cdot \vec{g}\left(\vec{x}^N\right)}{\left(\vec{g}\left(\vec{x}^{N-1}\right)\right) \cdot \vec{g}\left(\vec{x}^{N-1}\right)} \tag{2.90}$$

Then line mimisation is performed along this search direction $\vec{s}^N$. The gradient is calculated again and the process restarted if the desired accuracy is not reached yet. The search directions satisfy:

$$\vec{s}^N \mathbf{B} \bar{s}^M = \delta_{NM} \quad \forall N, M \tag{2.91}$$

Practically speaking, the conjugate gradient algorithm finds the minimum of a quadratic function with k degrees of freedom in $k+1$ steps. Another quasi-Newton scheme implemented in VASP is the damped molecular dynamics, which will not be used in this thesis.

How to choose between these algorithms? DIIS has problems when forces increase along the search direction. In that case, seeing that DIIS considers forces only in the scheme, it will move uphill instead of downhill in energy. There can also be problems due to rotation of the system, which changes the Hessian matrix in cartesian coordinates. To avoid all of these, CG algorithm will be mostly used through this thesis.

2.7.6 Iterative schemes for Kohn-Sham eigenstates

Different iterative schemes have been studied, some relying on a self-consistent cycle and some on a total energy minimization. As stated before, self-consistency was revealed to be way more efficient for small-gap insulators and metals, while it is at least competitive with Car-Parrinello paradigm for semiconductors and insulators.

An iterative approach is considered efficient if it minimizes the number of operations that scales with a higher power of the number of plane waves (for example the orthogonalization of the eigenstates goes as N^3). **The sequential conjugate-gradient algorithm** [226, 227] can be used also for

electrons, but orthogonalization process needs to be performed for each update of the eigenstate. On the other hand, the **residuum minimization method (RMM)** [225, 228] minimizes the norm of the residuum vector, defined as:

$$R(\psi_m) = \left(\hat{H} - \varepsilon_{mapp}\hat{S}\right)\psi_m \tag{2.92}$$

where $\hat{S}$ is the overlap matrix [229] and $\int \psi_m \hat{S} \psi_n d\mathbf{r} = 1$. The minimization of $\|R(\psi_m)\|$ is free of orthogonality constraints and it makes this algorithm faster. However, **RMM** and **RMM-DIIS** (same algorithm combined with a direct inversion in the iterative subspace) have the drawback of converging to the local minimum closest to the initial state, instead of the global one.

This is why in this thesis we will alternate RMM-DIIS with the **Davidson-block iteration scheme** [230, 231]. In this method a subset of all bands is chosen, the orthogonalized residual vectors of the presently considered subspace are added to optimize, the Raighly-Ritz optimization in the space spanned by these vectors and finally the residuals calculated from the yet optimized bands are added. This method is 1.5 to 2 times slower than RMM-DIIS but it is more stable and does not produce the risk of missing the eigenstates.

Depending on the dimension of the system, both RMM-DIIS and Davidson algorithms have been used. VASP offers also a reasonable compromise via the "Fast" algorithm: the first 5 steps are performed via blocked Davidson, then DIIS is used. This avoids to fall just into the local minima of the system reducing the computational effort.

2.7.7 VASP input and outputs

A typical VASP calculation requires at least four basic input files: INCAR, POTCAR, POSCAR and KPOINTS. These input files contain all the parameters that the user sets and represent the choices presented so far between the different options available for a density functional theory calculation. The previous sections must not be misled as the evolution towards a computational black box, which works in every situation. The user knowledge of the computational alternatives (which basis has been chosen, which relaxation method, when the relaxations are stopped, how the Brillouin zone is sampled, etc) is necessary, because no universal set of parameters exists. Every calculation demands an optimisation of its own and settings which are closely related to the properties of the materials involved. Using the wrong parameters can not only make a calculation unnecessarily long, but also deeply affect the reliability of the results. Here we focus then on the input parameters:

POSCAR is the file containing the lattice geometry and the ionic positions. It also can contain the starting velocities for Molecular Dynamics. The box for Periodic Boundary Conditions is defined through the three lattice vectors $\vec{a}$, $\vec{b}$ and $\vec{c}$. The number of atoms of each species is specified, and then positions of the ions are given either in Direct or Cartesian coordinates, meaning in fractions of $|\vec{a}\,|$, $|\vec{b}\,|$and $|\vec{c}\,|$or usual $x - y - z$. In the case of a surface, vacuum space is added in the z-direction to avoid self-interaction with the bottom of the slab.

INCAR is the file containing the actual control parameters, stating which calculations are to be performed and how, and which to be ignored. The main parameters necessary for structural relaxation are:

- ISTART = 0 if the calculations needs to start from zero, = 1 if it can exploit a previous structural relaxation; ICHARG = 0 to calculate electronic density from starting wavefunctions, = 1 to read from the previous structural relaxation, = 2 to use the superposition of atomic densities. A typical calculation starts with ISTART = 0 and ICHARG = 2, then switches to ISTART = 1 and ICHARG = 1 when a first relaxation has converged;

- IBRION = 0 if the ionic relaxation uses the Verlet algorithm (typically for molecular dynamics), = 1 for a quasi-Newton algorithm, = 2 for GGA, = -1 if the atoms are freezed in their actual positions (for PDOS/STM calculations). Throughout the thesis a GGA algorithm will be used;
- EDIFFG = 1E-03 is the stopping criterion for ionic relaxation, expressed in eV. When two following steps have an energy difference lower than these value, the calculation stops;
- NSW = X, where X is the number of ionic steps to be performed (if the energy requirements is not reached before);
- ALGO = VeryFast/Fast/Normal for the electronic relaxation algorithm. VeryFast is RMM-DIIS algorithm, Normal is Davison algorithm, while Fast uses Davison algorithm for the first 5 steps then RMM-DIIS. For large cells I often launched the first relaxation in VeryFast to then refine the result in Normal;
- NELMIN / NELM = X/Y are the minimum and maximum number of electronic steps to be performed for every ionic step, to reach the desired energy
- EDIFF = 1E-04 is the stopping criterion for electronic relaxation;
- ISMEAR determines how the partial occupancies are set, with SIGMA the amplitude of smearing in eV. 0 is for Gaussian smearing, for semiconductors with only a few k-points, is the default value with SIGMA = 0.2. 1 is Methfessel-Paxton order 1 which is better for metals. For semiconductors/insulators and a lot of k-points the tetrahedron method with ISMEAR = -5 is more advised.
- ISPIN = 1 to perform unpolarized calculations in spin, = 2 for polarized. I did not perform polarized calculations in my thesis;
- ENCUT = X, to choose the plane wave energy cutoff (in eV);
- NPAR / NCORE to choose the number of CPUs and nodes to use (depending on your computational capabilities);

POTCAR is the file where pseudopotentials are written. VASP code is supplied with a set of standard pseudopotentials of various atoms, LDA and PBE. Before starting a calculation, one should have the pseudopotentials of each atom involved in the system concatenated in POTCAR in order of appearance in POSCAR under the working directory.

KPOINTS is the file containing the grid of K-points to sample the Brillouin zone in the reciprocal space. If the points are manually inserted, the number of the points has to be written as first parameter. If the number is 0 it means a grid will be generated through the Monkhorst-Pack algorithm. The next lines define then the center of this grid (usually Γ) and the number of points for each reciprocal space direction. The larger the number of K-points, the more accurate the results should be and the more expensive the calculation is. A division in reciprocal space of less than 0.05Å^{-1} has been shown to provide converged structures and adsorption energies. In this thesis however we will not need a fine evaluation of the energies, because we will be more interested in the simulation of STM images, so usually for the surface cell of germanene nanosheets longer on $\vec{a}$ and $\vec{c}$ directions we will use a mesh of 2×5×2.

The output of main interest for a structural relaxation are CONTCAR, CHGCAR, WAVECAR, OSZICAR and OUTCAR.

CHGCAR and **WAVECAR** are the essential output of a structural relaxation, because they contain respectively the total charge density (expressed as $\rho(r) \cdot V_{cell}$) and wavefunctions after the last

electronic step of the calculations. They are the main goal of the structural relaxation, which takes the most computational time. These are the files that VASP reads when ISTART and ICHARG are set to 1, for example. When a CHGCAR and WAVECAR are available and well written, the following steps as Density of States calculations and STM simulation are not time consuming in comparison;

CONTCAR is a file with the same structure of POSCAR, but containing the ionic positions after the last ionic step (if the relaxation converged). This file can be copied as new POSCAR to continue the structural relaxation if the accuracy of EDIFF has not been reached yet.

OSZICAR contains information about the electronic steps, the free energy and its variations through the relaxation.

OUTCAR contains every operation that is performed during the relaxation.

The visualization of POSCAR, CONTCAR and CHGCAR files, as that of 2D slices of CHGCAR, will be performed via the VESTA software.

2.7.8 Simulation of STM images

VASP provide the tools to evaluate the result of an STM image. The idea is to exploit the Tersoff-Hamann model approximation of a point source to simulate an STM tip. A STM in constant current mode follows a surface of constant current. In the Tersoff-Hamann approximation this translates into a constant integrated $LDOS(x, y, z) = C$ isosurface [156], with C a real constant. The first step needed is then calculation of the isosurfaces of the partial charge densities between the Fermi level and a specified voltage, to be written in the **PARCHG** output. A structural relaxation is needed as first calculation. The additional input parameters are:

- ISTART = 1 and ICHARG = 11; every ICHARG value above 10 is assigned to not-self consistent calculations, 11 is used to read from CHGCAR (opposed to 12 from atomic densities).
- IBRION = -1, to not update ionic positions;
- LPARD = .TRUE to write the PARCHG output;
- EINT = X, to specify the energy range for the partial density calculation (equivalent to the voltage applied to the tip);
- NBMOD = -3 to use the value of EINT relatively to the Fermi level, as it happens for integrating the LDOS to obtain the STM current at a specified voltage;

Once the PARCHG file is ready, the HIVE software is used to produce the STM image [232]. The STM constant current mode is mimicked by mapping z on a grayscale. Two options are available:

- Mapping a particular value of the constant charge density C, expressed in $eV/Å^3$;
- Choosing C in order for the isosurface to have an height z between 2 and 4Å above the highest atom in POSCAR. The user set the desired value of z and the calculation is performed by the software;

This second option will be used in the following, with the distance usually set at 3Å. The default mapping sets the lowest value in z on the surface to 0Å, while the highest value is calculated accordingly. The software has one limitation compared to typical scanning probe microscopy softwares: it does not allow a plane subtraction to set a certain non-zero value as the reference and shift the other values accordingly. This is not problematic when a single STM image is needed. It can however

be deceiving when multiple STM images of the same surface under different applied voltages are observed. The relative height values will be then considered for a quantitative analysis.

Another thing to be considered is that the software assumes that the basis vectors of the cell are orthogonal, so in our case of hexagonal cells a skew of 30° is needed in order to obtain the proper surface. This skewing process will be still detectable in the images of chapter 4, in particular on the top atoms of germanene nanosheets. This is not a physical feature and it won't negatively affect our analysis of the results.

Other useful features of the HIVE software are:

- It is possible to draw profiles as in common image processing programs for STM;
- A function to add a finite radius to the tip is present in the tools. This is implemented through a graphical smoothing of the image, following the idea that the current follows the path of least resistance creating a sphere of radius R centered around the point-source [233]. This sphere smooths sharp depressions and sharp protrusions out of the image. An exact physical implementation would require a model for the tip geometry, which would be too computationally demanding. This kind of smoothing on the other hand can just reproduce qualitatively the experiments;

2.7.9 Projected Density of States calculation

The calculation of an equivalent of the experimental Local Density of States requires the calculation of the Projected Density of States on every site, either complete or lm-decomposed, in which case a sum back every contribution from the s, p_i and d_{ij} orbitals, with i,j = x,y,z, will be needed. The same parameters for ISTART, ICHARG and IBRION are necessary, being again a not self-consistent calculation with frozen atoms. Other parameters to write the **PROCAR** output containing these informations are:

- LORBIT = 10 or 11. In both configurations the Wigner-Seitz radius of every species is taken by the information in the POTCAR input. 10 gives as output the DOSCAR file (for complete DOS) and PROCAR file for projected DOS on every site. 11 gives DOSCAR and lm-decomposed PROCAR outputs. In this thesis the results are obtained most of the time via the sum back of the lm-decomposed PROCAR (or equivalent information in the vasprun.xml file, which contains the OUTCAR information in .xml format);
- ISYM = 0. This tag determines how VASP treats symmetry. For structural relaxation we used a default value of 2 to exploit an efficient way of conserving the symmetrization of charge density, which requires less memory. For PDOS we prefer VASP to assume that $\Psi(k) = \Psi^*(-k)$, not using symmetry and reducing the Brillouin zone accordingly;
- NBANDS tag depends on the number of electrons in the system, and we prefer to leave around 50 empty bands in the conduction band to launch the calculation (every band stores two electrons of opposite spin);
- EMIN and EMAX can be set to make the calculation more efficient;

At the end of the calculation the information contained in PROCAR or vasprun.xml is used to plot the DOS.

2.7.10 Molecular dynamics calculation

Molecular dynamics (MD) is used to study the temporal evolution of the system, in the scale of tenth of picoseconds due to computational limits. The computational requirements of long MD calculations require the modification of the parameters for a self-consistent cycle. The main tags for the INCAR file are:

- IBRION = 0 to tell VASP to perform Molecular Dynamics;
- MDALGO = 2. This tag sets the algorithm for the ensemble. 2 sets the Nose-Hoover thermostat to work in a canonical ensemble (constant temperature conditions). In addition, SMASS that determines velocities is set to 0;
- TEBEG and TEEND set the starting and final temperature. Even by setting the same temperature (for canonical ensemble) the system will be affected by T oscillations during the run, with the set temperature as average;
- As for self-consistent calculations, we need to set NSW, ALGO, NELMIN, NELMAX, ENCUT, EDIFF;
- POTIM = X. This tag sets the time-step, X is expressed in femtoseconds;
- MAXMIX = X. This tag sets the number of steps stored in the mixer of MD, to be able to reuse smoothly the charge density and the dielectric function on a larger timeframe. Usual number is 40-50;
- NBLOCK = X. This tag sets every how many ionic steps the XDATCAR, which contains the configurations, is updated. The number scales with NSW and POTIM, depending on the resolution of the analysis;
- LREAL = A, to evaluate the projection operator in real space, which is faster;
- NWRITE = 0, LWAVE = F and LCHARG = F to have the minimum verbosity of OUTCAR and not to write WAVECAR and CHGCAR;

The result can be analysed via the E vs N evolution in OSZICAR, or via the evolution of ionic configuration in XDATCAR, or just by studying the final configuration in CONTCAR.

Chapter 3

Scanning Tunneling Spectroscopy of Germanene on Al(111)

The search for a substrate for germanene is strictly connected with the persistence of its electronic properties. In this regard, the best choice would be a low reactive semiconducting substrate with a low surface corrugation. Graphene/graphite would have been the perfect substrate, but the growth of germanene around HOPG defects has been disproved [48].

The only semiconducting substrate of interest that was claimed to enable the germanene synthesis is MoS_2. The observed 2D Ge layer has a 3.8 Å lattice constant, $\sim$ 20% larger than MoS_2 (3.16 Å) [76]. The STS comparison between MoS_2 and the germanene islands grown near to the original substrate defects shows a V-shaped curve attributed to the islands. However, the STS spectrum of MoS_2 before Ge deposition is not shown. After briefly elaborating in the introduction that MoS_2 has a gap that varies varies from 1.2 to 1.8 eV depending on its thickness, the actual value of the band gap of MoS_2 next to the germanene islands is not discussed and no clear flat region is present in the spectrum, so the value of this "control measurement" is questionable. Even if the DOS is reproduced by the DFT calculation, the current in the gap-region is yet unexplained.

The dI/dV does not match either with the characteristics of pristine MoS_2 reported in a following paper by the same group [77]. In this work, the spectrum is symmetric around the Fermi level while in the other work the Fermi level seems pinned to the conduction band minimum. The V-shaped spectrum of the Ge/MoS_2 is asymmetric, but in the opposite way than reported in [76]. Again this asymmetry is ascribed to the W tip, but no analysis is performed to raise the confidence in the dI/dV characteristics. Later on, the spatial variation of the dI/dV map is linked to the variation of the position of the Fermi level due to charge puddles induced by a difference of charge donating impurities in MoS_2. Only an analysis of the density of defects on the pristine surface is reported, while no information is provided on how the dI/dV spectrum varies around these defects. These contradictions and the lack of a reproduced synthesis in literature leave the debate open on the actual electronic properties of germanium layers deposited on MoS_2.

As briefly detailed in section 1.3, the growth of germanene on a few metallic substrates has been claimed, part of which later disproved. It is the case of Ag(111) [65], Pt(111) [66] and Au(111) [72].

One of the most analyzed metallic substrates for germanene are Ge_2Pt crystals on Ge(110), by the group of Zandvliet in Njmegen and coworkers. After deposition, these crystals are terminated with a buckled honeycomb structure, with Δz=0.2Å, whose periodicity is close to the free-standing layer (2.4 Å vs 2.5 Å) [59]. The substrate is shown to be more conductive than the crystals termination, and the dI/dV analysis shows an asymmetric V-shaped curve [60]. This asymmetry is explained with homogeneous broadening due to the temperature [61], but an energy offset remained to be accounted for. The authors claim this to be due to the substrate interaction and/or the W tip convolution, but

no further analysis has been performed so far. No true check for the I-V characteristics of the tip was also provided. The effect of the substrate should also be analyzed in a more attentive way, because a metallic substrate with an almost free-standing germanene layer above with preserved electronic properties would be a severe step forward. The attention in this substrate was however limited and neither for MoS_2 nor for Ge_2Pt we can still be sure that the Dirac physics of germanene is maintained.

More attention was given to germanene on Al(111) [83], but less electronic information is available due to the time devoted to the understanding of the different reconstructions, meaning the 3×3 2T and 1H, and the $\sqrt{7} \times \sqrt{7}$R19° phases. While a metallic dI/dV characteristics was reported for the $\sqrt{7} \times \sqrt{7}$R19° reconstruction [98], no spectroscopic information is available about the 3×3. The observation of a Dirac cone is vital, because further attention dedicated to the system has to be proportionate to this feature.

In this chapter the growth of germanene on Al(111) will be described. The spectroscopic characterization of the 3×3 1H reconstruction starts with a complete monolayer, for which a high variability of the STS spectrum was surprisingly obtained. This variability demands the analysis of the submonolayer regime, in order to provide a metallic reference and account for the proper behaviour of the W tip. In this regime a low mechanical stability of the germanene nanosheets is observed, via their unintentional displacements and detachements. This instability is shown to influence the result of the STS analysis through clusterization on the apex of the tip of a family of species mixing W, Al and Ge. The STS spectra are then impossible to be interpreted with confidence without a proper reference of the tip behaviour. We will conclude that germanene nanosheets in the 3×3 1H reconstruction are metallic, and elaborate on the previous literature of STS spectroscopy on 2D materials following our findings.

3.1 Growth of germanene on Al(111)

The growth of germanene followed the recipe of Derivaz et al. [83] briefly presented in section 1.3, with some variations due to our experimental setup. The steps are presented in figure 3.1.

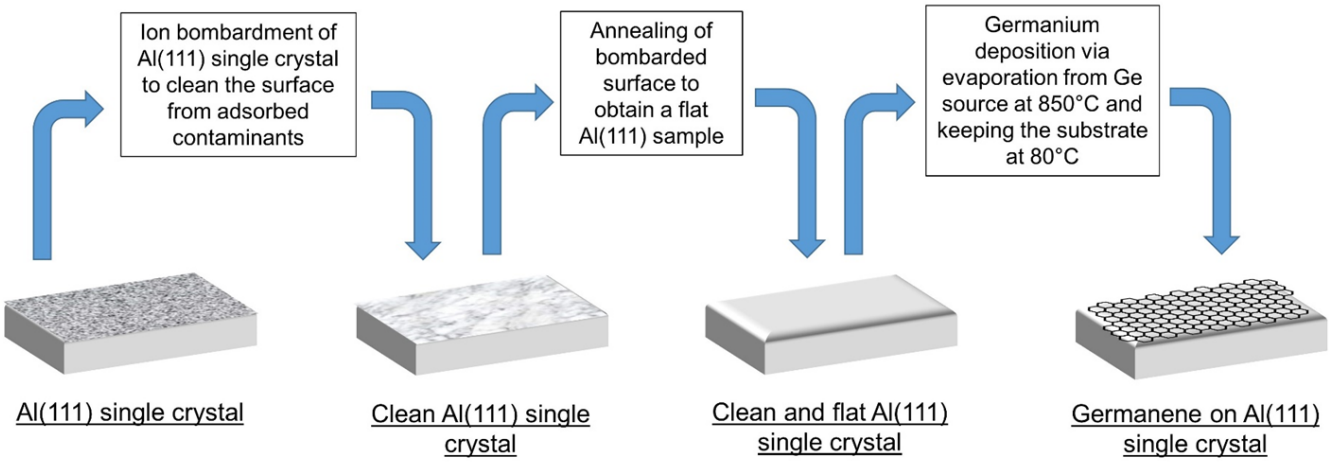

Figure 3.1: Steps of the preparation of germanene on Al(111).

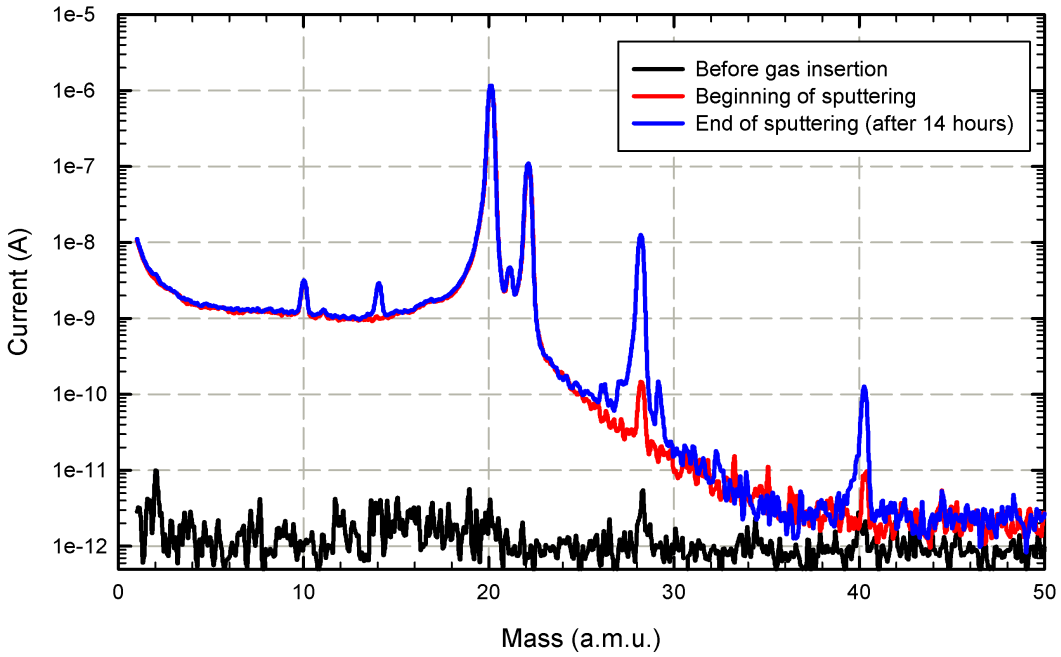

Figure 3.2: Quadrupole Mass Spectrometer spectra acquired before gas insertion into the preparation chamber (black), at the beginning of the sputtering (red) and at the end (blue). m = 22 is Ne-22, this isotope being present in a ratio of 9,25/100 in the atmosphere. m = 40 is Ne^{2+}.

Clean and well-ordered Al(111) surfaces were obtained by Ne bombardment (800V on the ion gun) of a commercial Al(111) single crystal. Al(111) has to be placed on the manipulator in the preparation chamber of the STM setup (see 2.4), and positioned in front of the gas outlet by maximizing the surface current generated by the impinging ions (usually in the range of 1-10 pA). In this position, the ion gun outlet is at $\sim$ 10 cm from the surface, forming an angle of $\sim 22°$ with the surface. The purity of the gas is checked via the QMS (figure 3.2) and the gas pressure is kept around 5 x 10^{-6} mbar. The N peak at mass number 28 has an intensity which is 4 orders of magnitude lower than the main peak of Ne at 20 (blue curve in figure 3.2). To avoid the formation of aluminium nitride on the surface, which is then difficult to sputter properly, a limit ratio of Ne/N of 2 orders of magnitude has been chosen (as in red curve of figure 3.2). When the ratio approaches this value, the sputtering is momentarily stopped, closing the gas outlet. The gas line is pumped with a primary pump for a few minutes, than new Ne is injected into the line. The sputtering can then be started again (with a QMS signal restored to the blue curve in figure 3.2).

After every bombardment an annealing cycle via resistive heating is performed at temperatures near surface melting, between 400 and 450°C, where the high mobility of surface atoms leads to a smoothing of the roughness generated by the sputtering. We need to stress that annealing is not a complete reforming process: the surface faces slow degradation after repeated bombardment and annealing cycles and the roughness increases over time. To get back the original flatness the single crystal has to be sent for laser polishing. The temperature is checked via a thermocouple and a pyrometer.

The cleanliness of the surface is checked via STM, as shown in figure 3.3. The evolution from a contaminated to a clean surface is not abrupt: as we see in figure 3.3(a), the first locations to become clean are the center of the terraces, while at the corner and terraces steps chemical contaminants in form of clusters are still found. The goal is to recover clean terraces, as those shown in figure 3.3(b). On the nm scale attention must be paid to black spots, which can be the signal of remaining oxidized sites on the surface. A clear metallic behaviour is observed in STS, as shown in figure 3.4, after 3-4 cycles of sputtering. Figure 3.4(a) shows STS between -1 and 1V, where a linear behaviour is expected for a metal like aluminium. The inset shows a featurless dI/dV curve, as expected. Figure

3.4(b) shows STS in a smaller voltage range, between -10 and +10 mV, and its dI/dV in the inset, which are going to be relevant for the following when using Al STS as a reference.

When Al(111) surface is ready, a Ge(001) crystal is degassed up to 800-850°C, until pressure is back in the 10^{-11} mbar regime (Al is kept in the STM chamber during the degassing). Ge crystal and Al(111) are positioned a few millimeters apart, in order for the solid angle of evaporation to cover the whole Al(111) surface. Aluminium is heated at temperatures around 80°C, measured via the thermocouple. Our evaporation system does not exploit a Knudsen cell and a quartz balance or a filament to measure the amount of material deposited, so we need to calibrate the sublimation process as a function of the time of deposition and the gas pressure (difference between base pressure with the Ge sample at T=700°C, when it is not sublimating yet, and at deposition temperature). The calibration has been perfected over time by checking the result via STM. A deposition of 3 hours with base pressure of 4-5 $\times 10^{-11}$ mbar and gas pressure of 6-7 $\times 10^{-11}$ mbar gives a full coverage. This value of pressure in the chamber slowly rises during the deposition, to finally reach a pressure of 1×10^{-10} mbar higher than base pressure in the end. We ascribe this to an indirect heating of Al(111) whose temperature grows up to 100°C during deposition.

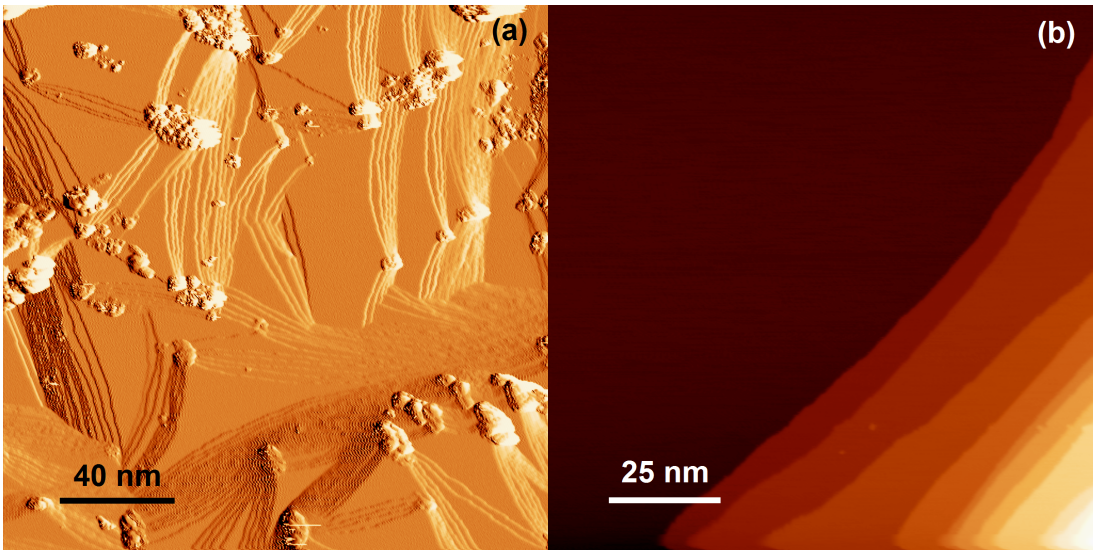

Figure 3.3: (a) Large scale STM current image of Al(111) surface that requires additional sputtering and annealing cycles to remove the presence of large clusters. These clusters are caused by chemical contaminants. (b) STM topography of clean Al(111) terraces. Parameters: V=-1V, I=50pA. T=77K.

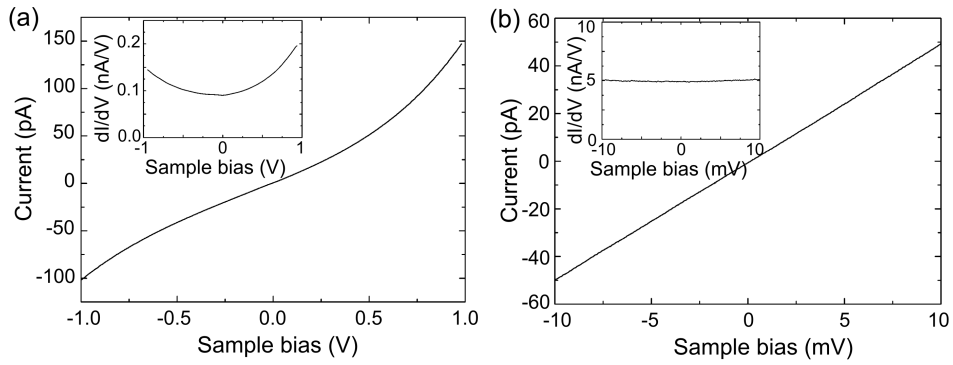

Figure 3.4: Average of I(V) curves and corresponding dI/dV spectra (upper insets) measured on clean Al(111) after sputtering at T=77K. (a) V=-1V, I=100pA, f=480Hz, ΔV=7mV. (b) V=-10mV, I=50pA, f=480Hz, ΔV=0.5mV.

3.2 Germanene spectroscopic characterization

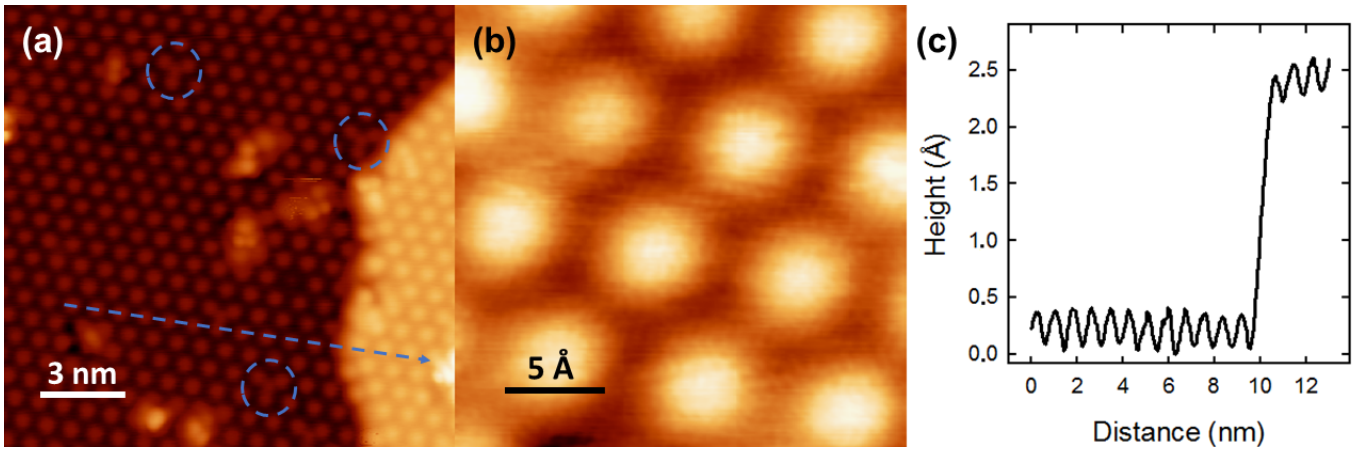

Figure 3.5: (a) Large scale filled-state STM image of monolayer germanene on Al(111). Typical Y-shape defects are shown in dashed circles. (b) Atomic scale image of germanene. Image parameters: sample bias V = -1 V, current I = 50 pA, temperature T = 77 K. (c) Profile shown in blue in figure (a).

Figure 3.5 shows a large scale STM image of a full layer of germanium on Al(111). The step of the terrace visible is of 2.3Å from top to top atoms (profile in fig. 3.5(c)), which is comparable with Al(111) step height. The periodic array of protrusions which is observed on every terrace is characterized by typical distances of 8.7 ± 0.2Å, which compares well with the reported periodicity of the 3×3 reconstruction of germanene (compared to Al(111) periodicity, or 2×2 compared to free-standing layer). The most often observed defect is an Y-shape structure, characterized by a protrusion on the hollow site of 3 lower Ge top atoms. Three of these Y-shape structures are highlighted in figure 3.5(a) by dashed circles. Via this and other images on this sample we calculated a concentration of Y-shape defects of 9×10^{11} cm^{-2}. The other bright protrusions observable are attributed to a slight extra amount of germanium which was evaporated compared to the mono-layer and adsorbed on the surface. The height of the terraces that compares well with a single terrace step of the substrate and the presence of 3D features is a strong indication, that above the monolayer, Ge tends to clusterize instead of starting the growth of a second layer.

The presence of defects on the surface could generate localized states in the I(V) and dI/dV characteristics and hinder eventual applications. For this reason, we started our analysis of the material properties with particular attention on their evolution around these defects. As figure 3.6 shows, spatially resolved tunneling spectra are quite reassuring. Twelve dI/dV spectra were acquired on different places of interest: the top of Ge atoms, the hollow sites and on the Y-shaped defect. The result shows a lack of spatial peculiarities: the same characteristics was observed everywhere, with two peaks at -0.18V and +0.20V and a small dip at the Fermi level, at zero bias. The local environment does not seem to influence the position of these peaks.

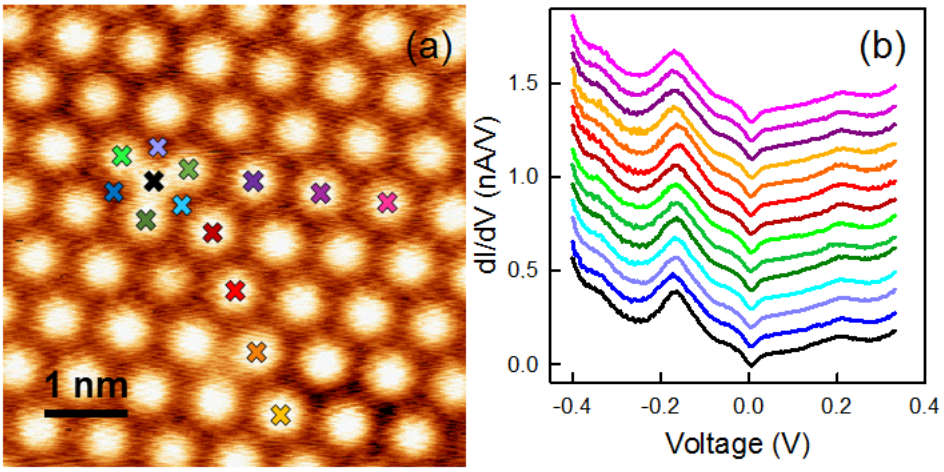

Figure 3.6: (a) Spatially-resolved tunneling spectra of a germanene area with an Y-shape defect, V = -0.4 V, I = 100 pA, T = 5 K. (b) Different spectra acquired at the location highlighted in (a).

This result however is not conclusive: even if there is an high spatial reproducibility on the same area, we observed substantial variations during the same run of measurement with the same tip but on different locations of the sample. A representative set of the dI/dV is presented in figure 3.7. Spectrum 3.7(a) has a finite value at zero bias, indicating the absence of an energy gap and a metallic behaviour. This is already in contrast with figure 3.6, where the density of states vanished at zero bias. We observed also higher energy gaps, as in figure 3.7(b) where the energy gap is of about 500 mV around the Fermi level. Smaller gaps as the one visibile in figure 3.7(c), with a width of 35 meV, were also found. We can span all the possible behaviours by showing figure 3.7(d), where the shape of the peaks around the Fermi level resembles a coherence-like behaviour as superconductors.

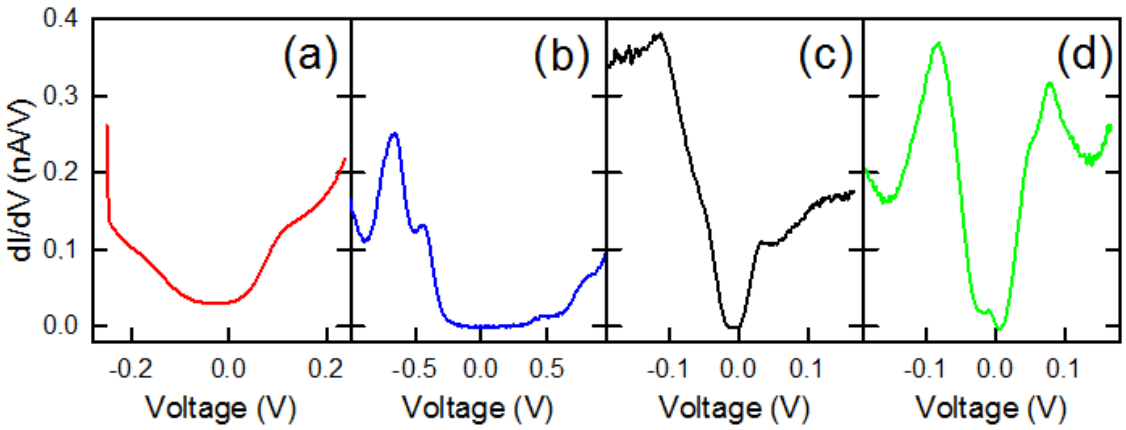

Figure 3.7: (a-d) Different dI/dV acquired on monolayer 3 x 3 germanene on Al(111), measured at different temperatures with different setpoint bias and currents. (a) 77 K, -0.25 V, 100 pA. (b) 77 K, -0.75 V, 100 pA. (c) 5 K, -0.2 V, 90 pA. (d) 5 K, -0.2 V, 60 pA.

All of these characteristics are physically true, and none of them are, in the sense that we can not assign one to germanene on Al(111) without further testing. We described in section 2.3 how scanning tunneling spectroscopy must always be interpreted by not forgetting the presence of the tip, which could be the source of all kind of artefacts. In our case we need to make sure that the LDOS of the tip is constant over a wide range of energy around the Fermi level. We are luckily dealing with a metallic substrate which can provide a fast testing of the tip properties. In the sample produced so far however this testing could not be achieved due to the full coverage of Al(111) with Ge. To provide an Al reference spectra we need to perform a sub-monolayer growth where bare Al areas can

be found and probed.

Figure 3.8(a) shows a germanene nanosheet grown on the border of an Al(111) terrace. Compared to what reported in section 3.1, the deposition time was shortened to 1 hours and 30 minutes, while maintaining the same references for base and gas pressure. The 3×3 reconstruction is shown for it's the subject of the study, but for completeness we need to say that in the sub-monolayer regime we started to observe also $\sqrt{7} \times \sqrt{7}$ domains, as shown in figure 3.8(b). This will be discussed in the next chapter.

In the sub-monolayer regime we are able not just to measure the height of terrace steps, but also the relative position of the germanene nanosheet compared to bare Al. As shown in the inset of figure 3.8(a), the result is that the average height of the island appears at the same level of the Al terrace, with just the top Ge atoms to protrude of 0.30Å on average. The presence of sparse clusters on the Al terraces does not affect the measurement of a proper metallic spectrum to acquire a reference for tunneling spectra.

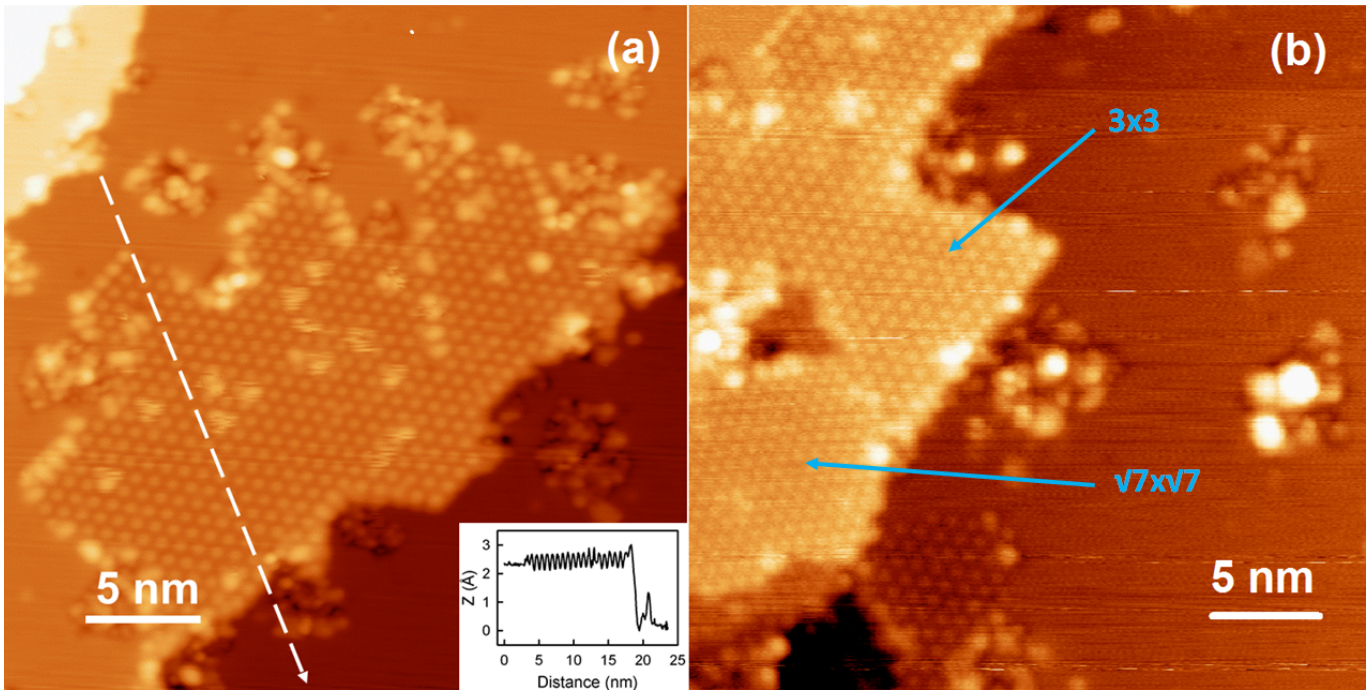

Figure 3.8: (a) STM image of submonolayer germanene growth on Al(111). V = -1.5 V, I = 50 pA. T = 77 K. Inset: height profile measured across the germanene island along the dashed line. (b) STM image of coexisting 3×3 and $\sqrt{7} \times \sqrt{7}$ in sub-monolayer regime. V=-1V, I=50pA, T=77K.

Measurement performed at 5K with a freshly prepared STM tip are shown in figure 3.9. We are reassured by a metallic behaviour on a large bias range (-1.0V to +1.0V) and in a reduced range (-0.1V to +0.1V). For the second range we performed a finer analysis to assess any possible influence of the tip-sample distance. The result is consistent with the spectra of the clean Al(111) shown in figure 3.4. The absence of slope variations and plateaux indicates the negligible contribution due to the surface states. Particulary worrying were the states at the K point, which in the 3D Al band structure projected onto the 2D Brillouin zone are positioned 0.7 eV below the Fermi level [85]. However, these states are characterized by a high parallel wave-vector, and this brings to a strong decay into vacuum, reducing the trasmission possibility and the chance to observe them via STS. We can then consider the spectra in figure 3.9 as a proof of the flatness of the Local Density of States of the tip on the whole range of energy of interest.

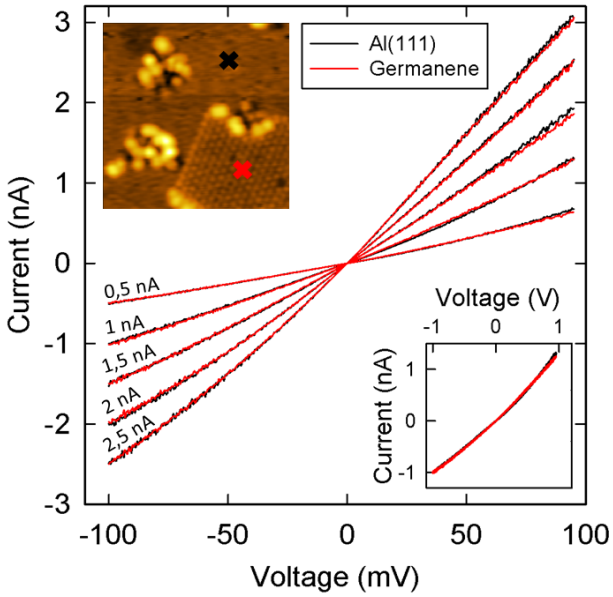

Figure 3.9: I-V curves measured as a function of setpoint current on Al(111) and germanene areas indicated by crosses in the STM image of the upper inset at 5 K. Inset: similar I(V) curves measured on a wider bias range with a setpoint current of 1 nA.

Around the same areas used for establishing the reference spectra we turn then to test the characteristics of a germanene nanosheet, as shown in inset of figure 3.9. We concentrated again more on the reduced bias range between -0.1V and +0.1V due to the expected dimension of the gap of free-standing germanene. However, no band gap is observed: all I(V) curves match the corresponding ones measured on Al(111). The clear metallic behaviour is an indication of the strong electronic coupling between adlayer and substrate, which changes the reconstruction and prevents the formation of the small band gap expected in germanene.

A question remains open: how to explain the discrepancy with the varying behaviours observed for the monolayer, when no reference spectra could be acquired? In fact additional measurements performed with the same tip shows, similarly to figure 3.7, characteristics deviating from the ideal metallic one. Remarkably, the same non-metallic behaviour was observed on Al nearby. Two examples in a small range of energy around the Fermi level are shown in figure 3.10.

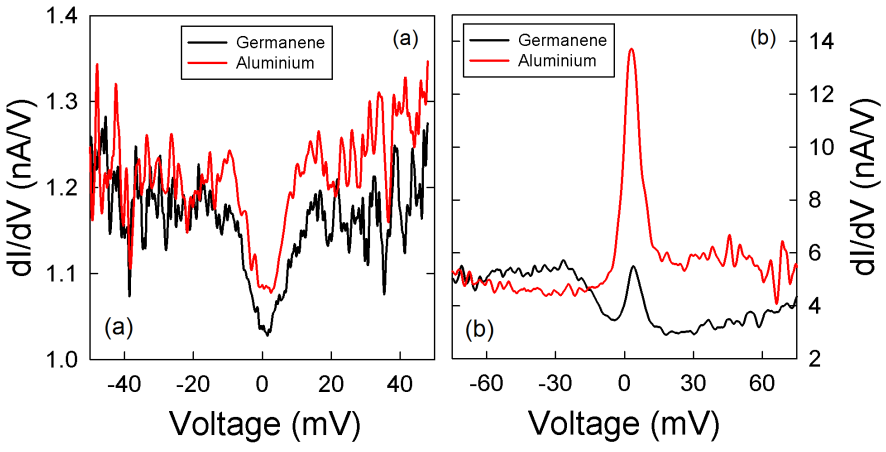

Figure 3.10: Two different example of dI/dV spectra measured on Al(111) and germanene of non-trivial interpretation. Both couple of spectra have been acquired at 5 K, (a) V = -0.5 V, I = 60 pA, (b) V = -0.1 V, 500 pA.

In figure 3.10(a) a dip in the density of states centered at the Fermi level can be seen on both spectra. On the other hand, figure 3.10(b) shows a strong peak, shifted by 3.5 mV above the Fermi level, on both Al(111) and germanene, even with a difference in intensity. Nor a dip nor a peak are expected for Al(111) surface, as we showed before, so we can rule out that these behaviours are to be ascribed to the germanene nanosheet. The responsible can be then found in the aging tip itself, which would produce the spectra visible in 3.7 and 3.10 via contamination as it probes the sample.

3.3 Tip-induced evolution of germanene islands

In section 1.3 we discussed about a remarkable tip-induced effect reported in literature: a state transition at room temperature between two ordered reconstructions of germanene on Al(111), the 2T characterized by two top atoms and an honeycomb contrast and the 1H with one top atom and a hexagonal contrast. During our run of measurements however we encountered more dramatic effects, despite low temperature.

A first family of events is represented in figure 3.11 : the detachment / destruction of the nanosheet during normal scanning conditions. Figure 3.11(a) shows the starting shape of the germanene island, which is atomically resolved in 3.11(b), confirming the presence of the typical 3×3 reconstruction. The profile height in the inset indicates again that we are dealing with a single layer. The difference between 3.11(a) and (c) is striking: part of the island has disappeared, and a large cluster on the right of the island is now present. Did the island turn into the cluster? At its place the bare Al surface is partially recovered, apart from some smaller clusters (see figure 3.11(d)) and a narrow crack which could be an indication that also some Al atoms were stripped during the process.

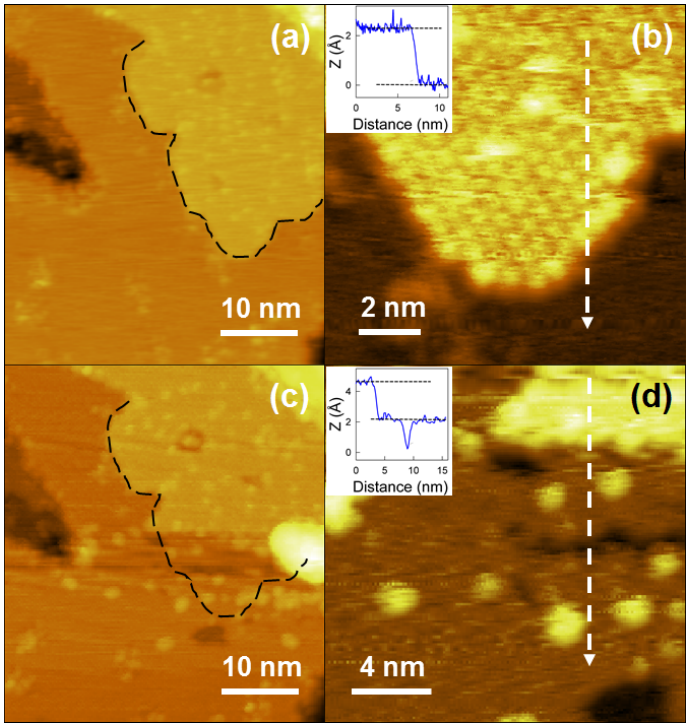

Figure 3.11: Initial STM topography of a germanene island. (b) Atomically resolved image of the lower edge of germanene island, showing the typical 3 x 3 structure. Inset: height profile across the germanene island along the dashed line. (c) STM topography of the island after its unintentional manipulation. (d) Zoom on the removed area, with height profile in the inset. All the images were acquired at 77 K, V = -1 V, I = 50 pA.

Another example of surface modification under scanning conditions is shown in figure 3.12. Topographic and current images are both shown for clarity. The starting situation is shown in figures 3.12(a) and 3.12(b). As it is often the case with STM, an adsorbate reduced suddenly the quality of the image. To get rid of it, an I(V) curve with closed feedback loop has been acquired in the top left part of the image. Unexpectedly, this resulted in the appearance of a germanene nanosheet in figure 3.12(c) and (d), with the usual 3×3 reconstruction. The microscope was left scanning without further intentional interaction, but the nanosheet rearrangement continued to evolve until an equilibrium position which is shown in figure 3.12(e) and (f). Between the starting I(V) curve and the stable rearranged area, 6 images were acquired, which corresponds roughly to 20 minutes. Due to the closed feedback loop, the tip approached the surface while the voltage was diminished, until zero was reached, to get farther away then with increasing voltage of the opposite sign. This means that there is a chance the tip went in a strong interactive regime with the surface, or even touched it, during the I(V) curve. Motivated by the absence of the terraces prior to the pulse, we can point at the STM tip as the responsible for the redeposition and displacement of the germanene adlayers. This has been a rare event during measurement, which we were not able to reproduce intentionally, but it emphasizes the fragility of the germanene adlayer and it is consistent with the weak adsorption energy of Ge atoms on Al(111) [88, 234].

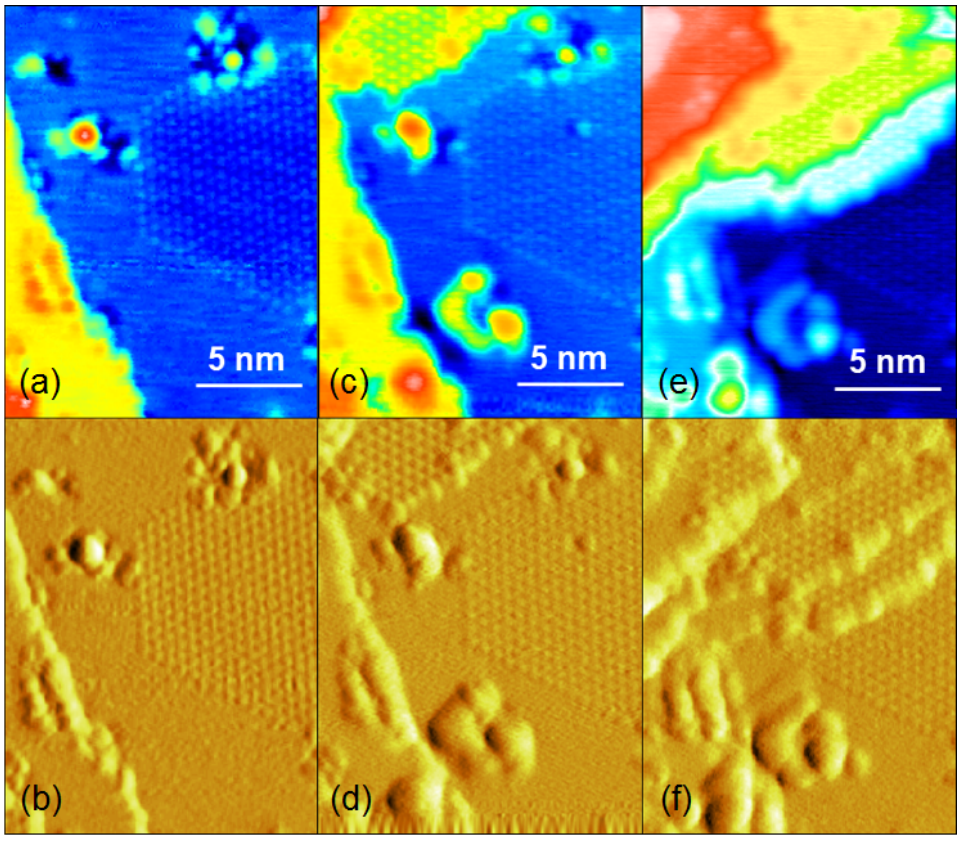

Figure 3.12: Sequence of STM images showing the real time appearance of germanene islands. (a) Initial configuration of a hexagonal germanene island, with the related current image (b). (c) and (d) Modified configuration. The new terrace is a monolayer germanene step as shown in (d). (e)-(f) Final equilibrium position, with a bilayer+monolayer. All the images have been acquired at 77 K, V = -1 V, I = 5 pA

The role of the tip in the mechanical instability of the Ge adlayer has an influence on its electronic properties. To further highlight the link, let us discuss what is shown in figure 3.13. Here we present a CITS of 256×256 pixels with a 64×64 STS grid. In topography we can clearly distinguish slices with a high density of glitches and regions with a lower level of noise. As for the spectroscopy, the analysis of spectra reveals the existence of two sets of dI/dV. The lower spectrum in 3.13(b) has a

peak at negative bias and an apparent band gap of 50 mV, which extends mostly in positive bias. The higher spectrum on the contrary has a similar peak but shifted nearer to the Fermi level. In this case the apparent gap is almost closed. If we study the positions of the two sets of spectra in the CITS grid (figure 3.13(c)) we realize a close correlation with the change of image quality. By plotting the intensity at the voltage relative to one of the peaks (for example at -20 mV of the lower spectrum), we reproduce exactly the two different regions of figure 3.13(a). Such a correlation is emphasized when a line of spectra is plotted along the dashed line indicated in the STM image (3.13(d)). There was not a dramatic modification of the surface while scanning in this case, but even so we assisted to a variation of the electronic characteristics between insulating and metallic behaviour. We point at the tip as the responsible of these variations, which will be discussed further in the next section.

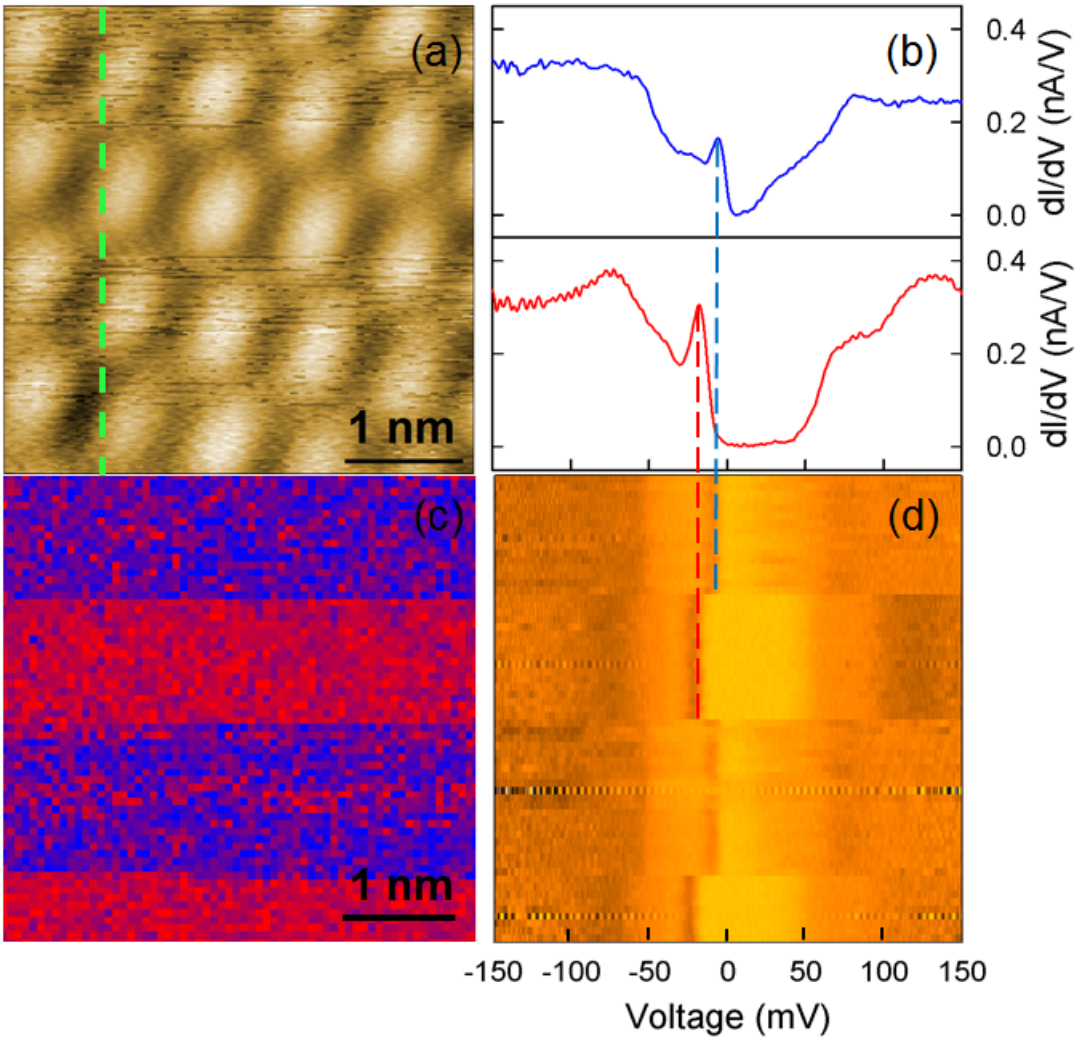

Figure 3.13: (a) Topography of a defect-free germanene area, V = -0.15 V, I = 50 pA, T = 5 K. (b) The two classes of spectra measured during the CITS. (c) Differential conductance map, measured at -20 mV, blue and red as in (b). (d) Strips view representation of the 64 spectra along the green line in (a).

3.4 Tip artefacts in spectroscopy of a 2D material

In figure 3.9 we demonstrated that a clean STM tip yields the same spectroscopic behaviour on bare Al(111) and on germanene nanosheets. The tunneling current is then dominated by the metallic band structure of the Al crystal close to the Fermi level, helped by the significant charge transfer which takes place between the Ge atoms of the adlayer and the surface [88, 97]. The reference of bare Al is crucial because the spectra deviate from a linear behaviour with continuous scanning of

the surface. The plethora of spectra shown in 3.7 and 3.10 then appears. Helped by the reference of the clean Al surface and by the understanding of dynamical phenomena, as those presented in 3.13, we suggest that these features are due to a non-constant density of states of the tip. As explained in section 2.3, this is a common artefact for STS but we want to stress that the probability of such an happening with germanene adlayers is quite high. In fact, while the adlayer seems strongly electronically influenced by the substrate, the mechanical stability of the layer is weaker. DFT simulations in literature [83, 88] indicate the absence of covalent bonding with Al(111). The bonding of Ge atoms with the jellium-like electronic distribution of Al(111) seems to be weak, and this could be promising for exfoliation of the layer on a semiconducting or insulating layer where the properties of the substrate will not hide those of the 2D material. However, we were not able to replicate the results of superlubric displacement of graphene nanosheet [235, 236] in a controlled manner. On the contrary, the manipulation of the surface has always produced dramatic transformation of the sheet, resulting in either clusterization (figure 3.12) or reshaping of the terraces (figure 3.13). The temporary formation of a second layer was also observed by Muzychenko and coworkers [237], which analyzed how the appearance of a germanene nanosheet above another layer led to the disappearance of an artificial resolution in STM images (similar to the artefacts reported in section 2.3). Differently from our measurement at low temperature, they reported the progressive disappearing of the second layer during successive scanning of the same area. This is in agreement with the difficulty to maintain Ge atoms in a plane, primary reason to look for a substrate for a deposition, and as also observed with high-resolution transmission electron microscopy where two-dimensional Ge clusters have been found to morph into stable three dimensional cluster [238].

We can then offer a tentative explanation of the different behaviours that were observed, basing the analysis on the possible likely terminations of the STM apex. The first candidate are obviously Ge clusters. Depending on the cause of adsorption, we can imagine bigger or smaller Ge structures. A small crystallite can account for the largest apparent band gaps observed in figure 3.7, consistent with the band gaps reported in literature for Ge nanocrystals [239]. The extra material compared to the monolayer is a possible source of these crystallites, or the phenomena as those reported in figure 3.12. Less dramatic events can also produce a lower amount of material, like just small clusters or a few atoms. In this case the wide range of Ge_n clusters which have been predicted can be invoked [240]. The HOMO-LUMO separation could account for the gap found in STS measurements [241, 242]. On the other hand, we can not be just incurable optimist by invoking order in chaos: amorphous Ge clusters could also self-assemble on the tip. The resulting structure might have a density of states relatively high in the vicinity of the Fermi level. In this case Efros and Shklovskii predicted the possibility of a band gap induced by the electron-electron repulsion. Their calculation [243] can explain the observation of spectra with a small apparent band gap.

Germanium is not the only element in the landscape: it could also interact with the tungsten forming the tip, or aluminium atoms of the surface. Just one tungsten atom would be needed to create a WGe_n with energy gap spanning the energies from 3 eV (WGe_3) to 1.5 eV (WGe_{17}) [244, 245]. Adsorbing Al atoms on the tip is more difficult to obtain, but we observed missing areas of Al during the dynamic manipulation of the surface (figure 3.11(d)). Also we can not rule out the presence of mixed Al-Ge clusters on the tip. This opens the possibility to other physical phenomena which could explain other spectral features. For example, the peak of figure 3.10(b) could be due to a Fano resonance, if the tunneling occurs through the energy level of the Al impurity resulting from interference effects [246]. The zoology of Al-rich clusters is wide. Depending on the number of Al atoms, it has been shown that some clusters become more stable with a magic number of Al and Ge atoms A. typical example is Al icosahedral clusters consisting of 13 atoms, whose stability increases by substituting an Al atom with a Ge atom [247, 248]. For this stoichiometry the resulting apparent band gap would be of ~ 1.3 eV. However, Al physics does not stop here: the presence of Ge in Al films was shown to enhance the superconductivity of the structure, above the critical temperature of Al [249, 250]. The

existence of superconducting clusters at the end of the tip could account for a vanishing DOS at the Fermi level or the observation of coherence peaks-like, similar to the spectra observed in figure 3.7(d).

Finally, we can address the glitches observed in figure 3.13. Examination of Ge clusters with transmission electron microscopy have revealed the transformation of the clusters under the electron beam [238]. These transformations can reach different equilibrium geometries or even lead to the fragmentation of the clusters with time, causing the appearance of different features in the tunnelling spectra, and even the aforementioned glitches.

Even if the necessity to consider all the possible artefacts due to the non-ideal tunnel junction is a consolidated notion in the STM community, we felt the need to stress it for the relatively young field of 2D materials, in particular those departing from the renowned stability of graphene. As justified by band-structure calculations of section 1.2, when decoupled by a substrate a typical V-shaped DOS vanishing at the Dirac point, signature of a Dirac cone, is usually measured with STS [251]. The key point is the electronic decoupling from the substrate, which can not yet be performed for silicene and germanene, and other group IV 2D materials. Even for graphene itself when a substrate is present an STS check of the tip DOS is fundamental: an example is provided by Zhang and coworkers in their analysis of the giant phonon-induced conductance of graphene flakes on SiO_2 [252]. In their case, the DOS of the tip was checked on a clean Au(111) surface before and after every graphene sample analysis (supporting material of [252]). Without calibration, V-shaped spectra were obtained. However, after calibration these spectra were never observed and instead the analysis of the inelastic tunneling was made possible.

So far only a few works have observed a differential conductance with a V-shape centred at the Fermi level for silicon and germanium 2D materials [61, 76, 78, 80]. Although the Dirac fermion nature of the charge carriers has still to be proved in these examples via magnetic field experiments, the majority of the experimental works has nonetheless reported tunnelling spectra that differ from the V-shape characteristic in the region of the Fermi level [54, 98, 253, 254, 255, 256, 257, 258, 259, 260]. This behaviour has been attributed to the strong electronic coupling between the silicene and germanene sheets with the host substrates. The extra attention we claim, necessary for STS of a 2D material, is justified also by a careful inspection of all the experimental spectra reported for the (4×4) phase of silicene grown on the Ag(111) surface, the most studied one next to graphene, which reveals significant deviations between the measured characteristics. For example, Ref. [253] and [254] show differential conductance curves consisting of two symmetric branches increasing with bias at both polarities, whereas the curves displayed in Ref. [255], [256] and [257] have a clear asymmetric shape. Moreover, the Fermi level is inconsistently positioned close to the negative branch [253, 255] or to the positive branch [256, 257]. Also, some spectra are featureless around the Fermi level [253, 254, 258], while others show many peaks [54, 256, 257, 259]. Similar variations have been found for germanene grown on Pt/Ge(110) islands [59, 61, 60]. Different reasons were invoked to explain these variations, among them, the temperature of the measurements and spatial fluctuations of the electronic coupling between the sheet and the underlying substrate. With our work we want to stress once more for future analysis how much the tip role is important for an atomically thin layer of atoms deposited on a (mostly metallic) substrate.

Chapter 4

Germanene edges on Al(111)

2D materials edges are of a scientific interest from a lot of points of view. The very high mobility of pristine graphene, 200.000 cm^2 $V^{-1}s^{-1}$ [21], and all the possible applications resulting from the non-trivial physics introduced in chapter 1, are hindered by the lack of a band-gap and the difficulty to scale the production of high-quality graphene on a large scale [261, 262]. Cutting graphene into nanoribbons (GNRs) resulted in an approach able to open a band-gap while maintaining the high-mobility [263, 264]. This has been made possible by the progress in bottom-up techniques which led to an atomically precise control over the final structures [265].

Based on their edge configurations, GNRs have been classified into three families: armchair GNR (AGNR), zig-zag GNR (ZNGR) and chiral GNR (CGNR), with a periodicity of the edge of 0.426 nm, 0.246 nm and a mixture of armchair and zig-zag. The properties of GNRs strongly depend on the edge types and the distance between edges.

ZGNR can be turned into half-metallic by applying an external field [266] or by chemical modification [267]. The zig-zag edge of GNR exhibits also a special edge state [268], which consists of a pair of flat bands approaching the Fermi level from both sides, strongly localized on the edge [269]. The zig-zag edges on one side and on the other of the GNR are ferromagnetic, but their coupling is antiferromagnetic: spin up electrons are localized at one zigzag edge and spin down at the other, and the magnetic moments are smaller in the ends than in the middle [270]. This is a promising property for spintronics because the currents of spin-up and spin-down can pass through the two antiferromagnetic couple edges independently.

On the other hand, AGNR properties depend strongly on the pattern of the edge: an AGNR is metallic if $N = 3M + 2$ and conducting if $N = 3M$ or $3M + 1$ (M is an integer and N indicates the width of the AGNR in the direction perpendicular to the edge)[271]. Three classes of aromatic patterns have been found for AGNRs and the band-gap is inversely proportional to the width. To obtain materials with band-gaps similar to Ge or InN (around 0.7 eV), the width of the ribbons must be between 2 and 3 nm. If larger bang gap ribbons are needed (like Si, 1.1 eV, or GaAs, 1.4 eV), their width must be reduced to 1-2 nm [272].

GNRs of different edge, width and termination belong to different electronic topological classes [273]. The engineering of a junction of GNRs with different topological invariant $\mathbb{Z}$ leads to an edge band structure which is determined purely by the coupling between adjacent topological interface states [274, 275].

Silicene [276, 277, 278] and germanene nanoribbons [279, 280, 281] have been predicted to have similar properties to GNRs. However, due to the constraints imposed by the limited number of available substrate for their synthesis, substrates which are all metallic, the edge properties certainly depend on the interaction of the ribbons with the underlying substrate. So far, little attention has been devoted to germanene edges in the Ge/Al(111) system [282]. In this chapter the experimental observations of the 1D interface between germanene nanosheets and Al(111) will be described, through STM and STS. These observations will be then interpreted through the comparison of DFT simulations of the interface and the structure of nanosheet and STM images.

4.1 STM/STS of germanene nanosheet edges on Al(111)

As shown in section 3.2, germanene nanosheets grow not on but in Al terraces. For both existing reconstructions, 3×3 and $\sqrt{7}\times\sqrt{7}$, the 1D interface with Al(111) appears in most cases as a straight line of top atoms. This tends to build nanosheet with a hexagonal shape (figure 4.1(a)). Following the established atomistic model for the 3×3 and $\sqrt{7}\times\sqrt{7}$ phases, this means that the preferential edge for 3×3 is in the zig-zag direction, which connects neighboring top atoms (figure 4.1(b)). This is the predominant edge observed for graphene islands grown by Chemical Vapor Deposition (CVD) on Cu foil [283]. The edge which joins first neighbors in $\sqrt{7}\times\sqrt{7}$ reconstruction is armchair (figure 4.1(c)). This is a similar behaviour to the graphene islands grown by CVD on a SiC(0001) [284]. However, it has to be remembered that the STM images provide an information only about the top atoms and none regarding the exact interface between the nanosheet and Al(111). Initially the interface will be supposed to be composed by full honeycombs as for graphene nanosheets.

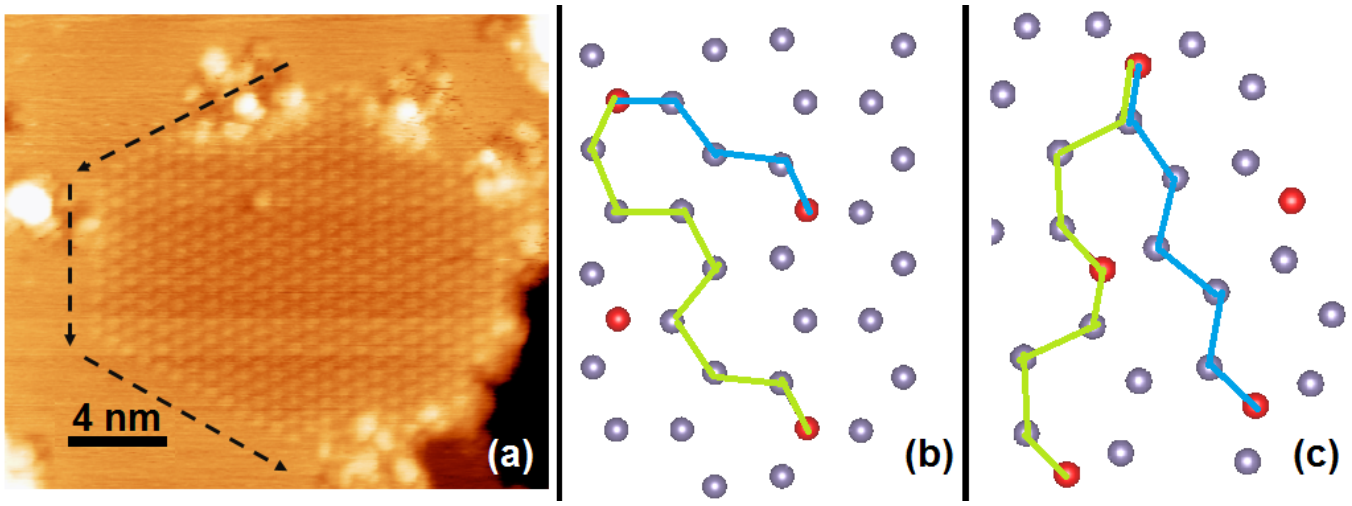

Figure 4.1: (a) Usual nanosheet with edges that follow first neighbor top atoms. (b-c) Zig-zag edge in blue and armchair in green for the 3×3 (b) and $\sqrt{7}\times\sqrt{7}$ (c) phases. Ge top atoms are indicated in red, Ge lower atoms in purple.

Differently from other published works, we did not observe a high concentration of domain borders inside $\sqrt{7}\times\sqrt{7}$ nanosheets due to the low amount of Ge deposited, which places us in the first fraction of growth.

For both 3×3 and $\sqrt{7}\times\sqrt{7}$ reconstructions the relative contrast of top atoms which are placed on the edges is higher than the one measured on the center of the islands. With freshly prepared tips a maximum height difference of 0.5Å was measured (figure 4.2). However, a marked difference exists between both phases. An additional configuration for the edge atoms of 3×3 phase is present on the surface, in which the edge atoms are nearer ($\sim$7.5Å, instead of 8.57Å) and form an angle of $\sim$ 145° instead of 180° with the internal top atoms network. This configuration is characterized by a much stronger contrast, typically more than 1Å.(figure 4.3).

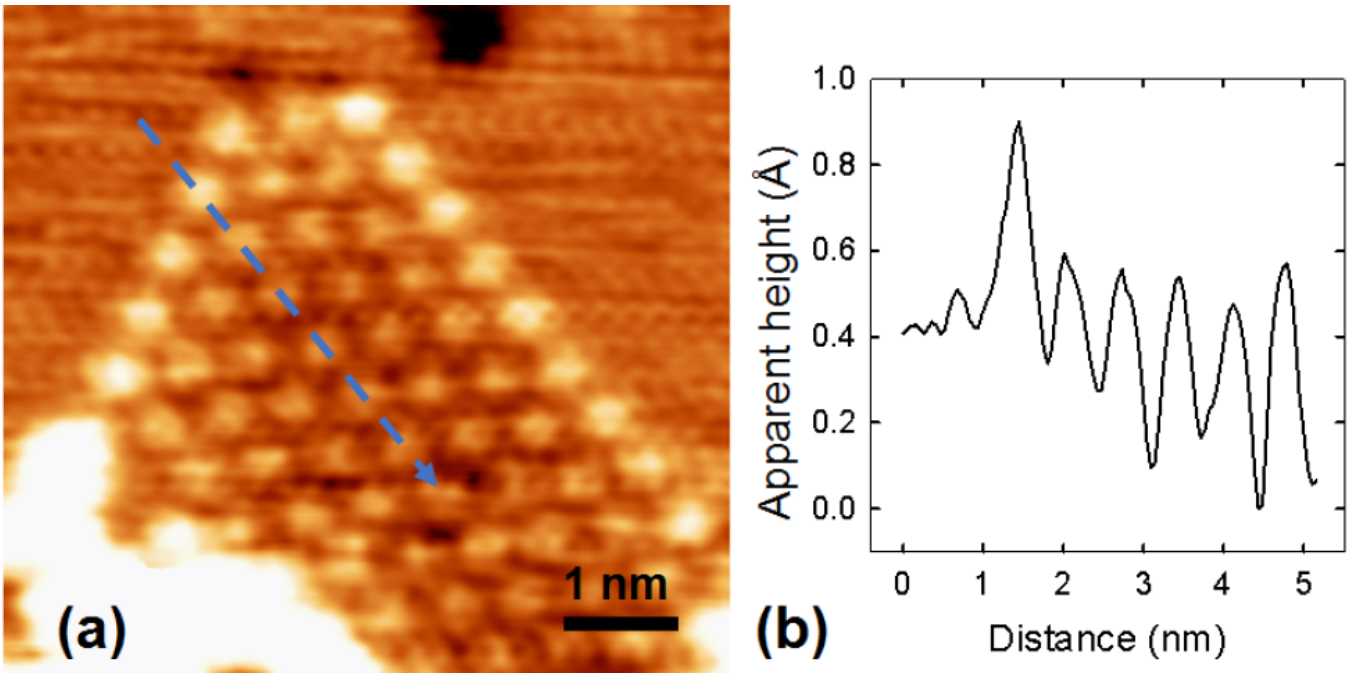

Figure 4.2: (a) $\sqrt{7} \times \sqrt{7}$ nanosheet of germanene, V=-1V, I=50pA. (b) Height profile along the direction of blue arrow in (a).

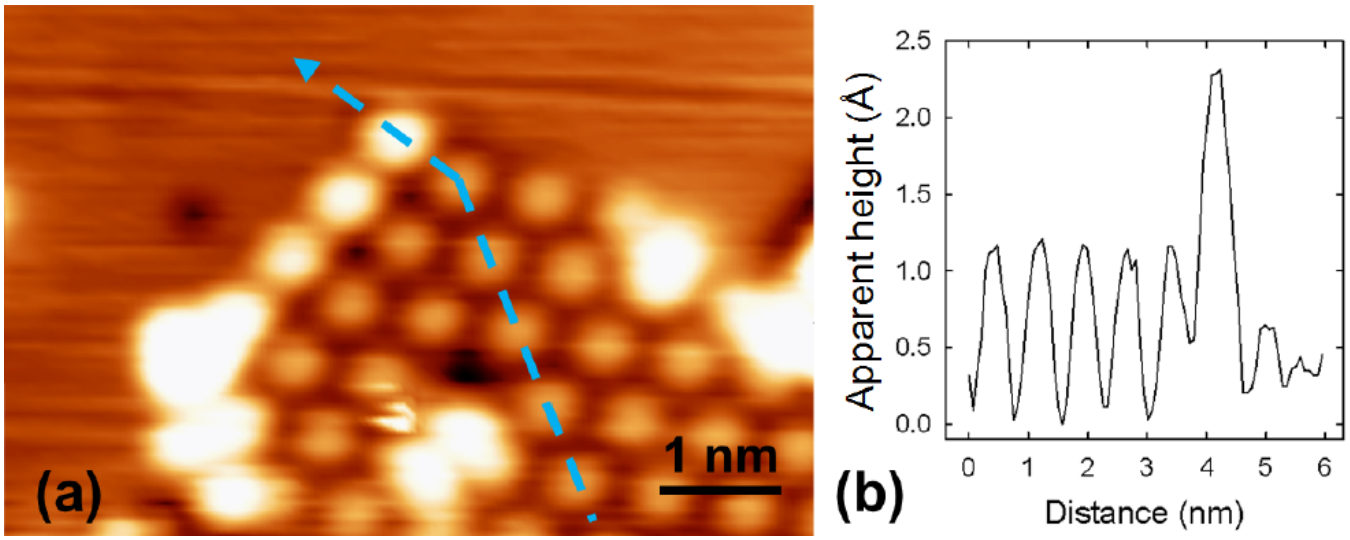

Figure 4.3: (a) 3×3 nanosheet with shiny shifted edge, V=-1.5V, I=50pA. (b) Height profile along the direction of blue arrow in (a).

The $\sqrt{7} \times \sqrt{7}$ 180° configurations is stable at 77K and 5K under all scanning conditions. In contrast, a transition between 180° and 145° configurations for 3×3 reconstruction was detected while scanning, with a higher frequency of switch at a lower scanning voltage. Figure 4.4(a-j) shows a series of subsequent images acquired at V=-0.1V and I=10pA. Every image was acquired at scan speed of 1.5 Hz per line, for a total of 40 minutes of acquisition. Figure 4.4(a) shows the initial 180° edge (scanning from bottom to top). In figure 4.4(b) a 145° edge atom is present but disappears while scanning (from top to bottom). While no 145° atom is observed in (c), multiple instabilities are observed in (d), to finally obtain a fully formed 145° edge in (e). Another transition is observed in (f) for one of the two atoms, which is recovered in (g). The edge has stabilized in (h).

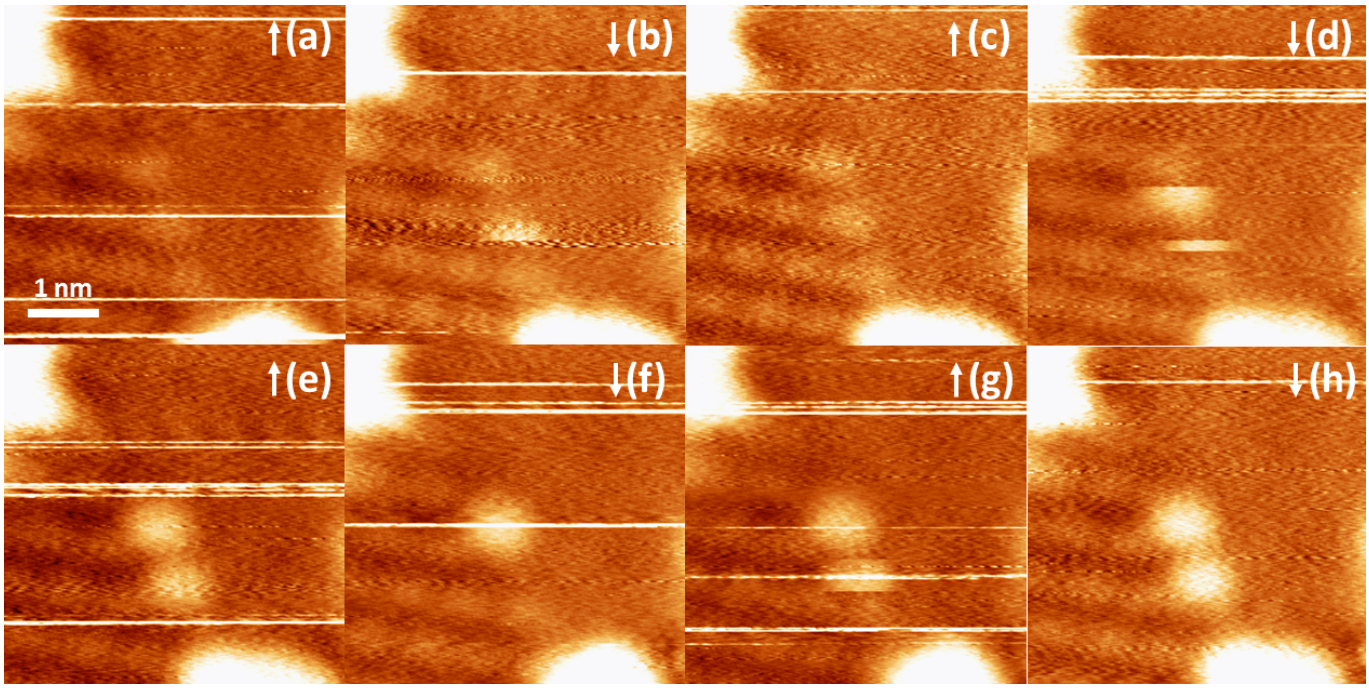

Figure 4.4: Subsequently acquired STM images of a 3 × 3 edge, T=5K, V=-0.1V, I=10pA. The direction of scanning (upward/downward) is indicated by the arrow.

Due to the working principle of STM, the possible origin of the difference in contrast is unclear. Possible candidates are:

- A physical difference in height of the edge atoms compared to Al(111) atoms and the rest of germanene nanosheet;
- A difference in integrated local density of states (LDOS) between the chosen voltage for the image and Fermi level at the edge;
- A difference in chemical identity at the edge;

The LDOS hypothesis would also provide a tentative explanation of the transition in figure 4.4, via a switch in the electronic states probed in the band structure of the material. This hypothesis can be tested by repeated imaging at different scanning conditions, or in an equivalent manner by performing STS at the edge and the internal part of the nanosheet. As figure 4.5 shows for negative voltages, the contrast is not voltage-dependent down to -20 mV. A more extended analysis in figure 4.6 shows that while the edge contrast is not affected by the voltage, this cannot be said for the germanene nanosheet itself, whose relative height compared to Al(111) diminishes for high positive voltages ($>$ +1.2V). The disappearance of top atoms is not due to a tip degradation, because successive imaging at high negative voltages (-2V) provides the same topography as figure 4.6(a). We were not however able to discriminate this difference via STS at higher voltages compared to figure 3.10, where the comparison between the I(V) curves of the germanene nanosheet and the Al(111) surface was shown.

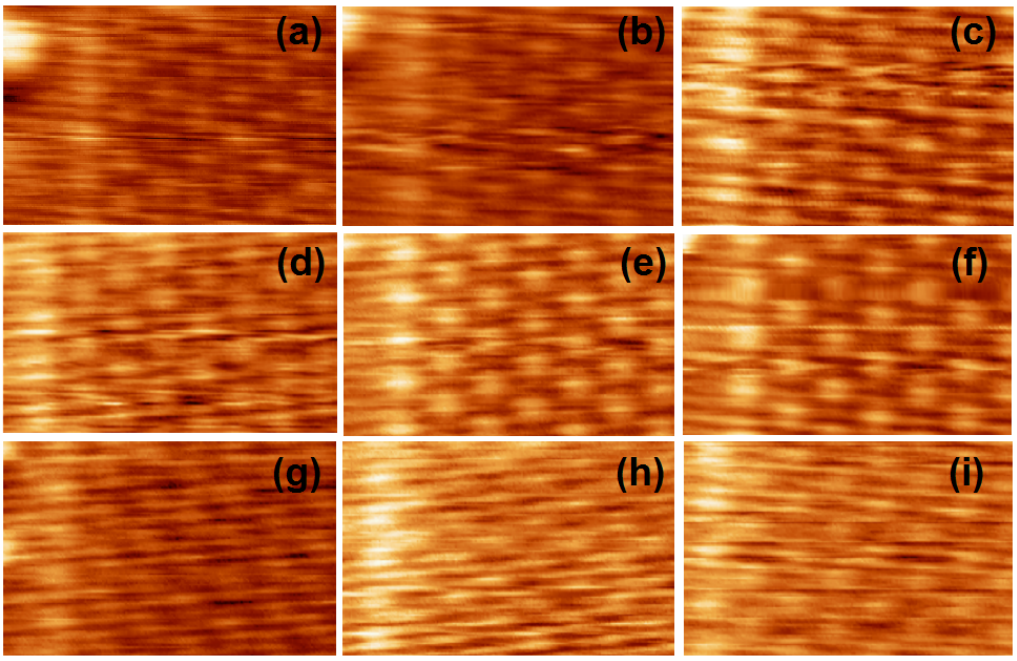

Figure 4.5: Voltage-dependent STM images of 3×3 nanosheet edge at 77K. I=10pA. (a) -1.5V, (b) -1.3V, (c) -1.1V, (d) -1V, (e) -0.5, (f) -0.1V, (g) -0.05, (h) -0.03, (i) -0.02V.

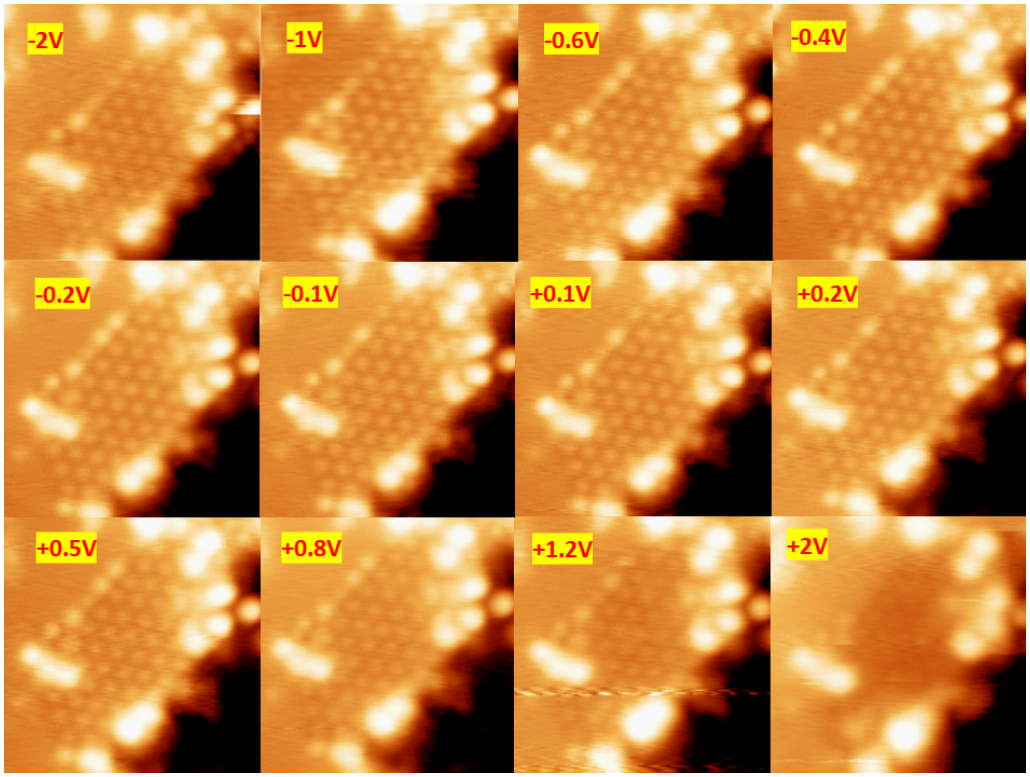

Figure 4.6: Voltage-dependent STM images of 3×3 nanosheet at 5K. I=10pA.

The explanation turns then towards a possible chemical or structural origin of the contrast, which will be analyzed via DFT. The idea is that, due to a edge reconstruction, edge atoms are placed in an uplifted/shifted position or intermixed, with no variation (or slight one) of the local density of states. The reconstructed edge allows a transition between 145° and 180° configurations for the 3×3 reconstruction only.

4.2 Theoretical investigation of the Ge/Al(111) interface

4.2.1 Crystal structure from STM measurements

STM imaging is not the best tool to probe the crystal structure of a surface and cannot give a conclusive answer on its own. However, high current/low voltage images can test the relative contrast of the underlying layer of germanene on Al(111) to a certain extent. The STM image presented in Fig. 4.7(a) has been acquired at T=5K, V=-0.1V and I=1nA. Let's consider the 3 triangles highlighted in this figure. In the first on the left, there is one area of darker contrast, or what we would call a hole. In the adjacent triangle three holes are visible. They form a clover. In the last triangle, it is again one hole. Observing the holes while the atoms are not individually resolved is useful, as it happens for graphene. This observation is reproduced by the DFT model, as shown Fig. 4.7(b), and it is a peculiarity of an honeycomb layer with top atoms at that position. A similar analysis was reported by Muzychenko et al. [237]. While this narrows the models to be analyzed to just honeycomb lattices, it does not tell anything about the ratio between Al and Ge atoms in the underlying layer, and gives even less information about the nature of the first substrate layer, either a full Al layer or a Ge/Al alloy (as suggested by Fang [95]).

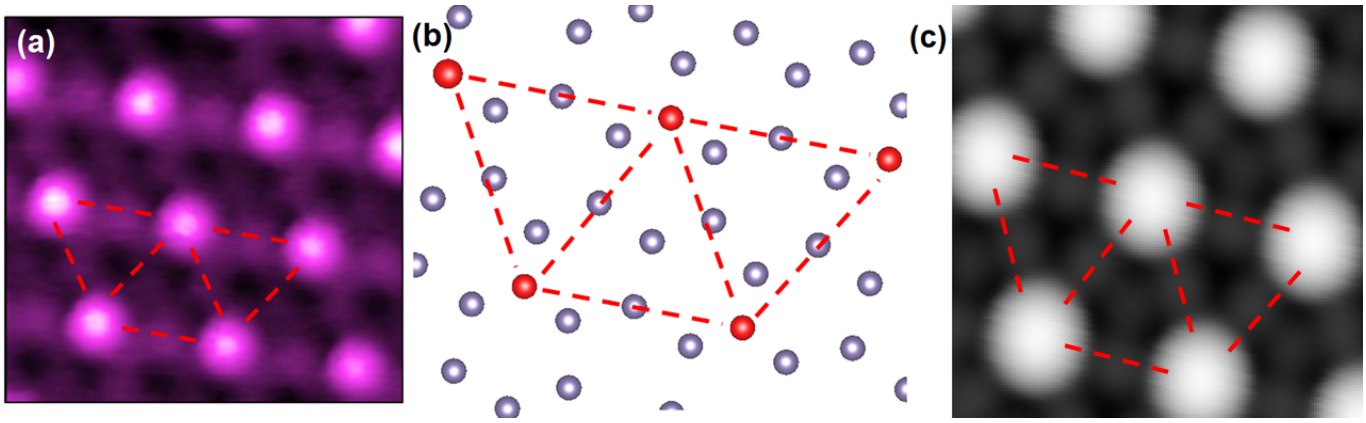

Figure 4.7: (a) STM image of a 3×3 germanene nanosheet, V=-0.1V, I=1nA. (b) Alternance of contrast in triangles explained via atomistic model. (c) Simulated STM image from the model in (b), V=-0.1V, distance between the tip and the central top Ge atoms of 3Å.

4.2.2 Comparison of the growth mechanism of silicene and germanene

To explain the observed structure, a few models have been proposed which take into account the possible Al/Ge intermixing, as discussed in section 1.3.1, and there is no conclusive argument to distinguish between them.

In this study it is interesting to know what happens for silicene, the Si analogue of graphene. The most studied substrate for silicene is Ag(111) [285]. The steps of its growth are reported in figure 4.8. In the first step adsorbed Si atoms tend to create faceting of the terraces towards ⟨110⟩ orientation (Figure 4.8(a)). When the edges are saturated of Si, island growth starts at the center of the terraces (Figure 4.8(b)). At first, these islands are not arranged in a crystal structure (Figure 4.8(b-c)). When their area is sufficiently large, the silicene structure starts to be observed (Figure 4.8(d)). In this process, Si atoms substitute Ag atoms, which recreate new terraces elsewhere (Figure 4.8(e-f)). The 2D layer growth keep on these new terraces also. It stops after the faceting of the new terraces steps is over.

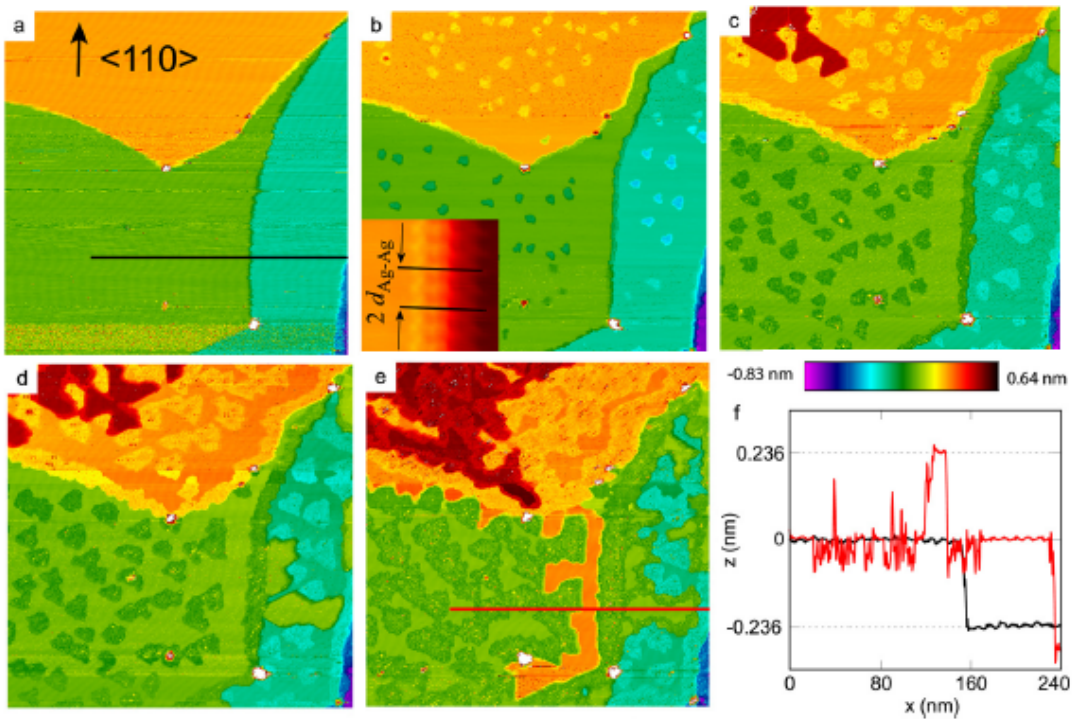

Figure 4.8: Silicene phases of growth on Ag(111). First faceting occurs, in (a), then small islands are formed in center terrace, before with no crystal ordering. Finally we see new terraces of Ag, as in (e), where faceting also occurs. Reproduced from [285]

Silver does not then play a passive role in the stabilization of the silicene layer. It is actually a very dynamic process. Due to the similitudes between silicene and germanene in the interaction with the respective metallic substrates, it can be expected a similar behaviour for germanene on aluminium. The Si/Ag(111) system has already been studied via DFT [286, 287], showing how a Si adatom prefer to insert in the first Ag layer. This system is then used as a reference system to validate the following calculations. These calculations are here reproduced in the form reported by Satta, M. et al. [287]. The two cells in figure 4.9 are compared. The slab is composed by 1 Si atom and 4 layers of 9 Ag atoms, with a cell dimension of 8.66 × 8.66 × 28 Å. A 3×3×1 Monkhorst-Pack grid is used to sample Brillouin zone, and a plane wave energy cut-off of 300 eV. The result for a 3 ×3 Ag cell shows that the substitution of an Ag atom by a Si atom is 0.558 eV more favorable than the adsorption of a Si adatom, in agreement with literature.

Let's focus now on Ge on Al(111). The total energy as a function of the lattice parameter (or the volume) is minimized for an Al(111) cell to ensure that the following analysis is not affected by a remaining internal stress. This follows the Murnaghan equation [288]. This minimization leads for a 3 × 3 Al cell to a lattice parameter of 8.5753 Å. This value compares well with the experimental parameter of 8.58 Å reported in literature [289]. A 4 × 3 cell will need to be longer of 2.8584 Å in the (100) direction in order not to introduce a stress to the surface. A 5 × 3 cell will be 2.8584 × 2 = 5.7168 Å longer, and so on in a similar manner for the other scaling of the Al(111) cell that will be presented. A Ge atom on a 3 ×3 Al(111) cell, with the same parameters as for Si/Ag(111), gives the opposite result to silicon: the Ge adatom configuration is preferred by 0.8 eV. We tested also a 9×9 Al(111) cell to avoid possible image interactions between Ge adatoms of periodic cells: the Ge adatom is still the best configuration, by 0.67 eV. For the 9×9 cell two Ge adatoms are compared to two Ge substitutional atom in a dimer: the result is that Ge adatoms have a 1.3 eV lower energy. This is a clear indication that Ge does not substitute Al in a bulk configuration, in contrast to the growth of its Si counterpart.

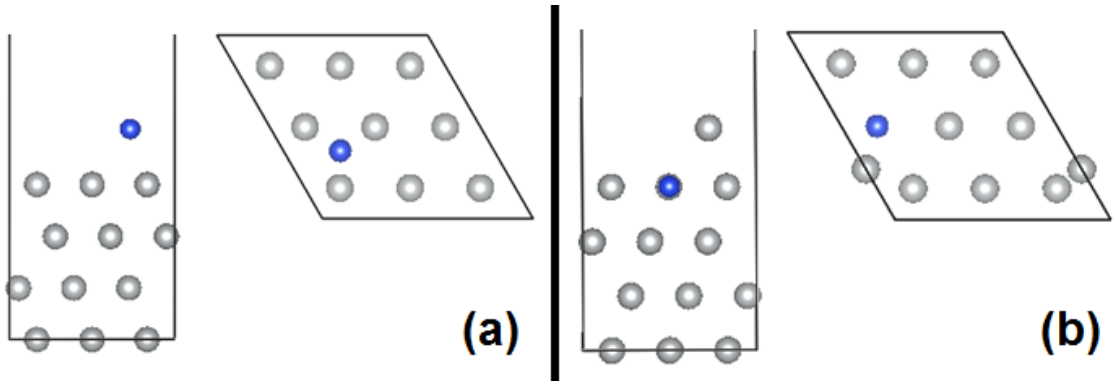

Figure 4.9: Side [010] and top [001] views of (a) Si adatom (blue ball) and (b) Si adsorbed atom on Ag(111) (grey spheres). In the [001] view only the top Ag layer is shown. The bottom Ag layer is fixed.

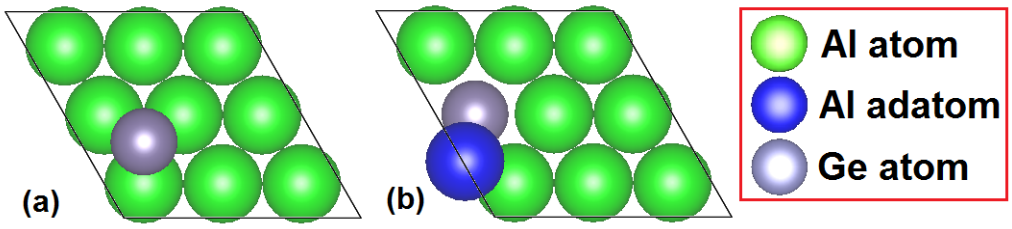

Figure 4.10: Ge growth on Al: (a) Ge adatom, (b) Ge substitutional atom. View from [001], only the top Al layer is shown.

4.2.3 Adsorption of Ge on Al(111)

In agreement with the results of the previous section, numerous clusters are present on the terraces, at the initial stage of the growth. Some examples are shown in Figure 4.11. The samples prepared with a very low amount of deposited Ge atoms have shown that these clusters are the first to grow. However, this does not seem to be the seed for future nanosheets, because a germanene nanosheet was never observed at the center of a terrace isolated from the step. On the contrary, all the nanosheets seem to have grown starting from Al terraces step.

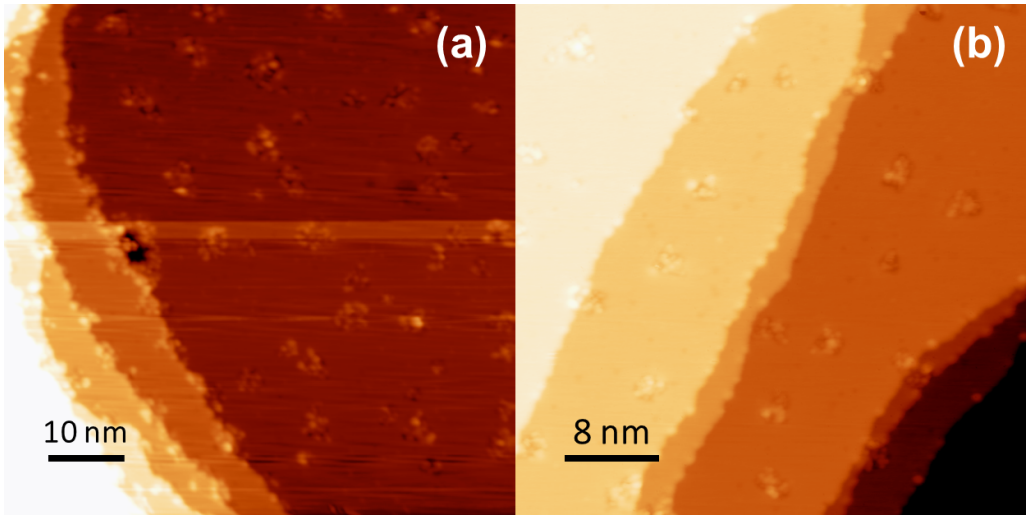

Figure 4.11: STM images showing the Al(111) surface modification initiated by a low amount of deposited Ge atoms. (a) V=-1.5V, I=50pA. (b) V=-2V, I=50pA.

A more realistic situation is then considered, to find the lowest energy configuration for a Ge atom in presence of an Al terrace. A cell with one Ge atom and 4.5 layers of 108 Al atoms each is used, with a cell size of 34.3012 x 25.7259 x 28 Å. Figure 4.12 shows a summary of the possible configurations analyzed. The lower energy is found when the Ge atom is next to the Al terrace, on the step below. When the Ge atom is above the step or on in the middle of a terrace, the configuration is 0.38 and 0.46 eV higher in energy. The reason for this preference could be the higher number of saturated chemical bonds. In figure 4.13 the charge density isosurfaces are shown for a Ge atom next to the terrace step and right above it. The charge density isosurfaces have 4 protrusions for the atom next to the terrace (4.13(a-c)), indicating 4 weak bonds with Al atoms, while only 3 are present when the Ge atom is above the step (4.13(d-f)). A few substitutional configurations have also been tested. When a Ge atom is absorbed in the step and the expelled Al is placed above the step, the configuration naturally evolves in the most stable one one, with Ge next to the terrace. The configuration where the Al atom is placed far away on the terrace has a substantially higher energy (+1 eV). The configuration with Al next to the substitutional Ge on the lower terrace has a moderate higher energy (+0.4 eV), due to its interaction with Ge.

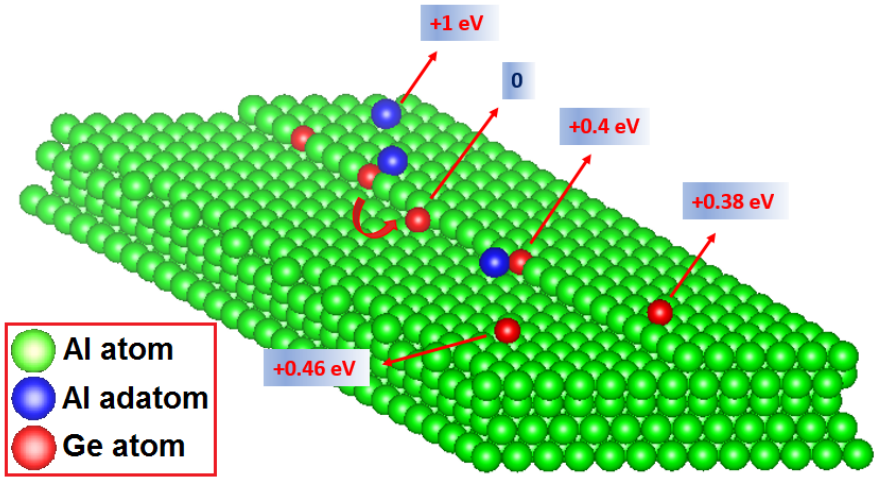

Figure 4.12: Sketch to summarize the different studied configurations of Ge atoms on top of an aluminium terrace. The energy of each configuration is indicated.

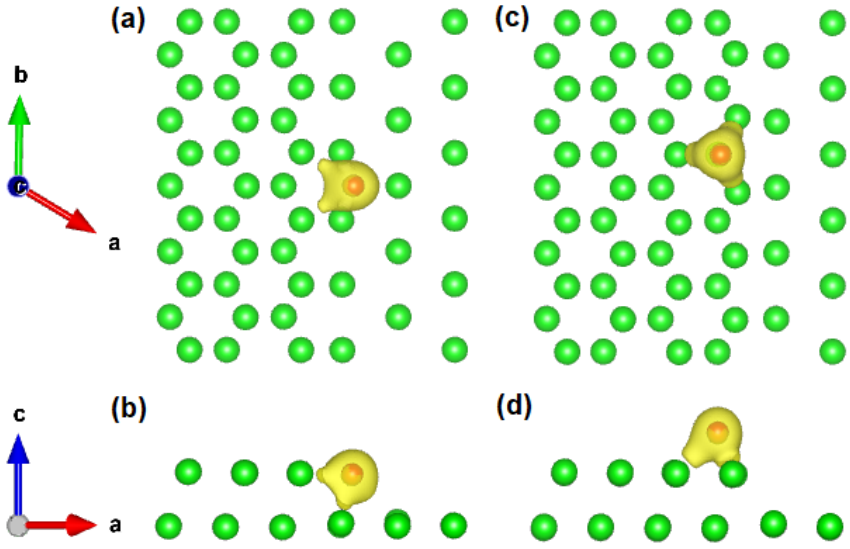

Figure 4.13: Charge density isosurfaces at 0.23 eV/Å^3 for Ge next to the terrace (a-b) and above the step (c-d). Only the two top Al layers are shown. Views from [100] and [010].

To ensure that even in presence of a terrace the Ge atom does not prefer to expel an Al atom, Molecular Dynamics was performed. A Nose Hoover Thermostat (NVT) was used, with 190eV energy cut, steps of 1fs and different virtual temperatures between 150 and 350 K. Al terraces become disordered for the finite temperature but in the first 500fs the Ge atom does not insert.

A second Ge atom was also tested, with different positions around the first one, outside or inside the terrace, and the best position is found to be next to the terrace and to the first atom, with a gain of 0.23 eV compared to the other positions. The third atom continues the straight line next to the terrace.

A last hypothesis to test the possible insertion of Ge atom is the dimer as a diffusion unit (Figure 4.14). A configuration with 2 atoms of Ge inserted in the terrace step, with 2 Al expelled, is tested. A first comparison can be made between the charge density of the dimer and of 2 adatoms (Figure 4.15). It can be seen that while the adatoms interact strongly between each other (Figure 4.15(a)), in the case of the dimer these interactions seem more directed towards neighboring Al (Figure 4.15(b)). The direct comparison of the two configurations however is made difficult by relaxation of the configuration in Figure 4.14(b) into a less stable configuration compared to (a) in which Al atoms seem to be "pushing out" Ge atoms from the terrace. However, static DFT does not bring to Ge expulsion before reaching the energy requirements. Molecular dynamics is then performed. The result is shown in Figure 4.16(a). One Ge atom and one Al atom, originally in the terrace, have been expelled in the first 1.5 ps of dynamics. To test if the second Ge atom was not expelled because the original top Al were too close, a similar dynamic is studied, for a configuration where Al atoms are not placed as first neighbors. This configuration leads to Figure 4.16(b): again one Ge atom and one Al atom have been expelled from the terrace, in this case within a longer timeframe of 3 ps before the process is complete. While the initial formation of the dimer seems to be energetically unfavorable, its evolution could bring to a mixed layer of Al and Ge.

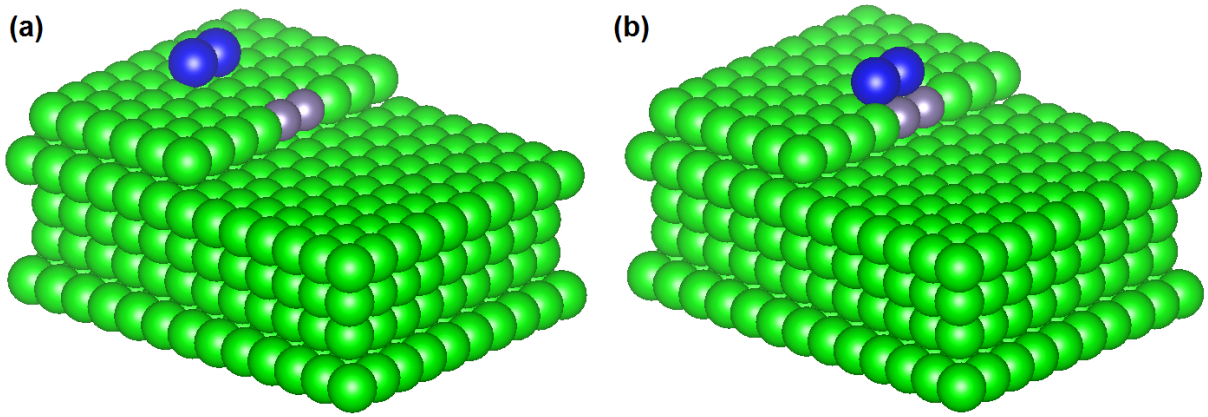

Figure 4.14: Cells to test dimer hypothesis.

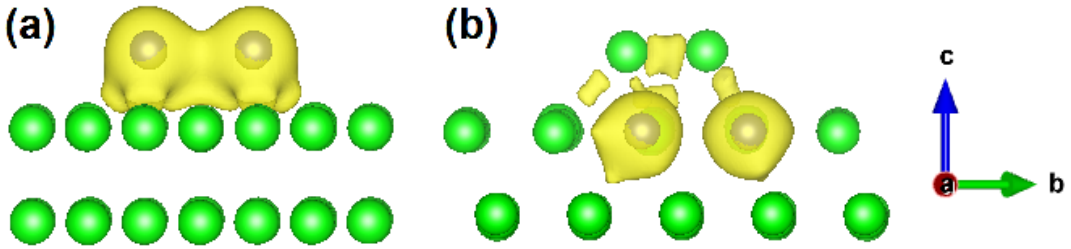

Figure 4.15: Comparison between charge density at 0.23 eV/Å^3 of (a) 2 Ge adatoms and (b) 2 Ge atoms in dimer into Al terrace. Only the two top Al layers are shown. View from [100].

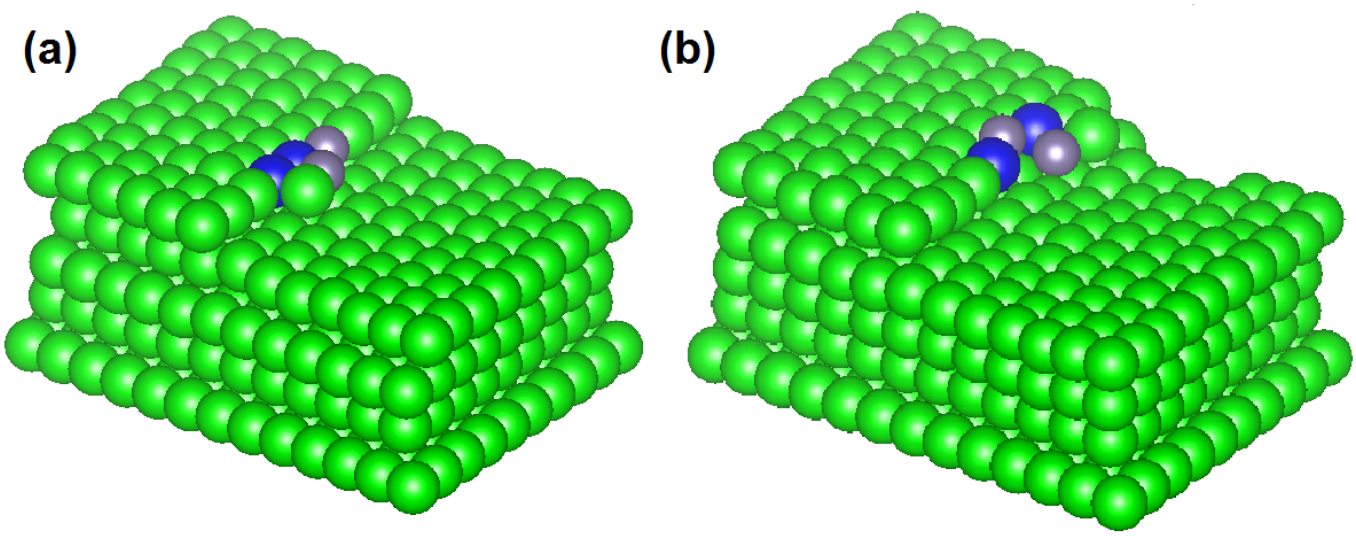

Figure 4.16: Resulting configuration of the terrace structure (just first layer) after MD for 1.5 ps (a) and 3 ps (b) on two different b configurations.

In conclusion, while some Al/Ge intermixing could take place in the germanene nanosheet, the most suitable position where this could happen is near the interface with Al(111) where the dynamic growth process started or ended.

4.3 3 × 3 germanene nanosheet on Al(111): full Ge structure

In order to reproduce the experimental observations of section 4.1, we start the analysis of the germanene nanosheets on Al(111) by using the simplest atomistic model, which involves a structure of the nanosheet composed of only Ge atoms and terminated on the edge by a full honeycomb. This structure will be then adapted in the following sections to reproduce in a finer way the experiments. The first feature to be analyzed is the difference in contrast between the edge top atoms and the center of the nanosheet.

4.3.1 Simulated STM contrast of the nanosheet edge

The first cell to be simulated has the following dimensions: 57.1687 × 8.57534 × 22.21886 Å. It contains two Al(111) layers of 60 Al atoms each, one whose positions are fixed and one allowed to relax. As a third layer a germanene nanosheet containing 36 Ge atoms (4 top), surrounded by two stripes of Al(111) surface to fill the left space in this layer (24 atoms). A 2×5×2 Monkhorst-Pack grid is used to sample the Brillouin zone, Davison algorithm is used for ionic relaxation with a plane wave energy cutoff of 210.3 eV. These parameters will be used for the following calculations of similar germanene cells, unless when differently stated. Preliminary calculations showed that a larger cell along the [010] direction avoiding a forced periodicity on the edge provided the same results for the 3× phase.

The starting Al interlayer distance is 2.40Å, and Ge buckling is set 1.48Å above the adjacent Al(111) surface (which can be more easily used as reference in STM). After relaxation, the Al interlayer distance is 2.32Å, and Ge buckling increases to 1.73Å. The ionic relaxation did not lead to a substantial variation in the structure, in particular the positions of the top atoms on the edge are not higher than the central top atoms.

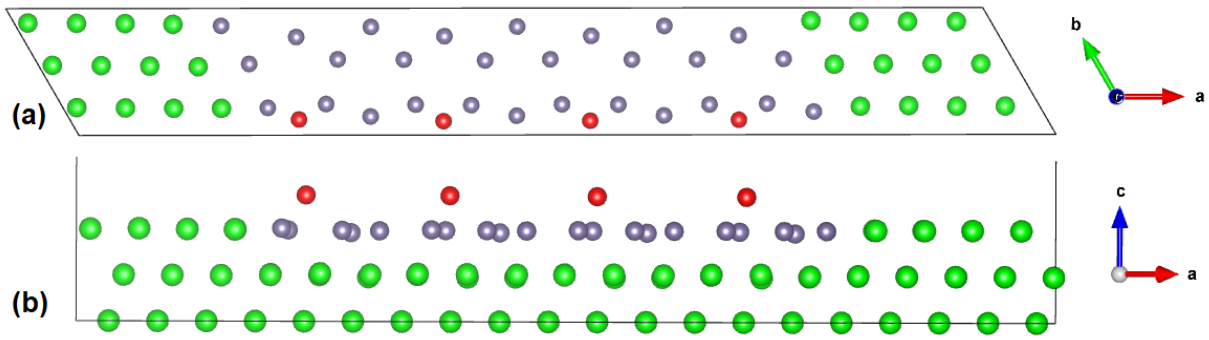

Figure 4.17: Relaxed full-Ge germanene nanosheet on Al(111) cell. (a) [001] and (b) [010] views. In the [001] view, only the top Al layer containing the germanene nanosheet is shown.

In addition to the interaction between germanene nanosheet and the Al(111) plane below, the interaction between Ge and Al on the edge is also important to be analyzed. Figure 4.18 displays a charge density map of the system, viewed from the (100), (010) and (001) faces. It appears that the charge is mainly concentrated around and between the Ge atoms, confirming their covalent bonding. The charge however forms some protrusions towards the interface between the germanene layer and the Al(111). These protrusions extend more toward the substrate than the lateral Al (matching with literature [88]). We can see from figure 4.18(c) that the presence of the edge perturbs the charge between some Ge atoms (red circles), diminishing the charge density in this region compared to the center of the nanosheet. In figure 4.19 the evolution of charge density slices in the (100) direction can be observed, starting from the first Al(111) line until the first top atom on the left edge, where the charge protrusions are more pronounced. The transition between the charge density of Al and that of Ge appears to be abrupt enough to indicate the absence of a strong covalent bonding.

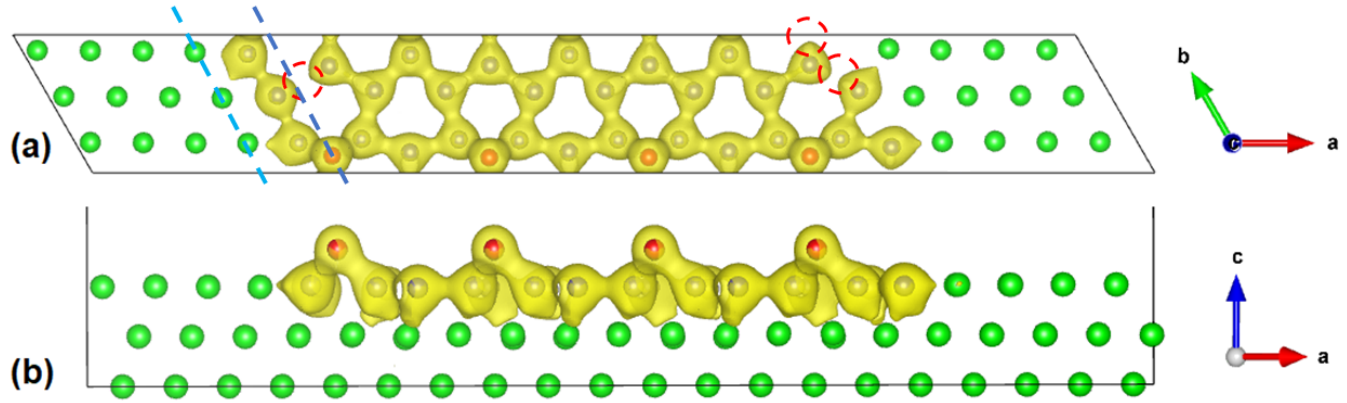

Figure 4.18: Charge density isosurfaces at 0.23 eV/Å^3, (a) [001] and (b) [010] views. In the [001] view, only the top Al layer containing the germanene nanosheet is shown. The red circles show lower density region induced by the presence of the germanene/Al(111) interface. The light blue and dark blue dashed lines in (a) represent the initial and final plane for Figure 4.19.

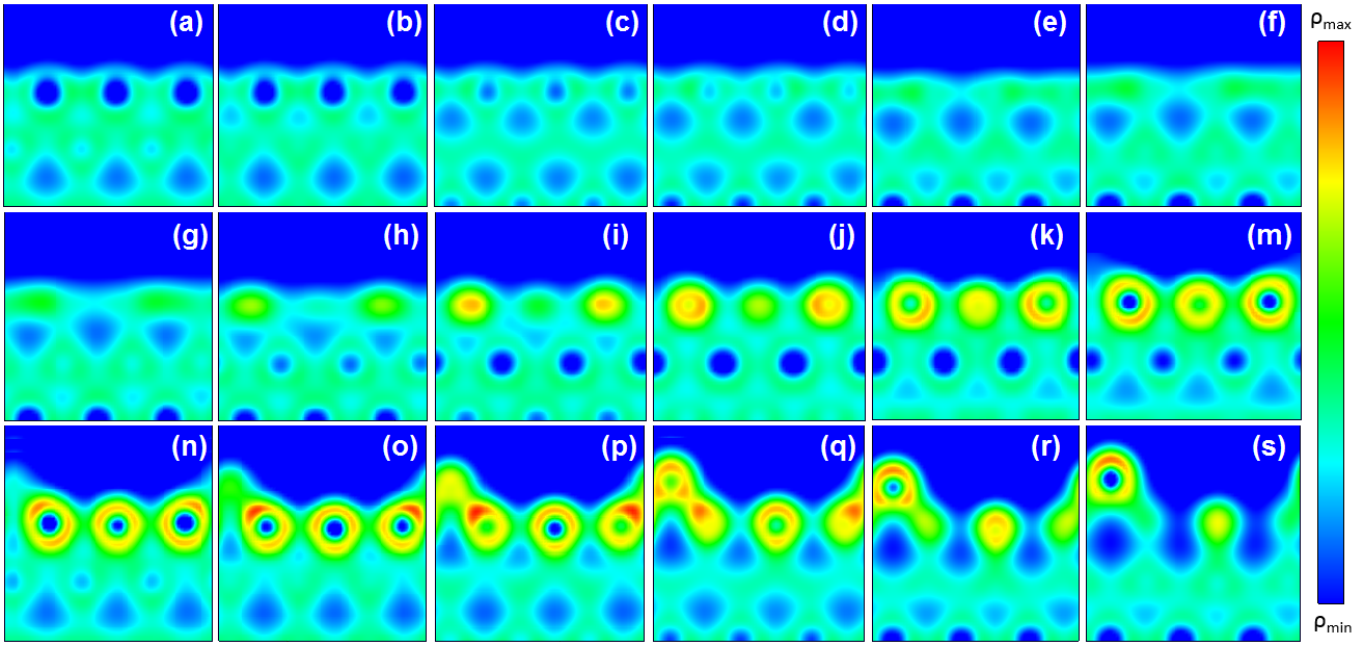

Figure 4.19: 2D charge density slices from first Al row next to the edge (light blue dashed line in Figure 4.18(c) to first top Ge atom (dark blue dashed line in Figure 4.18(c), covering $\sim$ 4.16Å from (a) to (s), $\sim$ 0.245Å at each step.

The bonding nature of Ge/Al interface does not seem to provide an indication for the origin of the difference in contrast observed in experimental STM images. We proceed then to simulate a pseudo-STM image of the cell, as detailed in section 2.7.8. The result in figure 4.20 does not show any difference in contrast on the edge, on both sides. The simulated apparent height of the Ge top atoms is $\sim$ 1.8Å, as the physical buckling. We study the dependence of the pseudo-STM image as function of the applied voltage (figure 4.21). Experimental Al(111) STM images are usually voltage-independent and the surface can be used as a reference for z values. Due to how the z mapping of the pseudo-STM images is performed, a plane subtraction on the Al(111) can not be performed. This produces as a result the false impression that the height of the Al(111) varies, while the variation occurs in the relative integrated DOS between germanene and Al(111). For negative voltages the dependence does not show particular features from -2V to -0.25V; at opposite bias, the contrast between Al(111) and the germanene nanosheet becomes stronger. To compare with experimental

observations the contrast can be quantitatively expressed through the relative electronic contrast of the top Ge atoms compared to the Al(111) surface in Figure 4.22(a). Due to the apparent lowering of germanene nanosheet compared to Al(111), the electronic contrast diminishes for positive voltages. When we observe a few selected profiles, we can see that from -2V to +0.75 (black to red curve in Figure 4.22(b)) the germanene nanosheet goes down and the buckling is 1Å, to partially recover at +2V, influencing also the apparent height of the top Ge atoms which comes back to 1.4Å. This reproduces the trend observed in figure 4.6 for positive voltages. In simulated images, the top atoms never disappear. It has to be remembered that the resolution here attained through the calculations is very high compared to a real-life STM tip.

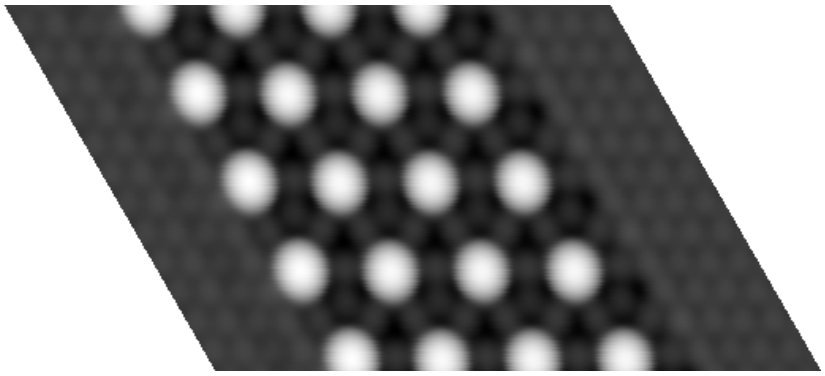

Figure 4.20: Simulated pseudo-STM image of a a cell containing the germanene nanosheet. The cell is 4 times longer on [010] to show an extended edge. V=-1.5V.

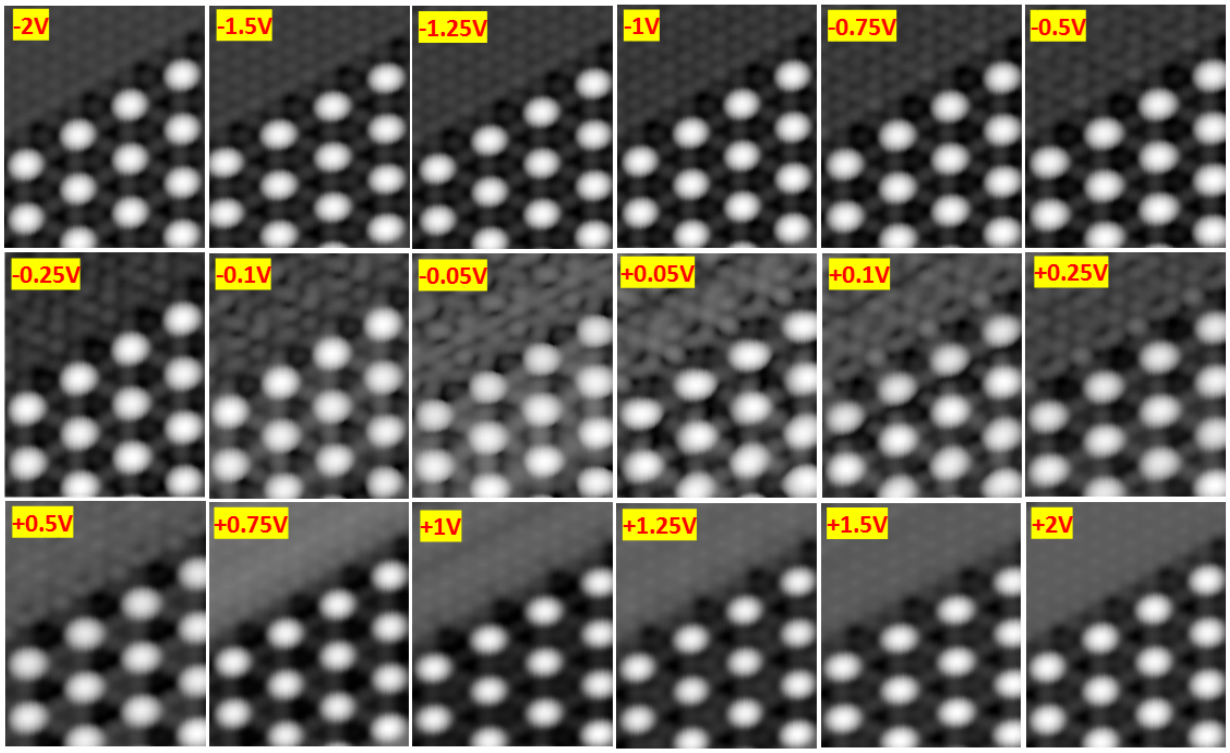

Figure 4.21: Simulated voltage dependent pseudo-STM images of germanene/Al(111) interface STM images. Every image is cut to show just the edge.

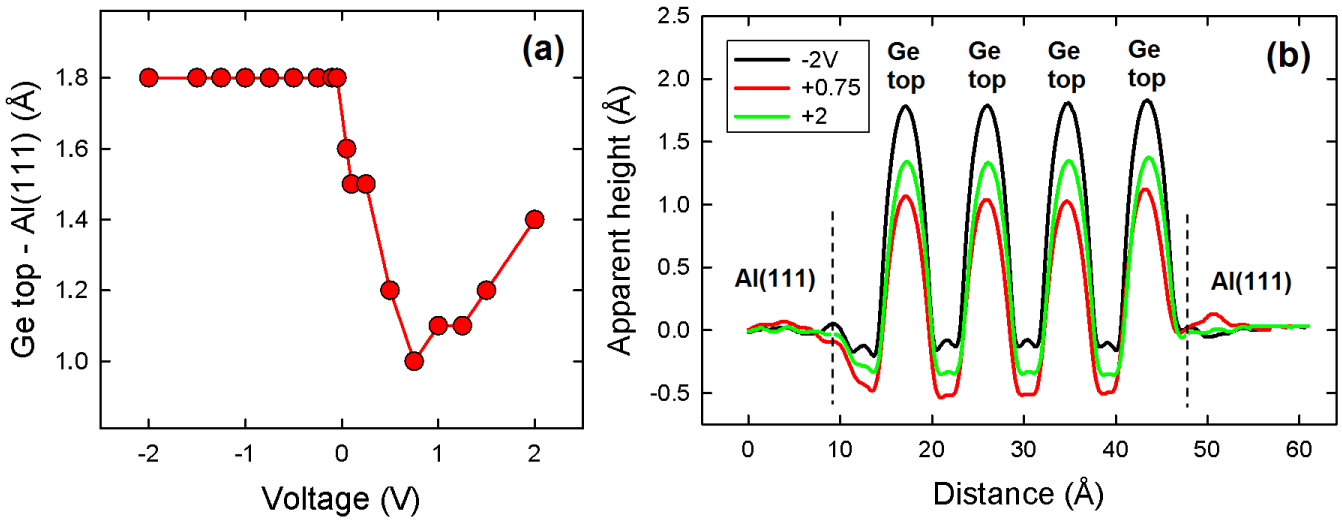

Figure 4.22: a) Voltage dependence of the simulated apparent height of the Ge top atoms relative to the Al(111) surface. (b) Selected profile for extremal points for extremal points -2V, +0.75V and +2V.

4.3.2 The particular case of the 145° oriented edge

The full Ge nanosheet does not reproduce a difference in contrast in the STM images between the edge and the center of the nanosheet. Before turning to other atomistic models, the other feature of the 3×3 phase, the 145° edge, is addressed. Figure 4.23 presents a tentative geometrical explanation for this shift. The original top atom in red is lowered at the same level of the germanene nanosheet, while the light-blue atom is raised. The apparent distance between this new top atom and the nearest one is lower (7.58Å). The segment joining both atoms makes an angle of 31° with the 180° direction (or 149° if considering the supplementary angle). Figure 4.24(a) shows an experimental image of a germanene nanosheet presenting both shifted edges, depending on the crystal orientation. This can be reproduced by choosing respectively a triclinic cell with 120° between $\vec{a}$ and $\vec{b}$ vectors (Figure 4.24(b)), or an angle of 60° (Figure 4.24(c)).

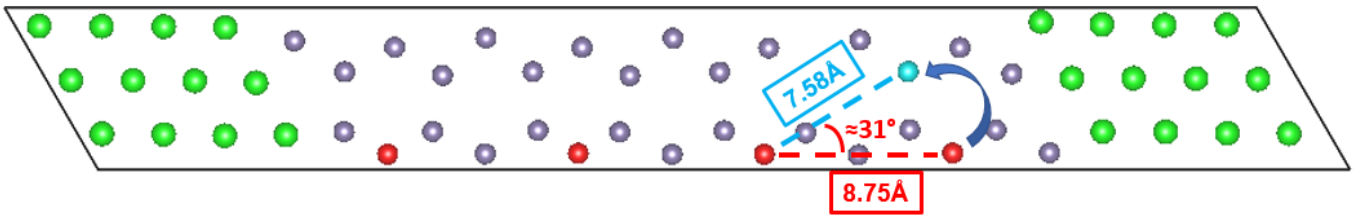

Figure 4.23: Possible structural model of the hypothetical cell showing a shift of 145° for the edge top atom. View from [001], only the top Al layer containing the germanene nanosheet is shown.

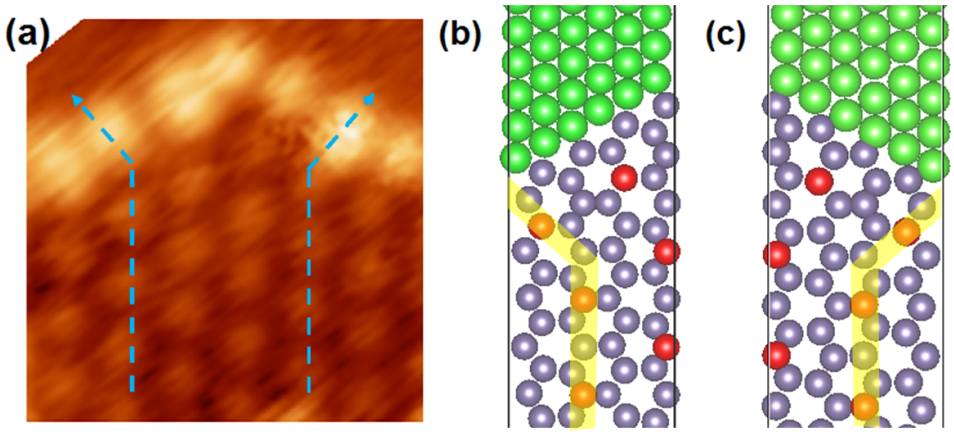

Figure 4.24: (a) STM image of two adjacent edges where the 145° configurations are seen. Tentative model to account for the configuration by choosing a 120° (b) or 60° (c) triclinic cell. The yellow stripes follow the top atoms which can be resolved in STM.

Before relaxation, all top atoms of the new 145° cell are put at the same z position, with a buckling of 1.73Å. After relaxation, the buckling of the 3 straight top atoms increases to $\sim$ 2.2Å, while the shifted top atom is in a lower position, 1.65Å. The angle evolves from $\sim$ 149° to $\sim$ 156°. The difference in electronic contrast can be detected also in the pseudo-STM image (figure 4.25), even if the difference in the profile is halved (0.3Å). The difference in free energy between the two relaxed structure is 85.5 meV, with the 180° structure as most favorable. This energy corresponds to the thermal energy of $\sim$ 986K. However, it is smaller than the energy transition per unit cell from 2H to 1T configurations of germanene via a tip-induced switch [88]. It can then be considered as a suitable threshold.

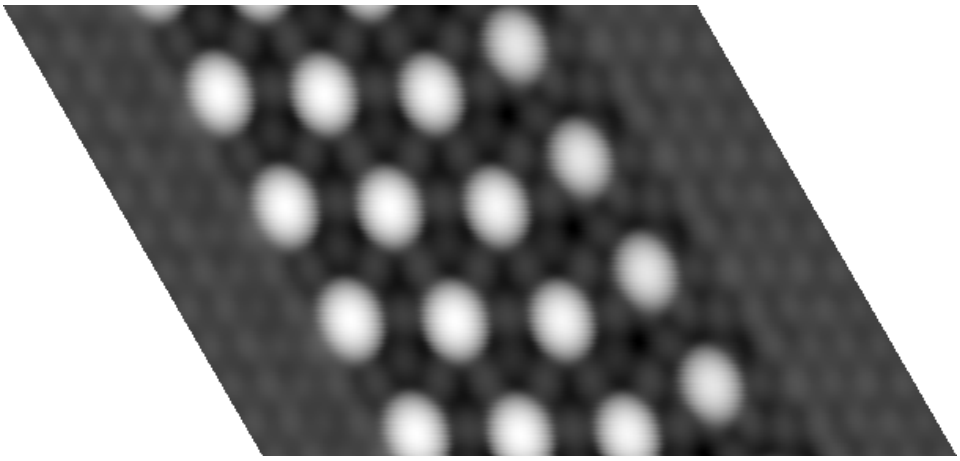

Figure 4.25: Simulated pseudo-STM image of a 1x4 cell of the germanene nanosheet in the shifted configuration, at V=-1.5V, d=3Å.

To summarize, the model of a full-Ge nanosheet on Al(111) reproduces the voltage-dependent STM images only far from the edges. No contrast is present on the edges, differently from experimental observations. A geometrical explanation can be given for the case of the 145°.

4.4 3×3 germanene nanosheet on Al(111): Al as top atom on the edge

4.4.1 Simulated STM contrast of the edge

The discussion of section 4.2 inspires the search for models which integrate Al atoms in the edge structure. For example, we can imagine to exchange Ge top atoms with Al atoms, to obtain a chemically induced contrast. The relaxation of a cell similar to Figure 4.17 but with 2 Al atoms as top on the edges is studied. The starting buckling of all atoms is $\sim$ 1.8Å. At the end of the relaxation, Al atoms buckling is $\sim$ 2.25Å, while Ge top atoms 1.95Å. The bonding character of the full Ge structure is mostly preserved (Figure 4.26), apart from a lower charge density around Al top atoms. The physical difference in height between Al top atoms and Al(111) on the side is preserved in STM image electronic contrast (Figure 4.27 for V=-1.5V). In the profile in figure 4.27 Al simulated apparent height matches the physical one at $\sim$ 2.3Å, while Ge one is lower ($\sim$ 1.7Å), producing a difference in height between Al and Ge top of 0.6Å.

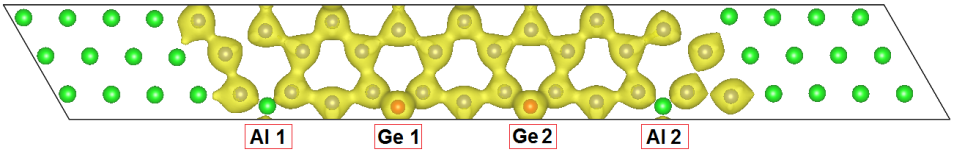

Figure 4.26: Charge density isosurfaces at 0.23 eV/Å^3 in the (001) plane of a germanene nanosheet containing two top Al atoms on the edge (Al 1 and Al 2). Only the top Al layer containing the germanene nanosheet is shown.

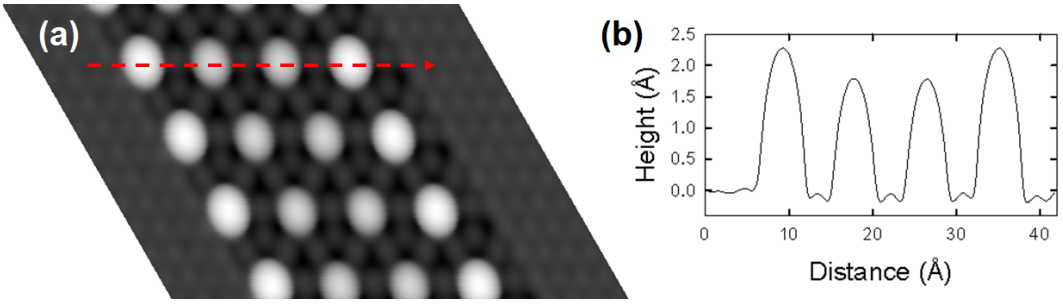

Figure 4.27: (a) Simulated pseudo-STM image of germanene nanosheet with Al on top at the edge, V=-1.5V. (b) STM profile along the direction of red arrow in (a).

The voltage dependence of pseudo-STM images in figure 4.28 shows that the difference in contrast between Al edge and Ge central top atoms is a maintained for every voltage between -2V and +2V. Similar to the full Ge nanosheet (figure 4.21), there is an overall variation of the relative contrast between Al(111) and the lower part of germanene nanosheet. This variation is detailed in figure 4.29(a) for a larger range, $\pm$3V. For negative voltages the contrast of top Al relative to Al(111) is almost constant around 2.2Å. Between -0.5V and -0.25V it diminishes to 2.1Å, and to 2Å around -0.1V/-0.05V. It continues to decrease until a minimum value of 1.5Å at +1/+1.25V. For higher voltages there is an oscillation at higher values, between 1.6Å and 1.8Å, but without a full recovery of the value at negative voltages. The relative contrast of Al and Ge top atoms follows a different trend (figure 4.29(b)): starting from 0.5Å at -3V, it grows to 0.7Å at -1V/-0.75V, to rapidly decrease to 0.4Å at -0.25V, value which is then constant until +3V.

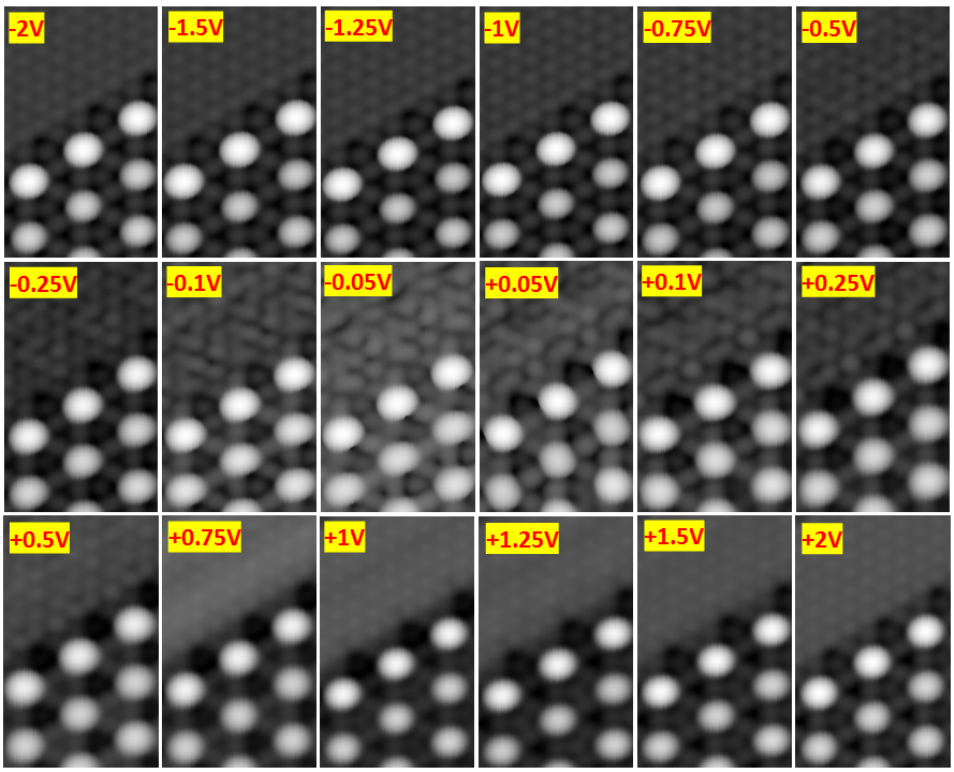

Figure 4.28: Simulated voltage dependence of germanene/Al(111) interface STM images with Al as top atom on the edge. Every image is cut to show just the edge.

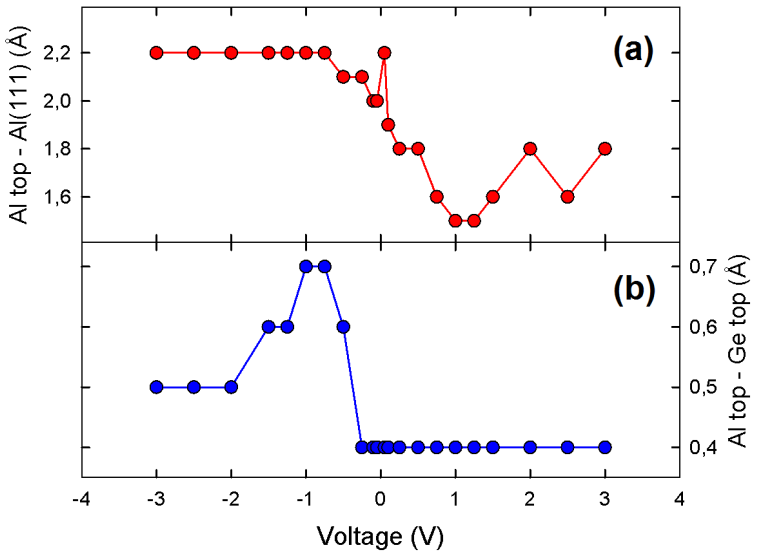

Figure 4.29: (a) Voltage dependence of the simulated apparent height of the Al top atoms relative to the Al(111) surface. (b) Voltage dependence of simulated apparent height of the Al top atoms relative to the Ge top atoms.

The Al top/Ge top trend can be explained through the analysis of the local Density of States of the relative atoms. As it can be seen in figure 4.30, the value of LDOS for Al atoms is always lower than Ge atoms. However, the difference is minimum between -1.3 eV and -1 eV, where they almost coincide. This value in energy corresponds to the interval between -1 eV and -0.77 eV, due to the Fermi level positioned at -0.33 eV (purple line in figure 4.30, calculated by VASP with the DOS). The integral of this value then has a growing/decreasing trend around this peak. The difference of

DOS value at positive voltage is higher than negative, explaining the lower contrast above -0.5V. However, during the voltage dependent experimental STM images the transition between the 180° and 145° structures takes place very often (as it can be observed also in figure 4.6). The 145° edge has an higher electronic contrast than the 180° edge and this hinders the measure of the dependence of a pure 180° configuration for the whole range of voltages.

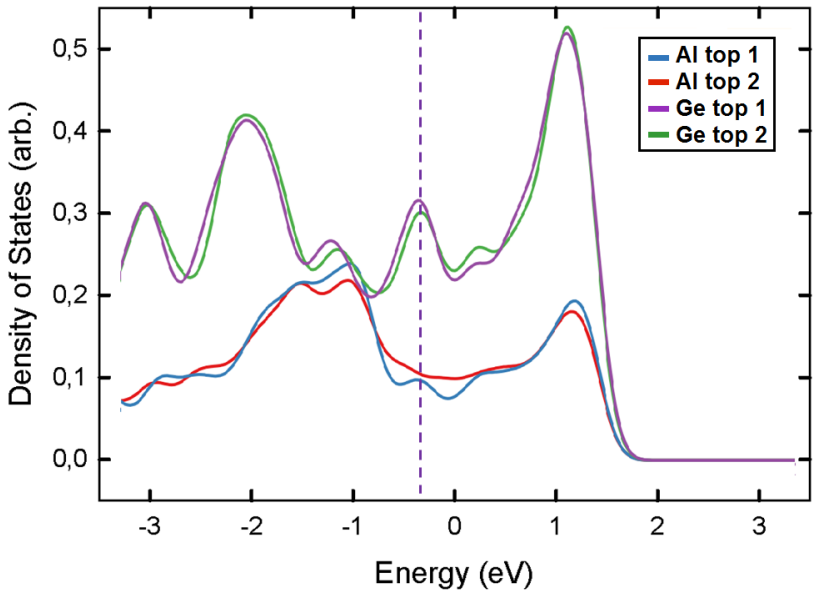

Figure 4.30: Density of states projected on Al atoms on the edge (red/blue) and Ge top atoms (green/violet).

4.4.2 The particular case of the 145° oriented edge

We have just shown that the presence of an Al top atom on the edge of a germanene nanosheet explains a difference in electronic contrast in pseudo-STM images, induced by a difference in chemical identity. We turn then our attention to the 145° edge, in order to find a structure to perform a tip-induced transition. The same idea of the full Ge structure (Figure 4.23) is applied. The same Al-Ge substitution is performed as for full Ge structure, to form an angle of 145-150°. The relaxed structure however does not maintain the desired feature: the raised Al atom goes down to the nanosheet level, while another Ge atom goes up at the same level of the others, slightly shifted from 180°.

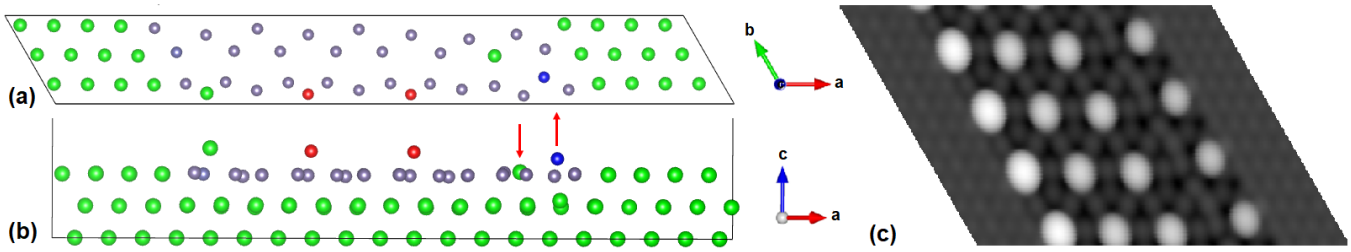

Figure 4.31: (a) [001] and (b) [010] views of 145° relaxed cell with Al on the edge for the 145° configuration. In the [001] view, only the top Al layer containing the germanene nanosheet is shown. (c) Simulated pseudo-STM image, V=-1.5V.

The difference in the apparent height at the nanosheet edge was then reproduced via the substitution of the Ge top atom on the edge with an Al top atom. A straightforward application of this idea to a 145° configuration in a nanosheet with full honeycombs on the edge does not produce a stable configuration. In the following sections we will analyze how the match with experimental observations can be improved by modifying the structure of the edge.

4.5 Composition of the 3×3 germanene nanosheet on Al(111) with incomplete unit cell on the edge

Atomic surroundings are important to preserve the buckling during relaxation. Up to this point our model considered a nanosheet with closed honeycomb cells. Such a lattice gives rise to a small contrast in the simulated pseudo-STM images between the left side and the right side of the germanene nanosheet. However, this difference might be difficult to resolve experimentally, due to convolution effect induced by the finite-size of the apex. As graphene zig-zag edges are metastable and tend to form reconstructions at room temperature [290], another hypothesis can be tested: removing half a zig-zag row of Ge atoms, or a full one (purple and light-blue atoms in figure 4.32), could help the Al buckling to be preserved.

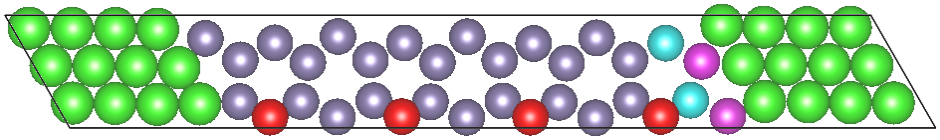

Figure 4.32: Half zig-zig row (purple atoms) and full zig-zag row (purple+light blue) atoms to be removed in order to maintain buckled structure. View from [001], only the top Al layer containing the germanene nanosheet is shown.

The removal of a full zig-zag row from the Al-edge structure produces a bright 145° relaxed configuration (Figure 4.33). However, a configuration with an atom in the 145° position is the only one stable. The relaxation of a 180° structure (Figure 4.34(a)) leads the Al atom to go down to the nanosheet level, while a Ge atom (in red in Figure 4.34(b)) goes up. This evolution recreates a 145° edge with an inversed contrast: the Ge edge atom is lower than the Ge central atoms, as shown in Figure 4.34(c).

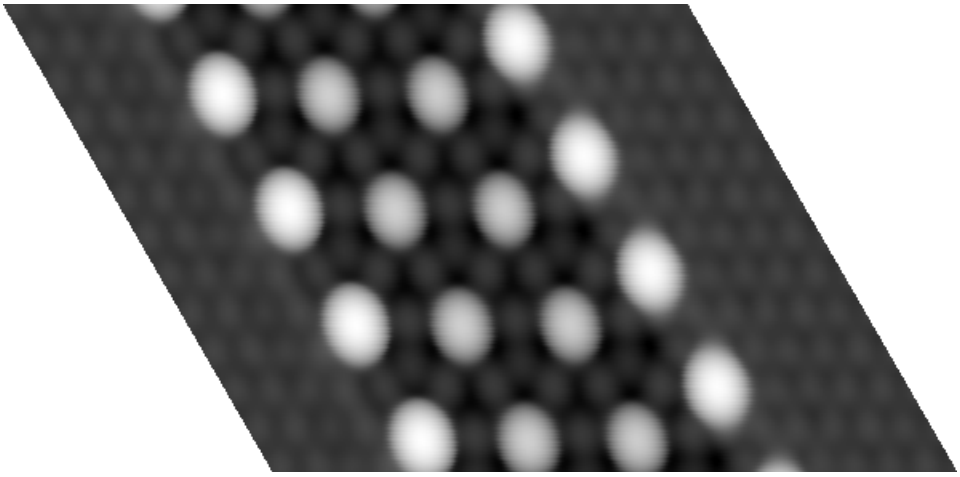

Figure 4.33: Simulated pseudo-STM for 145° structure with a full zig-zag line of Ge removed on the edge, V=-1.5V.

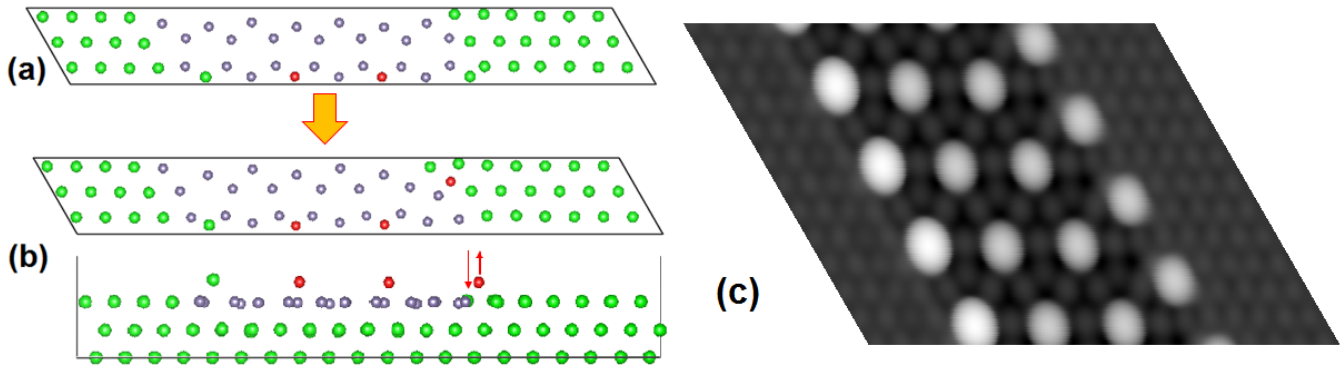

Figure 4.34: (a) Starting cell, view from [001], and (b-c) relaxed cell, views from [001] and [010], of 180° structure with a full zig-zag row of Ge removed on the edge. In the [001] view, only the top Al layer containing the germanene nanosheet is shown. (d) Simulated pseudo-STM image of relaxed cell, V=-1.5V.

The result is different with the removal of half a zig-zag row. In this case, the 180° structure remains intact (Figure 4.35(a), and related pseudo-STM image in figure 4.35(b)). This applies also to 145° (Figure 4.35(c-d). The shifted edge evolves however towards a 160° angle. The energy difference in this case is just 10 meV, with the 160° structure as the least energetic. Observing the structures in Figure 4.35(a) and (c), it can be seen that the transition would only require to move the Al atom between two sites far $\sim$ 2.88Å, without other structural modification. The charge density map in Figure 4.36 does not show a significantly increased interaction with Al atoms on the edge also. The relative height of the Al edge atom to the Ge top atoms is 0.215Å for both configurations, and 2.4Å relative to the Al(111) surface. In STM images at V=-1.5V, this difference is 0.5 Å and 1.6Å. The contrast evolves again consistently with the DOS difference, with a larger range in energy where Al and Ge DOS has similar value (between -1.4V and -0.8V in Figure 4.37), for both configurations. The Fermi level is again -0.33V. This leads to a larger region in negative voltages where the relative buckling is higher (Figure 4.38(b)).

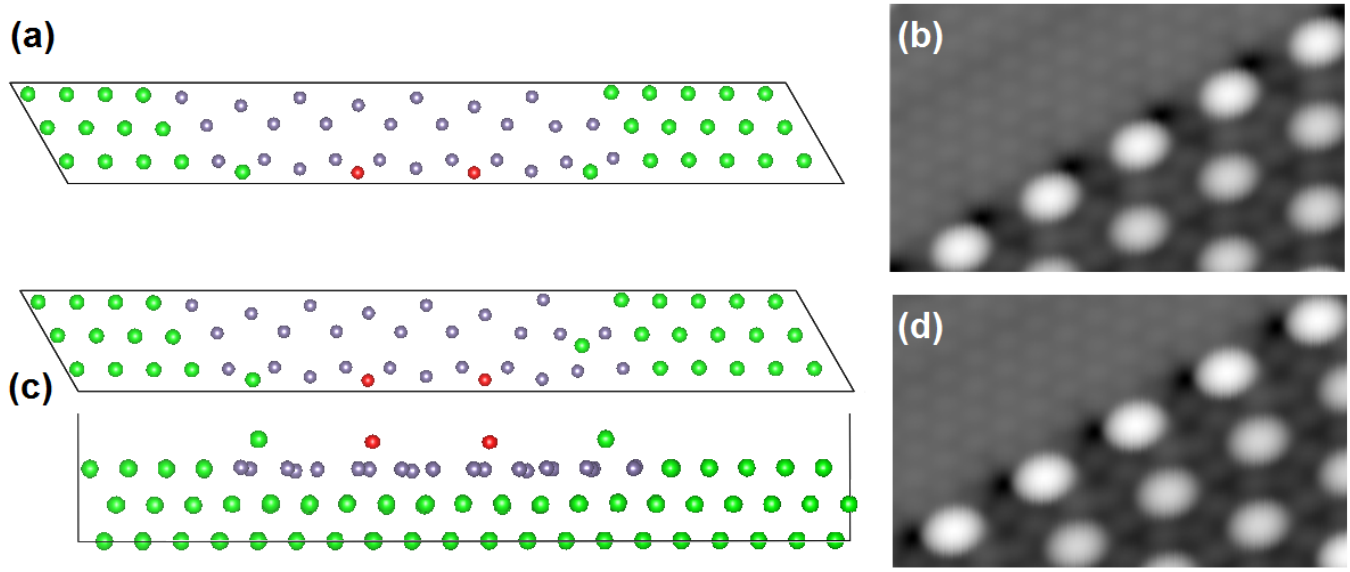

Figure 4.35: (a) Relaxed cell of 180° structure with half a zig-zag row of Ge removed on the edge, view from [001]. (b) Simulated pseudo-STM image of the edge, V=-1.5V. (c) Relaxed cell of 145° structure with half a zig-zag row of Ge removed on the edge, views from [001] and [010]. (d) STM image of the edge, V=-1.5V. In the [001] views, only the top Al layer containing the germanene nanosheet is shown.

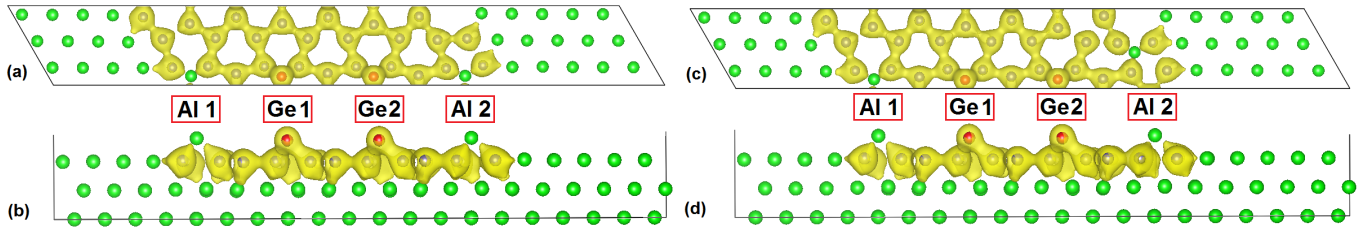

Figure 4.36: Charge density isosurfaces at 0.23 eV/Å^3, views from [001] and [010] directions, for 180° (a-b) and 145° (c-d) structures. In the [001] views, only the top Al layer containing the germanene nanosheet is shown.

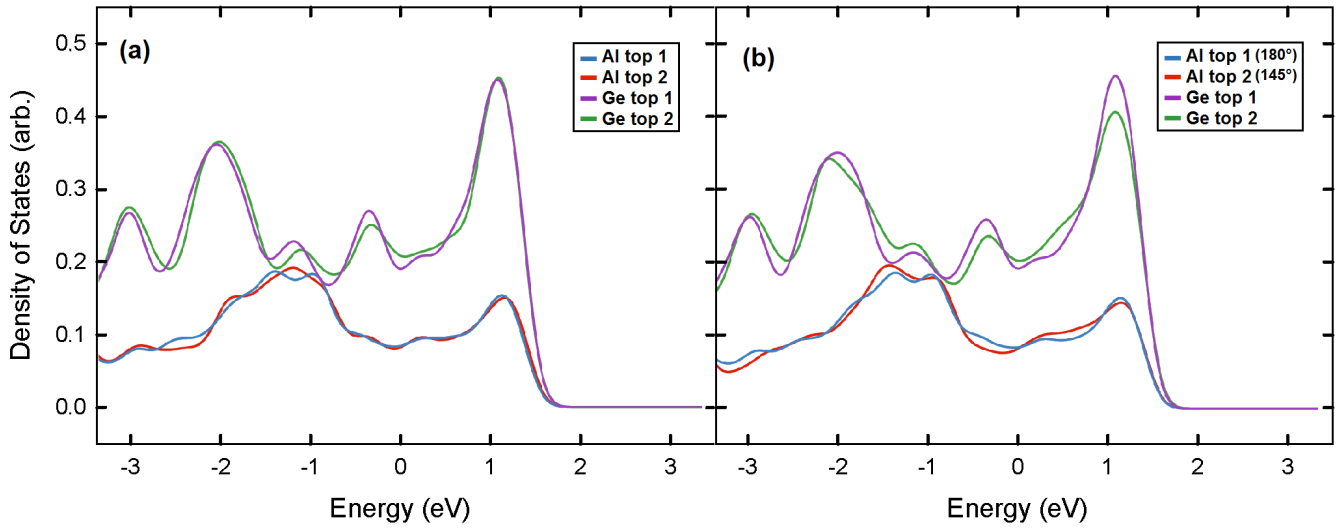

Figure 4.37: Densities of states projected on Al atoms on edge and Ge top atoms for cell with half zig-zag row less, (a) 180° and (b) 145° structures.

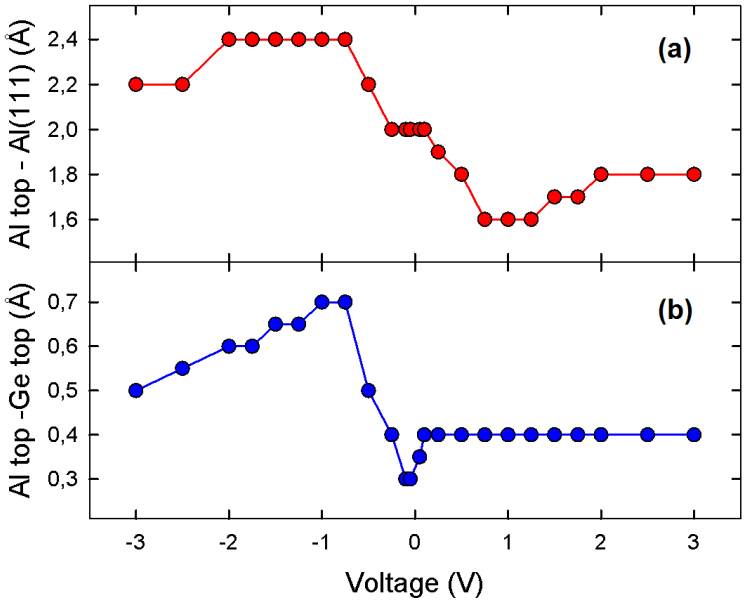

Figure 4.38: (a) Voltage dependence of the simulated apparent height of the Al top atoms relative to the Al(111) surface.(b) Voltage dependence of the simulated apparent height of the Al top atoms relative to the Ge top atoms.

The model with a modified edge structure shows a better agreement with experiments than the full honeycomb model. The speculated transition mechanism would account also for a configuration with a smaller angle, with Al moving in a straight line along the interface. However, the edge shown in Figure 4.35 would not sustain the Al buckling due to the vacancy of a Ge atom. This Ge atom can be added as in Figure 4.39. If we consider also the intermediate angles in the neighboring triangular sites, this modified edge allows to access a total of 5 different configurations. The interest in studying these configurations lies in the comparison between our report of a transition only between 180 and 145° at low temperature, and the STM measurements at room temperature (as those reported by Muzychenko et al. [237]) where the difference between top atoms on the edge is less evident and it could be mistaken for a full line. This could possibly be explained by a transition between different configurations that happens faster than the scan frequency, helped by the higher thermal energy, in which only the more energetically favorable configuration can be almost resolved.

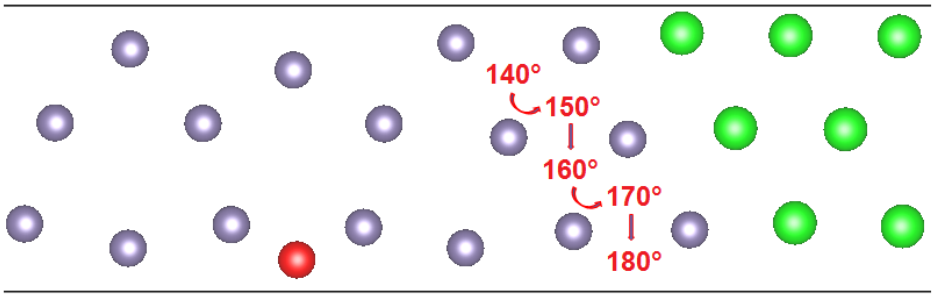

Figure 4.39: Possible shifted configurations. View from [001], only the top Al layer containing the germanene nanosheet is shown.

Angle (°)	**Distance (Å)**	**ΔE (mV)**
138	7.67	+33
151	7.98	+31
160	7.64	+29
172	8.47	0
178	8.57	+45

Table 4.1: Table of comparison for different shifted structures. The angle and distance from the nearest top atom are given after relaxation, while the energy difference is given from the lowest energetic configuration.

Table 4.1 shows the angle after relaxation of the possible configurations, which are not far from the starting ones. All configurations are contained in a 45 meV range. However, only the 138°, 160° and 178° configurations could account for the experimental distances, while the 151° and 172° are too far from the nearest top Ge. Among the three most favorable configurations, the 160° yields the lowest energy and a transition towards 138 and 178° would require respectively 4 and 16 meV, thus remaining in an acceptable range. These configurations show a similar evolution as a function of the applied voltage and DOS. The simulated STM images of these three configurations are seen in Figure 4.40. From left to right, the transition between the 138° and the 178° configuration occurs while maintaining an higher electronic contrast for the edge Al atom than the Ge central top atoms of the nanosheet.

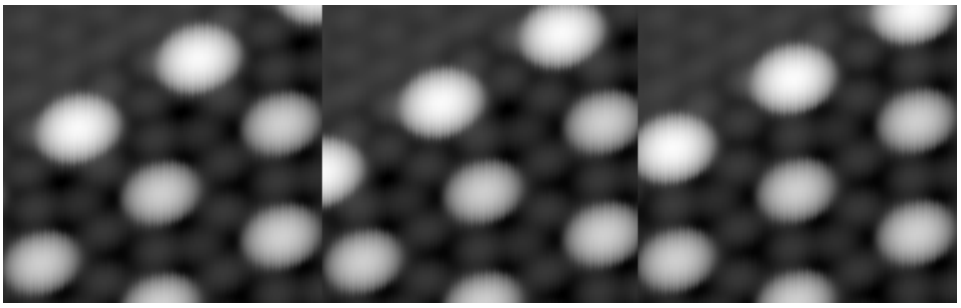

Figure 4.40: Pseudo-STM images of 138°, 160° and 178° configurations, V=-1.5V, d=3Å

To summarize, we showed how a full Ge honeycomb is not able to account for all the features observed experimentally via STM and STS. A modified structure with full honeycombs and Al as atom on top on the edge provides a chemically induced contrast, but it is not able to explain the shifted edges. A modification of the interface between germanene nanosheet and Al(111) is necessary to account for a shifted edge and a transition mechanism within an acceptable energetic range.

4.6 $\sqrt{7} \times \sqrt{7}$ germanene nanosheet on Al(111) edges

The $\sqrt{7} \times \sqrt{7}$ reconstruction has a few differences in comparison with the 3×3 phase. Due to the preferential armchair edge, the choice of the cell to be relaxed is less evident than the zig-zag edge of the 3×3 phase. Every new armchair row adds a full honeycomb, so the only degree of freedom in this sense is adding half a row. Another choice to be made is the position of top atoms. The zig-zag row has a simple alternance No Top - Top - No Top (NTN) atoms in the [100] direction, as in Figure 4.17, while the armchair row has a longer periodicity of No Top - Top - Top - No Top (NTTN) atoms, as shown in figure 4.41, where No Top rows are light blue and Top rows in red). We will first choose a cell with No Top rows on the edge (as that in figure 4.42), to "protect" the top atoms during relaxation. The unit cell has the following dimensions: 57.1687 × 7.52758 × 22.218 Å.

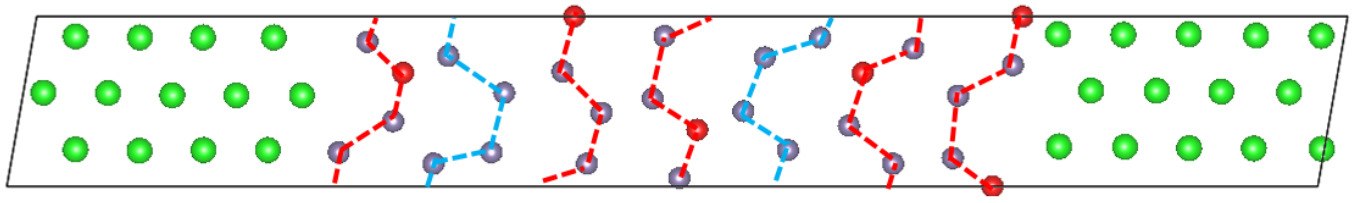

Figure 4.41: An example of the armchair-terminated $\sqrt{7} \times \sqrt{7}$ phase. View from [001], only the top Al layer containing the germanene nanosheet is shown.

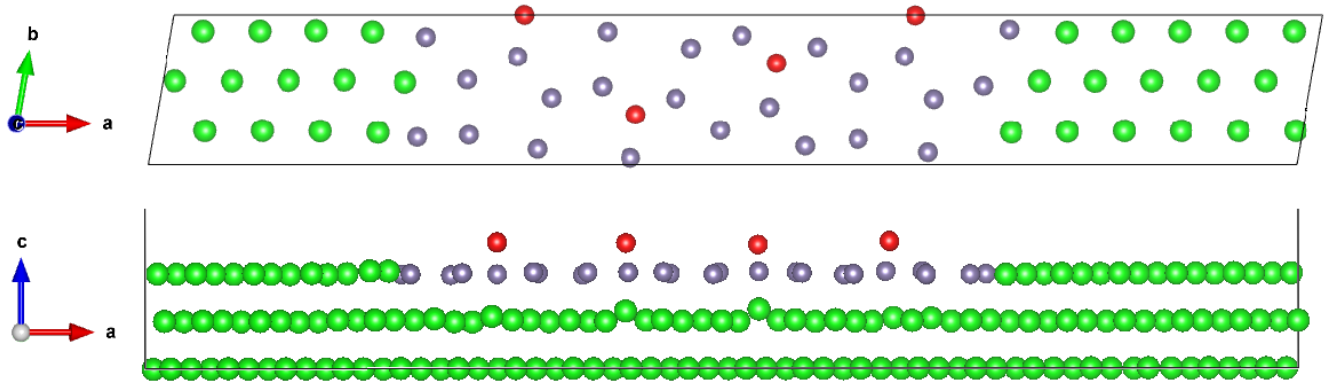

Figure 4.42: Relaxed $\sqrt{7} \times \sqrt{7}$ NTTNTTN cell, [001] and [010] views. In the [001] view, only the top Al layer containing the germanene nanosheet is shown.

As reported in [98], the Al atom below the Ge top is uplifted, possibly due to the stronger interaction between the $\sqrt{7} \times \sqrt{7}$ reconstruction and the Al(111) surface. Similar to the 3×3 phase, the structural relaxation does not generate a natural contrast on the edge in STM images. It can be chemically induced via the substitution of Ge on the edge with a top Al atom. The model is shown in Figure 4.43(a). From left to right, the buckling of the top atoms after relaxation, relative to the Al(111) surface, is of 1.40 / 1.69 / 1.60 / 1.42 Å. The Ge top atoms are then between 0.18 and 0.27 Å higher than Al ones on the edge. However, the simulated STM image shows a brighter edge (Figure 4.43). The profile in Figure 4.43(c) shows the apparent heights of the top atoms as 2.11 / 1.96 / 1.87 / 2.09 Å. The contrast is then reversed due to chemical difference between Al and Ge.

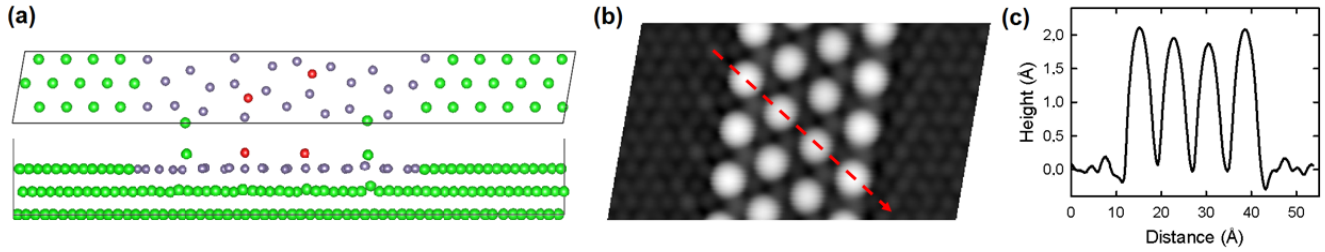

Figure 4.43: (a) Relaxed $\sqrt{7} \times \sqrt{7}$ NTTNTTN cell with Al on top on the edge, [001] and [010] view. In the [001] view, only the top Al layer containing the germanene nanosheet is shown. (b) Simulated pseudo-STM image of the cell in (a), V=-1.5V. (c) Profile in (b).

To summarize, the established atomistic model for the $\sqrt{7} \times \sqrt{7}$ reconstruction of germanene on Al(111) does not produce an electronic contrast in the STM images between the nanoribbons' edges and their central part. The substitution of the border top atoms with Al atoms, as performed for the 3 $\times$ 3 reconstruction, produces an electronic contrast of chemical origin on the border. This conclusion is strengthened in the case of the $\sqrt{7} \times \sqrt{7}$ reconstruction by the fact that the top Al atoms on the border are physically lower than the top Ge atoms in center. Therefore, both reconstructions' edge involves then the presence of Al atoms in their structure. The edge properties of germanene on Al(111) are then to be reconsidered for practical applications via the consideration of the Al/Ge mixing.

Chapter 5

Transport properties of $GeCH_3$

The interest in the analysis of the transport properties of $GeCH_3$ microflakes is manifold. First of all, germanane has been predicted to show the Quantum Spin Hall Effect at room temperature when a strain is applied [145]. Such an advancement would be an incredible jump from the experimental temperatures reached via the TMDs. On the other hand, $GeCH_3$ has features of interest also for classical (not spin connected) electronics. A quite high mobility of 1.4×10^4 cm^2/Vs for holes and 6.71×10^3 cm^2/Vs for electrons along armchair direction has been predicted by theoretical calculations [143]. However, no experimental measurement has been reported so far. For 2D materials, the mobility measurement relies on other properties of the material: the understanding of the relative conductivity of the surface states compared to space charge region and bulk states, the doping and the ratio between the in-plane and out-of-plane resistivity. These properties depend themselves on the quality of the synthetized sample and not a lot has been done at the microscopical level to link the morphology and the defects with the electrical properties.

In this chapter the physical characterization of $GeCH_3$ microflakes at the single flake level will be presented. First, the identification of two different species of flakes will be linked to their different chemical properties. For those whose optical properties matched with what reported in literature so far, the transport properties will be studied in order to understand if the conduction is mainly bidimensional (intra-layer) or tridimensional (inter-layer). The doping character of the flakes will be extracted by field effect measurements.

5.1 $GeCH_3$ synthesis

The microflakes has been provided by Geoffreoy Prevost (INSP, Paris) in the context of a collaboration with the group of E. Lhuillier (INSP, Paris). The synthesis of the $GeCH_3$ microflakes has been performed by modifying a procedure reported by Jiang et al. [138] in the supplementary material of Livache et al. [139].

The first step is the synthesis of the precursor, $CaGe_2$. In a typical reaction, stoichiometric amounts of Ca and Ge were loaded into a quartz tube in a N_2 filled glovebox. The content of the tube was purified by three evacuation-refill cycles and sealed under vacuum using a natural gas/O2 torch. The quartz tube was placed in a tube furnace and heated to 1050 °C for 18 h, then cooled to 400 °C at 5°C/hr after which the tube furnace was turned off and was allowed to cool to room temperature. The CaGe2 was stored under an inert atmosphere.

The $GeCH_3$ synthesis is made from $CaGe_2$ through a topochemical transformation: during the reaction, the Ge crystalline planes inside $CaGe_2$ crystals are preserved and the calcium is deintercalated and replaced by CH_3. First, a three-neck round bottom flask was taken into a N_2 filled glovebox, to which iodomethane and acetonitrile were added. The flask was then connected to a Schlenk line and immersed into liquid nitrogen until the solution was frozen into a solid. CaGe2, water, and a stir bar were added to the flask while the contents were frozen. The contents of the flask had a molar ratio (CaGe2: iodomethane: water: acetonitrile) of 1: 30: 10: 60. The flask was evacuated and refilled with nitrogen three times, and the methylation proceeded for seven days at room temperature. At this point, the reaction mixture was again frozen by immersing the flask in liquid nitrogen, and loaded into a glovebox filled with N_2. The methyl-terminated germanane was separated using vacuum filtration, washed with acetonitrile, then dried under vacuum on a Schlenk line. It was finally redispersed in an isopropanol solution.

5.2 Choice for a host substrate

The metallic substrate chosen for the multi-probe measurement of $GeCH_3$ transport properties is higly doped Si(111)-B crystal (resistivity smaller than 1 mΩ·cm), with a thin native oxyde layer which grows after exposition to air. The Si(111)-B surface forms multiple surface reconstructions, depending on the conditions:

- The well-known 7×7 reconstruction, which is related to the crystalline symmetry and can be formed with by n-doped Si(111) crystals [291, 292];
- The $\sqrt{3} \times \sqrt{3}$ reconstruction, where an active role is played by the Boron dopants;

The 7×7 reconstruction is prepared by annealing under vacuum up to 900°, flashing multiple times at 1150°C to remove silicon oxide and then slowly cooling down in a few hours, with particular attention between 860° and 820° [293]. To obtain the $\sqrt{3} \times \sqrt{3}$ reconstruction the time to let the boron dopants diffuse to the surface must be significantly increased: the recipe for 7×7 is modified by leaving the Si(111) surface at 900° for at least 9 hours.

When the annealing is not performed properly, contaminants (mostly carbon) are left on the surface and during the 900° anneal they diffuse near the terrace steps creating the large contaminated areas shown in figure 5.1(a). In figure 5.1(b) the network of the contaminants is shown. On the lower terrace the proper $\sqrt{3} \times \sqrt{3}$ reconstruction is already present. This ordered area extends over all the surface when the annealing is performed correctly. An example of a large and well-ordered terrace is shown in figure 5.2(a). A few dangling bonds are visible on the surface, characterized by a bright contrast on the corresponding atom and an intermediate contrast on the 6 neighboring atoms. A closer look of the reconstruction is given in Figure 5.2(b). All the bright spots are Si adatoms on top

of individual B dopants, as it is shown in the inset. Due to the high p-doping of the Si sample, the Fermi level measured at zero volt in tunneling spectroscopy is pinned at the maximum of the valence band. This can be proved through STS, as it shown in figure 5.3.

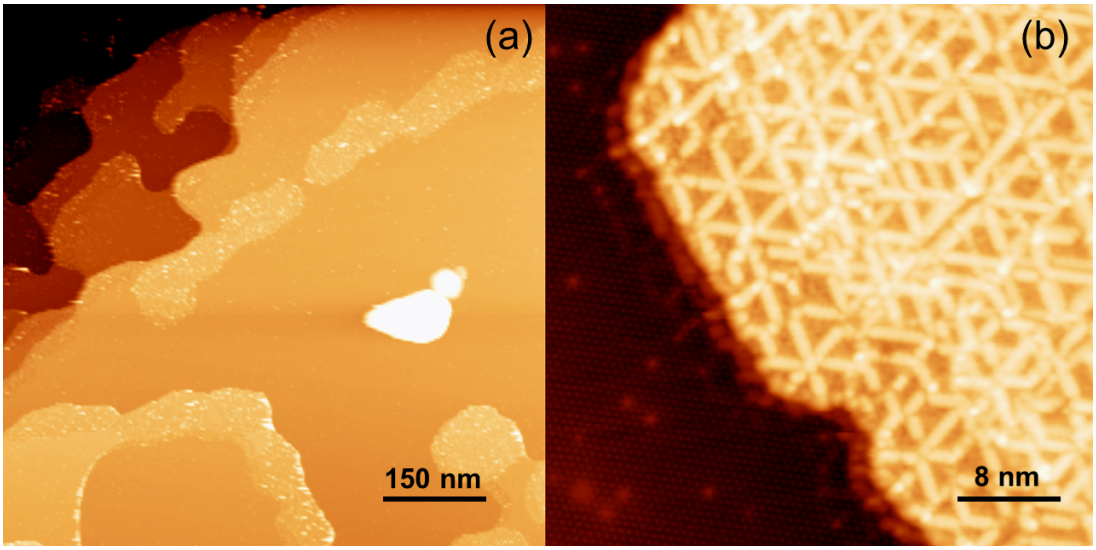

Figure 5.1: (a) Large scale STM image of the Si(111)-B surface not properly reconstructed due to contaminants, V=+1.5V, I=50pA, T=77K. (b) Zoom on a contaminated terrace. The $\sqrt{3} \times \sqrt{3}$ reconstruction can be seen on the lower terrace, V=+1.5V, I=50pA, T=77K.

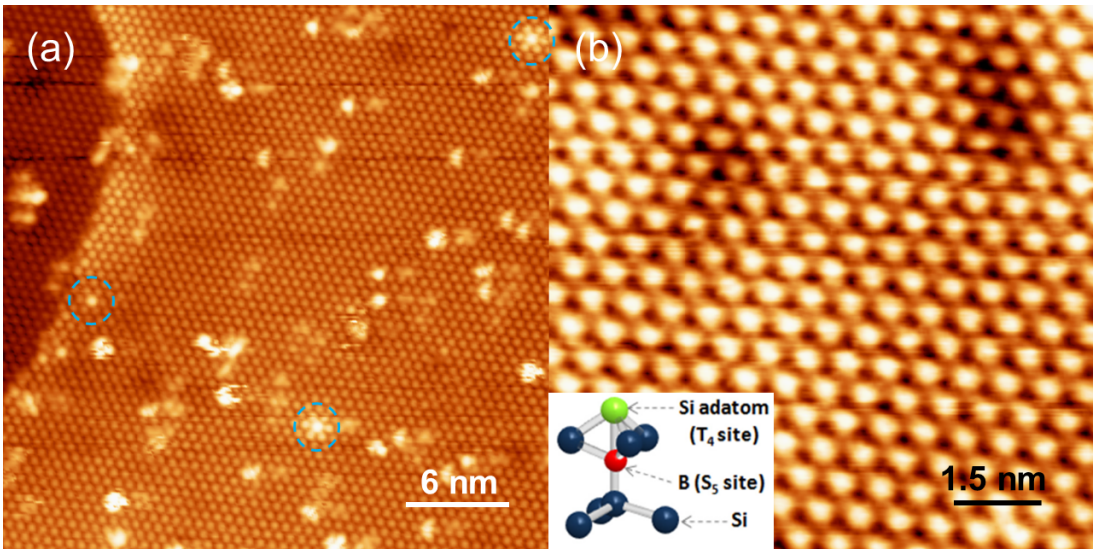

Figure 5.2: (a) $\sqrt{3} \times \sqrt{3}$ reconstruction of the Si(111)-B surface. A few dangling bonds are highlighted in blue circles. V=+1.5V, I=50pA, T=77K. (b) High resolution STM image of the $\sqrt{3} \times \sqrt{3}$ reconstruction of the Si(111)-B surface. Every bright circle is a Si adatom positoned on top of a B dopant, as shown in the model in the inset (which is reproduced from [294]). V=+1.5V, I=50pA, T=77K.

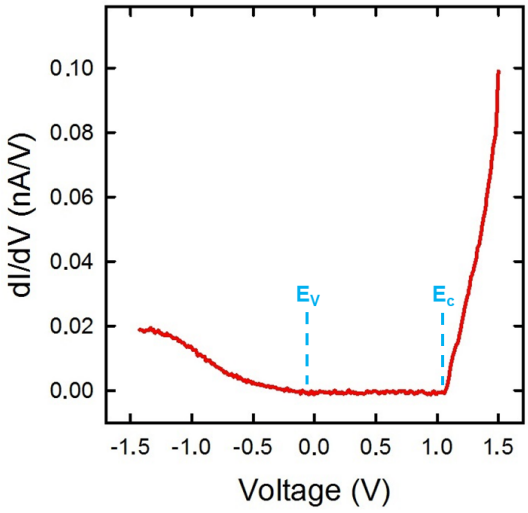

Figure 5.3: dI/dV characteristics measured on the Si(111)-B surface with a modulation technique, V=+1.5V, I=100pA, Δ_V=5mV, f=480 Hz, T=77K. The position of the maximum of valence band (E_V) and the minimum of conduction band (E_C) are shown.

When the Si(111)-B surface is ready, the sample is taken out in air so that, little by little, the surface gets oxidized. Then the microflakes are deposited from the isopropanol solution via dropcasting. The head of a pipette or a syringe is used to collect some of the solution by capillarity, and 4-5 droplets are deposited on the silicon surface already mounted on the sample holder, under a low flux of nitrogen to accelerate the isopropanol evaporation and leave as less as possible organic traces on the surface. The trace of the external circle of the droplets is nevertheless still visible (as in figure 5.4(a)). It greatly helps to find areas with the highest density of nanoflakes on the surface. A higher accumulation of microflakes is usually present around the border of the droplets, following the so-called coffee ring effect [295]. As shown in figure 5.4(b) there is almost no microstructure outside the border of the droplet, whose contrast is darker compared to the bare Si(111)-B surface due to the organic traces left by isopropanol after its evaporation. We note that at the physical border of the sample end the diffusive path of the droplets leads to a few areas containing a high density of microflakes, as visible in figure 5.4(c).

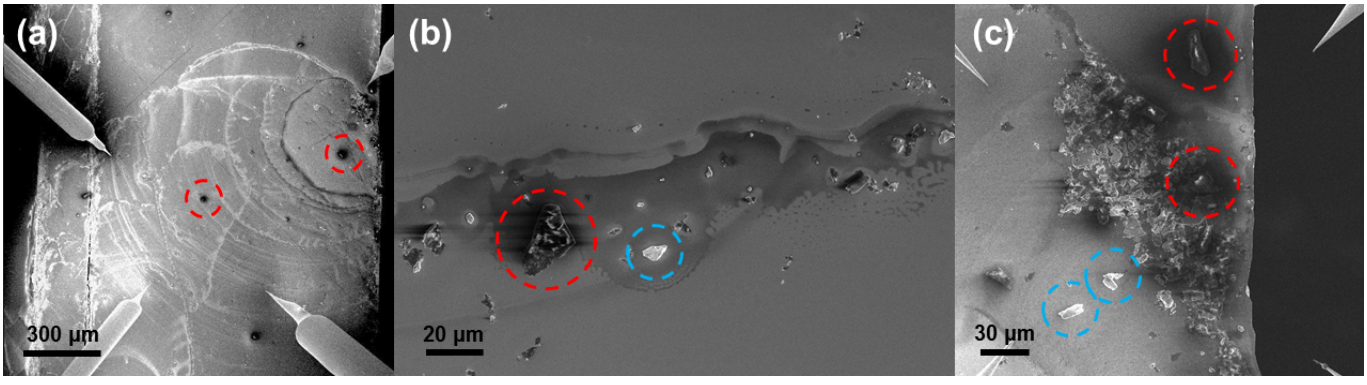

Figure 5.4: (a) Large scale SEM image of the $GeCH_3$/Si(111) sample, showing the outskirt of the droplets left by evaporation. (b) Zoom in the outskirt area. (c) SEM image of a strong accumulation area due to multiple droplet evaporation around a sample border. Red and blue dashed circles highlight different type of microstructures under the SEM irradiation. V=5kV, I=100pA.

Another feature of the colloidal structures is unveiled by a closer look at Figure 5.4: the presence on the surface of a variety of microstructures showing different behaviour under the SEM irradiation.

We note that we took the following care: a low voltage of 5kV to limit the interaction of the electron beam with the surface and a small 100pA current to not damage the sample surface. The first type of behaviour is obtained for microstructures that charge under the electron beam: these microstructures are visible both on large and small scales (red circles in Figure 5.4(a-c)). Charging strongly darkens the microstructures. The second behaviour corresponds to microstructures which do not charge, being on the contrary quite bright under the electron beam (blue circles in Figure 5.4(b-c)).

Figure 5.5 shows a tentative classification as a function of the surface area of the flakes above 4 μm^2, chosen as the smallest area to perform a suitable multi-probe measurement. The classification is labelled as tentative because the flakes are not always flat, so there is no perfect match between the area measured in the SEM images and the actual surface of the flakes. This discrepancy affects more the smaller flakes. 72 flakes have been considered for the analysis, of which 25 get charged under irradiation. As Figure 5.5(a) shows, the number of flakes decreases exponentially as a function of the surface area. Three flakes of growing dimension are shown (the bar scale is always 2μm). By counting the number of flakes which become dark when observed with the SEM, we notice that the percentage of charging flakes decreases with the surface area (fig 5.5(b)). For nanoflakes having a top surface between 40 and 80 μm^2 the probability to find a charging flake is around 50%. This probability rapidly grows to 100% for higher surface areas.

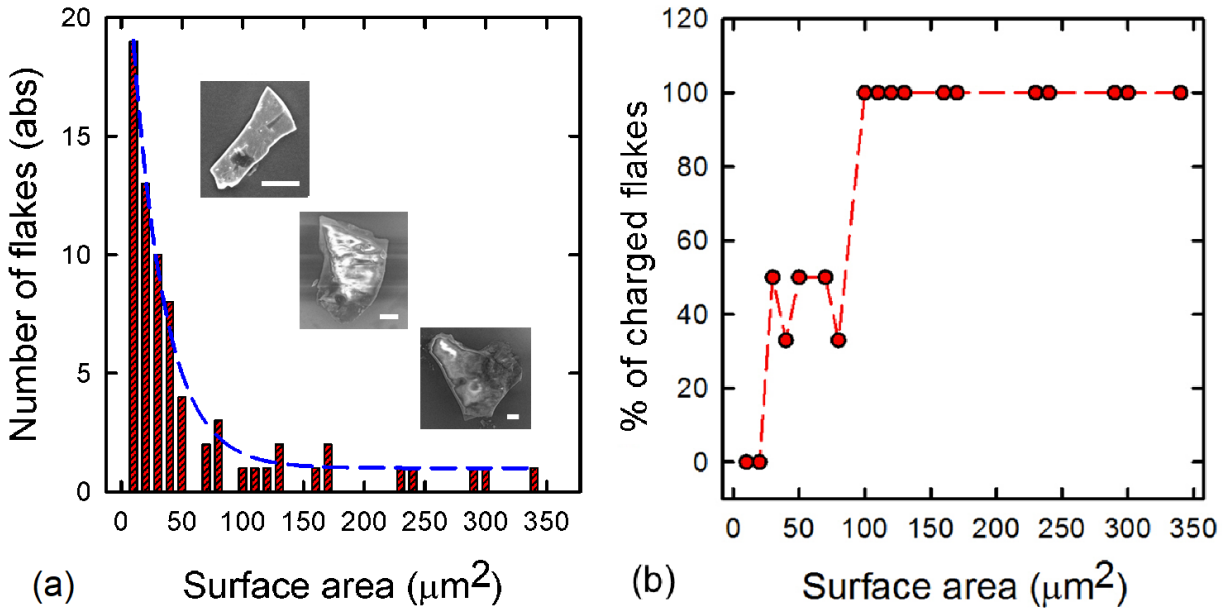

Figure 5.5: (a) Distribution of $GeCH_3$ microflakes found on the Si sample as a function of the size of their top surface. The SEM images of 3 flakes of increasing surface are also shown as insets. The scale bar is always 2μm. (b) Percentage of charged flakes as a function of the surface.

5.3 Chemical composition of the microflakes

To delve deeper into the different nature of the two microflakes' species, the chemical identification of the microstructures is performed through non-invasive spatial-dependent Raman spectroscopy. A second deposition on a gold substrate is performed, to make sure to get a featureless background in contrast to the Si substrates. Apart from a cleaning procedure of the gold substrate with acetone and isopropanol, the deposition is similar to the one achieved on the Si(111)-B surface. Due the fact that both cathodoluminescence and Raman signals are collected from the same spectrometer, a parabolic mirror is used to focus and collect the signal of the laser. Care has to be taken as the Raman map is shifted compared to SEM images of around 10 μm (depending on the magnification). To overcome this limitation, the Raman map is performed in a low density region where the microflakes are well

separated from each other. Figure 5.6(a) shows a region with microstructures which do not show any sign of charging. The superimposed grid is a 12x12 mesh of Raman spectra acquired with a laser wavelength of 532 nm and a diffraction grating of 600 lines. Only a peak is recurrent in the 144 spectra, around 300 cm^{-1}: the 6 more intense spectra are selected and averaged, and the result is shown in figure 5.6(b). This peak matches with the expected Raman peak of Ge at $\sim$ 295 cm^{-1}. It is then interesting to analyze the spatial dependence of the signal. Figure 5.7(a) shows the integrated signal between 230 and 360 cm^{-1}. As expected, the more intense areas are shifted compared to the physical position of the microflake. Taking into account of the instrumental shift mentioned above, they can be matched as in Figure 5.7(b).

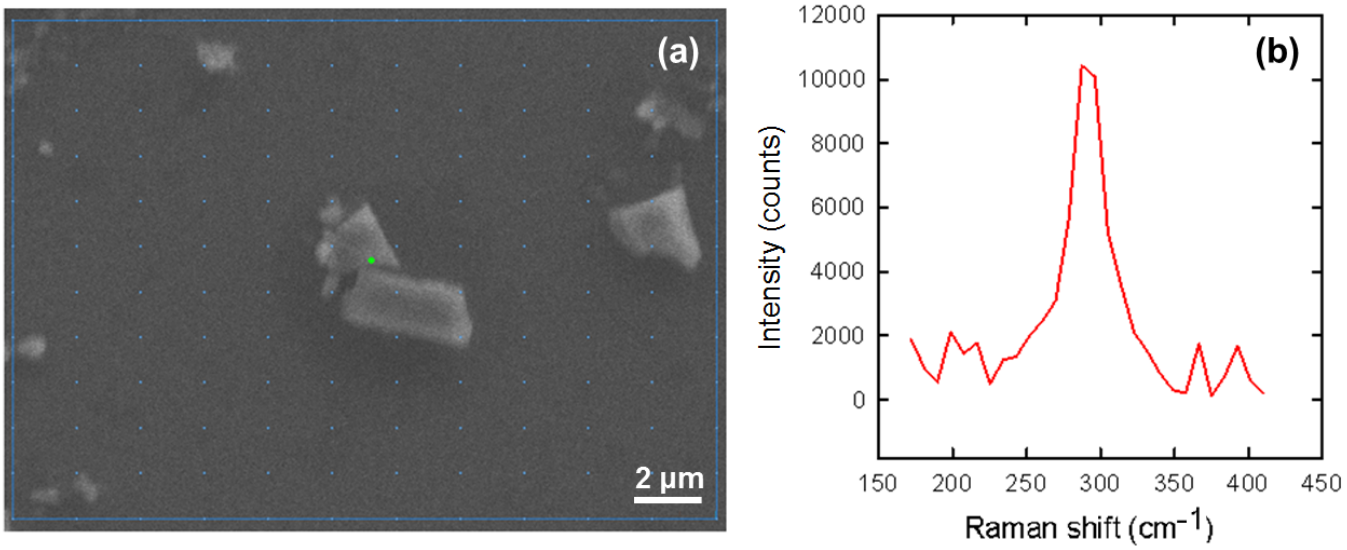

Figure 5.6: (a) SEM image of $GeCH_3$ microflakes, V=5kV, I=100pA. A 12x12 grid is superimposed, to indicate the acquisition points for Raman spectra. (b) Main Raman peak at 295 cm^{-1}, average of 6 curves.

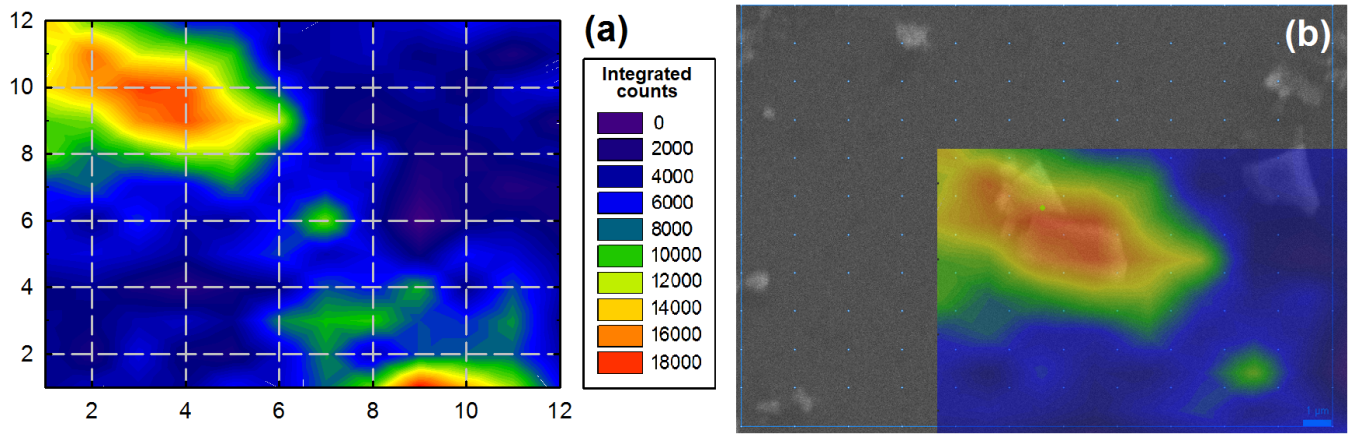

Figure 5.7: (a) Spatial map of the integrated intensity of the Raman signal between 230 and 360 cm^{-1}. (b) Superimposition of the Raman map and the SEM image, considering the shift due to the parabolic mirror.

To further confirm the presence of Ge in the composites and perform a more extended chemical analysis, Electron Diffraction X-Ray (EDX) joint to SEM imaging is performed. Figure 5.8(a) shows a SEM image of the area imaged in 5.4(b), with both types of microflakes. In Figure 5.8(b) the corresponding color maps for the main chemical elements are displayed: silicon (Si, in green), oxygen (O, in yellow) and germanium (Ge, in red). The carbon contained in the methyl groups is not

probed because these functional groups also belong to isopropanol, whose organic traces on top of the microflake would not prove a specific CH_3 bonding. Based on the comparison of the SEM image with the EDX mapping, it is clear that all the microstructures consist of germanium. Interestingly, a major difference is revealed by Figure 5.8(d): some flakes and in particular the smaller ones do not contain oxygen. When we correlate the charging effects seen in the SEM images with the chemical composition of the flakes, it turns out that the oxidized flakes are the ones that gets charged under the electron beam. Another example of EDX map confirms the nature of different microflakes (Figure 5.9).

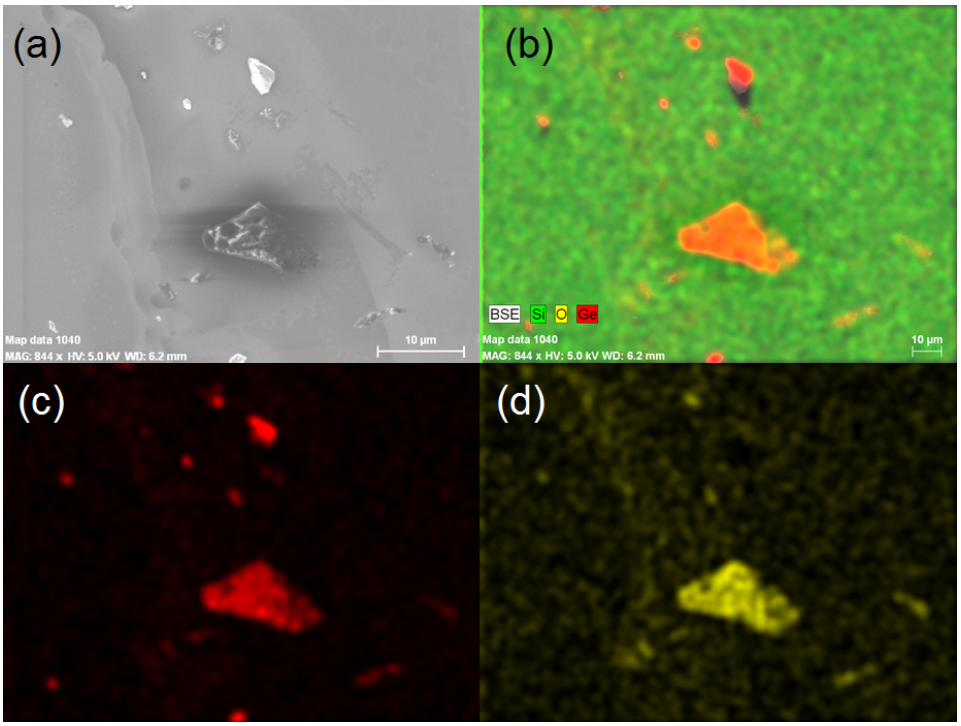

Figure 5.8: SEM-EDX map of two $GeCH_3$ microflakes. (a) SEM image, V=5kV, I=100pA. (b) Superimposition of EDX Si, O and Ge signal. (c) EDX map of Ge signal. (d) EDX map of O signal.

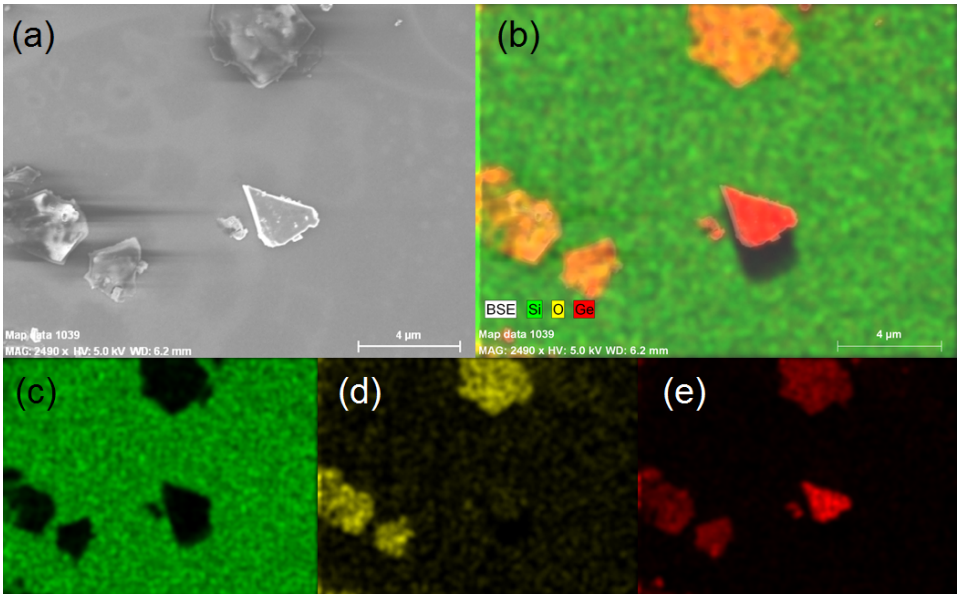

Figure 5.9: SEM-EDX map of an area containing multiple $GeCH_3$ microflakes. (a) SEM image, V=5kV, I=100pA. (b) Superimposition of EDX Si, O and Ge signal. (c) EDX map of Si signal. (d) EDX map of O signal. (e) EDX map of Ge signal.

The presence of oxygen in the EDX analysis could indicate the oxidation of some microflakes, but is also consistent with the presence of water molecules intercalated between the $GeCH_3$ layers (which were not evacuated by the annealing performed at $\sim 250°$ in vacuum). As detailed in subsection 1.4.2, $GeCH_3$ can oxidize when exposed to air during the synthetic process. No treatment with HCl was performed to remove the oxide and substitute the Ge-O bonds with Ge-Cl ones [140]. While the Raman signal was too weak to determine the presence of vibrational modes related to Ge-O bonds, it is possible to use cathodoluminescence (CL) and provide a deeper insight into the oxidation of the microflakes. CL was performed on the GeCH3/Au sample to have a local information about the optical properties. On a small area of gold no signal is detected above the background noise. When a larger area containing microflakes is excited as in Figure 5.10(a), a broad peak centered at 1.9 eV and with a fwhm of 250 meV is detected (Figure 5.10(b)). It is difficult to obtain a signal when exciting a single flake, as the one at the center of Figure 5.10(a), and it is necessary to integrate over the response of multiple not-oxidized flakes. These measurement confirm the recent results obtained in [141]. PL experiments show a peak at a similar energy that shifts to 1.6 eV for dehydrated flakes.

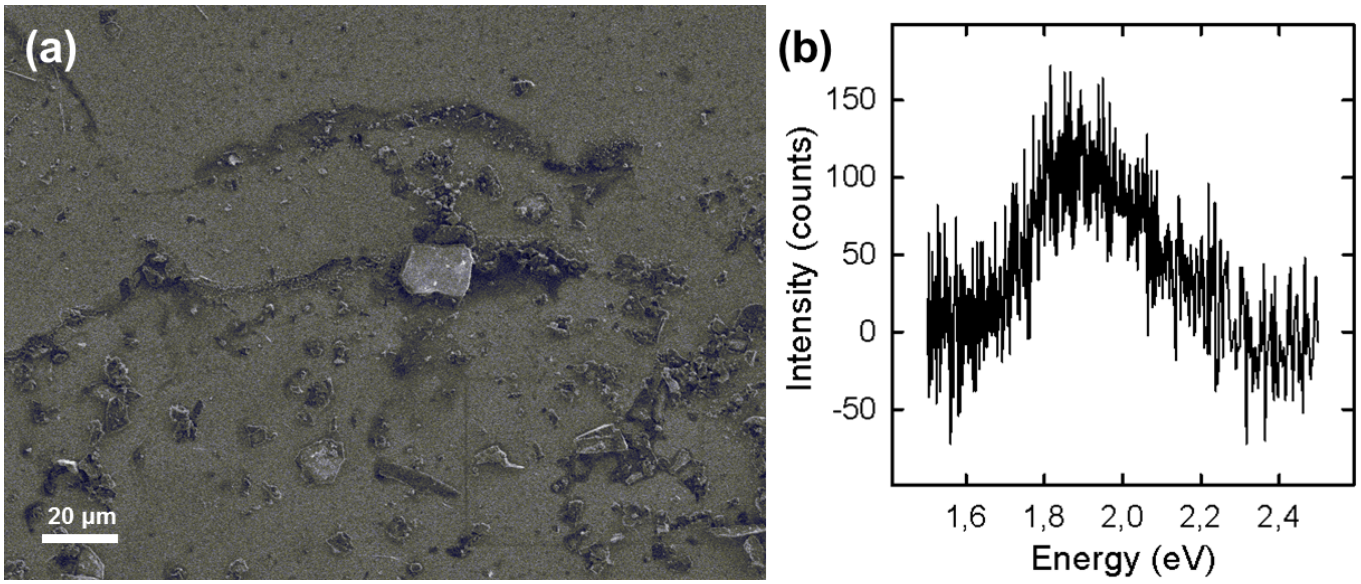

Figure 5.10: (a) SEM image of the area analyzed with cathodoluminescence, V=5kV, I=100pA. (b) Cathodoluminescence spectrum measured on the area seen in (a).

The origin of the emission above the band-gap lies into the distortion of the bonding framework of $GeCH_3$, which favors an optical transition to a lower valence band state with a higher oscillator strength than the 1.6 eV one [141]. To set oursevelves free from the disparity in oscillator strength, STS measurements were performed. One tip was contacted with a small microflake under study and used as ground. The sample was switched in floating mode and the high-resolution tip of the multi-probe equipment was approached in tunneling mode. The use of a STM tip as the ground forces the current to flow through the flake, avoiding possible artefacts in the data interpretation due to the band-gap of the Si(111)-B surface. The average of 20 spectra is shown in Figure 5.11(a). The slope of the curve changes around $\sim$ -0.8 eV and around $\sim$ +0.8 eV. This variation can be observed also in the numerical derivative in Figure 5.11(b). The central part of the spectrum matches with a band-gap of 1.5 - 1.6 eV. However, the spectrum is not flat and current flows inside the gap. This can be explained through the numerous states inside the gap that are produced by point defects, mainly Ge vacancies and Ge divacancies [142].

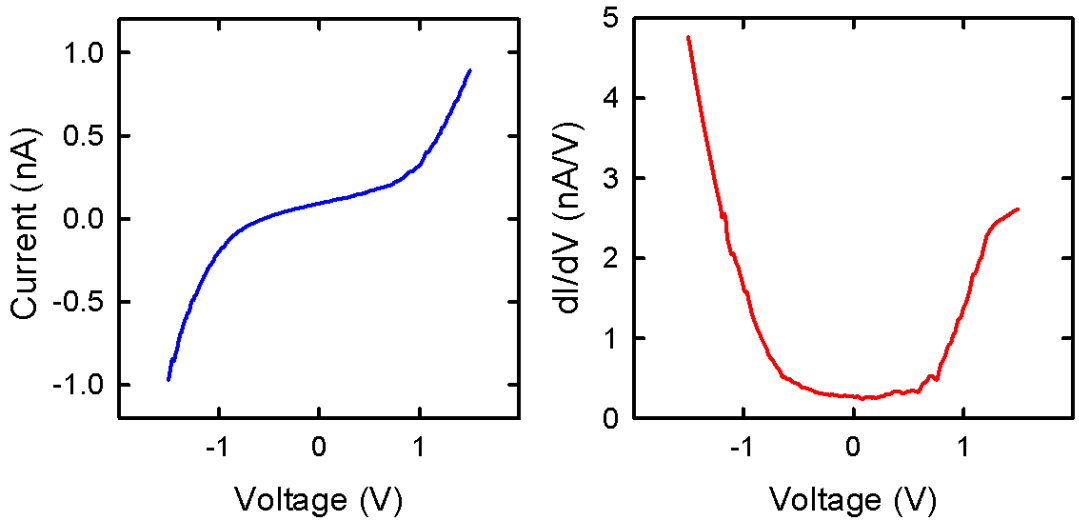

Figure 5.11: (a) Average of 20 STS spectra. V=-1.5V, I=1nA. (b) Numerical derivative of the spectrum in (a).

The STS characteristics confirms the electronic band gap of 1.6 eV. The emission around 1.9 eV is then produced by microflakes with intercalated water between the layers. The bandgap emission at 1.6 eV is not identified by cathodoluminescence due to its low quantum efficiency. This analysis however does not rule out the presence of a thin layer of oxide in the surface layers of the microflakes. The analysis of the surface shows that there are sufficient small and intact flakes to study the transport properties. We determine a ratio of 2:1 between non-oxidized and oxidized flakes.

5.4 Adhesion of the microflakes on the substrate

AFM has been used to determine the thickness of the microflakes, and consequently estimated the number of layers stacked together. Figure 5.12 shows an example of what we consider as a small flake measured in tapping mode. The flake's lateral dimensions are respectively 850 nm and 1.05 μm. As it is often the case, a cluster is present on the highest part and it has been cut out from the scanning area. Figure 5.12(a) shows the topographic image, (b) the derivative and (c) the phase signal. The profile, acquired along the blue segment in Figure 5.12(a), is shown in Figure 5.12(d). The microflake has a thickness in the range between 20 and 23 nm, which converts into a number of layers between 17 and 19.

This flake falls into the range of surface area below 4 μm^2. However, while larger flakes were observed via the optical camera of the AFM, it was difficult to actually image them because they were easily moved by the cantilever outside of the scanning area.

The adhesion between sample and tip can be characterized from the phase image in Figure 5.12(c). Phase imaging consists in the examination of the phase delay between the signal that drives the cantilever oscillation and its output signal. This mode is often more sensitive to elasticity, adhesion, and friction properties of the material than the amplitude signal in tapping mode and it allows to identify unnoticed features [296]. In Figure 5.12(c) glitches between the different scanning lines can be observed on the microflake, while no such difference is observed for the silicon substrate. This rules out an instability of the scan itself and it is an indication of the viscous response of the surface under the application of a force by the AFM tip in tapping mode and a lack of adhesion to the substrate. We notice that the area with a different response in Figure 5.12(c) extends beyond the microflake, partially on the substrate.

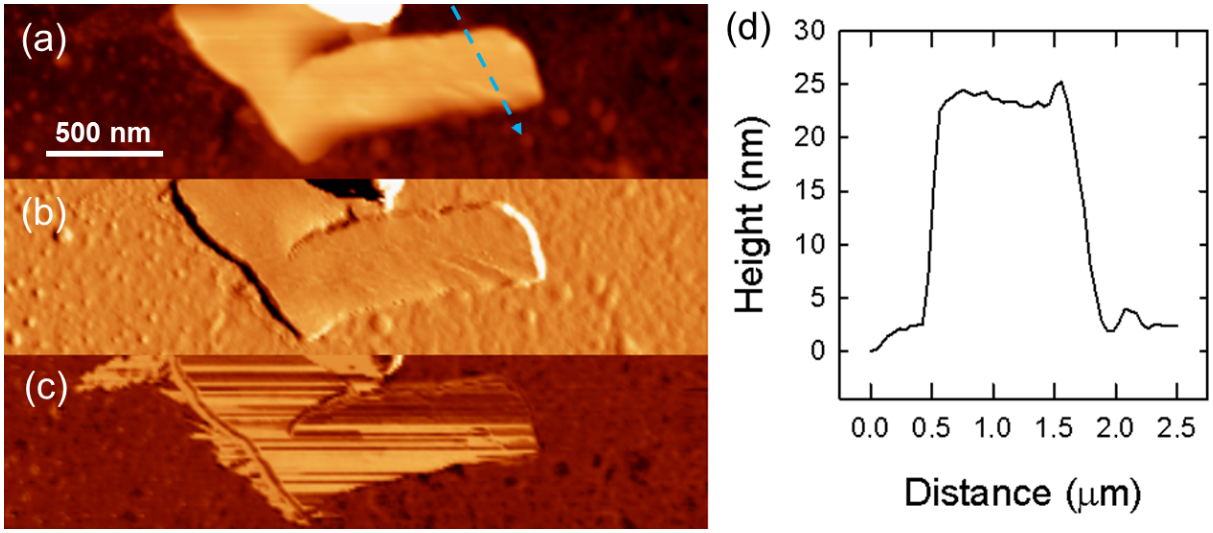

Figure 5.12: AFM cartography of a $GeCH_3$ microflake on Au substrate. (a) Topographic image. (b) Derivative. (c) Phase image. (d) Profile of image (a).

Similar observation are found with the STM tips that were subsequently used for the transport measurements. Both types of microflakes adhere to the tip and are then difficult to be released from the tips. A characterization of the adhesion probability as a function of the tip radius can be performed. We consider as tip radius the curvature radius measured in the SEM images. The adhesion on the tip is never observed for low radius apexes ($r < 250$ nm). Hydrated flakes stick for $r>250$nm, with an higher probability above 500 nm. Non-hydrated flakes stick only with radii higher than 500 nm. No effect is obtained by applying a voltage on the tip (up to ± 10 V) and the only working manipulation consists in applying a mechanical pressure on the surface, by pushing in the z direction with the piezo and then try to slide along $x - y$. The hydrated flakes tended to break during the release process (Figure 5.13), feature which was observed also during the application of a lower pressure in order to contact the tips (Figure 5.14). The non-hydrated flakes did not break during the process, but disappeared from the scan area. When looking at these particular flakes over larger areas, they could not be found. Such a lack of adhesion of the flakes onto the surface explains why the subsequent transport experiments were suddenly halted, as shown below.

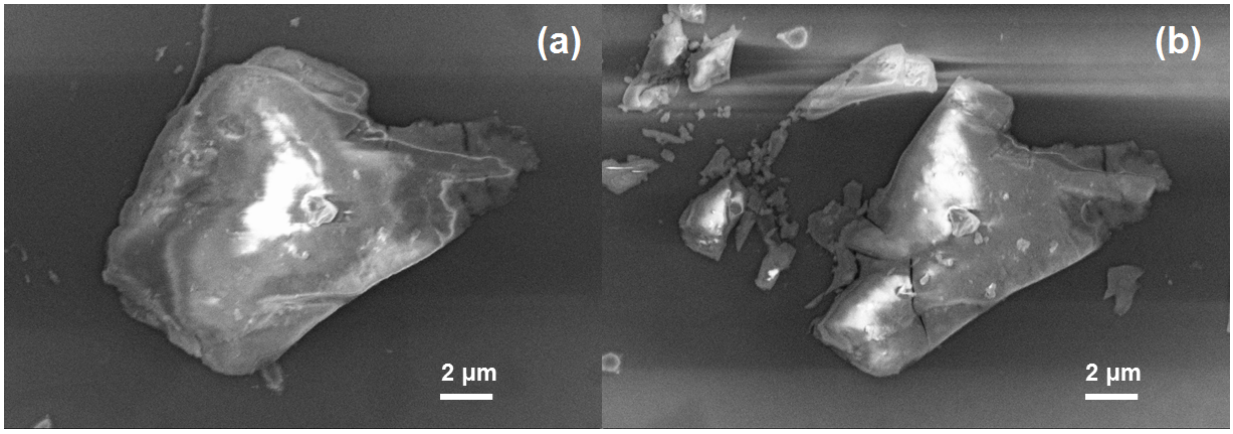

Figure 5.13: (a) SEM image of a hydrated flake. (b) SEM image of the same flake after it sticked to the tip and was released by applying a pressure towards the surface.

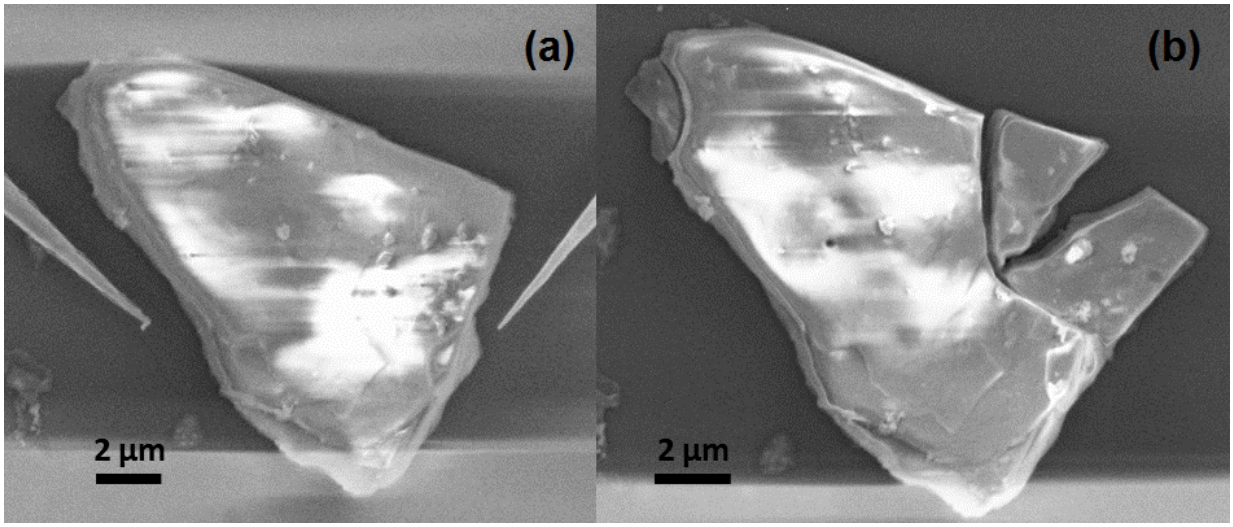

Figure 5.14: SEM image (a) before and (b) after contacting an oxidized flake with a STM tip to measure transport.

While the application of voltage did not produce any effect to detach a flake from the tip, when a second polarized tip is approached it produced a repulsive effect on the flake, for both polarities, thus preventing transport measurement of free-standing flakes. An example is shown in Figure 5.15. In Figure 5.15(a) the polarized tip 2 with +2V is far from the flake. In Figure 5.15(b) tip 2 is moved below the flake to attempt a back contact. Raising the tip induces a sliding motion of the flake along tip 3 as shown in Figure 5.15(c)-(d). This phenomenon was not found to depend on the magnitude of the applied voltage.

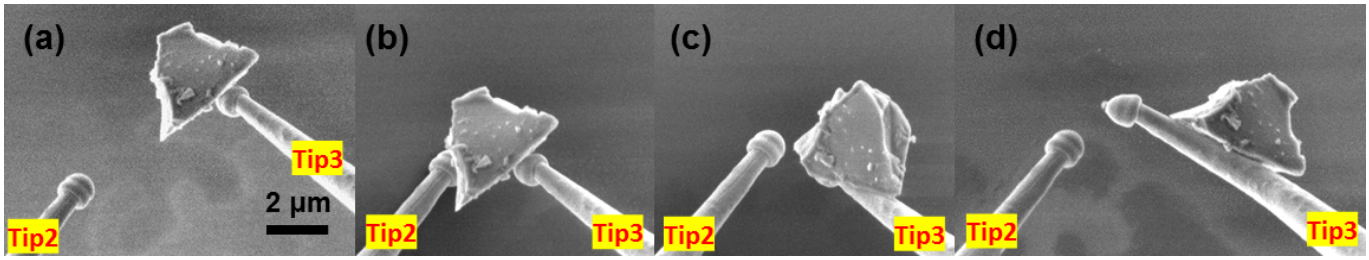

Figure 5.15: Manipulation of a flake with multiple probes thanks to electrostatic interactions. A bias of +2 V is applied to tip 2 whereas Tip 3 is grounded.

The bad adhesion of the flakes on their host substrate that leads to their attachment on the tips was then exploited to have a rough estimation of the thickness of the flakes. Figure 5.16 shows two examples for hydrated flakes. These flakes reveal a thickness one order of magnitude higher compared to Figure 5.12. The original flakes in horizontal position are shown in the corresponding insets. The flake in Figure 5.16(a) has a surface of 295 μm^2 and a thickness of $\sim$ 3 μm, while the flake in Figure 5.16(b) has a surface of 298 μm^2 and a thickness of $\sim$ 1.5 μm.

From the manipulation of the flakes and its cross-sectional observation, it is clear that the flakes are not a single crystal, accounting for the ease of water to be intercalated in the structure. In conclusion, based on the analysis of the microflake sizes, the highest probability to probe a non-hydrated flake occurs for a thickness in the range of 500 nm - 1 μm.

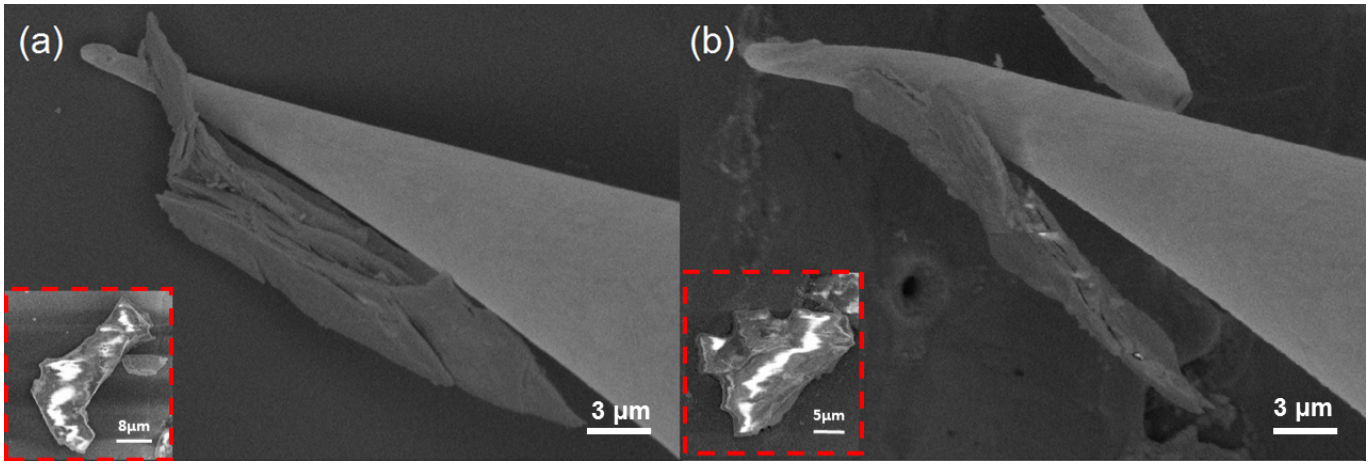

Figure 5.16: (a-b) SEM images of two microflakes whose thickness is in the μm range. The flake in flat position is shown as inset.

5.5 Analysis of the charging under SEM irradiation

The accumulation of charge under the SEM electron beam allows the identification of the hydrated flakes, but its origin is still unclear. Three main hypothesis can be considered:

- The charging influences mainly the topmost surface. This can be due to a thin layer of oxide present only in the surface layers or a higher number of surface defects which allowed the intercalation of water;
- The charging influences the whole flakes, due to their stronger insulating behaviour compared to unoxidized and dehydrated flakes;
- The charging is due to an insulating layer between the bottom of the flakes and the SiO_2 / Si(111)-B surface;

The intrinsic or extrinsic origin of the accumulation of charge is not equivalent when deciding which approach to choose for the transport measurement. If an insulating layer induces the accumulation of charge, the microflake can nevertheless be conductive. In this case, it is sufficient to contact the tips on the microflake, then stop the SEM imaging and wait long enough for discharge. At this point it should be possible to inject a current and perform transport measurement. On the contrary, if the accumulation of charge derives also from intrinsic properties the injection of current could be strongly hindered.

An insulating layer could be produced by the organic traces left after isopropanol evaporation, as those shown in Figure 5.4. In section 5.2 we mentioned that the solution is drop-casted on the sample under nitrogen flux. If a similar deposition is repeated without the nitrogen flux, the evaporation is slower and occurs in a more homogeneous way on the surface. The microflakes are then not just found on the major outskirts of the larger droplets. Numerous micro-droplets form, as those shown in Figure 5.17. The organic traces, differently from Figure 5.12, are detectable not only in the phase image (Figure 5.17(c)), but also in the amplitude and derivative ones (Figure 5.17(b-c)). During the drop-casting process the microflakes glide on the solvant until their final position. Without nitrogen flux, every micro-droplet leaves a halo of organic traces as those shown in Figure 5.17. Under nitrogen flux, the organic traces are concentrated on the outskirt of the larger droplets. However, the presence of the microflakes hinders the evaporation of the solvent present underneath. This is confirmed by Figure 5.12(c), where the viscous response measured in AFM still extends beyond the

surface of the microflake, suggesting the presence of a fluid. While nitrogen flux avoids the halo of the micro-droplets, both techniques do not avoid the microflakes to lie on a "bed" of organic material.

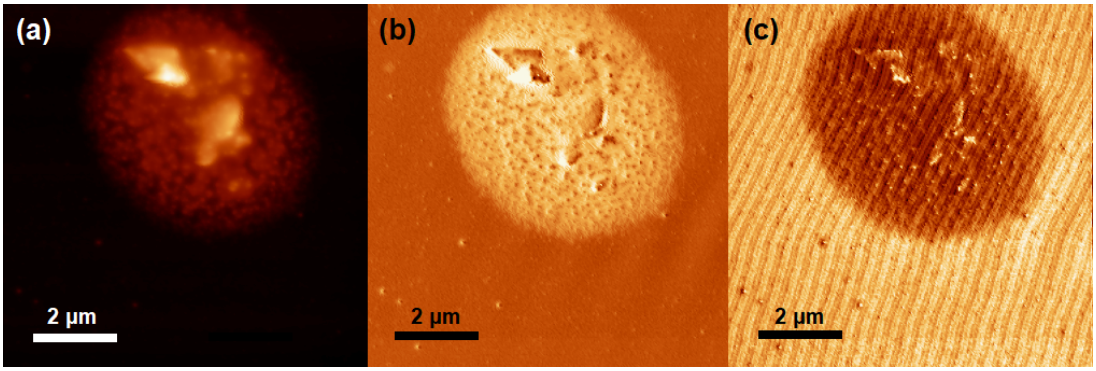

Figure 5.17: Tapping-mode AFM image of a $GeCH_3$/Au area. (a) Amplitude, (b) derivative and (c) phase images.

Are these organic layers insulating? When the sample is manipulated in the multi-probe STM and imaged via the SEM, the traces of isopropanol are best resolved when a negative voltage is applied on the four STM tips. An example is shown in Figure 5.18(a). Here, a voltage of -4V is applied on each tip. In this configuration a clear contrast is observed between the light-grey areas where less residue is present and the dark areas where a thicker residue has been left. This contrast is less evident in Figure 5.18(b), when a voltage of -4V is applied only on tip 3 to perform a tunneling approach on one of the darkest areas. No current was detected in the area below the tip during the approach. Before stopping the approach, the tip got deeply in contact with the surface, twisting its termination to produce a corkscrew shape. The tip apex is now roughly bent where indicated by the red arrow. A new approach is tried on an adjacent light-grey area (red arrow in 5.18(c)). Differently from the previous approach a current is detected, avoiding a new crash on the surface. The different approaches in Figure 5.18 demonstrate that isopropanol organic traces can create layers on the surface thick enough to be insulating.

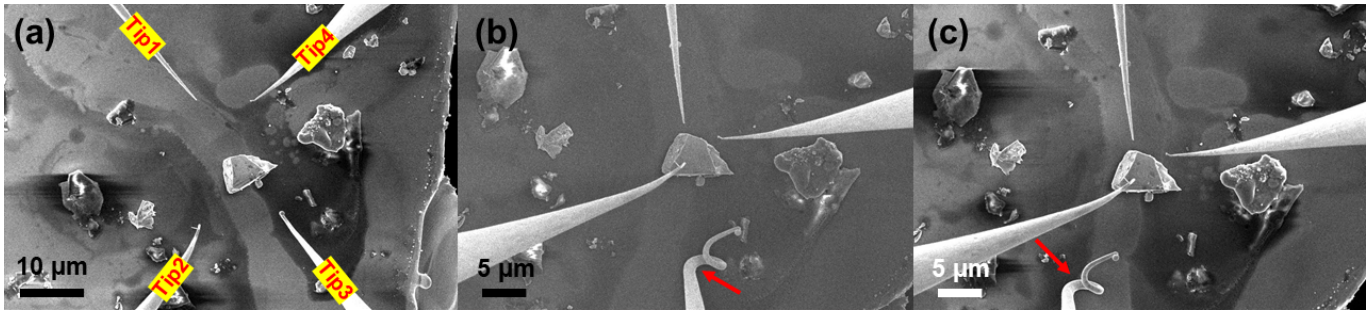

Figure 5.18: (a) Large scale SEM image of an area of the $GeCH_3$/Si(111) sample containing multiple flakes and solvant organic traces. A voltage of -4V is applied on the four tips. (b) Large scale SEM image of the same area in (a). No voltage is applied on tips 1, 2 and 4. -4V are applied on tip 3. (c) Large scale SEM image of the same area in (a) and (b). A voltage of -4V is applied on the four tips. SEM parameters: V=5kV, I=100pA.

To further prove that the organic layer is not only insulating, but the very source of the accumulation of charge, solvent substitution is performed with a lighter polar solvent, methanol.

- Part of the original flakes' solution in isopropanol is centrifuged at 7000 rpm for 1 minute;
- Methanol is then added and the solution is centrifuged again;

- Methanol is added and left evaporating at 5mbar and 50°;
- Methanol is re-added;

The final solution is drop-casted on a gold substrate and the result is observed with the SEM. Figure 5.19(a) shows an example of organic traces left by methanol after its evaporation. At the borders of the original droplets, a few microflakes can be observed. We notice that none of them are charged. A closer look at some flakes is given in Figure 5.19(b).

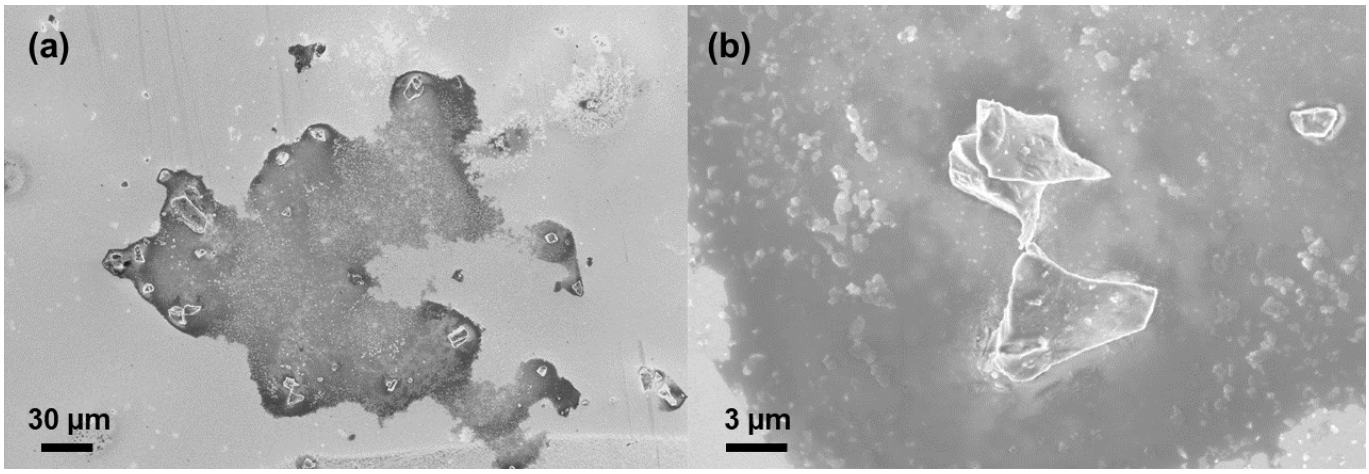

Figure 5.19: (a) Large scale SEM image of a droplet of methanol solution containing $GeCH_3$ on a gold substrate. (b) SEM image of $GeCH_3$ flakes. V=5kV, I=100pA.

The distribution of the flakes' surface on the Au sample is shown in Figure 5.20. As for the deposition from the isopropanol solution, the classification via the top surface is tentative because those flakes are not lying flat on gold. 74 flakes were analyzed. The number of flakes decreases exponentially as a function of the surface area, as it was the case for the isopropanol solution in Figure 5.5. No flake is found to charge under the SEM electron beam.

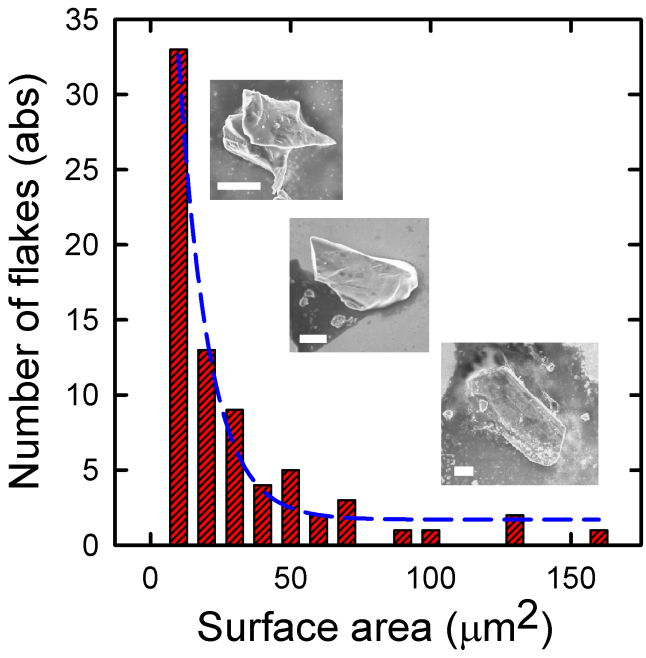

Figure 5.20: Distribution of $GeCH_3$ microflakes found on the Au sample from methanol solution as a function of the size of their top surface. The SEM images of 3 flakes of increasing surface are also shown as insets. The scale bar is always 2μm.

While Figure 5.5 data dealt with a deposition from an isopropanol solution on a Si(111)-B substrate, no qualitative difference was observed when the same deposition was repeated on a gold substrate to perform Raman and cathodoluminescence measurements. This comparison rules out a responsibility of the silicon oxide. The main role of the solvent in the accumulation of charge is then proved. Methanol is a lighter molecule than isopropanol: its evaporation from the interface between the bottom of the flake and the substrate leaves a thinner residue, which does not impede the discharge process after the SEM irradiation.

If the solvent is responsible of the accumulation of charge, however, why it affects mainly the hydrated flakes? An indication is given by the analysis of Figure 5.16. The hydrated flakes are poly-crystalline: this can be an intrinsic property of the synthesis, or the poly-crystallinity can be originated from an insufficient sonication before the drop-casting. The second hypothesis is supported by the higher number of flakes with a smaller area in Figure 5.20 from the methanol solution, which did undergo a few centrifugation steps compared to the isopropanol solution in Figure 5.5, and an absence of flakes with a surface larger than 170 μm^2. The poly-crystallinity then accounts not only for the ease of water intercalation, but for a larger surface too. The larger surface in turn produces an higher amount of non-evaporated organic trace between the flakes and the surface. This insulating layer is then responsible for an accumulation of charge under SEM irradiation.

In the next section, we will perform transport measurements on small flakes deposited from isopropanol. The reason is that the charging allows the identification of the hydrated poly-crystalline flakes, which are not representative of the properties of the intrinsic material.

5.6 Transport properties

5.6.1 Transport in non-hydrated microflakes

Non equidistant 4 tips

As explained in section 2.5.2, the safer configuration to measure the resistivity of a sample with multi-probe STM is a non equidistant configuration where only one tip is moved and the other 3 tips are left in contact at a fixed equal distance from each other.

Due to the very limited thickness of the native SiO_2 layer it is possible to approach the 4 STM tips in tunnel mode on the substrate where organic traces are not present. V=-4V and I=50pA are used as feedback parameters. The tips are then retracted of 3-4 μm and a tentative tunnel approach is performed on the flakes. A tunnel current is detected on the sample, avoiding any crashing of the tip. We note that the tips have already been used to characterize other flakes, accounting for their bad shapes.

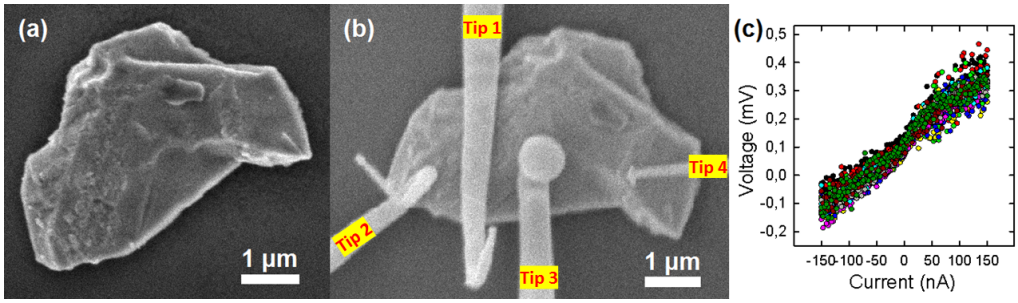

Figure 5.21: (a) SEM image of a $GeCH_3$ microflake. (b) SEM image of the flake contacted by 4 STM tips in a non equidistant configuration with $x = 1.8\mu$m. (c) Example of 20 curves acquired for a distance between tip 3 and tip 4 of $x = 1.8\mu$m.

Tips 1-2-3 are then contacted at 1 μm separation and not moved during the run of experiments, as seen in Figure 5.21(b). The position (within a certain acceptable uncertainty) of the second tip is known due to the moment the contact itself was created by moving the tip towards the flake. Tip 4 is moved from 600 nm to 2.8 μm, at the extreme of the sample. An example of 4-probe transport measurement is shown in figure 5.21(c). The independent variable is the current that is injected between tip 2 (the source, where a voltage is applied) and tip 4 (the sink, which is grounded). The voltage drop between tip 1 and tip 3 is measured as a function of the injected current. The data follow a linear trend and are reproducible between different curves. The noise level is low: for every injected current there is a maximum dispersion in the measured voltages of 0.15 mV. Figure 5.22(a-i) show the evolution of the position of tip 4. Compared to the acquisition of Figure 5.21, the measurements relative to $x = 1.2\mu$m which are shown in Figure 5.22(j) are much noisier (up to 0.6 mV) and will not be considered in the following analysis. Figure 5.22(k) shows the resulting resistances for the other values of x. The log scale is used to highlight how the resistance is always in the same range.

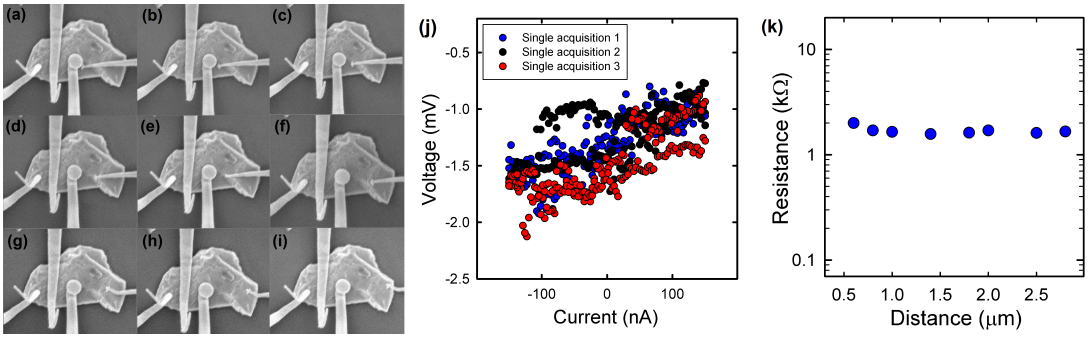

Figure 5.22: (a-i) Evolution of tip positions for a non equidistant 4-points measurements. (j) Selected 4-probe measurements curves for $x = 1.2\mu$m. (k) R vs x dependence. x is the distance between tip 3 and tip 4.

An offset is needed in order to fit with the equations in section 2.5. The 2D fitting curve and three 3D fitting curves in the range of the standard deviation are showed in Figure 5.23. R^2 of 2D fit is 0.57 while it is 0.69 for the 3D case. The 3D equation fits better the experimental data. The value of $\frac{\rho_{3D}}{2\pi}$ is $0.31 \pm 0.09 \cdot 10^{-3}\Omega\cdot$ m. This produces $\rho_{3D} = 1.9 \pm 0.6 \cdot 10^{-1}\Omega \cdot$ cm.

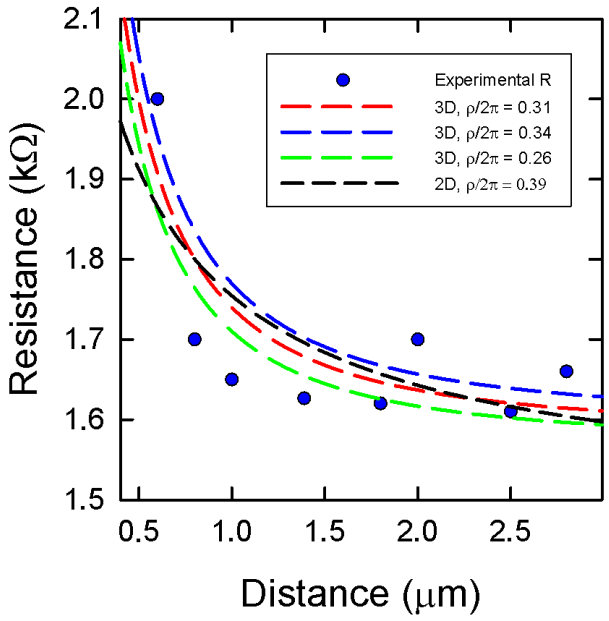

Figure 5.23: Fitting curves for 3D case and $\frac{\rho_{3D}}{2\pi} = 0.26$ (green), 0.31 (red) and 0.34 (blue) $\cdot 10^{-3}\Omega\cdot$ m, and 2D case for $\frac{\rho_{2D}}{2\pi} = 0.39 \cdot 10^{-3}\Omega\cdot$ m (black).

Near border correction

The good agreement of both models with the data is however questionable. A possible reason comes from the fact that both equations are valid for an infinite surface on both x and y. Tip 1 is in contact very near to the border of the sample. As it is fixed, it does not affect the x-dependence apart from a possible multiplication factor which affects in the same way every value of resistance. On the other hand, tip 4 moves and approaches the physical border of the sample, and this leads to a correction factor [297, 298]. Let's take a configuration with 4 equidistant tips at s from each other in a linear configuration (from tip 1 to tip 4, from left to right) perpendicular to a border, with tip 4 at a distance d from the border. This situation can be treated via the charge image method, by inserting a positive charge at distance $d + 3s$ and a negative one at d. This produces a voltage on tip 2 of value:

$$V_2 = \frac{I\rho}{2\pi}\left(\frac{1}{s} - \frac{1}{2s} - \frac{1}{2d+s} + \frac{1}{2d+5s}\right) \tag{5.1}$$

The equation for tip 3 is similar and this leads to $V = V_2 - V_3$:

$$V = \frac{I\rho}{2\pi s}\left(1 + \frac{s}{2d+s} - \frac{s}{2d+2s} - \frac{1}{2d+4s} + \frac{1}{2d+5s}\right) \tag{5.2}$$

This means that the bulk resistivity can be written as $\rho = 2\pi s(V/I)F = \rho_{meas} \cdot F(d/s)$ with:

$$F = \left(1 + \frac{s}{2d+s} - \frac{s}{2d+2s} - \frac{1}{2d+4s} + \frac{1}{2d+5s}\right) \tag{5.3}$$

In our case the 4 tips are not equidistant, and this simplifies the equation. For tip 2, tip 1 is fixed at 1 μm and tip 4 moves at 1+x; consequently, their images are at 8-x and fixed at 10 μm. For tip 3, tip 1 is fixed at 2 μm and tip 4 moves at x; consequently, their images are at 7-x and 9 μm. Then:

$$V_2 = \frac{I\rho}{2\pi}\left(1 - \frac{1}{1+x} - \frac{1}{8-x} + \frac{1}{10}\right) \tag{5.4}$$

$$V_3 = \frac{I\rho}{2\pi}\left(\frac{1}{2} - \frac{1}{x} - \frac{1}{7-x} + \frac{1}{9}\right) \tag{5.5}$$

$$V = V_2 - V_3 = \frac{I\rho}{2\pi}\left(\frac{22}{45} + \frac{1}{x} - \frac{1}{1+x} + \frac{1}{7-x} - \frac{1}{8-x}\right) \tag{5.6}$$

$$F' = \left(\frac{77}{45} - \frac{1}{x} - \frac{1}{1+x} - \frac{1}{7-x} - \frac{1}{8-x}\right)^{-1} \tag{5.7}$$

The correction factor is shown in blue in Figure 5.24. The corrected values of resistance are then plotted in red. The correction is very small, but has an effect on the previous fitting: the R^2 of the 3D fit is now 0.81, for $\frac{\rho_{3D}}{2\pi}$ of $0.40 \pm 0.09 \cdot 10^{-3}\Omega\cdot$ m, or $\rho_{3D} = 2.5 \pm 0.6 \cdot 10^{-1}\Omega \cdot$ cm. The best fit for 2D transport gives $\frac{\rho_{2D}}{2\pi} = 0.51 \pm 0.15\ \Omega \cdot$ m; it has also improved ($R^2 = 0.71$), but still worse than a bulk-like transport.

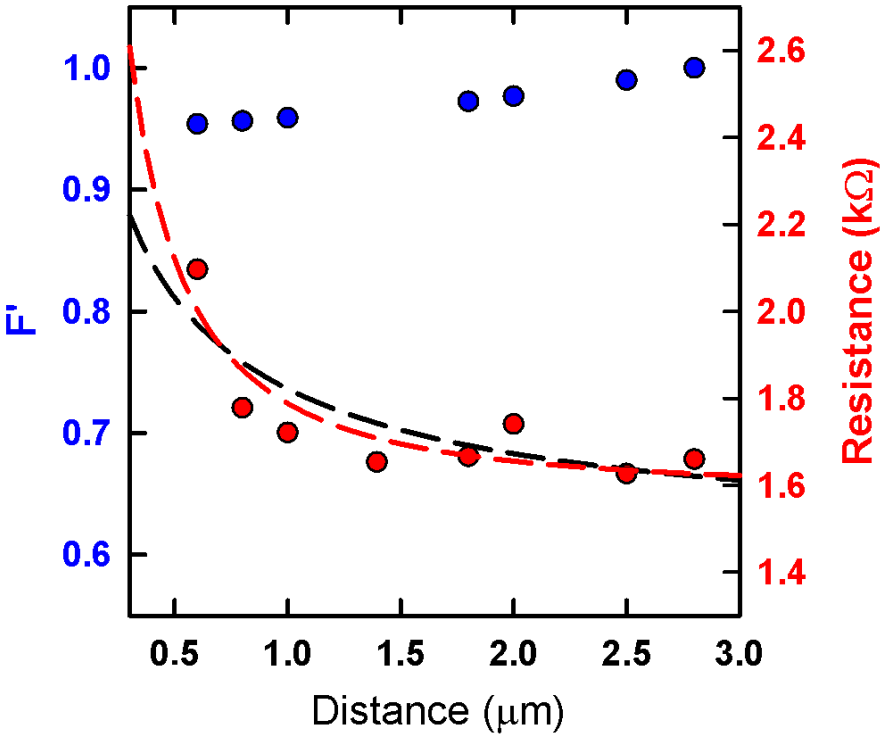

Figure 5.24: Correction factor F' (blue) and corrected resistances (red) for the dependence in Figure 5.22. The dashed curves are the best fit for 2D transport (black) and 3D transport (red).

Limited thickness correction

Another possible correction to be introduced is the one relative to the finite thickness of the microflake. The flake height is checked via the relative comparison of the piezoelectric elongation when the STM tip is in tunnel mode above the flake and above the Si(111) surface. Heights of $\sim$ 520, 560, 800 and 900 nm were found respectively for tips 1, 2, 3 and 4.

The resistivity of an infinite sheet of finite thickness t can be formally expressed as [298]:

$$\rho = R^{\text{line}}_{\text{sh}-2\text{D}} \cdot t \cdot F''\left(\frac{t}{s}\right) = \left[\frac{\pi}{\ln 2}\frac{V}{I}\right] \cdot t \cdot F''\left(\frac{t}{s}\right) \tag{5.8}$$

in the case where s is the inter-distance tips and:

$$F'' = \frac{\ln 2}{\ln\{[\sinh(t/s)]/[\sinh(t/2s)]\}} \tag{5.9}$$

This equation has been calculated via an approximated solution of Laplace's equation [299], but a similar charge image approach is also available through series expansion [297]. We try nevertheless to apply this factor to our case. The correction factor is shown in figure 5.25, blue curve. The corresponding corrected V/I values are shown in red. This value however grows with d, not fitting then with both Ohm law in 3D and 2D transport. On the other hand, it fits with a 3D model when field lines are perturbed by the geometry of the sample, aka $R = 3\rho x/S$, as it happens for the Si(111)-7×7 surface when the tip separation exceeds 100μm (see section 2.5.1). The fit gives $\rho_{3D}/S = 3.3 \cdot 10^{-2}$ k$\Omega\,\mu$m^{-1}. We can estimate an effective cross section of 1μm × 1.5μm, then $S = 1.5\mu\text{m}^2$. After unit conversion this gives $\rho_{3D} = 5 \cdot 10^{-3}\Omega \cdot$ cm.

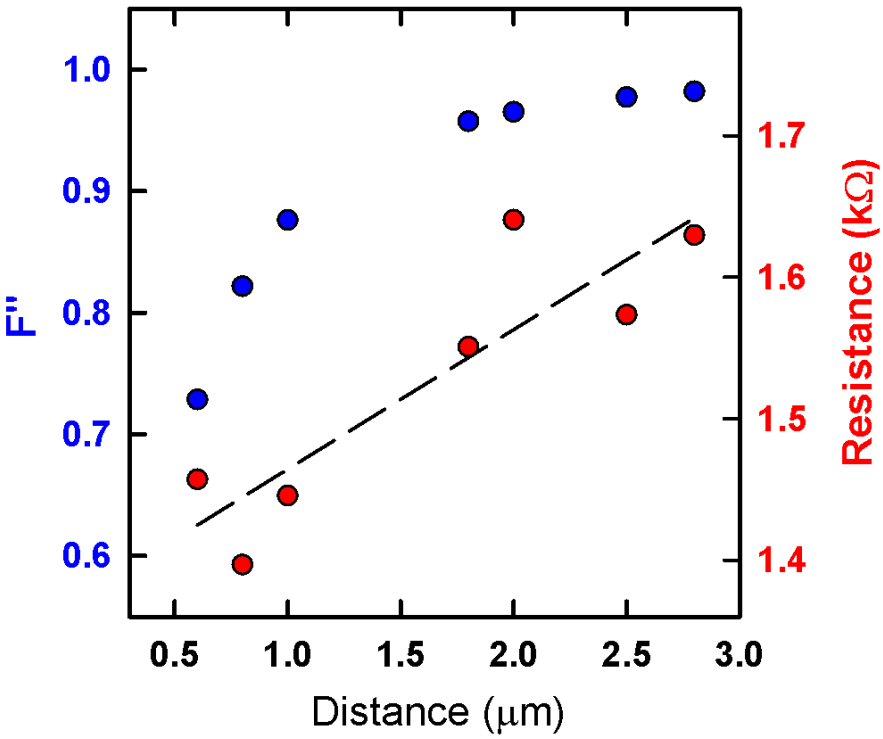

Figure 5.25: Correction factor F'' (blue) and corrected resistances (red) for the dependence in Figure 5.22. The black line is the linear fit for $R = 3\rho x/S$.

It is however questionable if the fit via the 3D model limited by geometry is not redundant in this situation. Using this equation after applying a thickness correction is like accounting for the same phenomenon twice. If this model actually applies, by observing the equation it could be concluded that without varying the position of V_1 and V_2 there should be no resistance variation. The rise in resistance for lower distance would then be explained by an interaction of the injecting tip on one of the two measuring ones. If this interpretation is valid, we can estimate the resistivity from $R = 3\rho x/S$ and the geometry of the flake. As before, we use an effective cross section of $1\mu\text{m} \times 1.5\mu\text{m}$, and $L = 3\mu\text{m}$. If $R = 1.7k\Omega$ on average, $\rho = 8.5 \times 10^{-2}\Omega\cdot$ cm. This treatment is not however fully satisfying, and we will move to a 4 equidistant tips configuration.

4 equidistant tips

Because of the large uncertainty of the correction factor, discriminating between 2D and 3D transport is not evident for non equidistant tips. It is rather straightforward for 4 equidistant tips, placed at a distance d one from the other. Indeed, for a 2D transport, the resistance is constant as a function of d. The field lines start to be influenced when the distance between the external tips ($3d$) becomes comparable to the thickness. As measured before, the typical non-oxidized flakes with a lateral size suitable for 4 probe measurement show a thickness in the range of the micrometer. For small d a 3D transport should respect a pure 3D equation, going as $1/d$ as detailed in section 2.5. A first example of this behaviour is shown in figure 5.26(a). The microflake has approximately an area of $10\mu\text{m}^2$ and a maximum linear distance available for the measurements of 4.5 μm. The thickness is estimated to be again around 1μm, as determined with the piezo elongation method. In figure 5.26(b) it can be seen that the dependence fits with the 3D model without geometrical limitation of the field lines (as visible in the inset). The fit yields a value of $\rho_{3D} = 6.6 \pm 0.4 \cdot 10^{-1}\Omega\cdot$cm. The experiments were not performed with a larger tip separation because tip 3 stuck to the microflake during the course of the analysis.

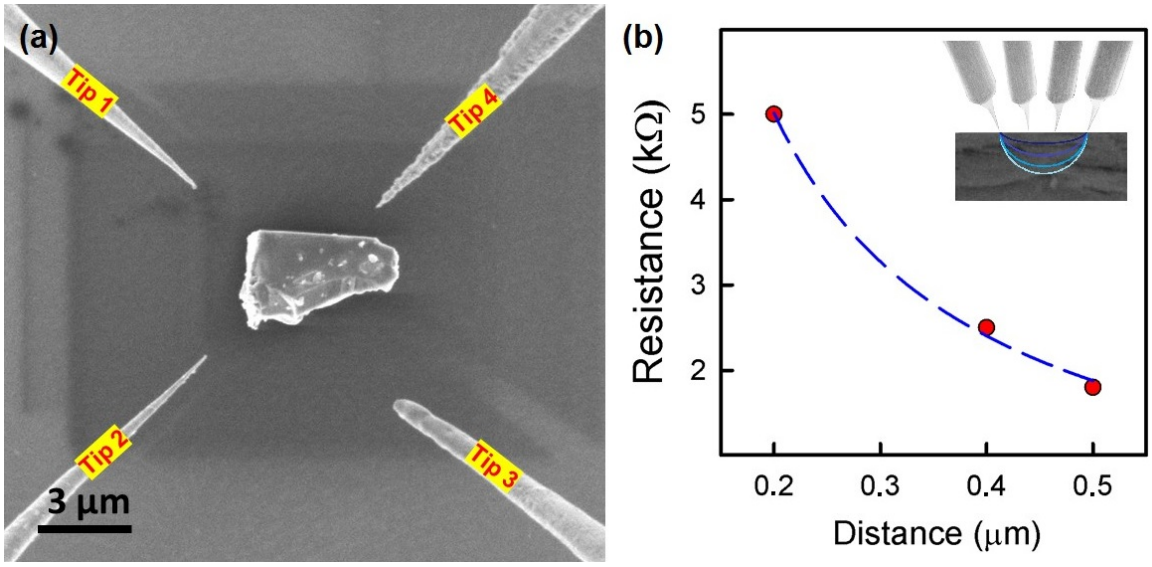

Figure 5.26: (a) SEM image of a $GeCH_3$ microflake with 4 STM tips in the vicinity of the flake. (b) 4-points linear equidistant transport measurement and fitting curve. The inset shows the current lines flowing into the volume.

On the other hand, transport on bigger flakes is expected to be limited by the geometry. An example is shown in Figure 5.27. Figure 5.27(a) shows the SEM image of the flake: its area is $\sim 26\ \mu m^2$, the maximum length is 10μm and the thickness is measured on average of 1μm with the piezo elongation method. The result of the measurement is shown in Figure 5.27(b).

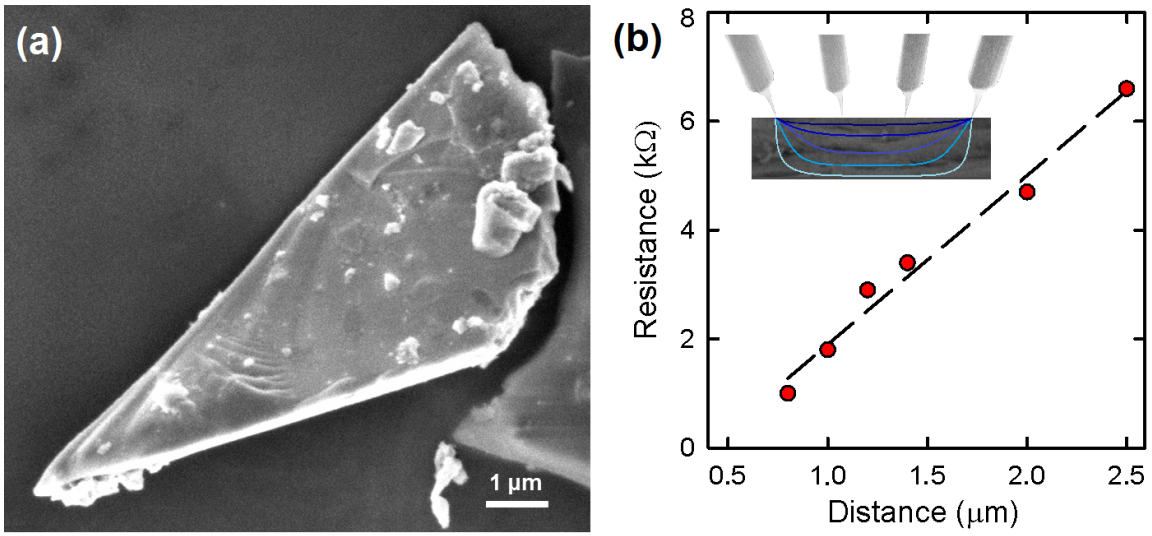

Figure 5.27: (a) SEM image of a $GeCH_3$ microflake. (b) 4-points linear equidistant transport measurement. The inset shows the current lines flowing into the volume, limited by the finite thickness.

The behaviour observed is linear, with a possible slope variation around 1.2 μm. The proportionality with $L = 3d$ confirms that the field lines are limited by the sample geometry, as in the inset of figure 5.27(b). The fit provides $\rho_{3D}/S = 1.03\ \mathrm{k\Omega}\mu m^{-1}$. We can estimate a thickness of 1 μm, and a minimum cross section of 2.5 μm (considering the measuring voltage tips). The resulting resistivity is $\rho_{3D} = 2.6 \cdot 10^{-1}\Omega\cdot$ cm. This value is in the same order of magnitude than the resistivity of the previous flake in Figure 5.26.

Transport along c axis

A 3D transport is a bit surprising, because 2D transport was expected for this layered material. The influence of the volume raises an important question, whether or not there is a negligible transport along the c direction of the microflake. It is often assumed that layered materials in nature have very different properties when intra- and inter-layer features are studied. The transport is usually favored inside the single layers. In the case of graphite, there is a factor of 100 between in-plane $\rho_{//}$ and intra-plane $\rho_{\perp}$ resistivities [300]. This asymmetry can grow to 10^3-10^4 for highly oriented pyrolytic graphite (HOPG) due to the reflection of π-electron waves by the characteristic stacking faults in the material [300]. MoS_2 has similar properties: resistivity in the 10-$10^3\Omega$ cm range has been reported for $\rho_{//}$ and 10^2-$10^5\Omega$ cm for $\rho_{\perp}$ [301]. Other values of resistivity are shown in the table 5.6.1. Some materials have properties that differ from this, but a few exotic phemonena like charge density wave are usually in place [302].

Material	$\rho_{\perp}/\rho_{//}$
Graphite [300]	10^2
HOPG [300]	10^3-10^4
MoS_2 [301]	10^2
$NbSe_2$ [302]	5
$TaSe_2$ [302]	20
$ZrTe_5$ [302]	10^2
BSCCO [303]	10^4

Table 5.1: Anisotropy in resistivity in layered materials.

It is difficult in our case to test the different resistivity of the in-plane vs out-of-plane ρ. One straightforward measurement could be a single tip I-V curve in contact and with the sample grounded, which would force the electric current to flow through the microflake towards the Si(111)-B surface. However, even if a tunnel current can be detected, confirming a transport in the c direction, it has to take into account the contact resistance and does not give an accurate value of ρ.

Another possibility is to find a flake where it is easier to contact its sides. An example is shown in figure 5.28. Tip 2 and tip 3 have been contacted on the side of the microflake, retracting them halfway between the tunnel position on the Si(111) surface and the tunnel position on the top of the flake, then approaching them manually into contact. This geometry resembles the square configuration, actually invoking the theorem of Van der Pauw for an arbitrary configuration. As a first measurement, tip 2 is used as source and tip 3 as sink. This means the injection happens through the volume and tip 1-4 measure the drop of voltage on the surface. An average of 20 curves gives a value of 800Ω (Figure 5.28(b)). A second measurement consists in using tip 1-2 as source-sink and tip 3-4 as V_1-V_2. This means that both injection/collection and the measurement of potential drop are forced to have a volumic characteristics. The result is a slightly higher value of resistance, $2k\Omega$ around 0V, with a lower resistance far from 0V of 0.8-$1k\Omega$ (Figure 5.28(c)). Another configuration which does not invoke Van der Paw is also tried: tip 4 as source, tip 2 as sink. This is another possible path of both current and voltage measurement between different planes. The result is an intermediate value of $1k\Omega$ (Figure 5.28(d)). The difference between transport along $a-b$ and along c does not seem then striking and it is safe to assume that both a surface component and a volume one are involved.

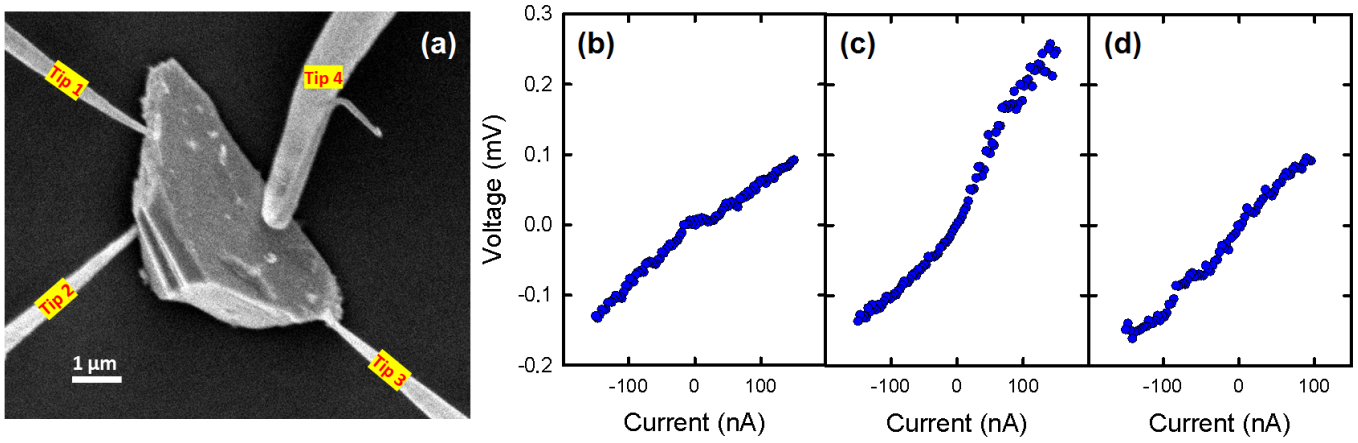

Figure 5.28: (a) SEM image of volumic contact of 4 tips on a $GeCH_3$ microflake. (b-d) Multi-probe STM acquisitions for the flake in (a). (b) Tip 2 is used as source, tip 3 as sink. (c) Tip 1 is used as source, tip 2 as sink. (d) Tip 4 is used as source, tip 2 as sink.

It is difficult to address the origin of this lack of anisotropy. A first candidate is poly-crystallinity due to the aggregation of the flakes in solution. These aggregates could be assimilated to stacking fault defects which usually strongly increase the resistivity in layered materials. Another possibility are the defects produced by the topochemical deintercalation process. The main defect to produce intragap states are the vacancies and divacancies of germanium [142], while the lack of CH_3 is not responsible of such states. These defects could also account for additional transport paths which reduce resistivity on the c axis. Additional measurements with single crystals are needed to answer this question.

Field effect mobility

The $GeCH_3$ flake in Figure 5.27 was chosen for a test of a measure of the field-effect mobility and the doping type. Up to now, the substrate was not biased, allowing floating measurements. Due to the presence of the SiO_2 layer, the Si(111) surface can act as an electrostatic gate. However, the oxide layer is thin, so there is a risk of breaking it by applying a too strong field. This would lead to a direct flow of charge between the highly doped Si(111)-B and the tips through the flake.

The tips are placed at $d = 2\mu$m from each other (as shown in Figure 5.30(a)). We observe that the switch between the floating measurement and the 0V applied from an external source connected to the substrate varies the value of R measured for this separation between the tips, from 4.8 to 2.4 kΩ, see Figure 5.29. Towards negative gate voltages, the measured resistance varies just slightly, from 2.4 to 2.8 kΩ. The same applies between +0.5 and +1.0V. However, at +1.5 and +2V the resistance is higher, 3.3 and 3.4 kΩ. For +2.5V, the oxide breaks and the microflake melts into a sphere (Figure 5.30(b)). By the radius of this sphere and the surface of the flake, a thickness of 1μm can be estimated, confirming the previous guess from piezo elongation.

By the weak trend observed in Figure 5.29 a tentative identification of the doping can be given. The system Si(111)-B/SiO_2/$GeCH_3$ can be thought as a Metal-Insulator-Semiconductor (MOS) capacitor. The application of a voltage on the metallic part acts on the accumulation or depletion of the semiconductor depending on its doping, and the measurement of the resistance via the 4-probe results in a higher or lower value depending on this. A negative gate voltage leads to a decrease of the resistance, while a positive voltage to its increase, suggesting a p-type doping behaviour, consistent with the literature [139].

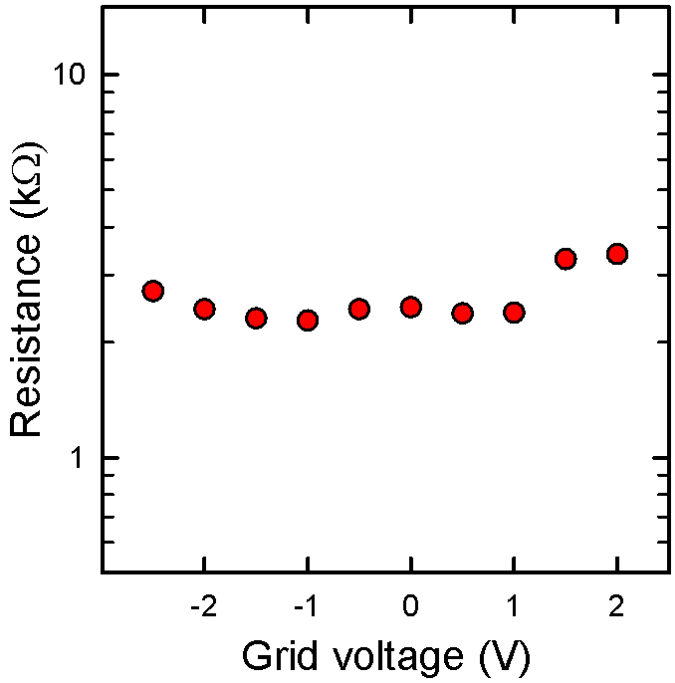

Figure 5.29: Resistance dependence as a function of the gate voltage applied to the Si(111) surface.

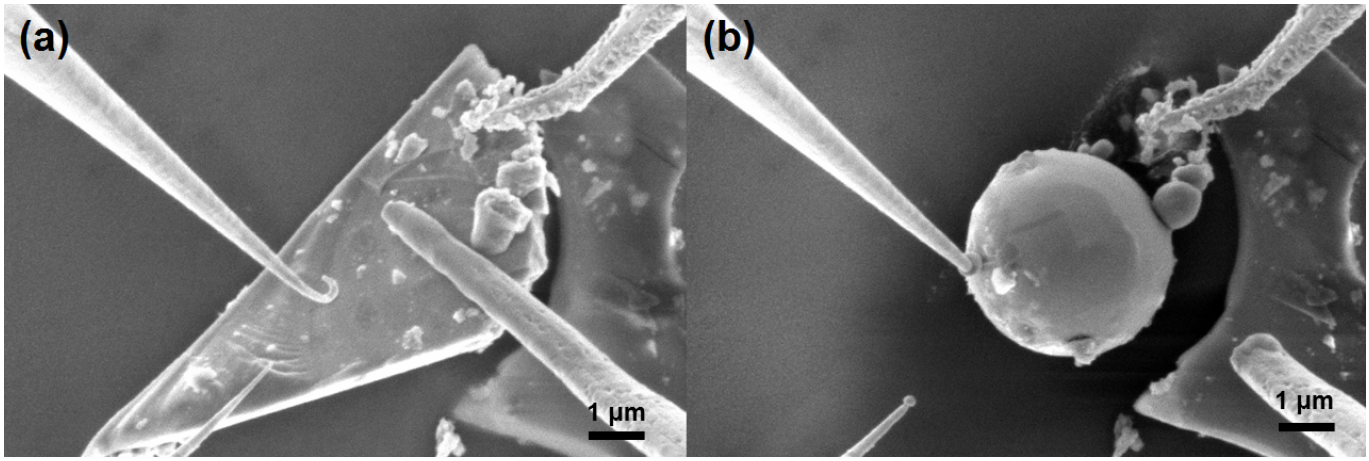

Figure 5.30: SEM image of the $GeCH_3$ microflake (a) before and (b) after its melting.

5.6.2 Transport in hydrated microflakes

The analysis of the non-hydrated microflakes allowed to understand the 3D character of transport in the $GeCH_3$ in exam, their p-doping and estimate a range for the resistivity. Some information can be also obtained by studying the hydrated microflakes.

It is usually impossible to find a tunnel current on the charged flakes. This result agrees so far with what presented in section 5.5. If an insulating layer is present and it is not possible to tunnel through it, the same result should be expected for the double tunnel junction that is formed by adding the microflake on top.

Section 5.5 does not present arguments about the absence of a thin layer of oxide. In the hypothesis that the oxide influences mostly the surface, Tip 1 and Tip 2 in Figure 5.31 are mechanically brought in contact to test the possibility of current injection through the volume. No current however is detected and the force applied during successive attempts of finding a better contact led to breaking both apexes (see Figure 5.31), indicating an insulating layer at the surface of the flake. Another attempt is made in a similar way by contacting Tip 3 and Tip 4 on the side of the microflake, to access multiple layers: the tips are approached on the Si(111)-B surface, then retracted by 200 nm and mechanically moved in contact until the tip apex is bent. Even in this case, no current is detected between the two tips. This is a strong indication of the joint presence of a thin layer of oxide due to air exposure and the intercalation of water due to polycrystallinity.

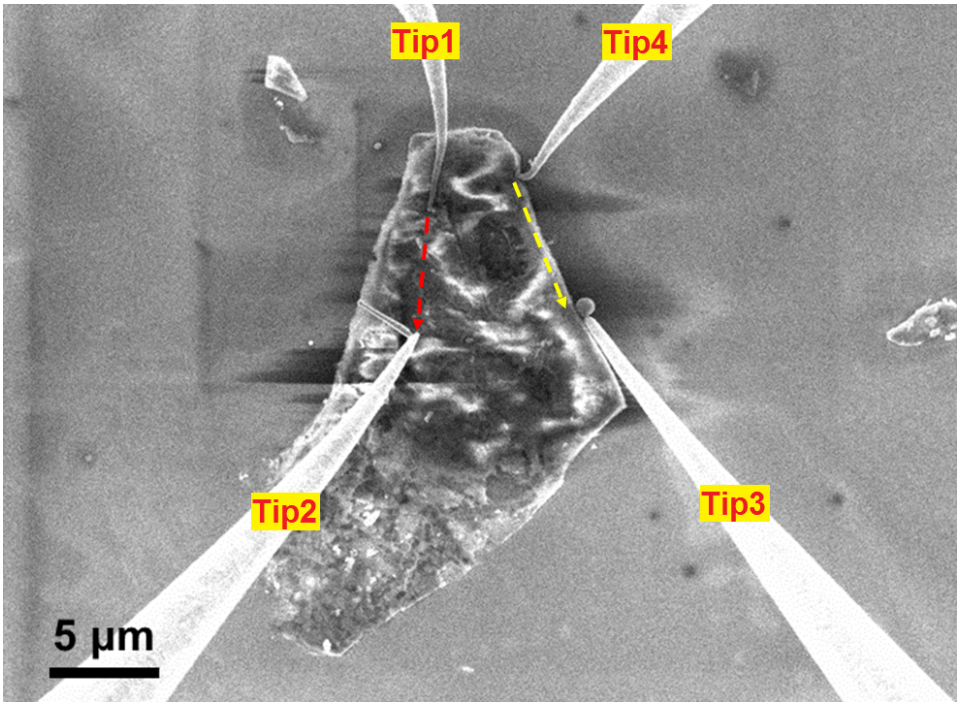

Figure 5.31: SEM image of an oxidized flake, with 4 tips in mechanical contact, V=5kV, I=100pA.

Only in a few particular situation it was possible to measure the transport properties of hydrated microflakes. In Figure 5.32(a) a high-density area is shown, the same already presented in Figure 5.4(c). A few charged microflakes are present. An uncharged microflake is centered between the four tips (highlighted by a red dashed circle). While the region in the lower part of the image is mostly free of microstructures, the microflake is in mechanical contact with a few other in the higher part (indicated by a red arrow). A closer look at the microflake in Figure 5.32(b) shows that it is also lying on a few charged microflakes. It is difficult to understand if the whole area of contact between the flake and the substrate is composed by other microflakes. A tip was contacted and used as ground contact,

and transport measurements were successfully performed. These measurements are reported in the following subsection. After the experiment, the mechanical manipulation of the surrounding area is performed in order to avoid any contact between the flake and other neighboring microstructures. The result is that the microflake charges under SEM irradiation. This experiment shows that the charge accumulated in an oxidized flake can be evacuated through another non oxidized flake.

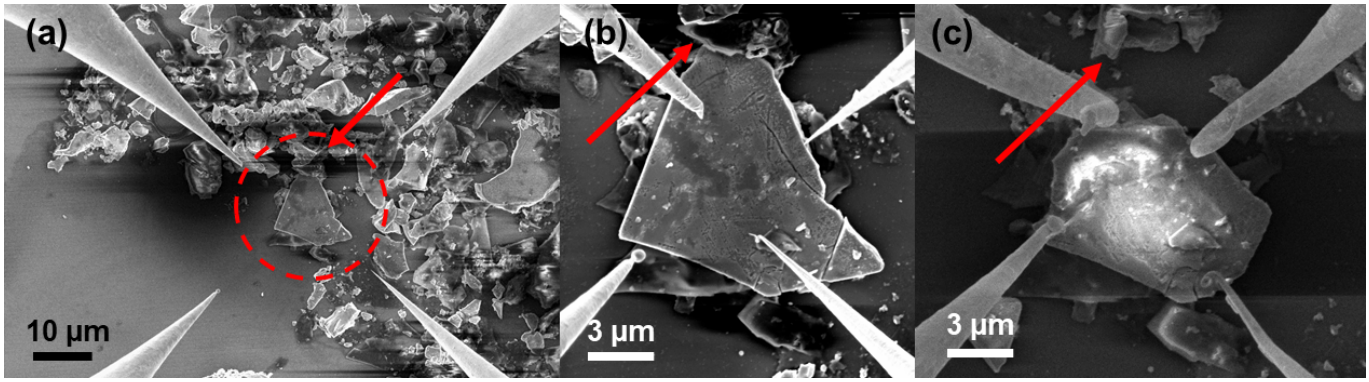

Figure 5.32: (a) Large scale SEM image of a high-density area of $GeCH_3$ microflakes on Si substrate. The dashed red circle indicates the microflake of interest; the red arrow its mechanical contact with other microflakes. (b) Higher magnification of the flake in (a). The point of contact is indicated by the red arrow. (c) SEM image of the $GeCH_3$ microflake in (a-b) after mechanical manipulation of its surroundings. The previous point of contact is indicated by the red arrow.

Anisotropy in transport

The flake in Figure 5.32 has a few defects on the surface, as it can be seen via an higher magnification in Figure 5.33(a). A large darker area is present on the left part of the flake, while multiple stripes creating angles of 120° between each other are present on the rest of the surface. These directions form an angle of 45 ° (or 15°) with the lower border of the microflake.

The specific directions of these defects raise the question on how they influence the transport properties. We assume that a 3D transport characterize the poly-crystalline flakes as well. On the other hand, the larger surface of these flakes allows to perform an angular dependence on a wide distance. While no large anisotropy was found along c in section 5.6.1, no indication was given yet about the anisotropy in the plane.

The four probe measurements are performed on the central part of the flake with a 4 μm square arragement of the probes. The variation of the resistance as a function of the direction of the current flow is shown in Figure 5.34. The change of the direction was achieved by rotating the square and the main directions are indicating in the red square in Fig. 5.34(b). The resistance slightly decreases from 9kΩ to 6kΩ, with a dip down to 1kΩ around 30°. R then grows back to $\sim$ 12kΩ at 90°. The variation between 0 and 90° measured between tips 1 and 4 matches the equivalent one between 180 and 270° measured between tips 2 and 3. A different behaviour is observed between 90° and 180°. The resistance grows from 35 kΩ to 100-130 kΩ around 110-130°, and then decreases back to 50 kΩ. A similar behaviour is observed in the 270°-360° with the maximum between 300 and 320°.

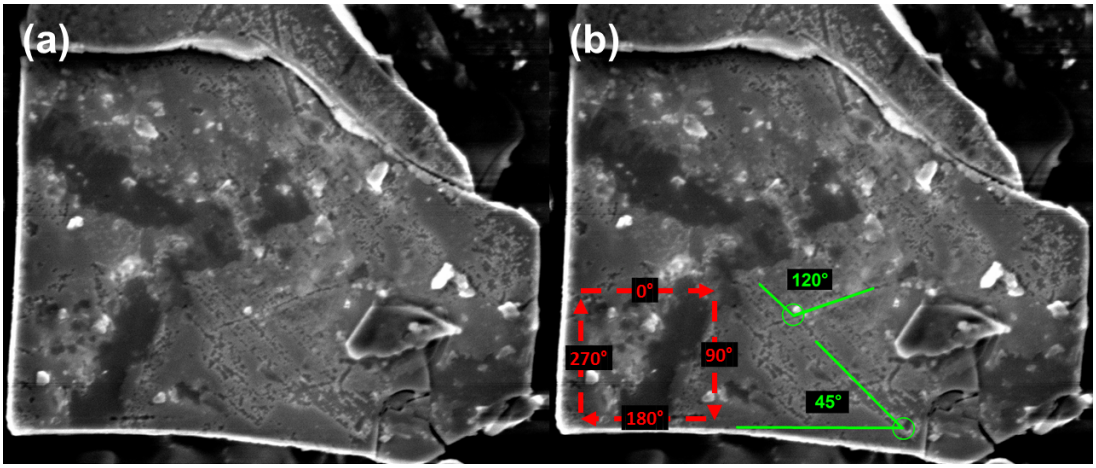

Figure 5.33: (a) Higher magnification of the flake at the end of the square angular dependence to highlight the pattern observed at the surface of the flake. (b) as (a), with labels for indicating the main directions of the current flow directions in the dependence (red) and angles between the typical stripes (green).

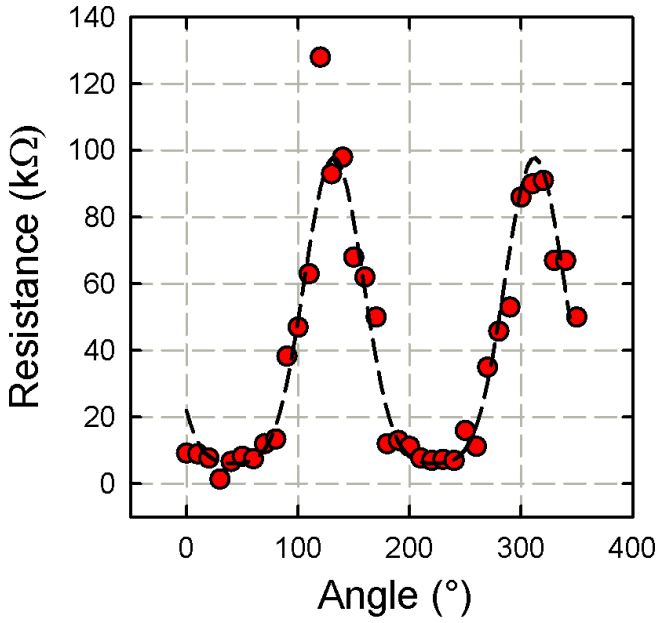

Figure 5.34: (a) Angular dependence of R vs θ in square configuration for the microflake in Figure 5.33. The dashed line is the fitted dependence with equations of section 2.5.2.

The angular dependence via the 4-points square configuration can be fitted following the equations of section 2.5.2. The best fit yields the conductances along the two main directions: $\sigma_x = 3.8 \pm 0.5 \cdot 10^{-6}\Omega^{-1}\square$ and $\sigma_y = 1.14 \pm 0.22 \cdot 10^{-6}\Omega^{-1}\square$; the x axis is rotated of 42.1°, which matches one of the main directions followed by the strips, as indicated in Figure 5.33(c). To obtain a 3D resistivity we need to calculate the reciprocal value of the conductance and multiply it for the supposed thickness of the flake (we use again 1 μm). The resulting resistivities are $\rho_{3D,x} = 26\Omega\cdot$ cm and $\rho_{3D,y} = 88\Omega\cdot$ cm, which are 2 order of magnitude higher than the resistivities found previously. As a further confirmation of the oxidation, the unoxidized flakes stay intact during the measurements by applying a pressure. Here it is not the case: between Figure 5.33(a) at the beginning of the experiment and Figure 5.33(b) at the end, the upper part of the flake and the triangular part to the right broke.

To summarize, we have shown that two different types of crystals exist in the methyl-terminated germanane batch. The largest, around 10 μm or more in lateral dimension, are polycrystalline, contain water molecules intercalated between the layers or have oxidized surfaces and become charged under electron irradiation due to the presence of isopropanol at the interface with the host substrate. The smallest, identified as the purest, have no water intercalated or oxide layer and are then suitable for transport measurements. These measurements showed a transport of holes, which occurs in the volume of the microstructure. This unexpected result for a lamellar material suggests the presence of defects and imperfection in the plane of the layers which call for better control of the synthesis of crystals to make possible the study of the fundamental physical properties of these crystals.

Conclusion

A main goal in materials science is the discovery and the characterization of new materials. Together with perovskites, 2D materials are on the cutting edge of research since 15 years. Despite this enormous effort, there are still numerous systems which received less attention despite the great perspectives they promise. This applies in particular to the IV group equivalents of graphene, as silicene and germanene. Between the different attempts at the synthesis of germanene, we decided to focus on the 2D germanium layer on Al(111). Experimentally, a germanene layer on Al(111) creates two reconstructions: the phase (3×3) and the phase $(\sqrt{7}\times\sqrt{7})$R19.1°. The $(\sqrt{7}\times\sqrt{7})$R19.1° was shown to be less stable in temperature than the (3×3) and be replaced by this phase during the growth. Its metallic characteristics was reported by Endo and coworkers. This information was not available for the (3×3) reconstruction when the thesis begun, although it is essential, because preserving of the spin-orbit band gap is strictly connected to the possible exploitation of the Quantum Spin Hall Effect.

The study via scanning tunneling spectroscopy of the Ge/Al(111) interface at low temperature (5K) showed a strong coupling between the germanene layer and the metallic substrate, which precludes the knowledge of the true nature of germanene. Interesting informations could however be sorted from our experiments for the 2D materials community. Our analysis showed the weak adhesion of germanene to the Al(111) surface. The perturbation induced by the tip while scanning produced displacements and rearrangements of the layers. Through these experiments, we were able to explain an unexpected variety of spectra, which was accounted through the frequent contamination of the apex of the tip of the microscope by atoms of the surface. This stressed the necessity of a reference for tunneling spectra when dealing with 2D materials, a practice which is often overlooked.

As for graphene, the difficulty in growing large areas of the same phase will possibly lead to the exploitation of nanoribbons of germanene. The growth of small-sized sheets to access a metallic reference for the previous study enabled the analysis of the edge structure. Observations by tunneling microscopy showed that these sheets grow in the plane of the aluminium atomic terraces, matching what is reported in literature. The germanene edges on Al(111) generally present a clearer contrast than the rest of the sheet for both phases. A dynamic transition between two kinds of border was also observed at very low temperature for the (3×3) phase. To better understand this change of contrast and the transition, ab-initio calculations based on density functional theory (DFT) have been performed. They show the key role of aluminium atoms in the formation of edges, whose contrast cannot be explained by a full Ge structure. The model with mixed border accounts also for the tip-induced transition that was observed for the (3×3) phase.

Finally we focused on multilayer stack of germanene terminated with methyl groups. Unlike single-sheet germanene which requires an epitaxial growth, germanane crystals can be chemically synthesized through a process called topotactical deintercalation by exploiting existing layered materials. The chemical synthesis ensures the electronic decoupling of the material from its environment and allows the exploitation of other characterization techniques outside ultra-high vacuum. As for

monolayer germanene, methyl-terminated germanane promises the observation of Quantum Spin Hall Effect at room temperature, in this case under the application of a strain. Two types of crystals are revealed in our multi-physics analysis. The largest are around 10 micrometres in lateral dimension and are polycrystalline. The intercalation of water between the layers is eased, as the oxidization of the surfaces. They can be spotted because they become charged under electron irradiation due to the presence of isopropanol at the interface with the host substrate. The smallest flakes did not contain oxygen and were the most prone to being characterized by ultra-high vacuum four-probe transport measurements. These measurements show an inter-layer transport of holes. This unexpected bulk transport for a lamellar material suggests the presence of defects and imperfection in the plane of the layers, which calls for a better control of the synthesis of these crystals.

Bibliography

[1] K v Klitzing, Gerhard Dorda, and Michael Pepper. New method for high-accuracy determination of the fine-structure constant based on quantized hall resistance. *Physical Review Letters*, 45(6):494, 1980. 5, 15

[2] Charles L Kane and Eugene J Mele. Quantum spin hall effect in graphene. *Physical review letters*, 95(22):226801, 2005. 5, 17

[3] Yuan Cao, Valla Fatemi, Shiang Fang, Kenji Watanabe, Takashi Taniguchi, Efthimios Kaxiras, and Pablo Jarillo-Herrero. Unconventional superconductivity in magic-angle graphene superlattices. *Nature*, 556(7699):43–50, 2018. 5

[4] LC Post, T Xu, NA Franchina Vergel, A Tadjine, Y Lambert, F Vaurette, D Yarekha, L Desplanque, D Stiévenard, X Wallart, et al. Triangular nanoperforation and band engineering of ingaas quantum wells: a lithographic route toward dirac cones in iii–v semiconductors. *Nanotechnology*, 30(15):155301, 2019. 5

[5] Rudolf Peierls. Quelques proprietes typiques des corps solides. *Annales de l'institut Henri Poincare*, 5(3):177–222, 1935. 7

[6] LD Landau. On the theory of phase transitions, part i. *Sov Phys JETP*, 7:19ff, 1937. 7

[7] Pierre C Hohenberg. Existence of long-range order in one and two dimensions. *Physical Review*, 158(2):383, 1967. 9

[8] BJ Alder and TE Wainwright. Phase transition in elastic disks. *Physical Review*, 127(2):359, 1962. 9

[9] N David Mermin. Crystalline order in two dimensions. *Physical Review*, 176(1):250, 1968. 9

[10] DR Nelson and L Peliti. Fluctuations in membranes with crystalline and hexatic order. *Journal de physique*, 48(7):1085–1092, 1987. 9

[11] Kostya S Novoselov, Andre K Geim, Sergei V Morozov, D Jiang, Y_ Zhang, Sergey V Dubonos, Irina V Grigorieva, and Alexandr A Firsov. Electric field effect in atomically thin carbon films. *science*, 306(5696):666–669, 2004. 10, 14

[12] Jannik C Meyer, Andre K Geim, Mikhail I Katsnelson, Konstantin S Novoselov, Tim J Booth, and Siegmar Roth. The structure of suspended graphene sheets. *Nature*, 446(7131):60, 2007. 10

[13] Taisuke Ohta, Aaron Bostwick, Thomas Seyller, Karsten Horn, and Eli Rotenberg. Controlling the electronic structure of bilayer graphene. *Science*, 313(5789):951–954, 2006. 10

[14] Khan MF Shahil and Alexander A Balandin. Graphene–multilayer graphene nanocomposites as highly efficient thermal interface materials. *Nano letters*, 12(2):861–867, 2012. 10

[15] Mildred S Dresselhaus, Gene Dresselhaus, PC Eklund, and AM Rao. Carbon nanotubes. In *The physics of fullerene-based and fullerene-related materials*, pages 331–379. Springer, 2000. 10

[16] Andrey Chuvilin, Ute Kaiser, Elena Bichoutskaia, Nicholas A Besley, and Andrei N Khlobystov. Direct transformation of graphene to fullerene. *Nature chemistry*, 2(6):450–453, 2010. 10

[17] Philip Richard Wallace. The band theory of graphite. *Physical Review*, 71(9):622, 1947. 10

[18] Stephanie Reich, Janina Maultzsch, Christian Thomsen, and Pablo Ordejon. Tight-binding description of graphene. *Physical Review B*, 66(3):035412, 2002. 10, 11, 14

[19] Kostya S Novoselov, Andre K Geim, SVb Morozov, Da Jiang, Michail I Katsnelson, IVa Grigorieva, SVb Dubonos, Firsov, and AA. Two-dimensional gas of massless dirac fermions in graphene. *nature*, 438(7065):197, 2005. 10, 14, 15

[20] RS Deacon, K-C Chuang, RJ Nicholas, KS Novoselov, and AK Geim. Cyclotron resonance study of the electron and hole velocity in graphene monolayers. *Physical Review B*, 76(8):081406, 2007. 13, 14

[21] SV Morozov, KS Novoselov, MI Katsnelson, F Schedin, DC Elias, John A Jaszczak, and AK Geim. Giant intrinsic carrier mobilities in graphene and its bilayer. *Physical review letters*, 100(1):016602, 2008. 14, 91

[22] Yuanbo Zhang, Yan-Wen Tan, Horst L Stormer, and Philip Kim. Experimental observation of the quantum hall effect and berry's phase in graphene. *nature*, 438(7065):201–204, 2005. 14

[23] Z Jiang, Erik A Henriksen, LC Tung, Y-J Wang, ME Schwartz, Melinda Y Han, P Kim, and Horst L Stormer. Infrared spectroscopy of landau levels of graphene. *Physical review letters*, 98(19):197403, 2007. 14

[24] Guohong Li and Eva Y Andrei. Observation of landau levels of dirac fermions in graphite. *Nature physics*, 3(9):623–627, 2007. 14

[25] Robert B Laughlin. Quantized hall conductivity in two dimensions. *Physical Review B*, 23(10):5632, 1981. 15

[26] David J Thouless, Mahito Kohmoto, M Peter Nightingale, and Md den Nijs. Quantized hall conductance in a two-dimensional periodic potential. *Physical review letters*, 49(6):405, 1982. 15

[27] Bertrand I Halperin. Quantized hall conductance, current-carrying edge states, and the existence of extended states in a two-dimensional disordered potential. *Physical Review B*, 25(4):2185, 1982. 15

[28] Allan H MacDonald and P Středa. Quantized hall effect and edge currents. *Physical Review B*, 29(4):1616, 1984. 15

[29] Yasuhiro Hatsugai. Chern number and edge states in the integer quantum hall effect. *Physical review letters*, 71(22):3697, 1993. 15

[30] B Andrei Bernevig and Shou-Cheng Zhang. Quantum spin hall effect. *Physical review letters*, 96(10):106802, 2006. 17, 18

[31] Hongki Min, JE Hill, Nikolas A Sinitsyn, BR Sahu, Leonard Kleinman, and Allan H MacDonald. Intrinsic and rashba spin-orbit interactions in graphene sheets. *Physical Review B*, 74(16):165310, 2006. 18

[32] Yugui Yao, Fei Ye, Xiao-Liang Qi, Shou-Cheng Zhang, and Zhong Fang. Spin-orbit gap of graphene: First-principles calculations. *Physical Review B*, 75(4):041401, 2007. 18, 19

[33] B Andrei Bernevig, Taylor L Hughes, and Shou-Cheng Zhang. Quantum spin hall effect and topological phase transition in hgte quantum wells. *science*, 314(5806):1757–1761, 2006. 18

[34] Markus König, Steffen Wiedmann, Christoph Brüne, Andreas Roth, Hartmut Buhmann, Laurens W Molenkamp, Xiao-Liang Qi, and Shou-Cheng Zhang. Quantum spin hall insulator state in hgte quantum wells. *Science*, 318(5851):766–770, 2007. 18

[35] Andreas Roth, Christoph Brüne, Hartmut Buhmann, Laurens W Molenkamp, Joseph Maciejko, Xiao-Liang Qi, and Shou-Cheng Zhang. Nonlocal transport in the quantum spin hall state. *Science*, 325(5938):294–297, 2009. 18

[36] Ivan Knez, Rui-Rui Du, and Gerard Sullivan. Evidence for helical edge modes in inverted inas/gasb quantum wells. *Physical review letters*, 107(13):136603, 2011. 18

[37] Sanfeng Wu, Valla Fatemi, Quinn D Gibson, Kenji Watanabe, Takashi Taniguchi, Robert J Cava, and Pablo Jarillo-Herrero. Observation of the quantum spin hall effect up to 100 kelvin in a monolayer crystal. *Science*, 359(6371):76–79, 2018. 18

[38] Sajedeh Manzeli, Dmitry Ovchinnikov, Diego Pasquier, Oleg V Yazyev, and Andras Kis. 2d transition metal dichalcogenides. *Nature Reviews Materials*, 2(8):17033, 2017. 18

[39] Cheng-Cheng Liu, Hua Jiang, and Yugui Yao. Low-energy effective hamiltonian involving spin-orbit coupling in silicene and two-dimensional germanium and tin. *Physical Review B*, 84(19):195430, 2011. 19

[40] Cheng-Cheng Liu, Wanxiang Feng, and Yugui Yao. Quantum spin hall effect in silicene and two-dimensional germanium. *Physical review letters*, 107(7):076802, 2011. 19

[41] Bernard Aufray, Abdelkader Kara, Sébastien Vizzini, Hamid Oughaddou, Christel Léandri, Benedicte Ealet, and Guy Le Lay. Graphene-like silicon nanoribbons on ag (110): A possible formation of silicene. *Applied Physics Letters*, 96(18):183102, 2010. 19

[42] Mohammed Rachid Tchalala, Hanna Enriquez, Andrew J Mayne, Abdelkader Kara, Gérald Dujardin, Mustapha Ait Ali, and Hamid Oughaddou. Atomic structure of silicene nanoribbons on ag (110). In *Journal of Physics: Conference Series*, volume 491, page 012002. IOP Publishing, 2014. 19

[43] Patrick Vogt, Paola De Padova, Claudio Quaresima, Jose Avila, Emmanouil Frantzeskakis, Maria Carmen Asensio, Andrea Resta, Bénédicte Ealet, and Guy Le Lay. Silicene: compelling experimental evidence for graphenelike two-dimensional silicon. *Physical review letters*, 108(15):155501, 2012. 19, 20

[44] Antoine Fleurence, Rainer Friedlein, Taisuke Ozaki, Hiroyuki Kawai, Ying Wang, and Yukiko Yamada-Takamura. Experimental evidence for epitaxial silicene on diboride thin films. *Physical review letters*, 108(24):245501, 2012. 19

[45] Lei Meng, Yeliang Wang, Lizhi Zhang, Shixuan Du, Rongting Wu, Linfei Li, Yi Zhang, Geng Li, Haitao Zhou, Werner A Hofer, et al. Buckled silicene formation on ir (111). *Nano letters*, 13(2):685–690, 2013. 19

[46] Maurizio De Crescenzi, Isabelle Berbezier, Manuela Scarselli, Paola Castrucci, Marco Abbarchi, Antoine Ronda, Fatme Jardali, Jejune Park, and Holger Vach. Formation of silicene nanosheets on graphite. *ACS nano*, 10(12):11163–11171, 2016. 19

[47] Daniele Chiappe, Emilio Scalise, Eugenio Cinquanta, Carlo Grazianetti, Bas van den Broek, Marco Fanciulli, Michel Houssa, and Alessandro Molle. Two-dimensional si nanosheets with local hexagonal structure on a mos2 surface. *Advanced Materials*, 26(13):2096–2101, 2014. 19

[48] Wenbing Peng, Tao Xu, Pascale Diener, Louis Biadala, Maxime Berthe, Xiaodong Pi, Yves Borensztein, Alberto Curcella, Romain Bernard, Geoffroy Prevot, et al. Resolving the controversial existence of silicene and germanene nanosheets grown on graphite. *ACS nano*, 12(5):4754–4760, 2018. 19, 20, 77

[49] Rik van Bremen, Qirong Yao, Soumya Banerjee, Deniz Cakir, Nuri Oncel, and Harold JW Zandvliet. Intercalation of si between mos2 layers. *Beilstein journal of nanotechnology*, 8(1):1952–1960, 2017. 19

[50] Hanna Enriquez, Andrew Mayne, Abdelkader Kara, Sébastien Vizzini, Silvan Roth, Boubekeur Lalmi, Ari P Seitsonen, Bernard Aufray, Thomas Greber, Rachid Belkhou, et al. Adsorption of silicon on au (110): An ordered two dimensional surface alloy. *Applied Physics Letters*, 101(2):021605, 2012. 19

[51] Mohamed Rachid Tchalala, Hanna Enriquez, Andrew J Mayne, Abdelkader Kara, Silvan Roth, Mathieu G Silly, Azzedine Bendounan, Fausto Sirotti, Thomas Greber, Bernard Aufray, et al. Formation of one-dimensional self-assembled silicon nanoribbons on au (110)-(2× 1). *Applied Physics Letters*, 102(8):083107, 2013. 19

[52] Sana Sadeddine, Hanna Enriquez, Azzedine Bendounan, Pranab Kumar Das, Ivana Vobornik, Abdelkader Kara, Andrew J Mayne, Fausto Sirotti, Gérald Dujardin, and Hamid Oughaddou. Compelling experimental evidence of a dirac cone in the electronic structure of a 2d silicon layer. *Scientific reports*, 7(1):1–7, 2017. 19

[53] Seymur Cahangirov, Martha Audiffred, Peizhe Tang, Amilcare Iacomino, Wenhui Duan, Gabriel Merino, and Angel Rubio. Electronic structure of silicene on ag (111): Strong hybridization effects. *Physical Review B*, 88(3):035432, 2013. 19

[54] Chun-Liang Lin, Ryuichi Arafune, Kazuaki Kawahara, Mao Kanno, Noriyuki Tsukahara, Emi Minamitani, Yousoo Kim, Maki Kawai, and Noriaki Takagi. Substrate-induced symmetry breaking in silicene. *Physical review letters*, 110(7):076801, 2013. 19, 89

[55] Guo-Wei Lee, Han-De Chen, and Deng-Sung Lin. Growth mode and structures of silicene on the ag (1 1 1) surface. *Applied Surface Science*, 354:187–195, 2015. 20

[56] H Oughaddou, S Sawaya, J Goniakowski, B Aufray, G Le Lay, JM Gay, G Treglia, JP Biberian, N Barrett, C Guillot, et al. Ge/ag (111) semiconductor-on-metal growth: Formation of an ag_2ge surface alloy. *Physical Review B*, 62(24):16653, 2000. 20

[57] Linfei Li, Shuang-zan Lu, Jinbo Pan, Zhihui Qin, Yu-qi Wang, Yeliang Wang, Geng-yu Cao, Shixuan Du, and Hong-Jun Gao. Buckled germanene formation on pt (111). *Advanced Materials*, 26(28):4820–4824, 2014. 20

[58] ME Davila, Lede Xian, Seymur Cahangirov, Angel Rubio, and Guy Le Lay. Germanene: a novel two-dimensional germanium allotrope akin to graphene and silicene. *New Journal of Physics*, 16(9):095002, 2014. 20

[59] Pantelis Bampoulis, Lijie Zhang, A Safaei, Raoul van Gastel, Bene Poelsema, and H J W Zandvliet. Germanene termination of ge$_2$pt crystals on ge (110). *Journal of physics: Condensed matter*, 26(44):442001, 2014. 20, 77, 89

[60] Lijie Zhang, Pantelis Bampoulis, Arie van Houselt, and Henricus JW Zandvliet. Two-dimensional dirac signature of germanene. *Applied physics letters*, 107(11):111605, 2015. 20, 77, 89

[61] CJ Walhout, Adil Acun, Lijie Zhang, M Ezawa, and Henricus JW Zandvliet. Scanning tunneling spectroscopy study of the dirac spectrum of germanene. *Journal of physics: Condensed matter*, 28(28):284006, 2016. 20, 77, 89

[62] Rik Van Bremen, Pantelis Bampoulis, Johannes Aprojanz, Mark Smithers, Bene Poelsema, Christoph Tegenkamp, and Harold JW Zandvliet. Ge_2pt hut clusters: A substrate for germanene. *Journal of applied physics*, 124(12):125301, 2018. 20

[63] Bogdana Borca, Carolien Castenmiller, Martina Tsvetanova, Kai Sotthewes, Alexander N Rudenko, and Harold JW Zandvliet. Image potential states of germanene. *2D Materials*, 7(3):035021, 2020. 20

[64] Chung-Huang Lin, Angus Huang, Woei Wu Pai, Wei-Chuan Chen, Ting-Yu Chen, Tay-Rong Chang, Ryu Yukawa, Cheng-Maw Cheng, Chung-Yu Mou, Iwao Matsuda, et al. Single-layer dual germanene phases on ag (111). *Physical Review Materials*, 2(2):024003, 2018. 20

[65] K Zhang, R Bernard, Y Borensztein, H Cruguel, and G Prévot. Growth of germanium-silver surface alloys followed by in situ scanning tunneling microscopy: Absence of germanene formation. *Physical Review B*, 102(12):125418, 2020. 20, 77

[66] M Svec, P Hapala, M Ondracek, P Merino, M Blanco-Rey, P Mutombo, M Vondracek, Y Polyak, V Chab, JA Martin Gago, et al. Silicene versus two-dimensional ordered silicide: Atomic and electronic structure of si-($\sqrt{19} \times \sqrt{19}$) r 23.4 °/pt (111). *Physical Review B*, 89(20):201412, 2014. 20, 77

[67] Chih-Sung Ho, Santanu Banerjee, Matthias Batzill, David E Beck, and Bruce E Koel. Formation and structure of a ($\sqrt{19} \times \sqrt{19}$) r23.4°-ge/pt (1 1 1) surface alloy. *Surface Science*, 603(9):1161–1167, 2009. 20

[68] Niels BM Schroter, Matthew D Watson, Liam B Duffy, Moritz Hoesch, Yulin Chen, Thorsten Hesjedal, and Timur K Kim. Emergence of dirac-like bands in the monolayer limit of epitaxial ge films on au (1 1 1). *2D Materials*, 4(3):031005, 2017. 20

[69] Maria Eugenia Davila and Guy Le Lay. Few layer epitaxial germanene: a novel two-dimensional dirac material. *Scientific reports*, 6:20714, 2016. 20

[70] Weimin Wang and RIG Uhrberg. Investigation of the atomic and electronic structures of highly ordered two-dimensional germanium on au (111). *Physical Review Materials*, 1(7):074002, 2017. 20

[71] Esteban D Cantero, Lara M Solis, Yongfeng Tong, Javier D Fuhr, Maria Luz Martiarena, Oscar Grizzi, and Esteban A Sanchez. Growth of germanium on au (111): formation of germanene or intermixing of au and ge atoms? *Physical Chemistry Chemical Physics*, 19(28):18580–18586, 2017. 20

[72] DA Muzychenko, AI Oreshkin, SI Oreshkin, SS Ustavschikov, Aleksei Vladimirovich Putilov, and A Yu Aladyshkin. The surface structures growth's features caused by ge adsorption on the au (111) surface. *JETP Letters*, 106(4):217–222, 2017. 20, 77

[73] F d'Acapito, S Torrengo, E Xenogiannopoulou, P Tsipas, J Marquez Velasco, D Tsoutsou, and A Dimoulas. Evidence for germanene growth on epitaxial hexagonal (h)-aln on ag (1 1 1). *Journal of Physics: Condensed Matter*, 28(4):045002, 2016. 20

[74] Junji Yuhara, Hiroki Shimazu, Kouichi Ito, Akio Ohta, Masaaki Araidai, Masashi Kurosawa, Masashi Nakatake, and Guy Le Lay. Germanene epitaxial growth by segregation through ag (111) thin films on ge (111). *ACS nano*, 12(11):11632–11637, 2018. 20

[75] Jian Gou, Qing Zhong, Shaoxiang Sheng, Wenbin Li, Peng Cheng, Hui Li, Lan Chen, and Kehui Wu. Strained monolayer germanene with $1\times$ 1 lattice on sb (111). *2D Materials*, 3(4):045005, 2016. 20

[76] L Zhang, P Bampoulis, AN Rudenko, Q v Yao, A Van Houselt, B Poelsema, MI Katsnelson, and HJW Zandvliet. Structural and electronic properties of germanene on mos_2. *Physical review letters*, 116(25):256804, 2016. 20, 77, 89

[77] Q Yao, Z Jiao, P Bampoulis, Lijie Zhang, AN Rudenko, MI Katsnelson, and HJW Zandvliet. Charge puddles in germanene. *Applied physics letters*, 114(4):041601, 2019. 20, 77

[78] Jincheng Zhuang, Chen Liu, Zhiyong Zhou, Gilberto Casillas, Haifeng Feng, Xun Xu, Jiaou Wang, Weichang Hao, Xiaolin Wang, Shi Xue Dou, et al. Dirac signature in germanene on semiconducting substrate. *Advanced Science*, 5(7):1800207, 2018. 20, 89

[79] Luca Persichetti, Fatme Jardali, Holger Vach, Anna Sgarlata, Isabelle Berbezier, Maurizio De Crescenzi, and Adalberto Balzarotti. van der waals heteroepitaxy of germanene islands on graphite. *The journal of physical chemistry letters*, 7(16):3246–3251, 2016. 20

[80] Zhihui Qin, Jinbo Pan, Shuangzan Lu, Yan Shao, Yeliang Wang, Shixuan Du, Hong-Jun Gao, and Gengyu Cao. Direct evidence of dirac signature in bilayer germanene islands on cu (111). *Advanced Materials*, 29(13):1606046, 2017. 20, 89

[81] Fengping Li, Wei Wei, Xingshuai Lv, Baibiao Huang, and Ying Dai. Evolution of the linear band dispersion of monolayer and bilayer germanene on cu (111). *Physical Chemistry Chemical Physics*, 19(34):22844–22851, 2017. 20

[82] Hsu-Sheng Tsai, Yu-Ze Chen, Henry Medina, Teng-Yu Su, Ta-Shun Chou, Yi-Hsuan Chen, Yu-Lun Chueh, and Jenq-Horng Liang. Direct formation of large-scale multi-layered germanene on si substrate. *Physical Chemistry Chemical Physics*, 17(33):21389–21393, 2015. 20

[83] Mickael Derivaz, Didier Dentel, Regis Stephan, Marie-Christine Hanf, Ahmed Mehdaoui, Philippe Sonnet, and Carmelo Pirri. Continuous germanene layer on al (111). *Nano letters*, 15(4):2510–2516, 2015. 21, 22, 25, 78, 88

[84] L De Santis and R Resta. Electron localization at metal surfaces. *Surface science*, 450(1-2):126–132, 2000. 21

[85] SD Kevan, NG Stoffel, and NV Smith. High-resolution angle-resolved photoemission studies of the surface states on al (111) and al (001). *Physical Review B*, 31(4):1788, 1985. 21, 83

[86] R Paniago, R Matzdorf, G Meister, and Al Goldmann. Temperature dependence of shockley-type surface energy bands on cu (111), ag (111) and au (111). *Surface science*, 336(1-2):113–122, 1995. 21

[87] A Varykhalov, D Marchenko, MR Scholz, EDL Rienks, TK Kim, G Bihlmayer, J Sanchez-Barriga, and O Rader. Ir (111) surface state with giant rashba splitting persists under graphene in air. *Physical review letters*, 108(6):066804, 2012. 21

[88] Regis Stephan, Mickael Derivaz, Marie-Christine Hanf, Didier Dentel, Natalia Massara, Ahmed Mehdaoui, Philippe Sonnet, and Carmelo Pirri. Tip-induced switch of germanene atomic structure. *The journal of physical chemistry letters*, 8(18):4587–4593, 2017. 22, 24, 86, 87, 88, 102, 106

[89] Yuki Fukaya, Iwao Matsuda, Baojie Feng, Izumi Mochizuki, Toshio Hyodo, and Shin-ichi Shamoto. Asymmetric structure of germanene on an al (111) surface studied by total-reflection high-energy positron diffraction. *2D Materials*, 3(3):035019, 2016. 22

[90] Dmitriy A Muzychenko, Sergey I Oreshkin, Vladimir I Panov, Chris Van Haesendonck, and Andrey I Oreshkin. Single and multi domain buckled germanene phases on al (111) surface. *Nano Research*, pages 1–9. 23

[91] G Liu, SB Liu, B Xu, CY Ouyang, HY Song, S Guan, and Shengyuan A Yang. Multiple dirac points and hydrogenation-induced magnetism of germanene layer on al (111) surface. *The journal of physical chemistry letters*, 6(24):4936–4942, 2015. 23

[92] Linyang Li and Mingwen Zhao. First-principles identifications of superstructures of germanene on ag (111) surface and h-bn substrate. *Physical Chemistry Chemical Physics*, 15(39):16853–16863, 2013. 23

[93] Yun-Peng Wang and Hai-Ping Cheng. Absence of a dirac cone in silicene on ag (111): First-principles density functional calculations with a modified effective band structure technique. *Physical Review B*, 87(24):245430, 2013. 23

[94] AJ McAlister and JL Murray. The al-ge (aluminum-germanium) system. *Bulletin of Alloy Phase Diagrams*, 5(4):341, 1984. 24

[95] Jide Fang, Peng Zhao, and Gang Chen. Germanene growth on al (111): A case study of interface effect. *The Journal of Physical Chemistry C*, 122(32):18669–18681, 2018. 24, 96

[96] Emanuel A Martinez, Javier D Fuhr, Oscar Grizzi, Esteban A Sanchez, and Esteban D Cantero. Growth of germanene on al (111) hindered by surface alloy formation. *The Journal of Physical Chemistry C*, 2019. 24, 25

[97] Weimin Wang and Roger IG Uhrberg. Coexistence of strongly buckled germanene phases on al (111). *Beilstein journal of nanotechnology*, 8(1):1946–1951, 2017. 25, 87

[98] Satoshi Endo, Osamu Kubo, Noriharu Nakashima, Seiya Iwaguma, Riku Yamamoto, Yoshinari Kamakura, Hiroshi Tabata, and Mitsuhiro Katayama. Germanene on al (111) grown at nearly room temperature. *Applied Physics Express*, 11(1):015502, 2017. 26, 78, 89, 115

[99] Natalia Massara. *Découverte et fonctionnalisation de nouveaux cristaux bidimentionnels*. PhD thesis, December 2019. 26

[100] Martin Pumera and Colin Hong An Wong. Graphane and hydrogenated graphene. *Chemical Society Reviews*, 42(14):5987–5995, 2013. 27

[101] Adriano Ambrosi, Chun Kiang Chua, Naziah Mohamad Latiff, Adeline Huiling Loo, Colin Hong An Wong, Alex Yong Sheng Eng, Alessandra Bonanni, and Martin Pumera. Graphene and its electrochemistry–an update. *Chemical Society Reviews*, 45(9):2458–2493, 2016. 27

[102] Jorge O Sofo, Ajay S Chaudhari, and Greg D Barber. Graphane: A two-dimensional hydrocarbon. *Physical Review B*, 75(15):153401, 2007. 27

[103] Louis Schlapbach and Andreas Züttel. Hydrogen-storage materials for mobile applications. In *Materials for sustainable energy: a collection of peer-reviewed research and review articles from nature publishing group*, pages 265–270. World Scientific, 2011. 27

[104] Liv Hornekær, A Baurichter, VV Petrunin, David Field, and AC Luntz. Importance of surface morphology in interstellar h2 formation. *Science*, 302(5652):1943–1946, 2003. 27

[105] Duminda K Samarakoon and Xiao-Qian Wang. Chair and twist-boat membranes in hydrogenated graphene. *ACS nano*, 3(12):4017–4022, 2009. 27

[106] Andrey A Fokin, Dennis Gerbig, and Peter R Schreiner. σ/σ-and π/π-interactions are equally important: multilayered graphanes. *Journal of the American Chemical Society*, 133(50):20036–20039, 2011. 27

[107] Yafei Li, Fengyu Li, and Zhongfang Chen. Graphane/fluorographene bilayer: considerable c–h··· f–c hydrogen bonding and effective band structure engineering. *Journal of the American Chemical Society*, 134(27):11269–11275, 2012. 27

[108] LC Lew Yan Voon, E Sandberg, RS Aga, and AA Farajian. Hydrogen compounds of group-iv nanosheets. *Applied Physics Letters*, 97(16):163114, 2010. 27

[109] Michel Houssa, Emilio Scalise, Kiroubanand Sankaran, Geoffrey Pourtois, VV Afanas' Ev, and Andre Stesmans. Electronic properties of hydrogenated silicene and germanene. *Applied Physics Letters*, 98(22):223107, 2011. 27

[110] Joelson C Garcia, Denille B De Lima, Lucy VC Assali, and Joao F Justo. Group iv graphene- and graphane-like nanosheets. *The Journal of Physical Chemistry C*, 115(27):13242–13246, 2011. 27

[111] O Pulci, P Gori, M Marsili, V Garbuio, R Del Sole, and F Bechstedt. Strong excitons in novel two-dimensional crystals: Silicane and germanane. *EPL (Europhysics Letters)*, 98(3):37004, 2012. 27

[112] Daniel C Elias, Rahul Raveendran Nair, TMG Mohiuddin, SV Morozov, P Blake, MP Halsall, Andrea Carlo Ferrari, DW Boukhvalov, MI Katsnelson, AK Geim, et al. Control of graphene's properties by reversible hydrogenation: evidence for graphane. *Science*, 323(5914):610–613, 2009. 27

[113] James S Burgess, Bernard R Matis, Jeremy T Robinson, Felipe A Bulat, F Keith Perkins, Brian H Houston, and Jeffrey W Baldwin. Tuning the electronic properties of graphene by hydrogenation in a plasma enhanced chemical vapor deposition reactor. *Carbon*, 49(13):4420–4426, 2011. 27

[114] Hongyan Jiang, Marvin Kammler, Feizhi Ding, Yvonne Dorenkamp, Frederick R Manby, Alec M Wodtke, Thomas F Miller, Alexander Kandratsenka, and Oliver Bünermann. Imaging covalent bond formation by h atom scattering from graphene. *Science*, 364(6438):379–382, 2019. 27

[115] Liv Hornekær. Stabilizing a c–h bond on graphene with sound. *Science*, 364(6438):331–332, 2019. 27

[116] Herbert Schäfer, Brigitte Eisenmann, and Wiking Müller. Zintl phases: transitions between metallic and ionic bonding. *Angewandte Chemie International Edition in English*, 12(9):694–712, 1973. 27

[117] Günther Vogg, Martin S Brandt, and Martin Stutzmann. Polygermyne—a prototype system for layered germanium polymers. *Advanced materials*, 12(17):1278–1281, 2000. 27, 28

[118] Hirotaka Okamoto, Yoko Kumai, Yusuke Sugiyama, Takuya Mitsuoka, Koji Nakanishi, Toshiaki Ohta, Hiroshi Nozaki, Satoshi Yamaguchi, Soichi Shirai, and Hideyuki Nakano. Silicon nanosheets and their self-assembled regular stacking structure. *Journal of the American Chemical Society*, 132(8):2710–2718, 2010. 27

[119] Mohamed Rachid Tchalala, Mustapha Ait Ali, Hanna Enriquez, Abdelkader Kara, Abdessadek Lachgar, Said Yagoubi, Eddy Foy, Enrique Vega, Azzedine Bendounan, Mathieu G Silly, et al. Silicon sheets by redox assisted chemical exfoliation. *Journal of Physics: Condensed Matter*, 25(44):442001, 2013. 27

[120] Elisabeth Bianco, Sheneve Butler, Shishi Jiang, Oscar D Restrepo, Wolfgang Windl, and Joshua E Goldberger. Stability and exfoliation of germanane: a germanium graphane analogue. *ACS nano*, 7(5):4414–4421, 2013. 27, 28, 29

[121] Patrick Odenthal, Igor Pinchuk, Adam Ahmen, Walid Amamou, Josh Goldberger, and Roland Kawakami. Epitaxial co-deposition growth of cage2 films by molecular beam epitaxy for large area germanane. In *APS Meeting Abstracts*, 2014. 27

[122] G Vogg, C Miesner, MS Brandt, M Stutzmann, and G Abstreiter. Epitaxial alloy films of zintl-phase ca (si1- xgex) 2. *Journal of crystal growth*, 223(4):573–576, 2001. 27

[123] Amanda H Trout, Yaxian Wang, Bryan D Esser, Shishi Jiang, Joshua E Goldberger, Wolfgang Windl, and David W McComb. Identification of turbostratic twisting in germanane. *Journal of Materials Chemistry C*, 7(32):10092–10097, 2019. 28

[124] W Beyer, J Herion, H Wagner, and U Zastrow. Hydrogen stability in amorphous germanium films. *Philosophical Magazine B*, 63(1):269–279, 1991. 28

[125] HD Fuchs, M Stutzmann, MS Brandt, M Rosenbauer, J Weber, A Breitschwerdt, P Deak, and M Cardona. Porous silicon and siloxene: Vibrational and structural properties. *Physical Review B*, 48(11):8172, 1993. 28

[126] U Dettlaff-Weglikowska, W Hönle, A Molassioti-Dohms, S Finkbeiner, and J Weber. Structure and optical properties of the planar silicon compounds polysilane and wöhler siloxene. *Physical Review B*, 56(20):13132, 1997. 28

[127] Xiaoguang Luo and Eva Zurek. Crystal structures and electronic properties of single-layer, few-layer, and multilayer geh. *The Journal of Physical Chemistry C*, 120(1):793–800, 2016. 28

[128] Zoltán Hajnal, Günther Vogg, Lex J-P Meyer, Bernadett Szűcs, Martin S Brandt, and Thomas Frauenheim. Band structure and optical properties of germanium sheet polymers. *Physical Review B*, 64(3):033311, 2001. 28

[129] Shishi Jiang, Elisabeth Bianco, and Joshua E Goldberger. The structure and amorphization of germanane. *Journal of Materials Chemistry C*, 2(17):3185–3188, 2014. 29

[130] Gabriella Coloyan, Nicholas D Cultrara, Ankita Katre, Jesús Carrete, Matt Heine, Eric Ou, Jaehyun Kim, Shishi Jiang, Lucas Lindsay, Natalio Mingo, et al. Basal-plane thermal conductivity of nanocrystalline and amorphized thin germanane. *Applied Physics Letters*, 109(13):131907, 2016. 29

[131] Justin R Young, Basant Chitara, Nicholas D Cultrara, Maxx Q Arguilla, Shishi Jiang, Fan Fan, Ezekiel Johnston-Halperin, and Joshua E Goldberger. Water activated doping and transport in multilayered germanane crystals. *Journal of Physics: Condensed Matter*, 28(3):034001, 2015. 29

[132] Nicholas D Cultrara, Maxx Q Arguilla, Shishi Jiang, Chuanchuan Sun, Michael R Scudder, R Dominic Ross, and Joshua E Goldberger. Group-13 and group-15 doping of germanane. *Beilstein journal of nanotechnology*, 8(1):1642–1648, 2017. 29

[133] Andrew C Serino, Jesse S Ko, Michael T Yeung, Jeffrey J Schwartz, Chris B Kang, Sarah H Tolbert, Richard B Kaner, Bruce S Dunn, and Paul S Weiss. Lithium-ion insertion properties of solution-exfoliated germanane. *ACS nano*, 11(8):7995–8001, 2017. 29

[134] Yiju Zhao, Demin Yin, and Youngki Yoon. Intrinsic performance of germanane schottky barrier field-effect transistors. *IEEE Transactions on Electron Devices*, 65(10):4188–4195, 2018. 29

[135] Nana Liu, Hui Qiao, Kang Xu, Yilian Xi, Long Ren, Ningyan Cheng, Dandan Cui, Xiang Qi, Xun Xu, Weichang Hao, et al. Hydrogen terminated germanene for a robust self-powered flexible photoelectrochemical photodetector. *Small*, page 2000283, 2020. 29

[136] BN Madhushankar, A Kaverzin, T Giousis, G Potsi, D Gournis, P Rudolf, GR Blake, CH Van Der Wal, and BJ Van Wees. Electronic properties of germanane field-effect transistors. *2D Materials*, 4(2):021009, 2017. 29

[137] Qihong Chen, Lei Liang, Georgia Potsi, Puhua Wan, Jianming Lu, Theodosis Giousis, Eleni Thomou, Dimitrios Gournis, Petra Rudolf, and Jianting Ye. Highly conductive metallic state and strong spin–orbit interaction in annealed germanane. *Nano letters*, 19(3):1520–1526, 2019. 29

[138] Shishi Jiang, Sheneve Butler, Elisabeth Bianco, Oscar D Restrepo, Wolfgang Windl, and Joshua E Goldberger. Improving the stability and optical properties of germanane via one-step covalent methyl-termination. *Nature communications*, 5(1):1–6, 2014. 29, 30, 118

[139] Clément Livache, Bradley J Ryan, Utkarsh Ramesh, Violette Steinmetz, Charlie Gréboval, Audrey Chu, Thibault Brulé, Sandrine Ithurria, Geoffroy Prévot, Thierry Barisien, et al. Optoelectronic properties of methyl-terminated germanane. *Applied Physics Letters*, 115(5):052106, 2019. 29, 30, 118, 138

[140] Shishi Jiang, Maxx Q Arguilla, Nicholas D Cultrara, and Joshua E Goldberger. Improved topotactic reactions for maximizing organic coverage of methyl germanane. *Chemistry of Materials*, 28(13):4735–4740, 2016. 30, 124

[141] Thaddeus J Asel, Warren LB Huey, Brenton Noesges, Egle Molotokaite, Szu-Chia Chien, Yaxian Wang, Aldriel Barnum, Chris McPherson, Shishi Jiang, Seth Shields, et al. Influence of surface chemistry on water absorption in functionalized germanane. *Chemistry of Materials*, 32(4):1537–1544, 2020. 30, 124

[142] Thaddeus J Asel, Eric Yanchenko, Xiao Yang, Shishi Jiang, Kevin Krymowski, Yaxian Wang, Amanda Trout, David W McComb, Wolfgang Windl, Joshua E Goldberger, et al. Identification of ge vacancies as electronic defects in methyl-and hydrogen-terminated germanane. *Applied Physics Letters*, 113(6):061110, 2018. 31, 124, 138

[143] Yu Jing, Xu Zhang, Dihua Wu, Xudong Zhao, and Zhen Zhou. High carrier mobility and pronounced light absorption in methyl-terminated germanene: insights from first-principles computations. *The journal of physical chemistry letters*, 6(21):4252–4258, 2015. 31, 117

[144] Chen Si, Junwei Liu, Yong Xu, Jian Wu, Bing-Lin Gu, and Wenhui Duan. Functionalized germanene as a prototype of large-gap two-dimensional topological insulators. *Physical Review B*, 89(11):115429, 2014. 31

[145] Yandong Ma, Ying Dai, Wei Wei, Baibiao Huang, and Myung-Hwan Whangbo. Strain-induced quantum spin hall effect in methyl-substituted germanane gech 3. *Scientific reports*, 4:7297, 2014. 31, 117

[146] Leo Esaki. New phenomenon in narrow germanium p-n junctions. *Physical review*, 109(2):603, 1958. 33

[147] Gerd Binnig, Heinrich Rohrer, Ch Gerber, and Edmund Weibel. Surface studies by scanning tunneling microscopy. *Physical review letters*, 49(1):57, 1982. 34, 36

[148] Nathali Alexandra Franchina Vergel. *Dirac antidot superlattices for electrons in III-V semiconductors*. PhD thesis, Lille 1, 2020. 35

[149] Gerd Binnig and Heinrich Rohrer. Scanning tunneling microscopy. *Surface science*, 126(1-3):236–244, 1983. 36

[150] Anne-Sophie Lucier. *Preparation and characterization of tungsten tips suitable for molecular electronics studies*. PhD thesis, McGill University, 2004. 37

[151] M. Berthe. *Electronic transport in quantum confined systems*. Theses, Université des Sciences et Technologie de Lille - Lille I, December 2007. 38, 48

[152] ARH Clarke, JB Pethica, JA Nieminen, F Besenbacher, E Lægsgaard, and I Stensgaard. Quantitative scanning tunneling microscopy at atomic resolution: Influence of forces and tip configuration. *Physical review letters*, 76(8):1276, 1996. 39

[153] L Limot, J Kröger, R Berndt, A Garcia-Lekue, and WA Hofer. Atom transfer and single-adatom contacts. *Physical review letters*, 94(12):126102, 2005. 39

[154] N Néel, J Kröger, L Limot, Thomas Frederiksen, Mads Brandbyge, and R Berndt. Controlled contact to a c 60 molecule. *Physical review letters*, 98(6):065502, 2007. 39

[155] N Néel, J Kröger, L Limot, K Palotas, WA Hofer, and R Berndt. Conductance and kondo effect in a controlled single-atom contact. *Physical review letters*, 98(1):016801, 2007. 39

[156] Jerry Tersoff and Donald R Hamann. Theory of the scanning tunneling microscope. *Physical Review B*, 31(2):805, 1985. 39, 50, 74

[157] William Sacks. Tip orbitals and the atomic corrugation of metal surfaces in scanning tunneling microscopy. *Physical Review B*, 61(11):7656, 2000. 39

[158] G Binnig and H Rohrer. Vacuum tunnel microscope. *Helvetica Physica Acta*, 55(2):128–128, 1982. 39

[159] RM Feenstra, WA Thompson, and AP Fein. Real-space observation of π-bonded chains and surface disorder on si (111) $2\times$ 1. *Physical review letters*, 56(6):608, 1986. 40, 41

[160] R.M. Feenstra, Joseph A Stroscio, and A. Fein. Tunneling spectroscopy of the si (111) $2\times$ 1 surface. *Surface science*, 181(1-2):295–306, 1987. 40

[161] Matteo Passoni, Fabio Donati, A Li Bassi, CARLO SPARTACO Casari, and CARLO ENRICO Bottani. Recovery of local density of states using scanning tunneling spectroscopy. *Physical Review B*, 79(4):045404, 2009. 41

[162] P Maartensson and RM Feenstra. Geometric and electronic structure of antimony on the gaas (110) surface studied by scanning tunneling microscopy. *Physical Review B*, 39(11):7744, 1989. 41

[163] John H Scofield. Frequency-domain description of a lock-in amplifier. *American journal of physics*, 62(2):129–133, 1994. 44, 45

[164] J Klein, A Leger, M Belin, D Defourneau, and MJL Sangster. Inelastic-electron-tunneling spectroscopy of metal-insulator-metal junctions. *Physical Review B*, 7(6):2336, 1973. 46

[165] Annabella Selloni, P Carnevali, E Tosatti, and CD Chen. Voltage-dependent scanning-tunneling microscopy of a crystal surface: Graphite. In *Scanning Tunneling Microscopy*, pages 168–171. Springer, 1985. 50

[166] David Tománek, Steven G Louie, H Jonathon Mamin, David W Abraham, Ruth Ellen Thomson, Eric Ganz, and John Clarke. Theory and observation of highly asymmetric atomic structure in scanning-tunneling-microscopy images of graphite. *Physical Review B*, 35(14):7790, 1987. 50

[167] S Ciraci, A Baratoff, and Inder P Batra. Tip-sample interaction effects in scanning-tunneling and atomic-force microscopy. *Physical Review B*, 41(5):2763, 1990. 51

[168] E Tekman and S Ciraci. Tip induced localized states in scanning tunneling microscopy. *Physica Scripta*, 38(3):486, 1988. 51

[169] R Dombrowski, Chr Steinebach, Chr Wittneven, M Morgenstern, and R Wiesendanger. Tip-induced band bending by scanning tunneling spectroscopy of the states of the tip-induced quantum dot on inas (110). *Physical Review B*, 59(12):8043, 1999. 51

[170] JM Soler, AM Baro, N Garcia, and H Rohrer. Interatomic forces in scanning tunneling microscopy: giant corrugations of the graphite surface. *Physical review letters*, 57(4):444, 1986. 51

[171] T Klitsner, RS Becker, and JS Vickers. Observation of the effect of tip electronic states on tunnel spectra acquired with the scanning tunneling microscope. *Physical Review B*, 41(6):3837, 1990. 51

[172] T Kwapiński and M Jałochowski. Signature of tip electronic states on tunneling spectra. *Surface science*, 604(19-20):1752–1756, 2010. 52

[173] JP Pelz. Tip-related electronic artifacts in scanning tunneling spectroscopy. *Physical Review B*, 43(8):6746, 1991. 52

[174] Sang-il Park, J Nogami, HA Mizes, and CF Quate. Chemical dependence of the multiple-tip effect in scanning tunneling microscopy. *Physical Review B*, 38(6):4269, 1988. 52

[175] Shuji Hasegawa, Ichiro Shiraki, Fuhito Tanabe, Rei Hobara, Taizo Kanagawa, Takehiro Tanikawa, Iwao Matsuda, Christian L Petersen, Torben M Hansen, Peter Boggild, et al. Electrical conduction through surface superstructures measured by microscopic four-point probes. *Surface Review and Letters*, 10(06):963–980, 2003. 57, 58

[176] Bert Voigtländer, Vasily Cherepanov, Stefan Korte, Arthur Leis, David Cuma, Sven Just, and Felix Lüpke. Invited review article: Multi-tip scanning tunneling microscopy: Experimental techniques and data analysis. *Review of Scientific Instruments*, 89(10):101101, 2018. 57, 59

[177] Leo J van der Pauw. A method of measuring the resistivity and hall coefficient on lamellae of arbitrary shape. *Philips technical review*, 20:220–224, 1958. 58

[178] Georg Kresse and Jürgen Hafner. Ab initio molecular dynamics for liquid metals. *Physical Review B*, 47(1):558, 1993. 62, 67

[179] Georg Kresse and Jürgen Furthmüller. Efficiency of ab-initio total energy calculations for metals and semiconductors using a plane-wave basis set. *Computational materials science*, 6(1):15–50, 1996. 62, 67

[180] Georg Kresse and Jürgen Furthmüller. Efficient iterative schemes for ab initio total-energy calculations using a plane-wave basis set. *Physical review B*, 54(16):11169, 1996. 62, 67

[181] Georg Kresse and Daniel Joubert. From ultrasoft pseudopotentials to the projector augmented-wave method. *Physical review b*, 59(3):1758, 1999. 62, 67

[182] Max Born and Robert Oppenheimer. Zur quantentheorie der molekeln. *Annalen der physik*, 389(20):457–484, 1927. 63

[183] David J Griffiths and Darrell F Schroeter. *Introduction to quantum mechanics*. Cambridge University Press, 2018. 63

[184] Douglas R Hartree. The wave mechanics of an atom with a non-coulomb central field. part i. theory and methods. In *Mathematical Proceedings of the Cambridge Philosophical Society*, volume 24, pages 89–110. Cambridge University Press, 1928. 63

[185] Douglas Rayne Hartree. The wave mechanics of an atom with a non-coulomb central field. part ii. some results and discussion. In *Mathematical Proceedings of the Cambridge Philosophical Society*, volume 24, pages 111–132. Cambridge University Press, 1928. 63

[186] Vladimir Fock. Näherungsmethode zur lösung des quantenmechanischen mehrkörperproblems. *Zeitschrift für Physik*, 61(1-2):126–148, 1930. 63

[187] Pierre Hohenberg and Walter Kohn. Inhomogeneous electron gas. *Physical review*, 136(3B):B864, 1964. 63

[188] Mel Levy. Electron densities in search of hamiltonians. *Physical Review A*, 26(3):1200, 1982. 64

[189] Walter Kohn and Lu Jeu Sham. Self-consistent equations including exchange and correlation effects. *Physical review*, 140(4A):A1133, 1965. 64, 66

[190] Paul Güttinger. Das verhalten von atomen im magnetischen drehfeld. *Zeitschrift für Physik*, 73(3-4):169–184, 1932. 65

[191] Hans Hellman. Einführung in die quantenchemie. *Franz Deuticke, Leipzig*, page 285, 1937. 65

[192] Richard Phillips Feynman. Forces in molecules. *Physical review*, 56(4):340, 1939. 65

[193] Axel D Becke. A new mixing of hartree–fock and local density-functional theories. *The Journal of chemical physics*, 98(2):1372–1377, 1993. 66

[194] Philip J Stephens, FJ Devlin, CFN Chabalowski, and Michael J Frisch. Ab initio calculation of vibrational absorption and circular dichroism spectra using density functional force fields. *The Journal of physical chemistry*, 98(45):11623–11627, 1994. 66

[195] David C Langreth and MJ Mehl. Beyond the local-density approximation in calculations of ground-state electronic properties. *Physical Review B*, 28(4):1809, 1983. 67

[196] Axel D Becke. Density-functional exchange-energy approximation with correct asymptotic behavior. *Physical review A*, 38(6):3098, 1988. 67

[197] John P Perdew, John A Chevary, Sy H Vosko, Koblar A Jackson, Mark R Pederson, Dig J Singh, and Carlos Fiolhais. Atoms, molecules, solids, and surfaces: Applications of the generalized gradient approximation for exchange and correlation. *Physical review B*, 46(11):6671, 1992. 67

[198] KEITH A BRUECKNER et al. Correlation energy of an electron gas with a slowly varying high density. *Physical Review*, 165(1):18, 1968. 67

[199] Viktor N Staroverov, Gustavo E Scuseria, Jianmin Tao, and John P Perdew. Comparative assessment of a new nonempirical density functional: Molecules and hydrogen-bonded complexes. *The Journal of chemical physics*, 119(23):12129–12137, 2003. 67

[200] Viktor N Staroverov, Gustavo E Scuseria, Jianmin Tao, and John P Perdew. Tests of a ladder of density functionals for bulk solids and surfaces. *Physical Review B*, 69(7):075102, 2004. 67

[201] John P Perdew, Kieron Burke, and Matthias Ernzerhof. Generalized gradient approximation made simple. *Physical review letters*, 77(18):3865, 1996. 67

[202] WJ Hehre, WA Lathan, R Ditchfield, MD Newton, and JA Pople. Gaussian 70 (quantum chemistry program exchange, 1970. 67

[203] José M Soler, Emilio Artacho, Julian D Gale, Alberto García, Javier Junquera, Pablo Ordejón, and Daniel Sánchez-Portal. The siesta method for ab initio order-n materials simulation. *Journal of Physics: Condensed Matter*, 14(11):2745, 2002. 67

[204] Peter Pulay. Ab initio calculation of force constants and equilibrium geometries in polyatomic molecules: I. theory. *Molecular Physics*, 17(2):197–204, 1969. 67

[205] Zijing Lin. Pulay forces in density functional theory for periodic and molecular systems. *Physics Letters A*, 299(4):413–417, 2002. 67

[206] John C Slater. Wave functions in a periodic potential. *Physical Review*, 51(10):846, 1937. 67

[207] Richard Car and Mark Parrinello. Unified approach for molecular dynamics and density-functional theory. *Physical review letters*, 55(22):2471, 1985. 67, 70

[208] Hendrik J Monkhorst and James D Pack. Special points for brillouin-zone integrations. *Physical review B*, 13(12):5188, 1976. 68

[209] D Jetal Chadi and Marvin L Cohen. Special points in the brillouin zone. *Physical Review B*, 8(12):5747, 1973. 68

[210] KN Kudin, JC Burant, JM Millam, SS Iyengar, J Tomasi, V Barone, B Mennucci, M Cossi, G Scalmani, N Rega, et al. Gaussian 03, revision c. 02. gaussian. *Inc.: Wallingford, CT*, 2004. 68

[211] Joachim Paier, Robin Hirschl, Martijn Marsman, and Georg Kresse. The perdew–burke–ernzerhof exchange-correlation functional applied to the g2-1 test set using a plane-wave basis set. *The Journal of chemical physics*, 122(23):234102, 2005. 68

[212] Mathis Gruber, Georg Heimel, Lorenz Romaner, Jean-Luc Brédas, and Egbert Zojer. First-principles study of the geometric and electronic structure of au 13 clusters: Importance of the prism motif. *Physical Review B*, 77(16):165411, 2008. 68

[213] DR Hamann, M Schlüter, and C Chiang. Norm-conserving pseudopotentials. *Physical Review Letters*, 43(20):1494, 1979. 68

[214] David Vanderbilt. Soft self-consistent pseudopotentials in a generalized eigenvalue formalism. *Physical review B*, 41(11):7892, 1990. 68

[215] G Kresse and J Hafner. Norm-conserving and ultrasoft pseudopotentials for first-row and transition elements. *Journal of Physics: Condensed Matter*, 6(40):8245, 1994. 68

[216] O Krogh Andersen. Linear methods in band theory. *Physical Review B*, 12(8):3060, 1975. 69

[217] DD Koelling and GO Arbman. Use of energy derivative of the radial solution in an augmented plane wave method: application to copper. *Journal of Physics F: Metal Physics*, 5(11):2041, 1975. 69

[218] M Weinert. Solution of poisson's equation: Beyond ewald-type methods. *Journal of Mathematical Physics*, 22(11):2433–2439, 1981. 69

[219] Erich Wimmer, Henry Krakauer, Michael Weinert, and Arthur J Freeman. Full-potential self-consistent linearized-augmented-plane-wave method for calculating the electronic structure of molecules and surfaces: O 2 molecule. *Physical Review B*, 24(2):864, 1981. 69

[220] Vasp workshop. 69, 70, 71

[221] Peter E Blöchl. Projector augmented-wave method. *Physical review B*, 50(24):17953, 1994. 69, 70

[222] Andrew M Rappe, Karin M Rabe, Efthimios Kaxiras, and JD Joannopoulos. Optimized pseudopotentials. *Physical Review B*, 41(2):1227, 1990. 70

[223] Joachim Paier, Martijn Marsman, K Hummer, Georg Kresse, Iann C Gerber, and János G Ángyán. Screened hybrid density functionals applied to solids. *The Journal of chemical physics*, 124(15):154709, 2006. 70

[224] Adam Kiejna, Georg Kresse, Jutta Rogal, Abir De Sarkar, Karsten Reuter, and Matthias Scheffler. Comparison of the full-potential and frozen-core approximation approaches to density-functional calculations of surfaces. *Physical Review B*, 73(3):035404, 2006. 70

[225] Péter Pulay. Convergence acceleration of iterative sequences. the case of scf iteration. *Chemical Physics Letters*, 73(2):393–398, 1980. 71, 72

[226] Michael P Teter, Michael C Payne, and Douglas C Allan. Solution of schrödinger's equation for large systems. *Physical Review B*, 40(18):12255, 1989. 71

[227] DM Bylander, Leonard Kleinman, and Seongbok Lee. Self-consistent calculations of the energy bands and bonding properties of b 12 c 3. *Physical Review B*, 42(2):1394, 1990. 71

[228] DM Wood and Alex Zunger. A new method for diagonalising large matrices. *Journal of Physics A: Mathematical and General*, 18(9):1343, 1985. 72

[229] James Hardy Wilkinson. *The algebraic eigenvalue problem*, volume 662. Oxford Clarendon, 1965. 72

[230] CG Davidson. 14) if f lag d 0 then. *Journal of Computational Physics*, 17:87–94, 1975. 72

[231] B Liu. Report on workshop "numerical algorithms in chemistry: Algebraic methods". *Lawrence Brekeley Laborartory, University of California: CA*, 1978. 72

[232] Danny EP Vanpoucke and Geert Brocks. Formation of pt-induced ge atomic nanowires on pt/ge (001): A density functional theory study. *Physical Review B*, 77(24):241308, 2008. 74

[233] Danny Eric Paul Vanpoucke. *Ab initio study of Pt induced nanowires on Ge(001)*. PhD thesis, Enschede, September 2009. 75

[234] Nan Gao, Hongsheng Liu, Si Zhou, Yizhen Bai, and Jijun Zhao. Interaction between post-graphene group-iv honeycomb monolayers and metal substrates: Implication for synthesis and structure control. *The Journal of Physical Chemistry C*, 121(9):5123–5129, 2017. 86

[235] Xiaofeng Feng, Sangku Kwon, Jeong Young Park, and Miquel Salmeron. Superlubric sliding of graphene nanoflakes on graphene. *ACS nano*, 7(2):1718–1724, 2013. 88

[236] Shigeki Kawai, Andrea Benassi, Enrico Gnecco, Hajo Söde, Rémy Pawlak, Xinliang Feng, Klaus Müllen, Daniele Passerone, Carlo A Pignedoli, Pascal Ruffieux, et al. Superlubricity of graphene nanoribbons on gold surfaces. *Science*, 351(6276):957–961, 2016. 88

[237] Dmitry A Muzychenko, Andrey I Oreshkin, Anna D Legen'ka, and Chris Van Haesendonck. Atomic insights into single layer and bilayer germanene on al (111) surface. *Materials Today Physics*, page 100241, 2020. 88, 96, 113

[238] S Bals, S Van Aert, CP Romero, Koen Lauwaet, Margriet J Van Bael, B Schoeters, B Partoens, E Yücelen, Peter Lievens, and G Van Tendeloo. Atomic scale dynamics of ultrasmall germanium clusters. *Nature communications*, 3(1):1–6, 2012. 88, 89

[239] Yoshiaki Nakamura, Kentaro Watanabe, Yo Fukuzawa, and Masakazu Ichikawa. Observation of the quantum-confinement effect in individual ge nanocrystals on oxidized si substrates using scanning tunneling spectroscopy. *Applied Physics Letters*, 87(13):133119, 2005. 88

[240] Wen-Cai Lu, CZ Wang, Li-Zhen Zhao, Wei Zhang, Wei Qin, and KM Ho. Appearance of bulk-like motifs in si, ge, and al clusters. *Physical Chemistry Chemical Physics*, 12(30):8551–8556, 2010. 88

[241] Yuichi Negishi, H Kawamata, F Hayakawa, Atsushi Nakajima, and K Kaya. The infrared homo–lumo gap of germanium clusters. *Chemical physics letters*, 294(4-5):370–376, 1998. 88

[242] Jinlan Wang, Guanghou Wang, and Jijun Zhao. Structure and electronic properties of ge n (n= 2–2 5) clusters from density-functional theory. *Physical Review B*, 64(20):205411, 2001. 88

[243] AL Efros and Boris I Shklovskii. Coulomb gap and low temperature conductivity of disordered systems. *Journal of Physics C: Solid State Physics*, 8(4):L49, 1975. 88

[244] Jin Wang and Ju-Guang Han. Geometries and electronic properties of the tungsten-doped germanium clusters: Wge n (n= 1- 17). *The Journal of Physical Chemistry A*, 110(46):12670–12677, 2006. 88

[245] I Chambouleyron and D Comedi. Column iii and v elements as substitutional dopants in hydrogenated amorphous germanium. *Journal of non-crystalline solids*, 227:411–417, 1998. 88

[246] Vladimir Nikolaevich Mantsevich and Natal'ya Sergeevna Maslova. Spatial effects of fano resonance in local tunneling conductivity in vicinity of impurity on semiconductor surface. *JETP letters*, 91(3):139–142, 2010. 88

[247] XG Gong and Vijay Kumar. Enhanced stability of magic clusters: A case study of icosahedral al 12 x, x= b, al, ga, c, si, ge, ti, as. *Physical review letters*, 70(14):2078, 1993. 88

[248] Xi Li and Lai-Sheng Wang. Experimental search and characterization of icosahedral clusters: Al 12 x-(x= c, g e, s n, pb). *Physical Review B*, 65(15):153404, 2002. 88

[249] JJ Hauser. Enhancement of superconductivity in aluminum films. *Physical Review B*, 3(5):1611, 1971. 88

[250] A Fontaine and F Meunier. Normal and superconducting properties of metallic grains (ai) embedded in a semiconductor (ge): Experimental evidence for an additional attractive mechanism between electrons. *Physik der kondensierten Materie*, 14:119–137, 1972. 88

[251] Guohong Li, Adina Luican, and Eva Y Andrei. Scanning tunneling spectroscopy of graphene on graphite. *Physical Review Letters*, 102(17):176804, 2009. 89

[252] Yuanbo Zhang, Victor W Brar, Feng Wang, Caglar Girit, Yossi Yayon, Melissa Panlasigui, Alex Zettl, and Michael F Crommie. Giant phonon-induced conductance in scanning tunnelling spectroscopy of gate-tunable graphene. *Nature Physics*, 4(8):627–630, 2008. 89

[253] Daniele Chiappe, Carlo Grazianetti, Grazia Tallarida, Marco Fanciulli, and Alessandro Molle. *Adv. Mater.*, 24(37):5088–5093, 2012. 89

[254] Yi Du, Jincheng Zhuang, Hongsheng Liu, Xun Xu, Stefan Eilers, Kehui Wu, Peng Cheng, Jijun Zhao, Xiaodong Pi, Khay Wai See, et al. *ACS Nano*, 8(10):10019–10025, 2014. 89

[255] Baojie Feng, Zijing Ding, Sheng Meng, Yugui Yao, Xiaoyue He, Peng Cheng, Lan Chen, and Kehui Wu. *Nano Lett.*, 12(7):3507–3511, 2012. 89

[256] A Díaz Álvarez, T Zhu, JP Nys, M Berthe, M Empis, J Schreiber, B Grandidier, and T Xu. *Surf. Sci.*, 653:92–96, 2016. 89

[257] Chun-Liang Lin, Ryuichi Arafune, Maki Kawai, and Noriaki Takagi. *Chin. Phys. B*, 24(8):087307, 2015. 89

[258] Carlo Grazianetti, Daniele Chiappe, Eugenio Cinquanta, Grazia Tallarida, Marco Fanciulli, and Alessandro Molle. *Appl. Surf. Sci.*, 291:109–112, 2014. 89

[259] Paola De Padova, Haifeng Feng, Jincheng Zhuang, Zhi Li, Amanda Generosi, Barbara Paci, Carlo Ottaviani, Claudio Quaresima, Bruno Olivieri, Mariusz Krawiec, et al. *J. Phys. Chem. C*, 121(48):27182–27190, 2017. 89

[260] Cameron Volders, Ehsan Monazami, Gopalakrishnan Ramalingam, and Petra Reinke. *Nano Lett.*, 17(1):299–307, 2016. 89

[261] Alexander N Obraztsov. Making graphene on a large scale. *Nature nanotechnology*, 4(4):212–213, 2009. 91

[262] Bing Deng, Zhongfan Liu, and Hailin Peng. Toward mass production of cvd graphene films. *Advanced Materials*, 31(9):1800996, 2019. 91

[263] Young-Woo Son, Marvin L Cohen, and Steven G Louie. Energy gaps in graphene nanoribbons. *Physical review letters*, 97(21):216803, 2006. 91

[264] Li Yang, Cheol-Hwan Park, Young-Woo Son, Marvin L Cohen, and Steven G Louie. Quasiparticle energies and band gaps in graphene nanoribbons. *Physical Review Letters*, 99(18):186801, 2007. 91

[265] Jinming Cai, Pascal Ruffieux, Rached Jaafar, Marco Bieri, Thomas Braun, Stephan Blankenburg, Matthias Muoth, Ari P Seitsonen, Moussa Saleh, Xinliang Feng, et al. Atomically precise bottom-up fabrication of graphene nanoribbons. *Nature*, 466(7305):470–473, 2010. 91

[266] Young-Woo Son, Marvin L Cohen, and Steven G Louie. Half-metallic graphene nanoribbons. *Nature*, 444(7117):347–349, 2006. 91

[267] Oded Hod, Verónica Barone, Juan E Peralta, and Gustavo E Scuseria. Enhanced half-metallicity in edge-oxidized zigzag graphene nanoribbons. *Nano letters*, 7(8):2295–2299, 2007. 91

[268] Y Niimi, T Matsui, H Kambara, K Tagami, M Tsukada, and Hiroshi Fukuyama. Scanning tunneling microscopy and spectroscopy of the electronic local density of states of graphite surfaces near monoatomic step edges. *Physical Review B*, 73(8):085421, 2006. 91

[269] L Pisani, JA Chan, B Montanari, and NM Harrison. Electronic structure and magnetic properties of graphitic ribbons. *Physical Review B*, 75(6):064418, 2007. 91

[270] De-en Jiang, Bobby G Sumpter, and Sheng Dai. First principles study of magnetism in nanographenes. *The Journal of chemical physics*, 127(12):124703, 2007. 91

[271] Francisco J Martín-Martínez, Stijn Fias, Gregory Van Lier, Frank De Proft, and Paul Geerlings. Electronic structure and aromaticity of graphene nanoribbons. *Chemistry–A European Journal*, 18(20):6183–6194, 2012. 91

[272] Verónica Barone, Oded Hod, and Gustavo E Scuseria. Electronic structure and stability of semiconducting graphene nanoribbons. *Nano letters*, 6(12):2748–2754, 2006. 91

[273] Ting Cao, Fangzhou Zhao, and Steven G Louie. Topological phases in graphene nanoribbons: junction states, spin centers, and quantum spin chains. *Physical review letters*, 119(7):076401, 2017. 91

[274] Daniel J Rizzo, Gregory Veber, Ting Cao, Christopher Bronner, Ting Chen, Fangzhou Zhao, Henry Rodriguez, Steven G Louie, Michael F Crommie, and Felix R Fischer. Topological band engineering of graphene nanoribbons. *Nature*, 560(7717):204–208, 2018. 91

[275] Oliver Gröning, Shiyong Wang, Xuelin Yao, Carlo A Pignedoli, Gabriela Borin Barin, Colin Daniels, Andrew Cupo, Vincent Meunier, Xinliang Feng, Akimitsu Narita, et al. Engineering of robust topological quantum phases in graphene nanoribbons. *Nature*, 560(7717):209–213, 2018. 91

[276] Yu-Ling Song, Yan Zhang, Jian-Min Zhang, and Dao-Bang Lu. Effects of the edge shape and the width on the structural and electronic properties of silicene nanoribbons. *Applied surface science*, 256(21):6313–6317, 2010. 91

[277] Paola De Padova, Claudio Quaresima, Carlo Ottaviani, Polina M Sheverdyaeva, Paolo Moras, Carlo Carbone, Dinesh Topwal, Bruno Olivieri, Abdelkader Kara, Hamid Oughaddou, et al. Evidence of graphene-like electronic signature in silicene nanoribbons. *Applied Physics Letters*, 96(26):261905, 2010. 91

[278] Motohiko Ezawa and Naoto Nagaosa. Interference of topologically protected edge states in silicene nanoribbons. *Physical Review B*, 88(12):121401, 2013. 91

[279] Yangyang Wang, Jiaxin Zheng, Zeyuan Ni, Ruixiang Fei, Qihang Liu, Ruge Quhe, Chengyong Xu, Jing Zhou, Zhengxiang Gao, and Jing Lu. Half-metallic silicene and germanene nanoribbons: towards high-performance spintronics device. *Nano*, 7(05):1250037, 2012. 91

[280] Qing Pang, Yan Zhang, Jian-Min Zhang, Vincent Ji, and Ke-Wei Xu. Electronic and magnetic properties of pristine and chemically functionalized germanene nanoribbons. *Nanoscale*, 3(10):4330–4338, 2011. 91

[281] Lars Matthes and Friedhelm Bechstedt. Influence of edge and field effects on topological states of germanene nanoribbons from self-consistent calculations. *Physical Review B*, 90(16):165431, 2014. 91

[282] Varun Sharma and Pankaj Srivastava. Aluminum doped germanene nanoribbons: A first principles investigation. *Integrated Ferroelectrics*, 204(1):58–62, 2020. 91

[283] Jifa Tian, Helin Cao, Wei Wu, Qingkai Yu, and Yong P Chen. Direct imaging of graphene edges: Atomic structure and electronic scattering. *Nano letters*, 11(9):3663–3668, 2011. 92

[284] S Neubeck, YM You, ZH Ni, P Blake, ZX Shen, AK Geim, and KS Novoselov. Direct determination of the crystallographic orientation of graphene edges by atomic resolution imaging. *Applied Physics Letters*, 97(5):053110, 2010. 92

[285] Geoffroy Prévot, Romain Bernard, Hervé Cruguel, and Yves Borensztein. Monitoring si growth on ag (111) with scanning tunneling microscopy reveals that silicene structure involves silver atoms. *Applied Physics Letters*, 105(21):213106, 2014. 96, 97

[286] R Bernard, Y Borensztein, H Cruguel, M Lazzeri, and Geoffroy Prévot. Growth mechanism of silicene on ag (111) determined by scanning tunneling microscopy measurements and ab initio calculations. *Physical Review B*, 92(4):045415, 2015. 97

[287] Mauro Satta, Stefano Colonna, Roberto Flammini, Antonio Cricenti, and Fabio Ronci. Silicon reactivity at the ag (111) surface. *Physical review letters*, 115(2):026102, 2015. 97

[288] FD Murnaghan. The compressibility of media under extreme pressures. *Proceedings of the national academy of sciences of the United States of America*, 30(9):244, 1944. 97

[289] H Brune, J Wintterlin, J Trost, G Ertl, J Wiechers, and RJ Behm. Interaction of oxygen with al (111) studied by scanning tunneling microscopy. *The Journal of chemical physics*, 99(3):2128–2148, 1993. 97

[290] Pekka Koskinen, Sami Malola, and Hannu Häkkinen. Self-passivating edge reconstructions of graphene. *Physical review letters*, 101(11):115502, 2008. 110

[291] RE Schlier and HE Farnsworth. Structure and adsorption characteristics of clean surfaces of germanium and silicon. *The Journal of Chemical Physics*, 30(4):917–926, 1959. 118

[292] Gerd Binnig, Heinrich Rohrer, Ch Gerber, and Eduard Weibel. 7× 7 reconstruction on si (111) resolved in real space. *Physical review letters*, 50(2):120, 1983. 118

[293] Shin-ichi Kitamura, Tomoshige Sato, and Masashi Iwatsuki. Observation of surface reconstruction on silicon above 800 c using the stm. *Nature*, 351(6323):215–217, 1991. 118

[294] Daejin Eom, Eonmi Seo, and Ja-Yong Koo. Surface-sensitive measurement of dielectric screening via atom and electron manipulations. *Physical Review B*, 94(19):195308, 2016. 119

[295] Dileep Mampallil and Huseyin Burak Eral. A review on suppression and utilization of the coffee-ring effect. *Advances in colloid and interface science*, 252:38–54, 2018. 120

[296] Robert W Stark, Tanja Drobek, and Wolfgang M Heckl. Tapping-mode atomic force microscopy and phase-imaging in higher eigenmodes. *Applied Physics Letters*, 74(22):3296–3298, 1999. 125

[297] Leopoldo B Valdes. Resistivity measurements on germanium for transistors. *Proceedings of the IRE*, 42(2):420–427, 1954. 133, 134

[298] Ilio Miccoli, Frederik Edler, Herbert Pfnür, and Christoph Tegenkamp. The 100th anniversary of the four-point probe technique: the role of probe geometries in isotropic and anisotropic systems. *Journal of Physics: Condensed Matter*, 27(22):223201, 2015. 133, 134

[299] John Albers and HL Berkowitz. An alternative approach to the calculation of four-probe resistances on nonuniform structures. *Journal of the Electrochemical Society*, 132(10):2453, 1985. 134

[300] K Matsubara, K Sugihara, and T Tsuzuku. Electrical resistance in the c direction of graphite. *Physical Review B*, 41(2):969, 1990. 137

[301] Hong Tang and S Roy Morrison. Optimization of the anisotropy of composite mos2 films. *Thin Solid Films*, 227(1):90–94, 1993. 137

[302] Edoardo Martino. Electrons leave the flatland: out-of-plane charge dynamics in layered materials. Technical report, EPFL, 2020. 137

[303] X-D Xiang, WA Vareka, A Zettl, JL Corkill, Marvin L Cohen, N Kijima, and R Gronsky. Metallization of the resistivity tensor in bi 2 sr 2 cacu 2 o x through epitaxial intercalation. *Physical review letters*, 68(4):530, 1992. 137